

LONDON'S GLOBAL UNIVERSITY



Fluid transport through porous media: A novel application of kinetic Monte Carlo simulations

A doctoral thesis by

Maria Apostolopoulou

In partial fulfilment of the requirements for the degree of

Doctor of Philosophy

at

University College London

Supervised by Prof. Alberto Striolo & Dr. Michail Stamatakis

UCL Chemical Engineering Department

July 2019

I, Maria Apostolopoulou confirm that the work presented in this thesis is my own. Where information has been derived from other sources, I confirm that they have been properly indicated in the thesis.

Signature

Date

Acknowledgements

I would first like to thank my supervisor Professor Alberto Striolo for his unwavering support and guidance throughout this PhD. Thank you for being honest and always there to provide your expertise, support, and guidance. I have truly appreciated all the opportunities you have given me and the trust you put in me to undertake this project.

I would also like to thank my co-supervisor Dr Michail Stamatakis for mentoring me through each step of the PhD. Thank you for always keeping an eye on the fine details, sharing your unique expertise and teaching me how to write code.

I am grateful to Halliburton and UCL chemical engineering department not only for the financial assistance that they offered me but also the priceless opportunity to work with industry leading experts and researchers.

A special thank you to Ron Dusterhoft and Richard Day for guiding me during my summer internship at Halliburton. It has been a pleasure working with you and the team.

Janette Cortez-Montalvo and Ubong Inyang, thank you for the long stochastic conversations and bringing this collaboration to life.

I would also like to thank Professor Ioannis Economou and his TAMUQ and Democritus team for collaborating with me during my PhD. Mirella, Hamza, Louka, and Manoli, I have learnt so much from all of you and hope you have enjoyed collaborating as much as I have.

Thank you to all my fellow [Room 310N] colleagues; Abeer, Tran, Tai, Zeynep, Anh, Sakiru, Dian, and Olivera, for all the funny moments and bubble tea breaks.

Lara Rasha, thank you for being such a cool and awesome friend.

Dina Ibrahim Abou El Amaiem, what to say? This journey wouldn't have been the same without having you with me. Thank you for all your support and sass.

Paul Nderitu, no words can describe how grateful I am to you. Thank you for always being there for me, listening to me talking about hops, trajectories, lattices, and the list goes on and on... I believe you are now a KMC expert, among all the other talents that you have. Most importantly, thank you for reminding me what matters the most, all your loving support, and making me a better person.

Finally, I would like to thank my wonderful parents, Sakis and Gogo, who have always been there for me every step of the way surrounding me with their endless love.

Abstract

With increasing global energy demands, unconventional formations, such as shale rocks, are becoming an important source of natural gas. Current efforts are focused on understanding fluid dynamics to maximise natural gas yields. Although shale gas is playing an increasingly important role in the global energy industry, our knowledge of the fundamentals of fluid transport through multiscale and heterogeneous porous media is incomplete, as both static and dynamic properties of confined fluids differ tremendously from those at the macroscopic scale. Transport models, derived from atomistic studies, are frequently used to bridge this gap. However, capturing and upscaling the interactions between the pore surface and fluids remains challenging.

In this thesis, a computationally efficient stochastic approach is implemented to simulate fluid transport through complex porous media. One-, two-, and three-dimensional kinetic Monte Carlo models were developed to predict methane transport in heterogeneous pore networks consisting of hydrated and water-free micro-, meso-, and macropores, representative of shale rock minerals. Molecular dynamics (MD) simulations, experimental imaging and adsorption data, which describe the surface – fluid interaction and the pore network features respectively were utilised to inform the KMC models.

The stochastic approach was used to (1) quantify the effect of the pore network characteristics (pore size, chemistry, connectivity, porosity, and anisotropy) on the transport of supercritical methane, (2) estimate the permeability of an Eagle Ford shale sample and evaluate the effect of proppants on permeability, and (3) to upscale atomistic insights and predict fluid diffusivity through different size pores. The results obtained were consistent with the analytical solutions of the diffusion equation, experimental data, and MD simulations, respectively, demonstrating the effectiveness of the stochastic approach. In addition, the applicability of less computationally intensive deterministic approaches was examined using multiple case studies; recommendations are provided on the optimal conditions under which each method can be used.

Impact Statement

As global energy demands continue to grow, shale rocks, a type of unconventional formations, are becoming an important source of natural gas. According to recent technoeconomic data, natural gas consumption has risen by 5.3% and natural gas is expected to have the highest production growth until 2050. Extensive efforts focus on understanding the complex behaviour of fluids (including their transport in the sub-surface) to maximise natural gas yields. This thesis addresses the important topic of gas permeability across unconventional sub-surface formations. This topic is critical for the development of conventional, and perhaps even more so for unconventional formations.

In this research study, a novel stochastic approach, based on Kinetic Monte Carlo (KMC) simulations is implemented to ultimately predict the permeability of pore networks, resembling those found in shales, based on experimental characterisations that include pore size distributions, geochemical composition, and imaging data. The KMC model was developed and validated in one-, two-, and three- dimensions (1D, 2D, 3D) and was proven to be suitable for studies of fluid transport in porous networks, a field where such data was previously lacking. The results obtained from large portions of this research study, included in this thesis, have already been peer reviewed and published, with two manuscripts pending. During my research I collaborated with many teams, most notably, the sponsor of this research, Halliburton, and TAMUQ. The output of the collaborative work with Halliburton was the demonstration of the importance of maintaining microfracture conductivity when using proppants, which has direct commercial application in the field of flow enhancement.

Compared to other computational approaches, for instance molecular dynamics simulations (MD), the low computational cost of the KMC method allows to address long-standing questions in the porous materials community, such as at what pore sizes can the transport properties of confined fluids be described by their bulk counterparts? This research study is also used to provide recommendations on how possible technological approaches, involved in the hydraulic fracturing design, can be applied to maximise gas

extraction, through 3D pore network modelling. Moreover, the insights obtained from the use of KMC to study fluid transport in porous media is transferable to numerous relatable fields, from waste management of radioactive materials to design of porous catalytic beds.

With further development of the KMC approach, coupled with the generation of digital libraries enhanced by AI models would potentially allow an end user to dynamically evaluate rock characteristics of new and already explored shale plays to optimise oil and gas production.

List of Publications

Apostolopoulou M, Day R, Hull R, Stamatakis M, Striolo A. A kinetic Monte Carlo approach to study fluid transport in pore networks. *J Chem Phys.* 2017;147(134703):1-10.

Cortez-Montalvo J, Inyang U, Dusterhoft R, Hu D, **Apostolopoulou M**. Laboratory evaluation of apparent conductivity of ultra-fine particulates. *SPE/AAPG/SEG Unconv Resour Technol Conf* Houston, Texas, 23-25 July URTeC-2902308-MS. 2018.

Apostolopoulou M, Dusterhoft R, Day R, Stamatakis M, Coppens MO, Striolo A. Estimating permeability in shales and other heterogeneous porous media: Deterministic vs. stochastic investigations. *Int J Coal Geol.* 2019;205:140-154.

Inyang U, Cortez-Montalvo J, Dusterhoft R, **Apostolopoulou M**, Striolo A, Stamatakis M. A Kinetic Monte Carlo Study to Investigate the Effective Permeability and Conductivity of Microfractures within Unconventional Reservoirs. *SPE Oklahoma City Oil Gas Symp held Oklahoma City*, Oklahoma, 9-10 April SPE-195220-MS. 2019.

Apostolopoulou M, Santos S.M, Hamza M, Bui T, Economou G.I, Stamatakis M, Striolo A. Quantifying Pore Width Effects on Diffusivity via a Novel 3D Stochastic Approach with Input from Atomistic Molecular Dynamics Simulations. *J. Chem. Theory Comput.* 2019, 15, 12, 6907-6922.

Apostolopoulou M, Stamatakis M, Striolo A. A novel 3D Pore Network Modelling Approach to Stochastically Evaluate the Impact of Pore Network Geometry, Chemistry and Topology on Fluid Transport. 2019, manuscript in preparation.

Contents

Chapter 1: Background and literature review	1
1.1 Shale gas opportunities – Motivation	1
1.1.1 Natural gas in the USA market economy	3
1.1.2 Natural gas in the UK market economy	4
1.1.3 Hydraulic fracturing, technological improvements, and risks	7
1.2 Shale gas characteristics	11
1.2.1 Chemical composition	11
1.2.2 Pore characteristics (porosity and pore size distribution).....	13
1.2.3 Matrix permeability	14
1.2.4 Anisotropy and heterogeneity in shales.....	16
1.3 Transport characteristics.....	17
1.4 Methods of analysis	22
1.4.1 Experimental methods	22
1.4.2 Computational methods	23
1.5 Thesis Structure.....	31
Chapter 2: Methodology – Kinetic Monte Carlo simulations	33
2.1 Introduction.....	33
2.2 From MC to KMC.....	33
2.3 Rare event dynamics and the timescale problem.....	34
2.4 Method requirements	36
2.5 The Master equation	37
2.6 Determination of the transition rates	39
2.7 From MD to KMC simulations: Bottom up approach.....	45
2.8 KMC algorithms	47
2.8.1 Rejection method.....	47
2.8.2 Rejection-free method.....	48
2.8.3 Random selection method	49
2.8.4 First reaction method	49
2.8.5 Direct method – Gillespie’s algorithm.....	50
2.9 More efficient selection algorithms	53
2.10 Selection of the random number generator.....	56
2.11 Summary	57
Chapter 3: Algorithm construction, validation, and application in 1D networks	59
3.1 KMC algorithm construction– Part I.....	60
3.1.1 From reactive to purely diffusive systems	60

3.2 A KMC approach to study fluid transport in 1D pore networks – Part II	74
3.2.1 Abstract	74
3.2.2 Introduction	74
3.2.3 Theoretical background.....	76
3.2.4 Simulation models and methodology.....	78
3.2.5 Results and discussion	87
3.3 Conclusions	94
Chapter 4: KMC algorithm extension to 2D; Studies in synthetic pore networks and shale samples.....	96
4.1 Estimating permeability in shales and other heterogeneous porous media: Deterministic vs. stochastic investigations – Part I.....	97
4.1.1 Abstract	97
4.1.2 Introduction	97
4.1.3 Methods.....	99
4.1.4 Systems investigated.....	110
4.1.5 Results and discussion	118
4.2 A Kinetic Monte Carlo study to investigate the effective permeability and conductivity of microfractures within unconventional reservoirs – Part II.....	138
4.2.1 Abstract	138
4.2.2 Introduction	139
4.2.3 Materials and methods.....	142
4.2.4 Results and discussion	149
4.3 Conclusions	155
Chapter 5: KMC algorithm extension to 3D; Studies in single pores and pore networks	159
5.1 Quantifying pore width effects on diffusivity via a novel 3D stochastic approach with input from atomistic molecular dynamics simulations – Part I	160
5.1.1 Abstract	160
5.1.2 Introduction	161
5.1.3 Methodology	163
5.1.4 Results and discussion	174
5.2 A novel 3D pore network modelling approach to stochastically evaluate the impact of pore network geometry, chemistry and topology on fluid transport – Part II	191
5.2.1 Abstract	191
5.2.2 Introduction	192
5.2.3 Methodology	195
5.2.4 Results and discussion	206
5.3 Conclusions	217
Chapter 6: Summary and future work	221

Appendix A	227
Validation of the KMC algorithm – Gillespie’s reaction networks	227
System 1	227
System 2	228
System 3	231
System 4	235
System 5	238
Chapter 7: References.....	242

List of Figures

Chapter 1

Figure 1. 1: World natural gas demand by selected regions. Reproduced from IEA's report. ¹	1
Figure 1. 2: Natural gas consumption per capita 2018 in tones oil equivalent. Reproduced from BP's report. ⁴	2
Figure 1. 3: Historic data and predictions regarding (A) the U.S gross energy trade, (B) the U.S net energy imports, and (C) the electricity generation from selected fuels. Reproduced and modified by EIA. ⁷	4
Figure 1. 4: Gas import by country in 2017, reproduced from National Statistics. ⁸	5
Figure 1. 5: Energy demand in the UK by sector. Image reproduced from National Statistics. ⁹	6
Figure 1. 6: Imports, production and exports of natural gas in the UK. Image reproduced from the UK National Statistics. ⁹	7
Figure 1. 7: Summary of the stages involved in the production of shale gas and oil, reproduced from the report produced by UK's Department of energy and climate change. ¹⁴	8
Figure 1. 8: A) Combination of horizontal drilling and hydraulic fracturing, reproduced from Soeder ¹⁶ , and B) representation of a mutli-fractured system, adapted from Cheng et al., ¹⁷ B1 shows the fractures generated after the hydraulic fluids have been channelled through the primary fractures (B.2), resulting to the generation of secondary fractures (B.3).....	9
Figure 1. 9: QEMSCAN chemical maps of Bowland sample at spacing resolution of (a) 10 micron and (b) 1 micron. Reproduced from Backeberg et al. ³⁶	12
Figure 1. 10: Example of heterogeneous distribution of grain density in a grain rich rock sample. Reproduced from Dullien. ⁶⁶	17
Figure 1. 11: Transition of the flow regimes as a function of the Knudsen number. Reproduced from Song et al. ⁷³	20
Figure 1. 12: Single component gas transport mechanisms through a narrow pore. Reproduced from Wang et al. ⁷⁶	21

Chapter 2

Figure 2. 1: Representation of a barrier which leads to a higher-energy state (A) and one which leads to a lower state (B).	36
Figure 2. 2: Length and time scales achieved during the modelling of film growth using DFT, MD, and KMC simulations, as reproduced by Kratzer. ¹⁵⁷	36

Figure 2. 3: Illustration of the transition state theory rate constant, reproduced from Voter. ¹⁵⁶	40
Figure 2. 4: Coarse-graining of a MD trajectory into a Markov chain. (Left) A possible MD trajectory (black) overlaid on the underlying PES of the system with red regions representing lower-energy basins. (Middle) Coarse-graining of PES minima into positions on a suitably defined lattice. Each lattice position represents the basin of attraction of a PES minimum. (Right) Coarse-graining of the continuous MD trajectory into a Markov chain of discrete hops between the basins/lattice positions. Reproduced from Andersen et al. ¹⁷⁷	46
Figure 2. 5: Gillespie's algorithm. ¹⁸³	53
Figure 2. 6: Binary tree data structure used to store propensities, noted as ar. For each partial sum there are only two assigned partial sums – propensities. Reproduced from Gibson and Bruck. ¹⁸⁶	55
Figure 2. 7: Log-log plot of the time required per event for different search schemes, reproduced and modified by Blue et. al. ¹⁸⁵ K=2 (circles), K=3 (squares), K=4 (triangles pointing up), K=5 (triangles pointing down), and binary tree (rhombus). Reproduced and modified from Blue et al. ¹⁸⁵	56

Chapter 3

Figure 3. 1: Representation of the 2D sample space in an off-lattice (left) and on-lattice (right) lattice system.....	61
Figure 3. 2: Representation of the possible pathways in a 1D domain with reflective boundaries. For N square voxels there are $2N - 2$ possible moves a molecule can make.	62
Figure 3. 3: Representation of a simple 3 voxel lattice. The possible pathways with rates $k(i)$, $i \in [1,4]$, are noted as green arrows.	62
Figure 3. 4: Frequency of event occurrence for different time intervals. The y-axis represents the time required for a transition to happen. Each bar represents a 0.1s and $0 \leq t \leq 8s$	64
Figure 3. 5: The time evolution of the population in the middle voxel as predicted from the stochastic and the deterministic approach for $0 \leq t \leq 300s$ (top panel) and $dtsample = 0.02s$. Representation of the samples taken, represented by red dashed lines and the occurrence of events, presented as asterisks (bottom panel).....	65
Figure 3. 6: The time evolution of the population in the middle voxel as predicted from the stochastic and the deterministic approach for $0 \leq t \leq 300s$ (top panel) and $dtsample = 1.73s$. Representation of the samples taken, represented by red dashed lines and the occurrence of events, presented as asterisks (bottom panel).....	66

Figure 3. 7: The time evolution of the population in the middle voxel as predicted from the stochastic and the deterministic approach for $0 \leq t \leq 300s$ (top panel) and $\Delta t_{\text{sample}} = 5s$. Representation of the samples taken, represented by red dashed lines and the occurrence of events, presented as asterisks (bottom panel)..... 67

Figure 3. 8: Correlation between the increasing sample size and the standard deviation of the error between the stochastic and deterministic model. The sample size increased by a factor of 10 in each simulation run..... 68

Figure 3. 9: Snapshots of concentration profiles at $t_0 = 0$ (panel A), $t_1 = 2ns$ (panel B), $t_2 = 9ns$ (panel C) and $t_3 = 0.1\mu s$ (panel D), as predicted by the KMC algorithm (blue line) and the 1D diffusion equation (red line)..... 71

Figure 3. 10: Concentration profile of the 30th and 100th voxel as a function of time. The blue line corresponds to the stochastic approach and the red line represents the solution of the 1D equation. 72

Figure 3. 11: Representation of our simulated system and the transition rates at the interfaces. Region 1 (R1) corresponds to the bulk methane reservoirs, Region 2 (R2) symbolises the layer of water formed outside of the pores and Region 3 (R3) represents the silicon oxide pore. 79

Figure 3. 12: Density profiles of water (red) and methane (blue) molecules inside 1nm wide slit-shaped pores. The dashed grey lines denote the borders of the water layer (region 2). Reproduced from Phan et al.⁸⁸ 81

Figure 3. 13: The KMC lattice implemented for the silicon oxide flux calculations. Reproduced from Apostolopoulou et al.¹⁴⁰ 84

Figure 3. 14: The KMC lattice implemented for the MFPT calculations. The methane molecule is initially placed in voxel No.86 and moves towards voxel No.1. Movement towards direction x_b is disabled. Reproduced from Apostolopoulou et al.¹⁴⁰ 86

Figure 3. 15: Representation of the network design used to calculate the molar flux. The light green colour corresponds to the gas methane region, the light purple denotes the water layer outside of the pore and the orange voxels represent the pore. Reproduced from Apostolopoulou et al.¹⁴⁰ 87

Figure 3. 16: Cumulative number of methane molecules (Q_t) in the permeate region (blue dots) as a function of time for the hydrated silica slit-shaped pore (left panel), the magnesium oxide (middle panel) and the aluminium oxide pore (right panel). The red line corresponds to a least-squares fitted line..... 88

Figure 3. 17: Results obtained implementing the KMC model presented here versus MD simulations by Phan et al.,⁸⁸ for flux (left panel) and permeability (right panel). The results obtained from both methods are presented with error bars. 89

Figure 3. 18: Mean First Passage Time profiles of 40 nm wide pores as obtained by KMC calculations and Phan et al.,⁸⁸(MD)..... 90

Figure 3. 19: Effect of the pore length on membrane flux (left panel) and the effect of pore length on the % of flux decrease as calculated from KMC simulations (right panel). The flux obtained for the different pore lengths is reported with error bars. 91

Figure 3. 20: Comparison between the KMC model and analytical expressions for the effect of pore length on the observed flux. 92

Figure 3. 21: Fluxes calculated for 1D pore networks with different pore connectivity (see Figure 3.15 for description of Type 1, 2, and 3 networks)..... 93

Chapter 4

Figure 4. 1: Schematic of simplified renormalisation Method algorithm; (left) matrix considered and the voxels' IDs; (middle) process for calculating kLB; (right) process of calculating the kUB; AM stands for arithmetic mean and HM for harmonic mean. Eq. (4.7) calculates the effective matrix permeability. 102

Figure 4. 2: Fictitious 5x5 lattice with the numbers representing the voxel ID; green-coloured voxels are assigned with permeability of 1nD, pink ones with 100 nD. 106

Figure 4. 3: KMC rates for the dual-porosity 5x5 lattice. Red arrows represent transitions from low- to high-permeability regions, and blue arrows indicate KMC rates for jumps between low-permeability regions. 107

Figure 4. 4: (Left): Log-scale PSDs considered in this study analysis. In all cases the distribution's μ , is 37.15 nm, while sigma ranges between 0.1 and 1. (Right): Example of spatial arrangement of the permeability coefficients for sigma=0.1. 112

Figure 4. 5: Networks consisting of micro- and mesopores (a-c) and macro- and mesopores (d-f). The colour bars show the permeability coefficients assigned, in μ D. 114

Figure 4. 6: Dual-permeability networks with different anisotropic distributions. Cases A and B exhibit high anisotropy and cases C and D have low and moderate anisotropy. The colour bars show permeability coefficients in μ D..... 115

Figure 4. 7: SEM image of an Eagle Ford sample, reproduced from Naraghi et al.¹⁰² Dark grey regions correspond to organic matter and light grey to inorganic. 117

Figure 4. 8: Validation of the branching algorithm. When the value=0, there is agreement between the two algorithms implemented in terms of the event selected at each time. 119

Figure 4. 9: Computational savings when implementing the branching algorithm in a 100x100 lattice. 120

Figure 4. 10: A) comparison between the target permeability used as an input for the calculation of the KMC rates and the calculated effective matrix permeability at the end of the simulations. The results provide the validation of the proposed process. B)

representation of the KMC lattice used for the validation process. The colour bar indicates the number of particles for the initial configuration.	122
Figure 4. 11: (A) Comparison of the three methods used in this study as a function of the distribution's sigma; KMC error bars are estimated to be smaller than the size of the marker. (B) Percent deviation of the deterministic models compared to the stochastic calculation. (C) Percent of volume comprised of micro-, meso- and macropores in each system shown in (A). Lines in (A) and (B) are guides to the eye. The matrices simulated here are isotropic with PSDs shown in Figure 4.4.	123
Figure 4. 12: Mean and confidence intervals of 10 independent KMC runs for each stochastic realisation. The network (Section 3.1) has log-normal PSD with $\mu=37.15$ nm and $\sigma=0.1$	126
Figure 4. 13: Mean permeability values calculated using the KMC method for the networks described in subsection 4.1.4.1. The error bars represent the confidence intervals for 99.9% confidence level.	127
Figure 4. 14: Sensitivity analysis on the pore type in dual-permeability networks (Figure 4.5) with varying component % volume amount; (A) shows results for the network consisting of micro- and mesopores; (B) for the network with meso- and macropores.	129
Figure 4. 15: Effective matrix permeability calculation using the three methods for networks with varying anisotropy (left) and diffusivity analysis in the x and y directions and the xy plane (right).	131
Figure 4. 16: Covariance matrix analysis of the anisotropic networks. Black x-axis shows the first principal component and the black y-axis the second. The purple arrows are vectors showing the preferential diffusion direction.	131
Figure 4. 17: Example of the permeability distribution within the organic matter (left), permeability distribution of the inorganic matter (middle) and the distribution of organic matter in the inorganic matrix (right). The colour bars represent permeability coefficients in μD	134
Figure 4. 18: Results of UFPs within the condensate portion of the Barnett Shale field that exhibit normalised cumulative production for an 11 well program on three pads using direct offset wells for comparison; UFPs were used for 5 of the 11 wells. Reproduced by Dahl et al. ²³⁶	141
Figure 4. 19: Reservoir setup for production history matching and analysis for two direct offset wells: Well 9 with UFPs and conductive natural fractures and Well 10 with no UFPs and no conductive natural fractures. (Left) unstructured gridding used for the simulation; (right) pressure distribution within the reservoir after 242 days. Reproduced by Dahl et al. ²³⁶	142

Figure 4. 20: Sawed Marcellus core after one half was treated with 0.001 lbm/ft ² of UFPs. Reproduced from Inyang et al. ²³⁷	144
Figure 4. 21: 11 × 10 × 1 mm KMC lattice; each lattice voxel is 1 × 1 × 1mm. The cyan voxels represent the low permeability rock matrix and the red ones an induced MF. Permeability of the cyan voxels (refer to Table 4.5) is calculated following the previously described process. Reproduced from Inyang et al. ²³⁷	145
Figure 4. 22: KMC lattice used to investigate the effect of the proppant concentration. The blue voxels represent the rock matrix, the red voxels represent the induced MFs, and the yellow regions are 2 nd MFs where proppants were homogeneously distributed. Reproduced from Inyang et al. ²³⁷	146
Figure 4. 23: Conceptual model used to represent the effect of a single proppant particle (blue sphere) within a compact rock matrix, where ht is height and bt is the base of the generated triangle corresponding to void space. Permeability of the void space and the compact rock matrix are denoted as kf and kmatrix, respectively. Reproduced from Inyang et al. ²³⁷	147
Figure 4. 24: Permeability distribution for the three systems considered. The colour bar displays the permeability in μD. For all three systems, an induced MF with uniform permeability is included. Reproduced from Inyang et al. ²³⁷	148
Figure 4. 25: Schematic of the three systems used to quantify the effect of the leakoff zone on the achieved permeability. Reproduced from Inyang et al. ²³⁷	148
Figure 4. 26: Conductivity of MFs prepared from Marcellus (left) and Eagle Ford (right) cores with and without 0.001 lbm/ft ² of UFP treatments.	150
Figure 4. 27: Relationship between the fracture width maintained and the conductivity achieved for the case of 50-nD matrix permeability.....	153
Figure 4. 29: Effective fracture width calculated for the untreated (U) and treated (T) Eagle Ford sample as a function of the confining stress experimentally applied. Purple represents the experimental data, and simulation results are red.	154
Figure 4. 30: Effective fracture width calculated for the untreated (U) and treated (T) Marcellus sample as a function of the confining stress experimentally applied. Purple represent the experimental data, and simulation results are red.	154

Chapter 5

Figure 5. 1: Schematic of the MD simulation set up (left), the criteria for determining the 3 regions that describe the density of confined methane (middle), and a 2D slice of a typical 3D KMC simulation set up (right). In the left panel, for visualization purposes, the solid support is silica. The dashed red lines in the middle panel identify Regions 1, 2, and 3, and serve as guides to the eye.	166
---	-----

Figure 5. 2: Schematic of the KMC algorithmic steps performed to simulate methane diffusion through pores of varying widths. 174

Figure 5. 3: Density of CH₄ close to the surface of the 5 substrates (bottom panel). The top panel shows the composition of the 5 solid supports, as reproduced by Bui et al.,¹⁹⁸ Colour code: Si=yellow, Mg= tan, Al=pink, K=purple, C=green, Ca=blue, O=red, and H=white. 175

Figure 5. 4: Density profiles for the 5 nm pores (black lines) and the 10 nm pores (blue lines). The top panel (Silica) provides the comparison between the 5 nm and 10 nm density profiles as a function of the distance from the pore wall. 176

Figure 5. 5: Diffusion coefficient calculated in Regions 1, 2, and 3, as well as in the whole simulation box (Total). Panel (A) shows the results obtained for the 5 nm pores, and panel (B) shows the results for the 10 nm pores, respectively. 180

Figure 5. 6: Diffusion coefficients in the X and Y direction, calculated in Regions 1, 2, and 3, as well as in the whole simulation box (Total). Panel (A) shows the results obtained for the 5 nm pores, and panel (B) shows the results for the 10 nm pores, respectively. 180

Figure 5. 7: Analysis of anisotropic diffusion in calcite. The y axis shows the % absolute deviation between Dx and Dy values measured in the three regions and the overall (Total) pore, using 3 different pore widths. 180

Figure 5. 8: Density (panel – A) and RDFs (panel – B) for the 3 systems used to represent systems with exceptionally strong solid-fluid interactions. 181

Figure 5. 9: Analysis of the surface interaction effect as a function of the physical extent of Regions 1 & 3 (panel A), number of molecules adsorbed (panel B), diffusivity in Regions 1,2, and 3 (panel C), and overall (total) diffusivity predicted using EMD simulations and the KMC model (panel D). 183

Figure 5. 10: Surface density profiles for the 3 silica-methane systems as a function of surface-methane interactions. Panel (A) shows the realistic silica surface, while panels (B) and (C) the surfaces that are 5 and 25 times more attractive, respectively. Methane molecules in the first and second adsorbed layer were considered for this analysis. 183

Figure 5. 11: (A) Representation of the 3D KMC non-periodic system. The red region represents the area where the molecules were initially distributed. The comparison between the analytical equation and the 3D KMC predictions for (B) Voxel 5 and (C) Voxel 10, respectively. 184

Figure 5. 12: Validation of the 3D KMC algorithm using a periodic system. 185

Figure 5. 13: Overall (D_{xyz}) diffusion coefficient as a function of the pore width for the 5 solid supports considered here for the whole pore. Comparison between KMC predictions and EMD data. Note that the deviation between KMC and MD data is less than 10%. 187

Figure 5. 14: Distributions considered for the networks' connectivity. A) Sigma=1 and constant, B) Mu=2, and constant, and C) Mu=5, and constant.....	197
Figure 5. 15: Representation of the 3D and 2D pore networks generated while considering porosity values 10%-50%. As porosity increases, the cluster connectivity increases.....	198
Figure 5. 16: Representation of three equivalent 3D pore networks with 25% porosity and high connectivity (mu=5). For every porosity value considered, 5 equivalent networks were generated.....	199
Figure 5. 17: Pore throat size distributions considered when (A) Sigma=1 nm and remains constant while mu changes, and (B) Mu = 25 nm and remains constant while sigma changes.	200
Figure 5. 18: Digital Libraries obtained from Part I of this chapter, presenting the relationship between the pore chemistry, the pore throat width, and the diffusivity....	201
Figure 5. 19: Representation of the 3D KMC lattice containing 10 voxels in the x, and y dimensions, and 5 voxels in the z, yielding a 500-voxel lattice. All boundaries are periodic.....	202
Figure 5. 20: The algorithmic steps implemented for the pore network generation using a stochastic approach.....	203
Figure 5. 21: Algorithm for 3D KMC independent runs.....	206
Figure 5. 22: Effect of the networks' connectivity on methane diffusivity. A - Results obtained when the networks' sigma value equals 1 and mu increases. B and C – Results for networks with low (mu=2), and high (mu=5) connectivity, respectively, with increasing sigma. The distributions representing the networks in A-C are shown in Figure's 1 A-C, respectively.....	208
Figure 5. 23: Relationship between the networks' porosity and methane diffusivity for (A) low connectivity (mu=2) and (B) high connectivity (mu=5) networks. The error bars are calculated considering 5 equivalent pore networks for each porosity value and applying Eq. (5.12).....	211
Figure 5. 24: Relationship between the pore throats width size distribution and methane diffusivity for (A) low connectivity and (B) high connectivity networks. For the mu of the pore throat widths, the distributions presented in Figure 5.17 – panel A are considered.	212
Figure 5. 25: Relationship between the pore throat width size distribution and methane diffusivity for (A) low connectivity and (B) high connectivity networks. For the sigma of the pore throat widths, the distributions presented in Figure 5.17 – panel B are considered.....	214

Figure 5. 26: The effect of pore throat chemistry on the self-diffusion coefficient of supercritical methane. Results for pore networks with low and high connectivity are shown in panels A and B, respectively.	215
Figure 5. 27: Sensitivity analysis on the impact of connectivity, porosity, and pore throat width size distribution on methane diffusion coefficient. Results for pore networks with low and high connectivity are shown in panel A and B, respectively.	216

Chapter 6

Figure 6.1: A stochastic approach to calculate matrix permeability using imaging, porosity and pore size distribution data.	225
--	-----

Appendix

Figure A. 1: Comparison between Gillespie's data (left panel) and the KMC code data (right panel).	228
Figure A. 2: Comparison between Gillespie's data (left panel) and the KMC code data (right panel) for the second system. Two different initial configurations are shown for the population of Y species together with the deterministic steady state $Y_s = 1000$	230
Figure A. 3: Comparison between Gillespie's data (left panel) and the KMC code data (right panel) for species Y1 and Y2 for $0 \leq t \leq 10$ s. The straight black line corresponds to the deterministic steady state $Y_{1s}, Y_{2s} = 1000$	232
Figure A. 4: Comparison between Gillespie's data (left panel) and the KMC code data (right panel) for species Y1 for $0 \leq t \leq 30$ s. The straight black line corresponds to the deterministic steady state $Y_{1s} = 1000$	232
Figure A. 5: Comparison between Gillespie's data (left panel) and the KMC code data (right panel). The population of species Y1 is plotted against the population of species Y2 for $0 \leq t \leq 30$ s.	233
Figure A. 6: The population of species Y1 as calculated by four independent KMC simulations for $0 \leq t \leq 30$ s, while using different starter numbers to initiate the u.r.n.g.	234
Figure A. 7: The population of species Y1 and Y2 in the case of mutual extinction (left panel) and in the case of species Y2 extinction (right panel).	235
Figure A. 8: Comparison between Gillespie's data (left panel) and the KMC code data (right panel) for species Y1 for $0 \leq t \leq 14$ s. Samples are exported for every 100 reactions simulated.	236

Figure A. 9: Comparison between Gillespie's data (left panel) and the KMC code data (right panel) for species Y1 for $0 \leq t \leq 14$ s. Samples are exported for every 100 reactions simulated..... 237

Figure A. 10: Comparison between Gillespie's data (left panel) and the KMC code data (right panel). The population of species Y1 is plotted against the population of species Y2 for $0 \leq t \leq 18$ s. Samples are exported for every 50 reactions simulated..... 237

Figure A. 11: Comparison between Gillespie's data (left panel) and the developed KMC (right panel). The time evolution of species Y1, Y2 and Y3 is plotted for every 100 reactions simulated..... 240

Figure A. 12: Comparison between Gillespie's data (left panel) and the KMC code data (right panel), over the time interval $0 \leq t \leq 3$ s. The time evolution of species Y1, Y2 and Y3 is plotted for every 250 reactions simulated. 240

List of Tables

Table 1. 1: Properties of major shales in USA, China, and Canada	16
Table 3. 1: Diffusion coefficient of methane and energy barriers (ΔF), as obtained from Phan et al., ⁸⁸ and probability of occupancy in Regions 2 and 3 for the three substrates considered.	80
Table 3. 2: Length of the water layer formed outside of the three pores and the probability of occupancy between regions 1 and 2.	81
Table 3. 3: The probability of occupancy between Regions 1, 2 and 3.	82
Table 3. 4: Description of the lattice implemented for the KMC model.	83
Table 3. 5: Flux and permeability calculations obtained by the KMC model	88
Table 4. 1: Voxel IDs and array of the corresponding permeability coefficients, as defined by Figure 4.2.	106
Table 4. 2: Input parameters used for the permeability simulations for all three methods.	109
Table 4. 3: List of the target permeability coefficients used as an input during our validation process.	122
Table 4. 4: Permeability calculation of the organic and inorganic matter, and the effective network permeability using EMT, simplified renormalisation and KMC methods. Error bars for matrix permeability calculation for Methods I and II are based on the minimum, maximum and average permeability using Eq. (4.18). The uncertainty assigned to the KMC calculation represents the confidence interval (99.9%).	134
Table 4. 5: Permeability calculation of the organic and inorganic matter, and the effective network permeability using EMT, simplified renormalisation and KMC methods. The organic matter is the high-permeability component. The uncertainty assigned to the KMC calculation represents the confidence interval (99.9%).	137
Table 4. 6: Effect of fracture width on effective matrix permeability	151
Table 4. 7: Effect of proppant concentration on permeability achieved.	151
Table 4. 8: Effect of the leakoff zone on permeability achieved.	152
Table 5. 1: Simulation box dimensions used to simulate the 5 nm and 10 nm wide pores using five solid supports.	164
Table 5. 2: Comparison between the thicknesses of regions 1 and 3, the density (in atoms/nm ³), and the number of molecules contained in all three regions formed, when considering slit pores of width 5 and 10 nm. The values reported for R1 & R3 represent	

the average of the two regions. The % difference between them is less than 5%, confirming the hypothesis regarding the non-changing properties in Regions 1 and 3.

177

Table 5. 3: The mineral composition of the five systems generated to investigate the impact of pore throat chemistry on the diffusivity of supercritical methane.

201

List of common abbreviations

AM	Arithmetic Mean
bcm	billion cubic metres
BET	Brunauer, Emmett, and Teller method
CT	Computer tomography
EMD	Equilibrium Molecular Dynamics
EMT/EMA	Effective Medium Theory/Approximation
GCMC	Grand-Canonical Monte Carlo
HM	Harmonic Mean
IEA	International Energy Agency
IUPAC	Union of Pure and Applied Chemistry
KMC	Kinetic Monte Carlo
LB	Lattice Boltzmann
LKMC	Lattice Kinetic Monte Carlo
MCMC	Markov Chain Monte Carlo
MF	Microfracture
MFPT	Mean First Passage Time
MSD	Mean Square Displacement
p.d.f	Probability density function
PES	Potential Energy Surface
PMF	Potential of Mean Force
PSD	Pore Size Distribution
SEM	Scanning Electron Microscopy
STD	Standard Deviation
u.r.n.g	Uniform random number generator

Nomenclature

A	= cross-sectional area (m^2)
bkl	= Klinkenberg's factor (atm)
D_f	= fractal dimension of the pore surface (dimensionless)
$D_{i,j}$	= diffusion coefficient (m^2/s)
D_k	= Knudsen diffusion coefficient in a smooth pore (m^2/s)
D_x	= diffusion coefficient on x-direction (m^2/s)
D_{xy}	= diffusion coefficient on xy plane (m^2/s)
D_y	= diffusion coefficient on y-direction (m^2/s)
E_a	= barrier energy (J)
g_m	= effective conductance (S)
g_x	= local conductance (S)
h	= Plank's constant ($m^2 \text{ kg} / s$)
J	= molecular flux (mol/m^2s)
k_B	= Boltzmann constant ($m^2 \text{ kg} s^{-2} K^{-1}$)
k_D	= is the Darcy permeability (m^2)
k_{eff}	= effective matrix permeability (m^2 or Darcy)
k_g	= apparent permeability, (m^2 or Darcy)
k_l	= true absolute permeability (m^2 or Darcy),
k_{LB}	= lower bound permeability (m^2 or Darcy)
k_{UB}	= upper bound permeability (m^2 or Darcy)
$k_{i,j}$	= permeability coefficient of the voxel located in row i and column j (m^2 or Darcy)
Kn	= Knudsen number (dimensionless)
K	= hydraulic conductivity (D x ft),
M	= fluid molar mass (g/mol)
N_A	= Avogadro number ($=6.023 \times 10^{23}$ atoms/mol)
N_C	= total number of columns (dimensionless)
N_R	= total number of rows (dimensionless)

- $P_p(t)$ = probability of a particle to enter voxel p (dimensionless)
 $P_q(t)$ = probability of a particle to enter voxel q (dimensionless)
 p = mean flowing pressure (atm)
 $R_{i,j}$ = pore radius of the voxel located in (i, j) (nm)
 r_{KMC} = KMC transition rate (s^{-1})
 R = universal gas constant ($=8.314 \text{ J/g mol}\cdot\text{K}$)
 T = temperature (K)
 u = a random number uniformly distributed (dimensionless)
 W_{pq} = propensity for a transition from voxel p to voxel q (s^{-1})
 W_{qp} = propensity for a transition from voxel q to voxel p (s^{-1})
 z = coordination number (dimensionless)

Greek Letters

- δ = distance between the centres of two consecutive voxels (nm)
 δ' = ratio of normalized molecular size to local average pore diameter
 ΔC = concentration difference, $C_{top}-C_{bottom}$ (mol/m^3)
 ΔP = pressure difference, $P_{top}-P_{bottom}$ (MPa)
 Δt = time step (s)
 η = fluid viscosity (cP)
 θ = porosity (dimensionless)
 τ = tortuosity (dimensionless)
 λ = mean free path (nm)
 ρ_{av} = average gas density (kg/m^3)
 $\varphi_{i,j}$ = weighting factor (dimensionless)

Background and literature review

Shale gas opportunities – Motivation

The increase in energy demand, driven by the growth of the global economy, is undeniable. The question is, what is the role of natural gas in the efforts to meet this increased demand, and how does the future look like for this fossil fuel? According to the International Energy Agency (IEA), by comparing the demand in OECD (Organisation for Economic Co-operation and Development) member countries, countries of non-OECD Europe/Eurasia and the rest of the world, it is possible to distinguish three markedly different patterns, as shown in Figure 1.1. Over the last 20 years, the latter group presented a steady growth in natural gas consumption, while the OECD showed a moderate growth and demand.¹ In non-OECD Europe/Eurasia, demand has remained relatively unchanged.²

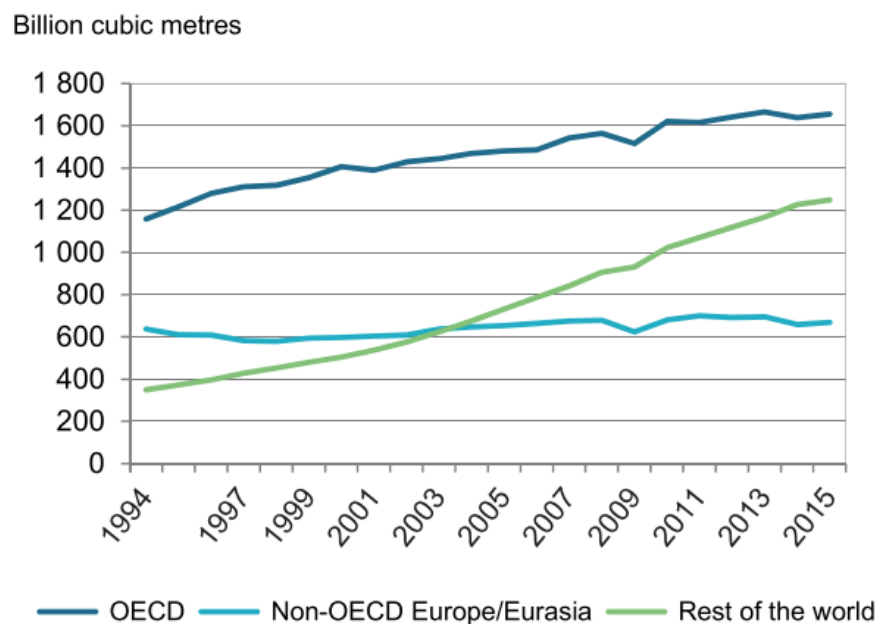


Figure 1. 1: World natural gas demand by selected regions. Reproduced from IEA's report.¹

The economic success related to shale gas production, especially in the United States (U.S), has generated great interest worldwide, but has also sparked controversy because of various sustainability issues associated with its exploitation and utilisation.³ According to BP's statistical review, in 2018, natural gas consumption rose by 195 billion cubic metres (bcm), or 5.3%, and this was one of the fastest rates of growth observed since 1984. Growth in gas consumption was driven mainly by the U.S (78 bcm), supported by China which also saw above-average growth of 17.7% (43 bcm), Russia (23 bcm) and Iran (16 bcm). The U.S gas consumption increase of 78 bcm last year is broadly equivalent to the entire gas consumption of the UK. Figure 1.2, reproduced by BP's statistical review, presents the 2018 natural gas consumption per capita.⁴

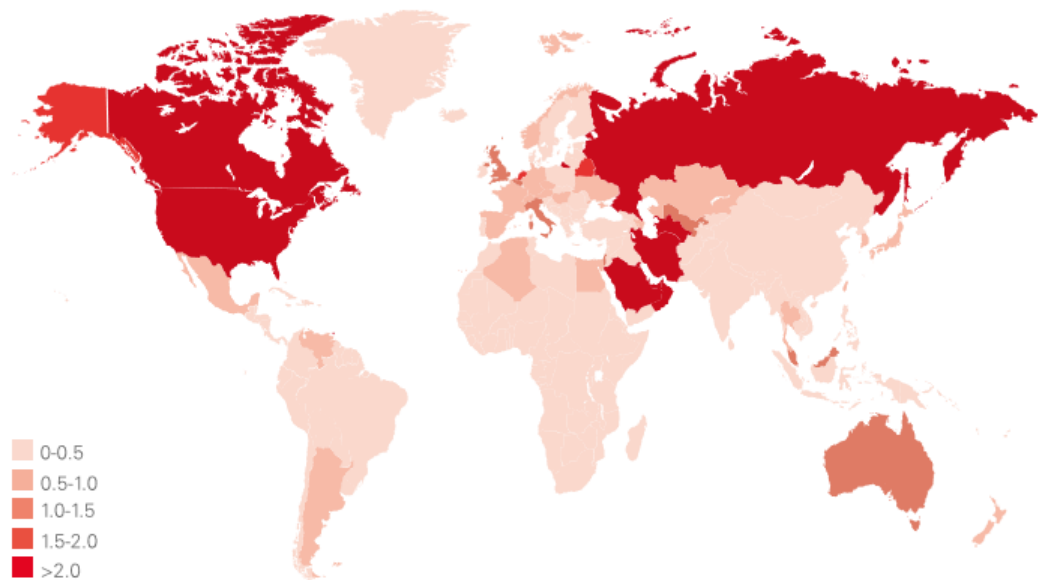


Figure 1. 2: Natural gas consumption per capita 2018 in tones oil equivalent. Reproduced from BP's report.⁴

This subsection discusses trends observed from the U.S and UK markets in more detail, as well as the technological improvements that have led to this increase in the natural gas production to meet the demand requirements.

Natural gas in the USA market economy

According to the latest edition of the World Energy Outlook (WEO), the United States is considered as a net energy exporter in 2020 and it is expected to remain as such until 2050. This is due to large increases in crude oil, natural gas, and natural gas plant liquids (NGPL) production coupled with slow growth in U.S. energy consumption. As a result of major transformations in the global energy system and recent technological advances, which are discussed below, natural gas seems to be gaining ground in the race to meet the upcoming growth in energy demand. In just a few decades, shale gas has become one of the most important energy resources for the United States, with significant contributions to the natural gas production in the country.^{2,5} However, as Cooper et al.⁶ highlight many nations with shale gas reserves lack the skills, knowledge and infrastructure of the US, leading to doubts about the economic viability and sustainability of shale gas outside the US.

Natural gas, which belongs in the fossil fuels family, has and will remain to have the highest production growth with relative low prices, according to EIA's predictions for up until year 2050.⁷ These predictions are made using the National Energy Modelling System (NEMS), an integrated model that captures interactions of economic changes and energy supply, demand, and prices. Based on the model's predictions, natural gas consumption is expected to increase across end-use sectors (industry, transport, aviation, buildings, appliances and lighting, etc.), while liquefied natural gas exports are believed to rise. It has also been observed that due to the historically low prices of natural gas, the energy sector has shifted towards its usage to generate electricity. Figure 1.3, reproduced from EIA's 2019 report, presents the U.S gross energy trade, net energy imports and % electricity generation from selected fuels in panels A, B, and C respectively.⁷

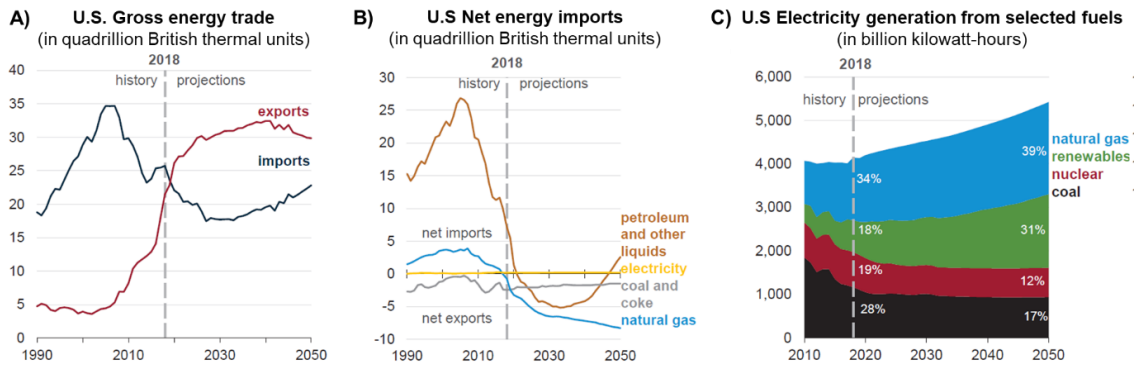


Figure 1. 3: Historic data and predictions regarding (A) the U.S gross energy trade, (B) the U.S net energy imports, and (C) the electricity generation from selected fuels. Reproduced and modified by EIA.⁷

Overall, natural gas production in the U.S is expected to grow 7% per year from 2018 to 2020, when the average growth rate from 2005 to 2015 was around 4%. A significant proportion of this natural gas volumes emanate from shale gas and tight oil plays. After 2020, natural gas production is expected to continue its upward trend in growth due to the size of the resources, which extend over nearly 500,000 square miles, and due to improvements in technology that will allow for the development of these resources at lower costs.⁷

Natural gas in the UK market economy

As previously discussed, gas demand can be broadly broken down into two main sectors; domestic consumption and gas for electricity generation, with demand for industry, commercial, public administration and other sectors. Gas is one of the key pillars of the UK's energy mix, accounting for over 30% of the UK's energy production and second only to oil. Gas production from the UK's Continental Shelf (UKCS) is considered sufficient to meet nearly 60% of all energy demand. Gas is particularly important for electricity generation where it meets around 40% of the fuel required in power stations, due to the substantial decline of coal usage in power generation. It is also critical for space heating, domestically and in offices, hotels and restaurants. In 2017 gas met nearly two thirds of total domestic energy demand in the UK.⁸

In year 2017/2018, the UK natural gas production remained relatively stable at 465 Terawatt-hour (TWh), a 0.3% increase, while total gas demand decreased by 3% to 875 TWh. In particular, final consumption decreased by 2.8 % to 495 TWh, with decreases in the domestic (-4.6%), public administration (-4.4%) and commercial (-3.4%) sectors. In contrast, industrial usage increased by 3.2%, the principal reason being an 8.4% increase in gas used in the chemicals sector. Excluding chemicals, industrial usage rose just 2%. Net imports were decreased by 4.5%. In particular, imports of Liquefied Natural Gas (LNG) decreased by over a third to 80 TWh, with imports of LNG from Qatar dropping by 40%. In contrast pipeline imports increased by 8.2%, with increased imports from Belgium and Norway more than compensating for a halving of imports from the Netherlands. Figure 1.4 presents the UK gas imports by country for the 2017/2018 period. Overall in the UK, the increased output from renewable and nuclear energy is the main reason for the reduced demand for gas for electricity generation. In 2017/2018 natural gas demand for electricity generation dropped by 4%.⁸

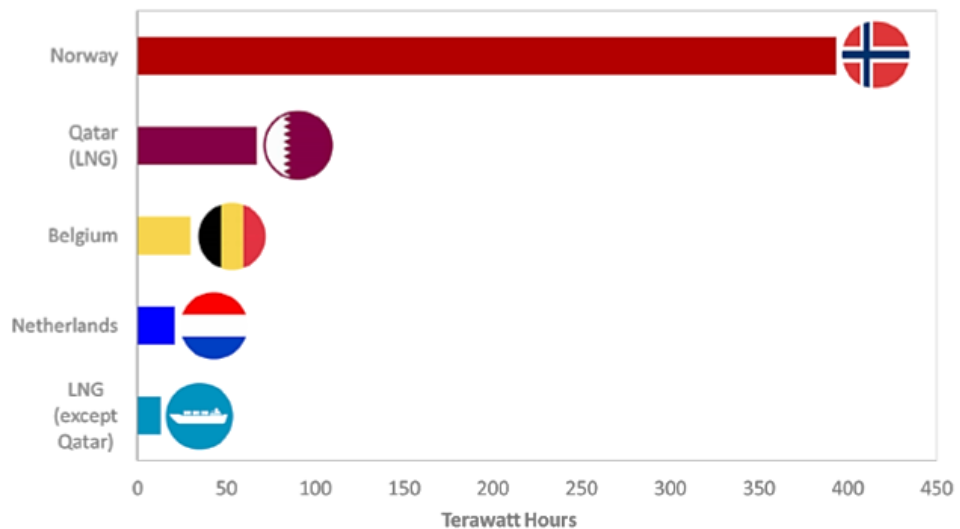


Figure 1. 4: Gas import by country in 2017, reproduced from National Statistics.⁸

In the year 2018/2019, UK production of natural gas was down by 5.7% in the first quarter of 2019 compared with the same quarter of 2018, and 6.8% lower from March to end of June compared to the March-June period in 2018. The decrease observed in the first

quarter is mainly due to the closure of the Theddlethorpe Gas Terminal and due to unfavourable weather conditions. The temperatures reported in the 2018/2019 period were substantially higher (+42%) compared to the previous year, when the "Beast from the East" brought very low temperatures. Figure 1.5 presents a breakdown for the UK's energy demand in the period 2016-2019.⁹

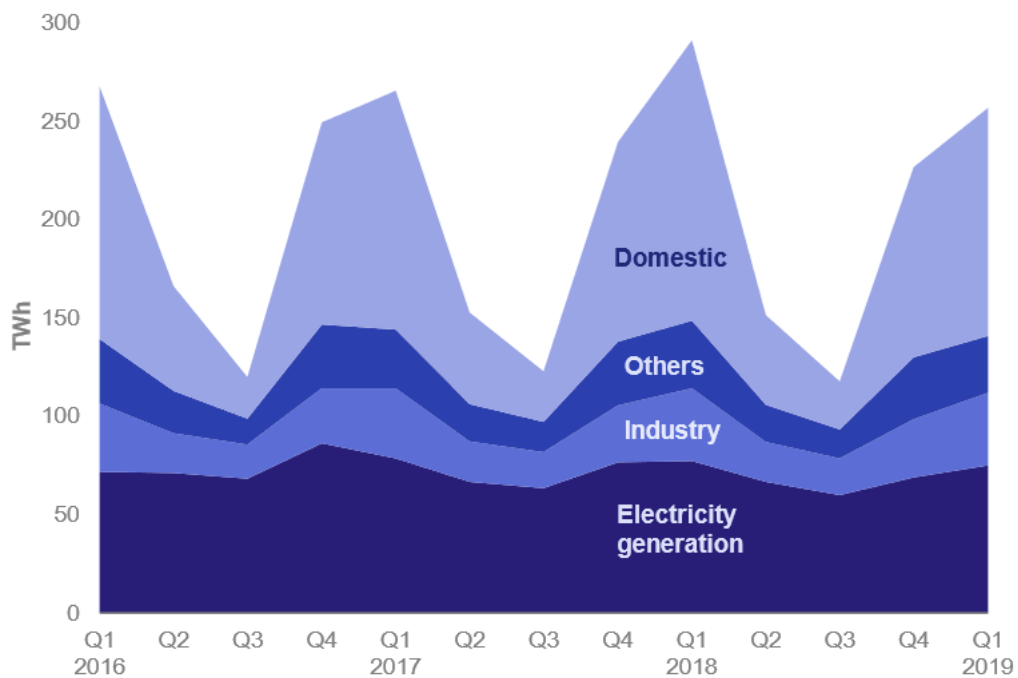


Figure 1. 5: Energy demand in the UK by sector. Image reproduced from National Statistics.⁹

The reduction in demand led to an overall decrease in imports, especially in February and March, when a reduction of 14% was recorded. While in April imports returned to typical levels, net imports remained low (down by 15%) as exports doubled, showing a 15% increase compared to April 2018, due to the trade deal with the Republic of Ireland. Demand for gas for electricity generation was decreased by 2.9%, compared to the previous year.⁹ Figure 1.6 is reproduced from the UK National Statistics and represents the production and nominated flow trades of natural gas in the UK for the period 2016-2019.⁹

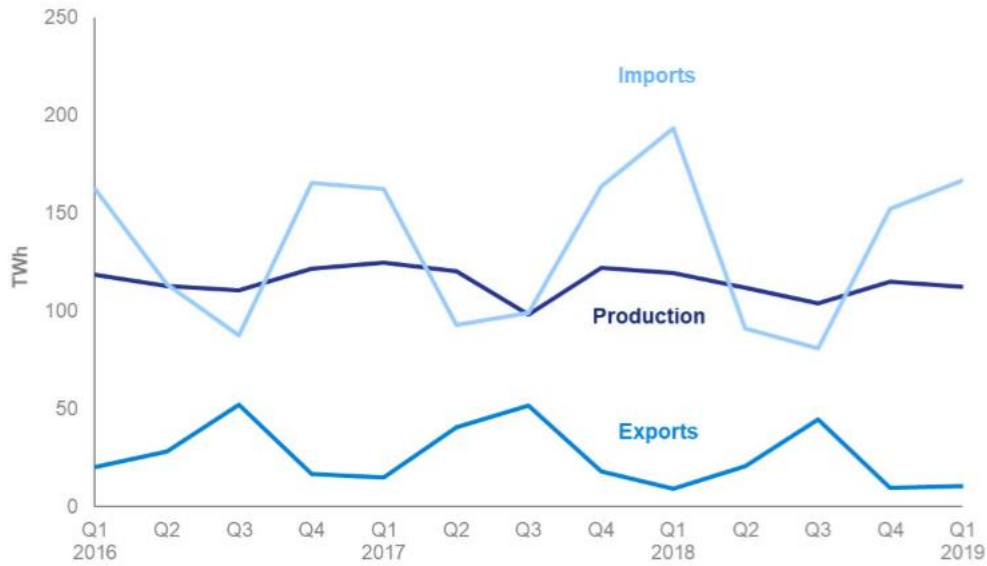


Figure 1. 6: Imports, production and exports of natural gas in the UK. Image reproduced from the UK National Statistics.⁹

Many recent studies aiming to access the UK's shale gas potential identify the Bowland Shale Formation as the most promising shale gas play.^{10–12} However, the challenges involved in successfully planning and exploiting a shale gas play are not insignificant with many associated uncertainties and risks. In a recent study, Cooper et al.¹³ discuss the sustainability of UK shale gas in comparison with other electricity options. The authors conclude that for shale gas to become sustainable in the UK, the environmental impacts need to be significantly reduced.¹³ The following section provides an overview of those environmental risks.

Hydraulic fracturing, technological improvements, and risks

Hydraulic fracturing, or fracking, is a well stimulation technique of extracting natural gas stored in impermeable rocks, such as shale rocks, that are found approximately between 1.5 and 2.5 km below the surface. The workflow of a successful shale gas production operation consists of 4 stages as summarised in Figure 1.7. In the UK, operators need to receive approval for each step by independent regulators and public consultation.¹⁴

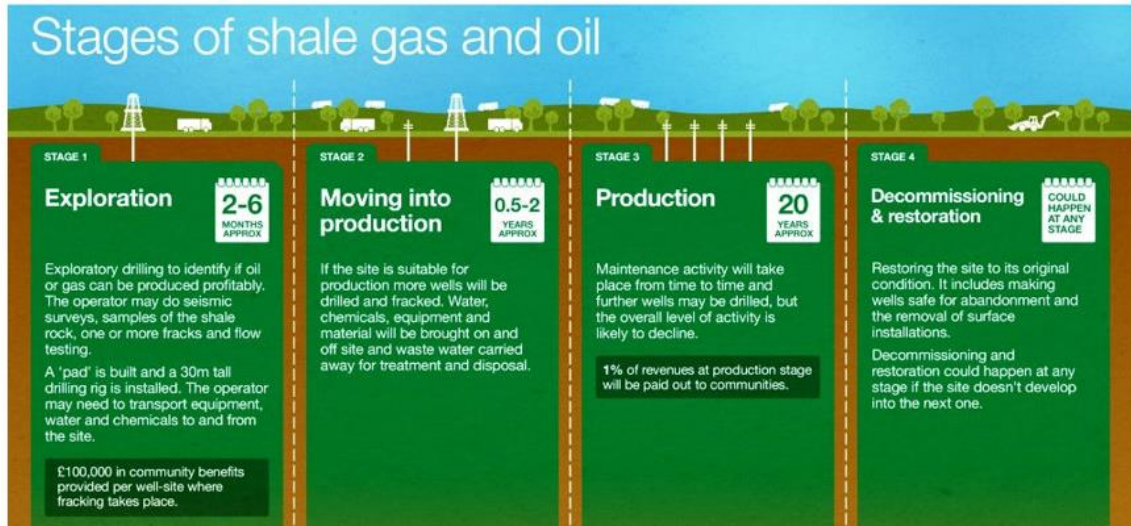


Figure 1. 7: Summary of the stages involved in the production of shale gas and oil, reproduced from the report produced by UK's Department of energy and climate change.¹⁴

The first stage is exploration and it allows companies to investigate how much oil and gas is in place, and whether its extraction is commercially and socially sustainable. During the exploration stage, well pads that are usually 1-2 hectares long are created together with water storage and disposal, and other operational facilities. Successful exploration is followed by the pre-production stage, where more wells are drilled. The pre-production stage starts with the creation of a long vertical bore, known as a wellbore. When the wellbore reaches a depth between 2.5-3 km, the kick-off point is reached, and horizontal drilling follows next, as shown in Figure 1.8 – panel A. The drill makes a 90 degree turn and it continues to extend horizontally for up to 1.5 km. Then, a perforated gun is loaded and fired to generate primary fractures into the rock matrix, see Figure 1.8 – panel B.2.¹⁵ After a period of 3 to 4 months, following the completion of the pre-production stage, the hydraulic fracturing process begins (production stage). Fracking fluids are injected at a very high pressure, leading to the generation of cracks in the rock, secondary fractures, as shown in Figure 1.8 – panel B.3, through which the trapped oil and gas flow into the main horizontal and vertical fractures that were generated during the initial drilling process. The final stage is decommissioning, to ensure that wells are

made safe for abandonment, all equipment has been removed and the site is left in its original condition.¹⁴

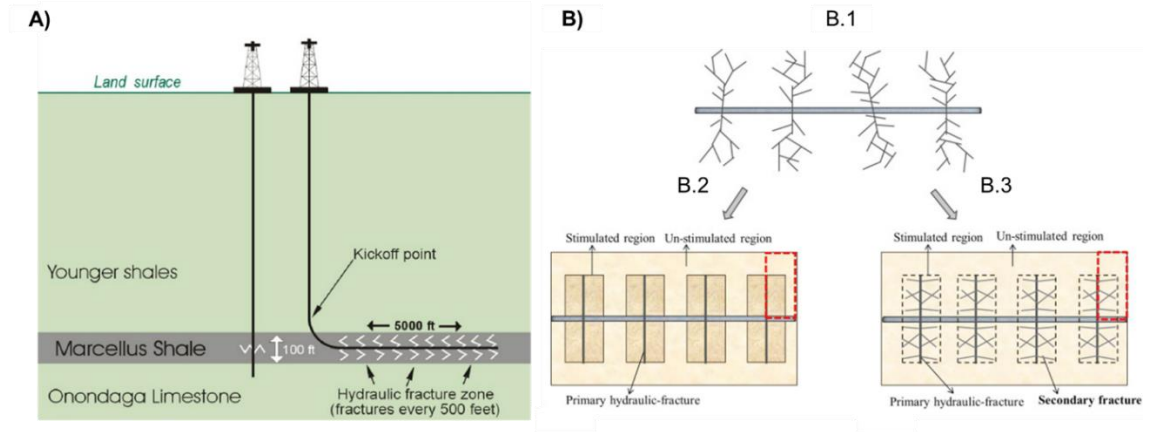


Figure 1. 8: A) Combination of horizontal drilling and hydraulic fracturing, reproduced from Soeder¹⁶, and B) representation of a multi-fractured system, adapted from Cheng et al.,¹⁷ B1 shows the fractures generated after the hydraulic fluids have been channelled through the primary fractures (B.2), resulting to the generation of secondary fractures (B.3).

Hydraulic fracturing was first reported in 1940, but it was not until 1950 until it became mainstream. Over the past decade, the combination of horizontal drilling and hydraulic fracturing has provided access to large volumes of unconventional oil and gas resources which were previously uneconomic to produce due to their low permeability.^{18,19} The technological improvements that have enabled increased hydrocarbon recovery from these impermeable rocks, at a lower operational cost, mainly concern the development of improved hydraulic fracturing fluids and proppants. Advances in the design of the secondary fractures and well spacing, have also played a significant role in the success behind this hydrocarbon recovery method.²⁰

Hydraulic fracturing fluids are predominantly water based (~90%) with the other 10% consisting of chemical additives.¹⁵ The selection of additives and their concentration within the hydraulic fracturing mixture varies, depending of the site's characteristics, and is commonly a trade secret.²¹ Until today, in the U.S with the exception of state-specific

laws, disclosure of the chemicals present in fracturing fluid is primarily based on self-regulation, and natural gas companies can voluntarily report the chemical composition of the mixtures used. In 2011, the Groundwater Protection Council and the Interstate Oil and Gas Compact responded to public protests and established the FracFocus.org website, where fracking companies are encouraged to release the list of chemicals used as additives for the hydraulic fracturing fluids used during their operations.²² For most of the commercially used fracking fluids, the additives are grouped into three categories; acids that are used to dissolve minerals, friction reducing chemicals that are used to generate a slippery form of water, and disinfectants to prevent bacteria growth. Recently efforts are focused on the generation of “green” hydraulic fracturing fluids, that are free of toxic chemicals.²³

Proppants, commonly made of sand and clay, are used to maintain the pressure induced fractures open, so oil and gas can be channelled to the main fractures, while the pressure drops due to the recovery of the hydrocarbons.¹⁵ The first proppants used were made of silica, but over the years, glass, resin coated sand, sintered bauxite and kaolin, and fused zirconia have been also used as proppants.²⁴ One of the most important features of proppants is their size range, usually between 105 μm and 2.38 mm.²⁵ Depending on the completion design, a mixture of various proppant sizes can be used. This technique has however been found to cause permeability reductions. Another critical feature is the proppant suspension in the fracturing fluid, as it affects the way the proppants are delivered to the wellbore and the generated fractures.²⁴

In the UK, shale gas deposits are known to exist in North of England (Bowland formation), the Weald Basin which mainly encompasses Sussex, Surrey and Kent, and in the Midland Valley south-west of Scotland. In 2011, Cuadrilla was the first company that was granted approval to perform the pre-production and production stage. However, shortly after the first wells were drilled, a series of microseismic events, which also took place during the hydraulic fracturing process, resulted in public outrage and operations were immediately suspended.²⁶

Besides microseismic events, which can cause small earthquakes and damage to infrastructure, other risks associated with the hydraulic fracturing process are leakage due to poor casing, leading to the contamination of aquifers with toxic elements.²⁷ Groundwater can be found in shallow or deep aquifers, which are located approximately 30 meters below the surface.²⁸ Another risk is the leakage of methane that has been recovered during the drilling and fracturing process. Methane has been found to be 10 times more pollutant than carbon dioxide as a greenhouse gas. The safe disposal of the used fracturing water is another concern of the public, and environmental agencies, as it contains dissolved gas, naturally occurring radioactive materials (NORM), chemicals, and salts. Usually, this used water is stored in pits drilled in deep wells on-site or is sent off-site in water treatment facilities. Wells drilled at the preparation stage are usually encased in steel and cement to prevent the used water and hydrocarbons leaking into the groundwater aquifers. Moreover, it has been estimated that during hydraulic fracturing, 3-6 million gallons of water are used per well. Even though this amount of water is approximately as high as that required for agricultural purposes, it can have a notable impact on local water supplies.²⁷

Taking into consideration the risks associated with the hydraulic fracturing process but also the increase in energy demand, this research study aims to produce an accurate computational method to calculate the permeability of shale formations. This parameter is crucial for evaluating the sustainability and profitability of a shale play and for determining the impact of the potential risks, which could then lead to better decision making and strategic planning. Shale gas characteristics

Chemical composition

The term shale play is used to describe the geographic area, which contains an organic-rich fine-grained sedimentary rock and exhibits low production rates.⁵ Shale rocks are mainly composed of kerogen (organic part), quartz, clay, carbonates and pyrite (inorganic part). Secondary components such as uranium, iron, vanadium, nickel, and molybdenum can also be found in the shale matrix.^{5,29} Rock mineralogy is essential for

shale evaluation and the design of the fracture stimulation, as it can greatly affect the mechanical properties of rock. Shales with abundant quartz are usually very brittle, while shales with high clay content are less brittle.³⁰ Moreover, some of the clay minerals found in the shale formations slow the transport of water and natural gas and seem to affect the permeability of the matrix.^{5,31} In a successful shale play, it is estimated that the total clay content should be <50% in order to achieve satisfactory hydrocarbon recovery.³² The experimental techniques used to determine the mineralogy of a shale sample are Scanning Electron Microscopy (SEM) and X-ray diffraction (XRD).^{33–35} Backeberg et al.,³⁶ investigated the chemical composition of an obtained Bowland sample, as presented in Figure 1.9. It was reported that the majority of Bowland's inorganic matrix consists of clay minerals (~60% per volume). The clay contained mainly illite (80%), which is chemically almost identical to muscovite, kaolinite (14%) and minor smectite. The slit fracture presented in Figure 1.9 was found to consist of mainly quartz.³⁶

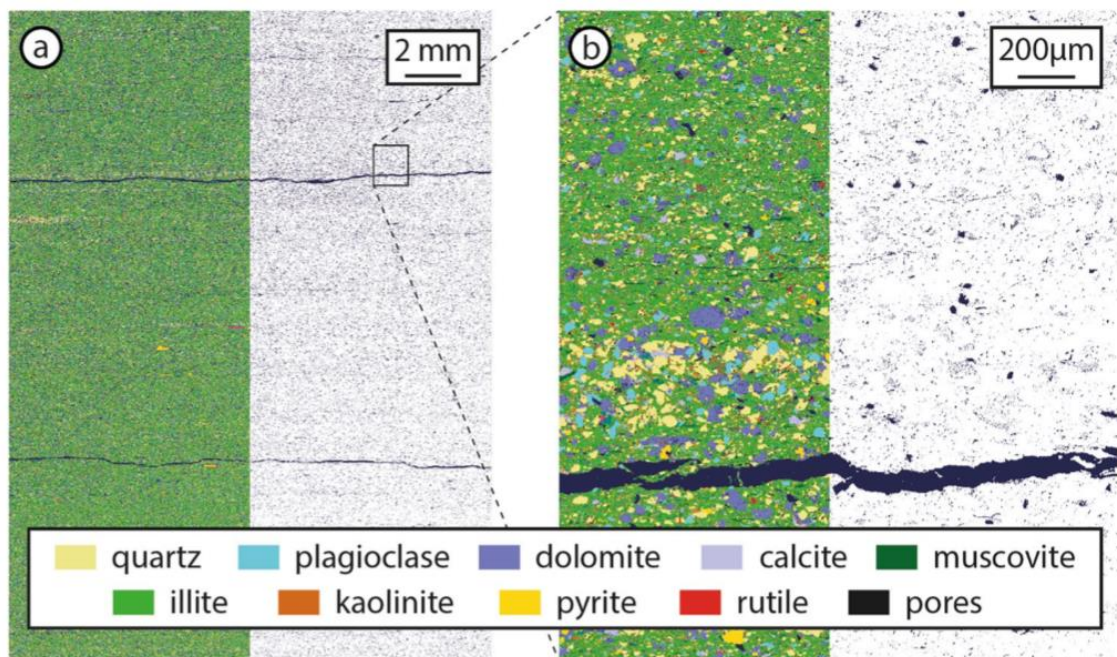


Figure 1. 9: QEMSCAN chemical maps of Bowland sample at spacing resolution of (a) 10 micron and (b) 1 micron. Reproduced from Backeberg et al.³⁶

Kerogen, which represents the majority organic matter contained in the shale rocks, can be classified into four types based on its chemical composition.³⁷ The kerogen type is a

parameter used to assess the potential of a reservoir to produce oil and/or gas and it is believed to be one of the controlling parameters of the transport and storage properties.³⁸ Spectroscopic techniques and elemental analysis can be implemented in order to determine the ratio of carbon, hydrogen and oxygen atoms.³⁷ Kerogen types I and II exhibit high initial hydrogen/carbon atomic ratio and low initial oxygen/carbon ratio, resulting to a high potential for hydrocarbon generation. On the other hand, type III presents low hydrogen/carbon ratio and comparatively higher oxygen/carbon ratio, which results in a moderate oil producing potential. However, this kerogen type may still generate abundant gas at greater depths. Type IV kerogen has the lowest hydrocarbon generating capability as it contains only aromatic components.^{30,37}

Pore characteristics (porosity and pore size distribution)

Porosity is a dimensionless parameter used to describe the volume fraction of the voids existing in a porous medium of total volume V . The calculated porosity depends on whether the method used could access the open or the closed pores of the porous material.³⁹ It is one of the most important rock parameters when evaluating a gas shale reservoir's production potential.^{34,40} Porosimetry methods used in the laboratory mainly include Gas Research Institute (GRI), Nuclear Magnetic Resonance (NMR), Mercury Injection Capillary Pressure (MICP) and Water Immersion Porosimetry (WIP) techniques.⁴¹ Shale rocks exhibit low porosity, mostly plate-like micro-porosity and little to no macro-porosity.³³

The evaluation of the pore size distribution (PSD) is fundamental in the understanding of permeability.⁴⁰ If A_p is the pore wall area, V_p is the pore volume and r_p is the pore radius, the PSD can be calculated from the derivatives $\frac{dA_p}{dr_p}$ or $\frac{dV_p}{dr_p}$ as a function of the pore radius. For shales rocks, as for most porous materials, the International Union of Pure and Applied Chemistry (IUPAC) classification system is adopted in order to describe the pore size. According to the IUPAC system, pores with diameters less than

2 nm are micropores, pores with diameters larger than 50 nm are macropores and intermediate pores are termed mesopores.³⁹ Depending on their size, shape and origin, pores are classified into four types: dissolved pores, organic matter associated pores, inter-granular pores and micro-fractures.^{42,43} Dissolved pores derive from the chemical interaction between the unstable minerals, found in the inorganic shale matrix and air or underground water molecules. Their diameter ranges between 100 nm and 300 nm. The pores formed during the kerogen thermal cracking, can have diameters up to 200 nm, while the inter-granular pores can reach 1000 nm.³³

Information regarding the pore structure of a porous material can also be derived from advanced imaging techniques including Focused Ion Beam Scanning Electron Microscopy (FIB-SEM), Field Emission Scanning Electron Microscopy/Transmission Electron Microscopy (FE-SEM/TEM), Small Angle X-ray Scattering (SAXS) and Computer tomography (CT) scan.^{34,44} For the purpose of characterising an ultra-fine pore structure with a generally broad PSD (micropores, mesopores and macropores), low pressure nitrogen adsorption and desorption, as well as high-pressure methane injection tests can be employed.³³

Matrix permeability

Permeability is a term used to assess the ability of a porous material to transmit fluids and is one of the most important properties in defining the flow capacity of a porous structure.⁴⁵ The dimensions of permeability are usually L^2 and relate to the cross-sectional area of the pore throats. However, a practical unit for expressing permeability is the Darcy (D). Permeability depends on a number of factors; pore characteristics, chemical composition, transport mechanisms, reactive fluids of high velocity flow effects. The true absolute permeability is considered to be an intrinsic property of the porous material, unchanged by different types of fluids. This rule holds for all liquids at laminar flow regime, but in the presence of low pressure gases, the calculated permeability might exceed the true absolute permeability of the rock.⁴⁶ This phenomenon, explained in the

following subsection, inspired Klinkenberg in 1941 to propose the following very useful relationship:⁴⁷

$$k_g = k_1 \left(1 + \frac{bkl}{p}\right) \quad (1.1)$$

where,

k_g = apparent permeability,

k_1 = true absolute permeability,

p = mean flowing pressure,

bkl = Klinkenberg's factor (constant for a specific gas at a specific porous structure)

Typical shale rock permeabilities are in the range of micro-Darcy (μD) and nano-Darcy (nd).^{48–50} Table 1.1 provides a summary of the permeability, porosity, and PSDs obtained for major shale formations found in the USA and China.

Table 1. 1: Properties of major shales in USA, China, and Canada

Formation Details	Pore throat diameter (nm)	Porosity (%)	Permeability (μD)	Source
Unknown Shale, in the Beaufort-Mackenzie Basin	23 (average)	7.5	-	Gu et al. ⁵¹
Unknown Shale, in the Appalachian Basin <i>(poor organic matter)</i>	8 (average)	7.2	0.1	Gu et al. ⁵¹
Unknown Shale, in Appalachian Basin <i>(rich organic matter)</i>	24 (average)	3.6	0.5	Gu et al. ⁵¹
Marcellus Shale, USA	10-100	9-11	0.1-0.7	Zou et al. ⁵²
Unknown Shale, Canada	12 (average)	4.9	0.2	Gu et al. ⁵¹
Haynesville Shale, USA	-	12	0.4	Wang et al. ⁵³
Haynesville Shale, USA	20	8-9	0.1-0.8	Zou et al. ⁵²
Eagle Ford Shale, USA	-	10	0.1-0.6	Wang et al. ⁵³
Barnett Shale, USA	-	4-7	~0.1	Wang et al. ⁵³
Barnett Shale, USA	5-750 (100 average)	4-5	0.1-0.5	Zou et al. ⁵²
Marcellus Shale, USA	-	5.5-7.5	0.7	Wang et al. ⁵³
Fayetteville Shale, USA	5-100	2-8	0.1-0.8	Zou et al. ⁵²
Utica Shale, USA	15-200	3-6	0.8-3.5	Zou et al. ⁵²
Fuling Shale, China	50-200	1.2-8.1	0.001-5.8	Zou et al. ⁵²
Shunan Shale, China	5-100	2-12	0.02-2.8	Zou et al. ⁵²
Yanchang Shale, China	3-100	0.8-3	0.01-0.7	Zou et al. ⁵²

Anisotropy and heterogeneity in shales

Anisotropy is the vectorial variation of a physical property at a certain point of the porous medium. This variation causes some properties of the porous medium to have different values in different directions.⁵⁴ Thus to describe the distribution of the anisotropic property in the medium, five independent variables need to be considered; the (x,y,z) spatial coordinates and the (θ , ϕ) angular coordinates for the orientation of the anisotropy.⁵⁵ Permeability is one of the shale rock properties that has been found to have this anisotropic behaviour, and is frequently suggested that the degree of anisotropy correlates to the amount of clay, kerogen, and porosity in the shale samples.^{36,56-58} In the reservoir formations, anisotropy is frequently the result of bedding presence.⁵⁹ Anisotropy is a crucial issue for the recovery of hydrocarbons, as it can greatly influence

the transport of fluids and the mechanism of fracture propagation during the hydraulic fracturing process.^{60–62}

Shale rocks are also found to be heterogeneous, due to the significant variations of porosity and PSDs observed (see Table 1.1).^{49,63,64} Heterogeneity is detected when a physical parameter (e.g. porosity, density, permeability, etc) exhibits variations within a sample. Studies suggest that the observed heterogeneity is a result of the intrinsic structure of the medium and depends on the composition and topology.⁶⁵ The presence of heterogeneity often results in anisotropy, however this is not always a necessary condition.⁵⁴ A way of macroscopically assessing the heterogeneity of a porous medium is by examining various samples and obtaining observing pore morphologies that are statistically different.⁶⁶ Figure 1.10 shows an example of heterogeneous grain density distribution. Dullien⁶⁶ suggests that a porous medium can be classified as homogeneous when the length scale of the heterogeneity is less than the length scale of the observation.

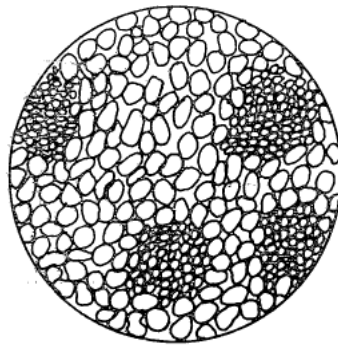


Figure 1. 10: Example of heterogeneous distribution of grain density in a grain rich rock sample. Reproduced from Dullien.⁶⁶

Transport characteristics

The term "fluid" is used to describe a continuum group of molecules, which are in reality discrete entities. The behaviour of fluids, from a molecular point of view, can vary significantly under confinement. As the distance between the pore walls decreases, the interactions between the molecules and the surface become more frequent and the

journey one molecule can travel shortens. According to the kinetic theory, one way to assess the average distance a molecule can travel, while following a straight trajectory before it collides with another molecule or the pore wall, is to calculate the mean free path.^{31,67}

$$\lambda = \frac{k_B T}{\sqrt{2} \pi d^2 \bar{p}} \quad (1.2)$$

where,

λ is the mean free path,

k_B is the Boltzmann constant,

T is the absolute temperature,

\bar{p} is the absolute average pressure,

d is the collision diameter of the gas molecules.

As Eq. (1.2) shows, the mean free path is proportional to the temperature and irreversibly proportional to the pressure for specific pore geometries. However, in order to predict the movement of a gas through a porous media and calculate its matrix permeability, a transport model needs to be defined.³¹ Darcy's law can describe the laminar viscous flow of one or more phases in a porous matrix, as long as the rate of the flow is proportional to the pressure gradient. This law, named after Hendry Darcy, describes the linear relation between the flux and the pressure gradient and has the following form for the case of incompressible fluids.⁶⁸ In Eq. (1.3) the subscripts 1 and 2, designate the up and downstream positions, respectively.

$$Q = AK \frac{(h_1 + z_1) - (h_2 + z_2)}{L} \quad (1.3)$$

where,

Q =the volume flow rate,

A =the area of porous media normal to the flow,

K =the hydraulic conductivity (permeability),

h =the pressure head (pressure divided by the specific weight),

z =the elevation,

L =the length of the flow path.

The unique and complex structure of the unconventional reservoirs exhibits special flow mechanisms that deviate from the Darcy's law description.⁶⁹ Many theories have been proposed, in order to identify the main characteristics responsible for this deviation. One of the prevailing theories suggests the coexistence of different flow regimes due to the various pore sizes found in the matrix.^{67,70} Other theories consider the chemical composition of the matrix and the anisotropic permeability to be equally important factors.³¹

Knudsen number is a dimensionless parameter that characterises the degree of rarefaction and can be used to identify the flow regime and hence the transport mechanism. It is expressed as the ratio of the mean free path λ and the characteristic length of the system as described below.⁷¹

$$Kn = \frac{\lambda}{\Lambda} \quad (1.4)$$

where,

λ =the fluid mean-free-path,

Λ =the macroscopic length scale of the physical system molecules.

There are four possible transport mechanisms; the Knudsen diffusion, the slip flow, the transition flow and the viscous flow. Knudsen diffusion is dominant in micropores and can also be found in the literature as pore diffusion or free-molecule flow. It describes the state of a low-pressure system, in which the effect of the pore walls is negligible. In

this case, the mean free path of the molecules exceeds the mean pore diameter, resulting to a Knudsen number greater than 10 ($Kn \gg 10$). As the Knudsen number decreases ($10^{-1} < Kn < 10$), the interaction between the fluid molecules and the pore wall become dominant and the flow regime falls into the category of transitional flow.^{67,72} In this regime the transport mechanism exhibits characteristics of free molecular flow, as well as slip flow. The slip flow, first introduced by Klinkenberg, occurs when the mean free path of the molecules is comparable to the size of the pore ($10^{-3} < Kn < 10^{-1}$). The interaction between the molecules and the pore wall become more dominant as a result of reduced fluid friction.^{31,47} As pressure increases, the intermolecular collisions, as well as the interaction between the molecules and the surface, elevate the wall shear stress experienced by the molecules. As a result, the mean free path decreases, and the rarefaction follows a similar trend. This type of flow corresponds to a continuum viscous flow regime ($Kn < 10^{-3}$).⁶⁷ Figure 1.11 presents a classification of the flow regimes as a function of the Knudsen number.⁷³

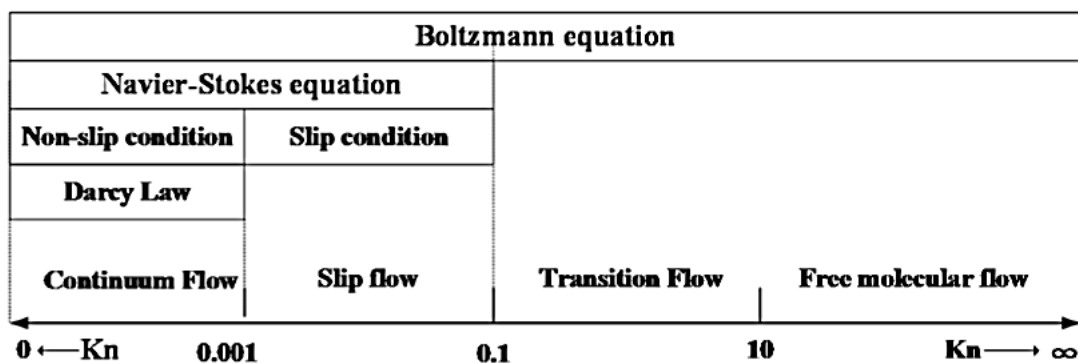


Figure 1. 11: Transition of the flow regimes as a function of the Knudsen number. Reproduced from Song et al.⁷³

Nevertheless, besides the four transport mechanisms described above, adsorbed-phase diffusion and capillary condensation flow could also be considered as possible transport mechanisms. Adsorbed-phase diffusion, also referred as surface diffusion, is the mechanism by which the gas molecules get adsorbed at fixed positions on the pore walls.

Since the diffusing molecules never escape from the force field of the pore walls, it is logical to consider the fluid within the pore as a single adsorbed phase.^{44,72} Although it is considered to be a slow process, it is believed to contribute substantially in the process of fluid transport.^{74,75} A schematic of the transport mechanisms discussed above is presented in Figure 1.12 for the case of a single component narrow pore.⁷⁶

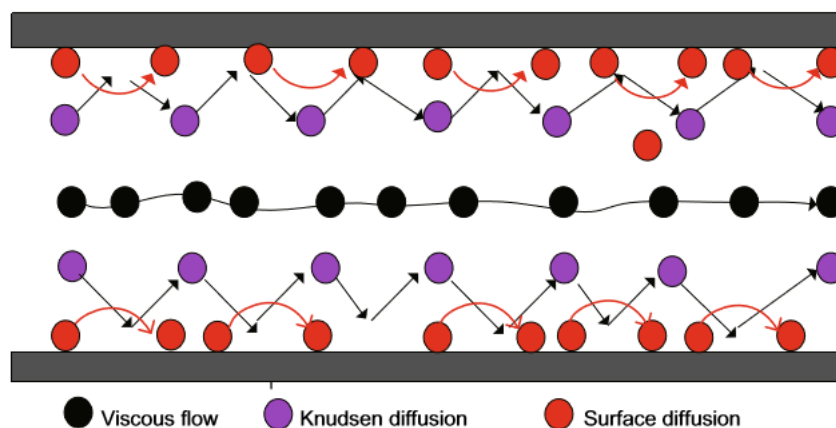


Figure 1. 12: Single component gas transport mechanisms through a narrow pore. Reproduced from Wang et al.⁷⁶

Another potential effect of the confinement, besides the increase of intermolecular forces, is the capillary condensation phenomena. When the pore pressure exceeds the critical pressure required to fill the pores with adsorbate, the molecules are forced to condensate below the saturation vapor pressure. This change in the phase of the fluid delays the transport of the vapor through the condensate filled pores.^{67,70}

To interpret kinetic data in heterogeneous and anisotropic systems, in terms of chemical composition and pore size, it is necessary to use a more complicated model which will account for micropore, mesopore and macropore diffusional resistances.⁷² This seems to be a non-trivial issue and different experimental, theoretical and computational methods have been suggested in the literature. Each approach exhibits certain advantages and limitations, which define the applicability of the method, the time scale of the analysis and the size of the samples used to extract the transport properties. The following section aims to review and compare those methods.

Methods of analysis

Shale rocks exhibit complex and highly heterogeneous pore networks. The chemical composition and the pore characteristics may vary significantly, even for samples taken from the same reservoir. Many experimental and computational methodologies have been implemented aiming to reveal the transport behaviour in such systems. This subsection provides a brief overview of the experimental methods commonly used to calculate the permeability of shale samples and a review of some of the most important computational approaches implemented to study the transport of fluids in porous media.

Experimental methods

The transport properties of a porous medium can be defined by obtaining the permeability, diffusivity and solubility coefficients. Several experimental techniques have been applied, in order to determine these coefficients in shale rocks. Some of the most common are the steady state method and the unsteady state method.^{77,78} However, by following an experimental approach, no distinction can be made between diffusion and convection (Darcy's law) and hence, the mechanism of fluid transport cannot be identified.⁷⁹

The steady state method, based on transmissibility measurements, can calculate the permeability coefficient of an intact porous media with length l and cross-sectional area A . A certain amount of a gas or liquid is loaded to one side of the membrane, resulting in a pressure P_1 . The other side of the membrane is left empty and usually kept at a pressure $P_2 = 0$ (vacuum condition). The amount of permeate $Q(t)$ that crosses the membrane over time t is being monitored and the permeability coefficient k can be calculated from the following equation:

$$k = \frac{Q(t)l}{AtP_1} \quad (1.5)$$

This method has been used extensively over the past 50 years to determine the permeability of the conventional reservoirs. The main advantage of the method is the

simple experimental set up required and the straightforward analysis of the data collected. However, using the steady state method to calculate the permeability of tight rock formations can become quite challenging, as a significant amount of time is needed for the system to reach equilibrium and then a steady state. Moreover, due to the low flow rates achieved, the accuracy of the method decreases.⁸⁰ Nevertheless, several authors have used the steady state method in order to perform permeation experiments on different tight rock formations using intact core samples.^{81–83} Due to the limitations of the steady state approach, for the tight rock formations, the non-steady state techniques of measuring permeability gained attention. Three of the most commonly used non-steady state techniques found in the literature are the pulse decay (or Brace method), the GRI method and the oscillating pressure method.

Computational methods

At present, the development and profitability of a shale play depends on its permeability. Shale rocks consist of organic and inorganic matter with pore sizes ranging from the micro- to the meso-scale.⁸⁴ This section provides a review of the computational methods reported in the literature for the calculation of transport properties in shales at various scales in ascending order.

From an atomistic perspective, Molecular Dynamics (MD) simulations have been widely implemented in fluid transport studies. Bhattacharya and Lie used this method in their studies, contacted in 1990, in order to solve the dynamical equations of confined gas particles between two thermal walls. They implemented non-equilibrium MD (NEMD) in order to simulate the heat transfer on their system and assumed that whenever a temperature jump was observed, it was due to fluid transport.⁸⁵ Botan et al., also used MD in order to capture the changes in adsorption and transport with temperature, pressure, pore size and concentration. Their model included values of the local chemical potential and density, which were calculated by using grand-canonical Monte Carlo (GCMC) simulations. As a next step, they used a lattice model in order to describe

transport at larger scales. The lattice was mapped into 3D structures obtained by using focused FIB-SEM and tomography. The main outcome of this work was the validation of the significant contribution micropores have on the actual gas flux.⁸⁶ Recently, Ozcan et al., conducted a NEMD concentration driven study to simulate the permeation of pure fluids and mixtures through a ZIF-8 membrane. They used biased forces to maintain the concentration of fluids at target values in the inlet and outlet of the membrane.⁸⁷ Phan et al., also calculated the permeability of various substrates using MD simulations for pure fluids and mixtures.⁸⁸ The details of this work are discussed further in Chapter 3. MD simulations however require at the expense of high computational effort, which leads to the so-called scale problem.⁸⁹

Although atomistic simulations can provide an accurate understanding of the transport mechanisms in confinement, upscaling requires significant computational effort. As a result, the systems investigated are frequently composed of a single pore, and a limited number of pore sizes/chemistries are explicitly considered.^{90,91} To bridge the gap from atomistic simulations in single narrow pores to large scale systems, transport models that correlate diffusivity and/or permeability to pore characteristics have been developed. Typically, these models account for the three types of diffusion mechanisms; Fickian, Knudsen, and surface diffusion.⁹²⁻⁹⁴ The contribution of each mechanism to the overall fluid transport is assigned by coefficients, derived either from experimental or computational data. These coefficients are used to enrich Darcy's equation. Most commonly, these models take into consideration effective stress and slip flow contributions, in order to produce expressions of the apparent permeability.

Albeit the fact that many transport models have been proposed, a gas transport model that simultaneously considers organic micropores, inorganic micropores and microfractures is still not available. Further, when using the available models at conditions different than those used to construct them, re-parameterisation becomes mandatory^{95,96}, as their accuracy is limited to the extent of the conditions used for the calculation of the coefficients.^{94,97,98} To describe shale gas flow through single

micropores, Darabi et al., proposed an apparent permeability model that considers various parameters (e.g. tortuosity, porosity, mean pore radius, absolute permeability, etc.).⁹⁹ Similarly, Malek and Coppens studied the effects of surface roughness on Knudsen regime diffusion in porous media.¹⁰⁰ These apparent permeability models have been widely applied to extended 2D or 3D pore network modelling studies, providing “local” apparent permeability coefficients.^{101,102}

The first efforts in predicting the effective permeability of the medium, given the “local” apparent permeability coefficients, were reported half a century ago,¹⁰³ with Renard and Marsily describing and assessing the available techniques at the time.¹⁰⁴ Among multiple deterministic methods, the Effective Medium Theory (EMT)^{105–108} was deemed suitable for (1) media exhibiting small heterogeneities with low variance and a log-normal permeability distribution, and (2) binary media containing less than 50% low-permeability pores.¹⁰⁴ Because of these initial observations, the EMT method has been applied in many different fields, including geological formations and sediments, composite media, heterogeneous catalysts and mixed-matrix substrates with fillers.^{109–113} It is generally accepted that when the low-permeability proportion exceeds a certain threshold, (i.e., 50%), EMT yields poor predictions.^{104,113} It has been suggested that this low performance is because of the overestimation of the network connectivity.^{112,114} While recent findings have helped improve our understanding regarding both the percolation threshold and the mechanisms responsible for poor EMT performance,¹¹⁵ a robust EMT approach with an evident identification of its limits of applicability is still elusive.

Another deterministic approach often used for estimating equivalent media permeability, particularly by the oil and gas industry, is King’s renormalisation approach.¹¹⁶ For this approach, one begins from a grid in a dimensional space (DS), constructed by considering 2^n cells per coordinate, yielding 2^{nDS} meshes. Aggregations are performed iteratively, with each iteration combining two cells per coordinate, thereby producing a less finely discretised grid, with $2^{(n-1)DS}$ meshes. The procedure is completed when one single mesh emerges.¹⁰⁴ As part of King’s renormalisation approach, an electric network

was used as analogous to a porous medium in which the inverse of permeability acts as a resistance.¹¹⁶ Le Loc'h proposed a simplified renormalisation technique that performs successive groupings between the meshes. If two meshes are in series relative to flow direction, point permeabilities are averaged using a harmonic mean. If the two meshes are in parallel with respect to flow, an arithmetic mean is used instead. The two approaches yield minimum and maximum permeability, respectively. The equivalent permeability is estimated as the geometric mean of these extremes.¹¹⁷ Kelkar recommended this approach as a reservoir characterisation strategy, and Naraghi et al., implemented it to calculate the permeability of an Eagle Ford sample.^{102,118} Renormalisation techniques share the EMT weakness when applied to systems with high heterogeneity, where highly permeable regions neighbour with low-permeable ones.¹¹⁶ Shale rock samples are indeed heterogeneous materials; thus the mentioned deterministic approaches might not be reliable tools to predict the effective rock permeability. However, the promise of fast estimates makes these deterministic approaches appealing to practitioners.

Advanced imaging of core samples reveals the complexity of the pore system within the shale matrix.^{36,119} The properties that define shale permeability are mainly porosity (pore size distribution – PSD), organic content (% of total organic carbon - TOC), and mineralogy.¹²⁰ The inorganic matter of shales is predominantly made up of quartz, carbonate and clays.^{38,42,121–123} State of the art computational methodologies have been developed to couple imaging data that reveal the chemical composition and pore size distribution of a rock sample, to generate realistic pore networks that resemble those in shales, and then perform mesoscale simulations to estimate the permeability using, e.g., computational fluid dynamics (CFD).^{101,124–126}

From a modelling perspective, Lattice Boltzmann (LB) simulations, is a mesoscopic CFD particle-based method that has been widely applied to simulate complex fluid flow and obtain transport properties.^{127–129} Simplified kinetic models, which incorporate only the essential physics of microscopic or mesoscopic processes, are used to obtain

macroscopic averaged properties that obey the desired macroscopic equations (Navier-Stokes equation). The fluid is divided into packets that act as particles. The LB method simulates the motion and collision of these particles on a lattice, and allows for the extension to multiphase flow, where particles representing fluid elements of two (or more) phases, carrying different averaged properties (pressure, density, etc), can be tracked while interacting with each other. Moreover, it is a method relatively easy to code and is ideally suited for parallel computing platforms. However, the computational cost of the method can be significantly high, even in a parallel environment.^{127,128} Additionally, the run-time scales are approximate to the inverse of real flow rate, which makes it difficult to capture accurately capillary-controlled displacement on sufficiently large samples to make reliable predictions of relative permeability.¹³⁰ In many studies, imaging data are used to reconstruct the pore network and LB simulations are implemented to simulate fluid flow, following Hazlett's¹³¹ work.^{132–135}

In 2009 Chen et al.,¹²⁵ implemented nanometer-scale SEM to visualise microscopic pores inside kerogen found in shales. Most of the pores found inside the kerogen had spherical morphology and were isolated from each other. The authors found that these pores were not connected to natural or hydraulic induced microfractures. To study the transport of fluids within the pore network they implemented LB simulations and evaluated the tortuosity and permeability in the three principal directions. From their analysis they found both Peclet and Reynolds numbers to be smaller than one, an indication that the transport was in the flow regime and diffusion was the main mechanism of transport. The permeabilities calculated showed an isotropic permeability distribution in the μD scale. Chen et al.,¹²⁵ highlighted the importance of selecting an appropriate sample size, an observation also made by Boek and Venturoli who studied the transport properties of Bentheimer sandstone samples using the same methodology. They reported a broad distribution of calculated permeabilities for samples with small size.¹³⁴

In a similar manner Zhang et al.,¹³⁶ implemented the LB methodology to simulate the gas flow characteristics of a 2D organic rich shale sample. They focused their analysis on the effect of the Knudsen number and slip flow effect. The flow rate was found to be proportional to the square of the capillary width when the Knudsen number was low and slip flow effects were absent. However, they observed that as the capillary width decreases the Knudsen number and velocity increases. They also observed that increase in the slip flow effect significantly enhances the absolute permeability.¹³⁶

Germanou et al.,¹³⁷ investigated the effect of solid matrix complexity on the intrinsic and apparent permeability using synthetic networks. To generate they networks they implemented the quartet structure generation set algorithm. They identified the specific surface area of pores, tortuosity, heterogeneity and degree of anisotropy to be critical parameters. For their calculations they implemented the finite volume method to solve the Navier-Stokes equations, using snappyHexMesh, a native mesher of the OpenFOAM CFD toolbox.¹³⁷

In order to achieve more accurate estimations, pore reconstruction techniques are essential. In the petroleum engineering field, Markov Chain Monte Carlo (MCMC) simulations are commonly used to recreate a 3D micropore structure, while considering properties such as porosity and connectivity, by using data obtained from 2D SEM images. After the pore structure is reconstructed, calculations of the matrix permeability can be performed, usually using LB simulations or apparent permeability models. Chen et al., implemented nanometre-scale SEM imaging to visualise the kerogen micropores in shale samples and conducted LB simulations to identify the permeability and tortuosity of the 3D reconstructed network. They found permeability to be anisotropic, and higher in the z direction, due to the reduced tortuosity.¹²⁵ Tahmasebi et al., proposed a multiscale methodology for 3D reconstruction of a shale sample at a bigger scale. Their three-step methodology consists of obtaining high and low resolution 2D images, to reveal the micro and macro structure of the pore network and combining them to generate a 3D pore network. They used Avizo® to calculate the 3D network permeability

and validate their proposed methodology.^{101,138} This type of approach is believed to create a new, more accurate, and most importantly, more realistic insight of the transport mechanisms that dominate the fluid transport through microporous channels and conductive natural fractures that are present in the rocks.

Stochastic approaches have been developed to assess the permeability of complex heterogeneous systems.¹⁰⁴ Such approaches capture the variability and complexity of permeability-controlling parameters, such as the porosity, PSD, and network connectivity. Among other stochastic approaches, Renard and Marsily identified Monte Carlo (MC) methods capable of quantifying the uncertainty of the permeability distribution. They suggested that a successful approach should implement a two-part workflow: (1) individual 'local' permeabilities should be stochastically generated and (2) deterministic techniques should be applied to scale up the model and simulate fluid flow through the complex pore network.¹⁰⁴ It should be evident that KMC approaches require significant computational resources, and their performance strongly depends on how well the pore network structure is known. A typical MC algorithm samples over a Gaussian distribution and randomly selects properties based on probability distributions.¹³⁹ Alternatively, KMC can follow molecular trajectories and yield permeability calculations with satisfactory accuracy and orders of magnitude lower computational cost compared to MD simulations.^{140,141,142}

A numerical integrator of the Langevin's equation of motion could be implemented instead of the KMC to describe the time evolution of the system. In fact, this approach has been implemented to simulate various systems, from the film growth to ion-DNA interactions.^{143,144} When comparing results obtained using the KMC against the numerical integrator of the Langevin's equation of motion, the selection of the integration step used in the latter method has pivotal impact to the accuracy of the results obtained. Reducing the integration step, to achieve more accurate results, could increase the computational cost of the method. Similarly, to obtain accurate KMC results a number of independent runs should be performed to ensure accurate results, which leads to

increased computational cost. Another approach to numerically solve the M-equation was proposed by Kolokathis and Theodorou¹⁴² who implemented their proposed methodology to simulated diffusion of xenon in silicalite-1. The authors found this numerical approach to be faster when compared against KMC simulations, the numerical solution of the master equation by the Euler method, and MD simulations by factors of about 10^4 , 10^3 , and 10^7 respectively.

Kinetic Monte Carlo (KMC) simulations have been widely used to obtain transport properties and simulate diffusive-reactive processes taking place on catalytic surfaces. There is a significant amount of literature in this research area, and some key examples include the work by Stamatakis and Vlachos¹⁴⁵, Darby et al.,¹⁴⁶, Alfonso and Tafel¹⁴⁷, Fragopoulos and Theodoropoulos¹⁴⁸, Rai et al.,¹⁴⁹, and Wang et al.,¹⁵⁰ For studies of fluid transport through porous media, Flamm et al.,¹⁵¹ implemented a lattice Kinetic Monte Carlo (LKMC) method to study diffusive-adhesive events, for systems subject to external fields. Karayannis et al.,¹⁵² studied the diffusion of small molecules in disordered media by employing KMC simulations and the time-dependent effective medium approximation (EMA). Comparative to the published literature on the application of KMC to study catalytic processes, its application in the study of fluid transport through porous media is relatively limited. As such, the focus of this work has been to develop a novel multiscale KMC simulation protocol in 1D, 2D, and 3D to stochastically simulate the transport of gases in porous media that resemble those found in shale rocks. To achieve this, a lattice is generated to represent the rock sample, which is transformed to a collection of voxels. Particles are inserted in the various voxels and fluid transport is simulated as the hop of these particles from one voxel to another. A KMC algorithm defines which particle moves towards which voxel at each simulation step. The diffusion of particles in a porous medium, where external fields are not present, can be described by the Brownian motion. KMC algorithms can generate random walks, which at limit correspond to the Brownian motion. The proposed KMC methodology is used to evaluate the contributions different types of pores (micropores, mesopores and macropores) on the fluid transport and

stochastically generate multiple equivalent 2D and 3D pore networks to obtain accurate statistics.

Thesis Structure

The remainder of this thesis aims to provide the theoretical background of the KMC implementation on diffusive systems and examples where the constructed KMC model was used to simulate fluid transport in 1D, 2D, and 3D systems.

Chapter 2 provides the fundamentals of the KMC simulations. Starting with an overview and historical evolution of the method, the transition from the MC to KMC simulations is explained. Diving into the technical aspects of the method, the discussion is steered towards the selection of the transition rates, which play a fundamental role in the accuracy of the method. Various computational approaches of obtaining those rates are discussed and evaluated. Then, the different types of KMC algorithms are provided, with emphasis on the selection of the event executed. From this description, it is evident that some methods are more computationally efficient than others, and the discussion continues with recommendations on how to further improve computational efficiency. The chapter ends with a review of available random number generators and the capabilities each one offers.

The KMC algorithm selected for the study of fluid transport in this thesis is based on Gillespie's KMC implementation for reactive systems. Chapter 3 is divided in two parts; Part I describes the transition from reactive to diffusive systems and in Appendix A the validation of the constructed KMC model is provided. In Part II the KMC model is implemented to reproduce a two-phase, two-species 1D transport study, initially conducted using MD simulations. After the method is validated, the KMC model is used to provide insights on the impact of pore length and pore network connectivity on the transport of gaseous methane. The KMC method shows significant computational savings and scalability, compared to the MD method previously implemented.

The next chapter is also organised in two parts. Part I details the development of a 2D KMC algorithm and its application on synthetic 2D pore networks to elucidate the effects resulting from pore size distribution, the impact of micro- and macropores, and the effects of anisotropy on the predicted matrix permeability. The 2D KMC model is also implemented to estimate the permeability of a shale sample obtained from the Eagle Ford formation. The results obtained in Part I are compared against two deterministic approaches that are frequently used due to their simplicity and computational efficiency. In Part II the 2D KMC model is used to investigate the effect of man-made microfractures and proppants on the permeability improvement of a shale sample. The matrix permeability calculated in Part I is used as an input for the matrix permeability. The insights obtained from Part II provide valuable recommendations on how to improve the permeability of source rocks using proppants.

In Chapter 5 the KMC model is further extended to 3D and validated against analytical and computational data. In Part I, the developed 3D KMC model is implemented to describe the fluid transport in micro- to meso-scale slit-shaped porous materials. It is demonstrated that atomistic molecular dynamics simulations for the self-diffusion coefficient of supercritical methane is reproduced, within a 10% uncertainty, by the stochastic approach at a significantly lower computational cost. The method is then used to predict the diffusion coefficient of methane in single slit-shaped pores with varying pore width and chemical composition. Part II investigates the effect of porosity, pore network connectivity, pore throat width and pore chemistry on the diffusivity of gasses. The results obtained are used to provide recommendations on how possible technological approaches, involved in the hydraulic fracturing design, can be applied to maximise gas extraction.

A summary of the main findings is provided in Chapter 6. Considering the strengths of the constructed KMC model, the areas that require further improvement and emerging computational technologies, a methodology is proposed for the continuation of this work.

Methodology – Kinetic Monte Carlo simulations

Introduction

KMC simulations are a form of stochastic Monte Carlo methods that describe the dynamical phenomena governing various processes, such catalysis, material fabrication, defect evolution in crystals and diffusion.^{141,151,153–155} This form of Monte Carlo algorithm that describes the system dynamically as it is moving from state to state, was first introduced in 1960 and the earliest application reported was in 1966 for the study of radiation damage annealing by Beeler.¹⁵⁶ KMC methods have proved to be a powerful tool, which enables access to longer time scales (from ms to hours) and larger spatial scales (from nm to μm) compared to other computational methods, at comparatively low computational expense.^{146,157}

From MC to KMC

The Metropolis algorithm, named after Nicholas Metropolis¹³⁹, was published in 1953 and describes a procedure of evolving a system from a given state to the desired one. Assuming that the transitions through the states are described by a probability distribution, old states are replaced by new ones using importance sampling.¹⁵⁸ This sampling technique is used when the region of importance has low probability of occurrence, for instance, it is at the tail of the probability distribution. Importance sampling assigns larger weights to the region of interest in order to obtain some samples from that particular region. However, in the limit of a large number of such replacements, one gets the correct probability density distribution.¹⁵⁹ Repeated applications of the Metropolis algorithm always bring the system into the correct ensemble – final state, regardless of the initial state of the system. Once the equilibrium ensemble (final state) is reached, the algorithm maintains the system at the equilibrium ensemble, regardless of the additional repetitions of the algorithm. The Metropolis algorithm remains the backbone of MC methods for its simplicity, versatility, and ability to provide shortcuts when generic sampling requires too much computational effort.¹⁶⁰

The transition from the Metropolis algorithm to the KMC simulations was the outcome of an effort to speed up the MC simulations, proposed by Bortz, Kalos and Lebowitz in 1975.¹⁶¹ In their proposed N-fold way algorithm, all events selected were considered, in contrast to the Metropolis algorithm which discards some of the events selected. To shift from MC to KMC the aspect of temporal evolution needs to be address, as an MC simulation counts the number of required steps to transition from the initial to the equilibrium state, after which time has no physical meaning. In the N-fold way, the time required for a transition to happen at a particular time t is calculated based on the total propensity at a specific time and a random number, drawn from a Poissonian distribution.¹⁶² More information regarding the definition of the propensity and the equations used to calculate the time required for a transition to happen is provided in section 2.8 of this chapter.

Rare event dynamics and the timescale problem

Significant methodological advances in the field of solid-state physics and fluid dynamics have enabled us to provide answers to fundamental and long-standing questions using a variety of computational methods. Deciding on which method is more suitable for a given problem depends on the length (quantum, microscopic, mesoscopic, macroscopic) and time scales required to observe the system's evolution. Density functional theory (DFT) can describe accurately a wide class of chemical bonds and has enabled the modelling of the microscopic dynamics involved in many important processes in materials processing or chemistry. However, to answer many questions of scientific or technological interest, larger timescales are required to obtain useful insights.¹⁵⁷ This is because in many cases, the system spends a significant proportion of time vibrating within a potential basin of the potential energy surface (PES) before it performs random transitional "jump" of sufficient momentum to another state.^{146,156}

The vibrational movements taking place on the picosecond scale, are orders of magnitude faster than the transitional state-to-state jumps, which can be considered as

rare events, due to their relatively low frequency. Hence, it can be assumed that between these rare events, the system is at a quasi-equilibrium state and that it has enough time to forget where it may have been in the past.¹⁴⁶ This property of the system is known as the Markov property.¹⁶³ MD simulations, which numerically integrate the Newtonian equations, have long been at the forefront of atomistic simulations to address such solid-state and fluid transport problems.¹⁶⁴ To accurately integrate Newton's equations, a relatively large amount of simulation steps, with significantly short time increments are required to capture the vibrational motion of the particles, limiting the technique to shorter timescales.

When the problem at hand requires monitoring of these state to state jumps, rather than focusing on the vibrational motion of the particles, statistical mechanics and Monte Carlo methods can be used to simulate the systems of interest.¹⁵⁷ The basic idea behind the KMC simulations is to describe the frequency at which these state-to-state transitions take place and determine equivalent transition rates constants that depend on the energy barriers between the states.¹⁴⁶ More specifically, the rate constants express the average fraction of systems crossing the barrier per unit time, in a quasi-equilibrated ensemble of systems. The waiting time period, before a transition takes place, depends on the energy barrier the system has to surmount in order to get from one energy basin (state) to another.¹⁵⁶ Figure 2.1 represents an example of a transition from a low energy to a high energy state ($\Delta E < 0$) and an example of a positive ΔE transition. As a result, the KMC focuses on the statistics of barrier crossing, rather than the vibrational motion of the particles, allowing us to access larger length and time scales. Figure 2.2 provides a graphical representation of the length and time scales achieved by implementing DFT, MD, and KMC tools to simulate film growth.

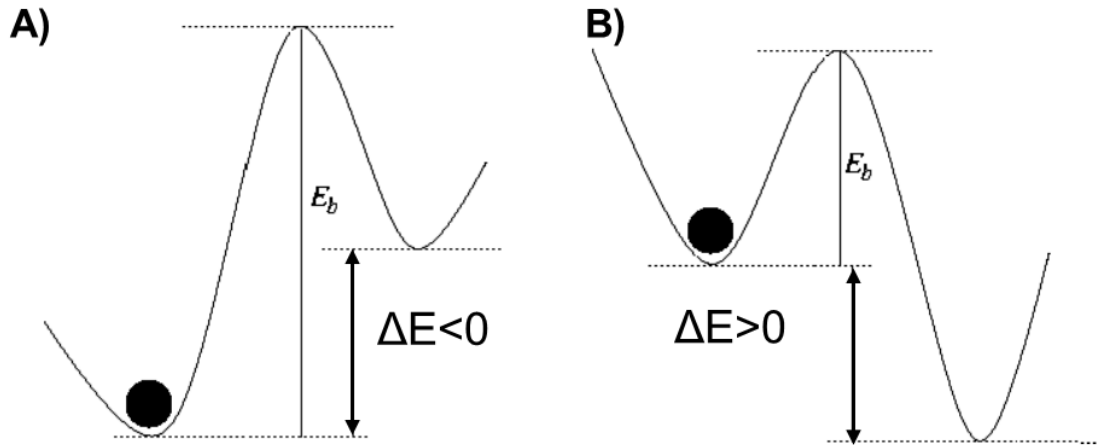


Figure 2. 1: Representation of a barrier which leads to a higher-energy state (A) and one which leads to a lower state (B).

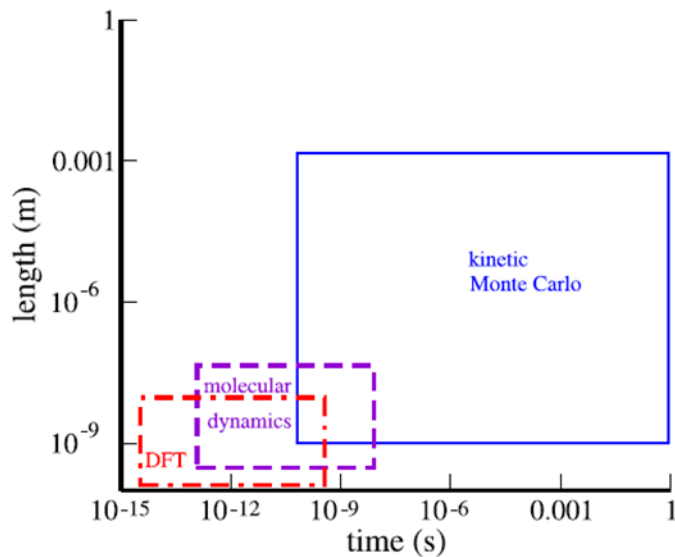


Figure 2. 2: Length and time scales achieved during the modelling of film growth using DFT, MD, and KMC simulations, as reproduced by Kratzer.¹⁵⁷

Method requirements

Through the discussion above, some of the requirements needed to develop an accurate KMC model have already been mentioned. These requirements are: 1) the satisfaction of the Markov property, 2) the satisfaction of microscopic reversibility, 3) the accurate determination of transition rates and 4) the correct selection of time increments. The

following subsections of this chapter detail the requirements of the KMC method and provide a mathematical description for their implementation. Subsection 2.5 deals with the first two requirements, subsection 2.6 addresses the calculation of the transition rates and subsections 2.8 and 2.9 describe the process of selecting events and calculating the time required for an event to happen.

The Master equation

The Master equation (M-equation) provides the means to describe a system in a "holistic" way, as it gives the time course of the probability density function (p.d.f). Hence, it can describe the p.d.f of each possible state of the system at a specific time. The key concept is that these systems consist of events that fall into the category of fast and frequent vibrations and slow rare transitions. The time gap between two rare events is orders of magnitude larger compared to the vibrations taking place and hence, one could argue that by the time the system finds its way to state n starting from state $n - 1$, the memory of all previous $n - 2$ states is lost. This statement can be translated in the following equality for the random variable X for any set of n successive times, (i.e. $t_1 t_2 \dots t_n$):¹⁶³

$$P_{1|n-1}(x_n, t_n | x_1 t_1; \dots x_{n-1}, t_{n-1}) = P_{1|1}(x_n, t_n | x_{n-1}, t_{n-1}) \quad (2.1)$$

Eq. (2.1) expresses the conditional probability density at time t_n , given the value x_{n-1} at t_{n-1} is explicitly defined and independent of all the states prior to state $n - 1$. Eq. (2.1) exhibits the Markov property and $P_{1|1}$ is called the transition probability. Hence, a Markov process is fully defined by the two functions $P_1(x_1, t_1)$ and $P_{1|1}(x_2, t_2 | x_1, t_1)$, because the whole hierarchy P_n can be constructed from them.¹⁶³

The M-equation is a differential form of the Chapman-Kolmogorov equation and describes the evolution of the probability of finding the system in state i at time t :¹⁶³

$$\frac{dP_i(t)}{dt} = - \sum_{j \neq i} r_{ij}^{\text{KMC}} P_i(t) + \sum_{j \neq i} r_{ji}^{\text{KMC}} P_j(t) \quad (2.2)$$

The M-equation describes the evolution of the system as a balance of probabilities. It accounts for all the inflow from states j to states i minus the outflow from states i towards states j . In that formulation, the probability of finding the system at states i ($P_i(t)$) and j ($P_j(t)$) is multiplied by the transition probabilities per unit time $r_{i,j}^{\text{KMC}}$ and $r_{j,i}^{\text{KMC}}$ which describe the i -to- j and j -to- i transitions, respectively.¹⁶³ Despite its simplicity, the M-equation can hardly be solved for more than two species. Kolokathis et al., proposed a methodology of analytically solving the M-equation for a system evolving on spatially periodic network of states.¹⁴² However, for the majority of systems where the analytical solution of the M-equation is unfeasible, a KMC algorithm can be employed to simulate the time evolution of the system.¹⁴⁶

To accurately describe the evolution of the system towards the thermodynamic limit, one needs to ensure that the microscopic reversibility is being satisfied. Hence, for any connected pair of states i and j , a detailed balance must be obeyed and when the system reaches equilibrium (steady state) the first part of Eq. (2.2) must be equal to zero. In that case, Eq. (2.2) takes the following form:

$$\sum_{j \neq i} r_{i,j}^{\text{KMC}} P_i^0 = \sum_{j \neq i} r_{j,i}^{\text{KMC}} P_j^0 \quad (2.3)$$

$$r_{i,j}^{\text{KMC}} P_i^0 = r_{j,i}^{\text{KMC}} P_j^0 \quad (2.4)$$

where, P_i^0 is the probability of finding the system at state i at equilibrium. Eq. (2.4) shows that for every elementary process $i \rightarrow j$ there is a reverse process $j \rightarrow i$ and that the average number of transitions from i to j is equal to the number of reverse transitions. Hence, the microscopic reversibility of the system is being satisfied at equilibrium. However, the detailed balance between states i and j , described by Eq. (2.4) must also hold true while the system is not yet at equilibrium. To ensure that the selected transitional rates capture correctly the dynamical evolution of the system towards equilibrium one can consider the Boltzmann relationship at equilibrium:¹⁴⁶

$$P_i^0 \sim \exp\left(-\frac{F_i(T)}{k_B T}\right) \quad (2.5)$$

This expression correlates the population of states P_i^0 with the free energy of state i ($F_i(T)$) at temperature T . At this point, by taking into consideration Eqs. (2.4) and (2.5) the relationship between the kinetic rates $r_{i,j}^{\text{KMC}}$ and $r_{j,i}^{\text{KMC}}$ can be expressed as:¹⁴⁶

$$\frac{r_{i,j}^{\text{KMC}}}{r_{j,i}^{\text{KMC}}} = \exp\left(-\frac{F_j(T) - F_i(T)}{k_B T}\right) \quad (2.6)$$

This relationship between rates $r_{i,j}^{\text{KMC}}$ and $r_{j,i}^{\text{KMC}}$, which originates from the description of the system at equilibrium, corresponds to a detailed balance of the system applicable for all times.¹⁴⁶

Determination of the transition rates

In order to implement KMC to study the dynamical evolution of the system, all the possible transition events – pathways have to be identified. Having knowledge of these rate constants for every state the system might visit, the resulting state to state trajectory produced by the KMC model should, in principle, be indistinguishable from the one generated by atomistic models, such as MD simulations.¹⁵⁶ To determine the rates for each pathway, statistical mechanical frameworks, such as transition state theory (TST) can be utilised.^{146,156} Although TST is considered to be approximate, it can be used as a rate determining technique for a solid-state diffusive event.¹⁵⁶ In TST the rate constant to escape from state i to state j is taken to be the equilibrium flux through a dividing surface area, as shown in Figure 2.3.

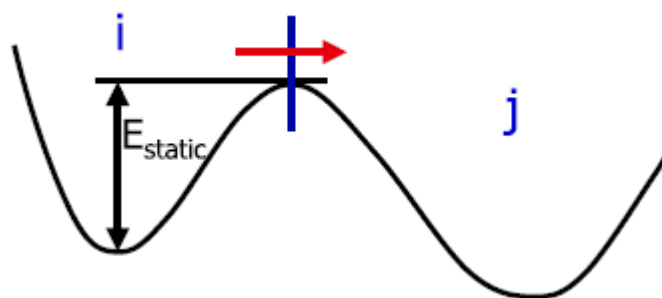


Figure 2. 3: Illustration of the transition state theory rate constant, reproduced from Voter.¹⁵⁶

One can obtain the TST rate constant, k^{TST} , by counting the number of successful jumps that lead to crossing the dividing surface area per unit time and by dividing this number by the number of trajectories on average that are in state i at any time. The particle equilibrates to the new position (state j) and vibrates around the new energy minima until it performs the next transition. That means that quasi-equilibrium needs to be reached in every potential energy basin before moving to the next one, otherwise dynamical memory left from the previous state will be transferred to the new state, making the assumption of a Markov chain invalid.¹⁵⁶

The implicit assumption in TST is that the successive crossings of the surface area are uncorrelated, each step forward is considered to correspond to a complete event. However, there is the possibility that the particle may re-cross the surface area one or more times before either falling into state j or falling back into state i . In that case TST rate constant overestimates the actual rate. This problem can be avoided by using a dynamical corrections formalism, in which trajectories are initiated at the dividing surface area and intergraded for a short time to allow the re-crossing events to occur. By using this dynamical corrections formalism, the multiple-jump events are also being considered.¹⁵⁶ The calculation of the TST transition rates K^{TST} is described by the following equation proposed by Eyring in 1935.^{146,165}

$$K^{\text{TST}} = k \frac{k_{\text{B}}T}{h} \frac{Q^{\ddagger}}{Q_{\text{reac}}} \exp\left(-\frac{E_{\text{a}}}{k_{\text{B}}T}\right) \quad (2.7)$$

where,

h = Plank's constant,

k = factor used as a transmission coefficient for re-crossings of the barrier,

E_{a} = barrier energy,

k_{B} = Boltzmann constant,

T = temperature,

Q^{\ddagger} = molecular partition function for the transition state,

Q_{reac} = molecular partition function for the reactants.

Eq. (2.7) shows that the free energy of a transition state comprises of a free energy factor associated with other degrees of freedom (except the reaction coordinate) and a kinetic energy along the reaction coordinate. The energy barrier described in Eq. (2.7) can be computed from density functional theory (DFT), the nudge elastic band (NEB), which requires knowledge of both the initial and final point, and the dimer method, which requires knowledge of only the starting point (initial configuration).^{166,167} The parameter k was initially introduced by Eyling as an ad-hoc fudge factor, in order to correct the rates for the cases when the trajectories would re-cross the transition state. This factor is designed to always reduce the rate and hence $k \leq 1$.¹⁶⁵ In the absence of more detailed information, the fudge factor can be assumed to equal 1 ($k = 1$).¹⁴⁶

Another way to determine the molecular partition function is through a harmonic approximation of the potential called harmonic-transition state theory (HTST). By following this approach, the molecular partition function can be expressed as a product of electronic, vibrational, rotational and translational contributions, as shown in Eq. (2.8)^{165,166}:

$$Q = q_{\text{elec}}q_{\text{vib}}q_{\text{rot}}q_{\text{tran}} \quad (2.8)$$

Each of these contributions q represent the sum of the respective contribution type and can be calculated from DFT along with the saddle point energy.¹⁴⁶

An alternative methodology of obtaining the reaction rate constants is by determining an activation energy plus a prefactor (or pre-exponential factor) and implementing Eq. (2.9).¹⁶⁸

$$r^{\text{KMC}} = \nu \exp\left[-\frac{E^{\text{act}}}{k_B T}\right] \quad (2.9)$$

where,

r^{KMC} = transition rate,

E^{act} = activation energy,

ν = prefactor.

By comparing the Arrhenius for in Eq. (2.7) to Eq. (2.9) it may be mistakenly assumed that the terms E^{act} and E_a are equivalent and that ν is given by the factors before the exponential in Eq. (2.7). In most of the cases, this is not correct, as the partition function in Eq. (2.7) often hides exponential factors that contribute to E^{act} . This Arrhenius form is applicable and useful only for systems where both the prefactor and activation energy are only temperature dependant, as it results in the transition rate constants that are temperature dependant.¹⁶⁸

Jansen¹⁶⁸ suggests there are two ways of calculating the transition rates using the Arrhenius form. As a first method he recommends using Eq. (2.9) to obtain the rate constant for the temperature range of interest and perform linear regression ($y=ax+b$) to the plot of $\ln(K)$ as a function of the $1/T$. According to Eq. (2.10) the b term will be equal to $\ln(\nu)$ and a equal to $-E^{\text{act}}/k_B$.¹⁶⁸

$$\ln(r^{\text{KMC}}) = -\ln(v) \frac{E^{\text{act}}}{k_B T} \quad (2.10)$$

A simpler, but less accurate approach, is to determine the factors in the partition functions that have the same exponential dependence as the activation barrier and calculate the transition rates at the temperature of interest. If the calculated transition rate constant is $r_{\text{cal}}^{\text{KMC}}$ the prefactor can be given by Eq. (2.11):¹⁶⁸

$$v = r_{\text{cal}}^{\text{KMC}} \exp\left[\frac{E^{\text{act}}}{k_B T}\right] \quad (2.11)$$

More recently, Neyertz et al.,^{169,170} presented an alternative method of calculating transition rate constants which is based on the analyses of MD trajectories. The proposed methodology is referred as trajectory-extending KMC (TEKMC).^{169,170} This approach consists of two stages: the trajectory analyses and the KMC stage. By analysing MD trajectories, TEKMC utilises a matrix of transition probabilities $p_{i,j}$ instead of calculating diffusive transition rates. The simulation box is divided into $a \times b \times c$ voxels which have the same size and shape. At first, the MD trajectories are used to record the diffusion of a target molecule in the various voxels and a probability matrix for the transitions $p_{i,j}$ between any two subcells i and j is defined based on the occupancy data collected. Then, a KMC simulation is performed using a number of walkers on the order of 5000. Each walker is initialised in a randomly assigned voxel and jumps towards other voxels according to the probability matrix obtained in the first step. The diffusion coefficient is then calculated by analysing the mean square displacement (MSD) of all walkers and implementing Einstein's equation.^{169,170}

The two critical parameters for implementing the TEKMC method are the time interval between the MD configurations, which was selected to be equal to the output frequency of the MD trajectories and the size of the voxels. To obtain the optimal voxel size, Neyertz et al.,^{169,170} proposed a lower limit in order to maintain the connectivity of the visited voxels. Through a process of trial and error, the optimal voxel size was identified by

matching the MSDs obtained from the KMC and MD simulations. Even though the TEKMC has been implemented to a number of diffusion related problems,^{171–174} when the dynamical properties of the system are unknown, defining the optimal voxel size becomes challenging and thus limits the applicability of the method.¹⁷⁵

For the case of diffusive processes, Jansen¹⁷⁶ proposed an equation to obtain the KMC transition rates based on the diffusion coefficient of molecules and the distance between two adjacent voxels. In Jansen's description, the focus is on how the position of a particle changes over time. He considered a system of a single particle in a square lattice, consisting of square voxels. If the centre to centre distance between two neighbouring voxels is l , x_a is the initial position of the particle, and x_b is the final position in the x -coordinate, then:¹⁷⁶

$$\frac{d\langle x \rangle}{dt} = \sum_{ab} r_{ab}^{\text{KMC}} P_b [x_a - x_b] \quad (2.12)$$

The x -coordinate changes as the particle hops from one voxel to another. The $[x_a - x_b]$ can possibly have three values:

- $[x_a - x_b] = l$, if $x_b > x_a$,
- $[x_a - x_b] = -l$, if $x_a > x_b$, or
- $[x_a - x_b] = 0$, if the particle has made a hop perpendicular to the x -axis, in which case $x_a = x_b$.

All these hops have a rate constant $r_{\text{HOP}}^{\text{KMC}}$ and are equally likely, resulting to $\frac{d\langle x \rangle}{dt} = 0$. The same holds for the y -coordinate. Looking at the square of the coordinates Eq. (2.12) becomes:¹⁷⁶

$$\frac{d\langle x^2 \rangle}{dt} = \sum_{ab} r_{ab}^{\text{KMC}} P_b [x_a^2 - x_b^2] \quad (2.13)$$

In Eq. (2.13) the $[x_a^2 - x_b^2]$ can be:

- $[x_a^2 - x_b^2] = 2lx_b + l^2$, if $x_b > x_a$,
- $[x_a^2 - x_b^2] = -2lx_b + l^2$, if $x_a > x_b$, or
- $[x_a^2 - x_b^2] = 0$, if $x_a = x_b$

Considering that the hops are still equally likely:¹⁷⁶

$$\frac{d\langle x^2 \rangle}{dt} = 2 r_{\text{HOP}}^{\text{KMC}} l^2 \quad (2.14)$$

The same expression holds true for the y-coordinate. The macroscopic equation for the diffusion in 2D:¹⁷⁶

$$\frac{d\langle x^2 + y^2 \rangle}{dt} = 4D \quad (2.15)$$

where, D is the diffusion coefficient. Combining Eqs. (2.14) and (2.15), results in the expression that translates the diffusion coefficient to the KMC rates:¹⁷⁶

$$r^{\text{KMC}} = \frac{D}{l^2} \quad (2.16)$$

From MD to KMC simulations: Bottom up approach

As discussed in section 2.3, many elementary processes of interest are classified as rare events, as they exhibit high activation barriers, usually much larger than $k_B T$.¹⁷⁷ An example of such processes are surface transitions, which are crucial in catalysis, and transport through heterogeneous porous media, where micro-pores co-exist with macropores. In both examples, fast transitions such as vibrations inside a PES basin or diffusion through the macropores take place frequently, while the time between consecutive high-barrier events is usually orders of magnitude longer. Looking at these systems from a macroscopic point of view, the time evolution manifests itself as a series of consecutive jumps from state to state filled with vibrational motion around PES minima, as shown in Figure 2.4.¹⁷⁷

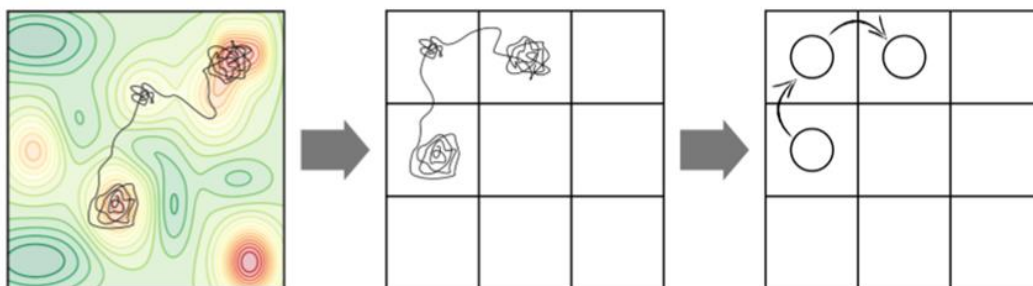


Figure 2. 4: Coarse-graining of a MD trajectory into a Markov chain. (Left) A possible MD trajectory (black) overlaid on the underlying PES of the system with red regions representing lower-energy basins. (Middle) Coarse-graining of PES minima into positions on a suitably defined lattice. Each lattice position represents the basin of attraction of a PES minimum. (Right) Coarse-graining of the continuous MD trajectory into a Markov chain of discrete hops between the basins/lattice positions. Reproduced from Andersen et al.¹⁷⁷

The idea behind the KMC is to generate stochastic trajectories that propagate the system from state to state by defining accurate transition rates via ensemble averaging over these trajectories. In practice, the challenge of implementing KMC algorithms that accurately capture these state-to-state transitions in a coarse-grained manner is to map the relevant PES minima into a lattice, without over- or under- simplifying the system's dynamics.¹⁷⁸ The TEKMC methodology described in subsection 2.6 can be considered as an example of such a bottom-up approach.^{169,170} When implementing the KMC algorithms to study crystalline substrates, the minima of the PES can be mapped onto lattice sites and the dynamics of the system can be considered as a sequence of discrete transitions, starting and ending at lattice sites (lattice approximation).¹⁵⁷ For the studies of fluid transport through heterogeneous porous media, the mapping of the sample space into a KMC lattice and the determination of transition rates are elusive and underreported. This research study is dedicated in addressing these challenges and proposes rigorous methodologies to address them. These topics are discussed in detail in Chapters 3, 4, and 5.

KMC algorithms

A way of solving the M-equation is via implementation of a KMC algorithm, especially when the analytical solution of the method is unfeasible. The KMC algorithm should yield a sequence of configurations and calculate the time between these configurations/transitions. All the realisations generated by the KMC algorithm must follow the statistics of the M-equation. There are many algorithms developed that yield such a sequence of configurations and which are statistically equivalent. Some of them are the random selection method, the first reaction method and the direct method.^{146,176} In this research study the direct method is implemented and detailed information regarding the method is given in subsection 2.8.1.5, as well as in Chapters 3–5, where the development of the 1D, 2D, and 3D KMC models is discussed. For completeness, the basic features of the random selection and first reaction method are provided below.

In principle, a basic KMC algorithm performs two main tasks, the selection of a transition taking place at a specific time, and the update of the system. For the selection of the transition events there are two main methodologies that can be implemented, the rejection and the rejection-free method.

Rejection method

For a system with j_{\max} possible events/transitions, $\{r_j^{\text{KMC}}\}$ is the list of the current set of rates. To identify which event n takes place at a specific time, while implementing a rejection KMC algorithm the next steps need to be followed:^{179,180}

Step 1: Scan the list of rates $\{r_j^{\text{KMC}}\}$ and identify a single global upper bound $\widehat{r^{\text{KMC}}}$ for which $\widehat{r^{\text{KMC}}} \geq r_j^{\text{KMC}} \forall j$.

Step 2: Select a uniformly distributed random number $u \in [0, j_{\max})$

Step 3: Calculate $j_{\text{exec}} = \text{Int}(u) + 1$

Step 4: Select event n if $j_{\text{exec}} - u < \frac{r_j^{\text{KMC}}}{\widehat{r^{\text{KMC}}}}$

Step 5: Repeat until successful

The efficiency of this algorithm is proportional to the ratio of attempted to accepted events and can be very low for the case of systems with broad distribution of rates. The rejection method can also become inefficient when there are one or more large rate constants. This can be addressed by implementing a form of importance sampling, as it was discussed in section 2.2. In these systems, the partition rates can be divided in two categories, one including transitions with high rates and one with small rates. The rejection method can be then applied and provides two estimates, one for each category. This categorisation of transition rates requires additional work, especially considering that after each simulation step, the KMC distribution changes and this process has to be repeated.^{179,180}

Rejection-free method

While implementing a rejection – free KMC algorithm, the following steps are followed:¹⁷⁹

Step 1: Calculate the sum $R^{\text{KMC}} = \sum_{j=1}^{j_{\text{max}}} r_j^{\text{KMC}}$, while retaining the partial sums R_j^{KMC} .

Step 2: Choose a random number $u \in [0, R^{\text{KMC}})$

Step 3: Search the list of partial sums until $R_{j_{\text{exec}}-1}^{\text{KMC}} \leq u < R_{j_{\text{exec}}}^{\text{KMC}}$

Step 4: Select the event j_{exec}

The efficiency of the rejection-free algorithm is 100%, since all events selected are accepted, however the computational cost required for each event selection depends on the size of the system. Typically, the cost becomes large, as j_{max} increases. A way to reduce the cost of each iteration is by sorting the rates from the largest to the smallest, in order to speed-up the termination of step 3.¹⁷⁹ However, more sophisticated algorithms, discussed in subsection 2.9, have been proposed to address this challenge.

Random selection method

The random selection method, or else referred to as the null–event method is one of the earlier employed KMC algorithms in which not all MC events (trials) are successful.¹⁸¹

The Metropolis algorithm is an example of a random selection algorithm. While implementing this type of KMC algorithm, the determination of the process taking place and the calculation of the time required for the transitions to happen can be split into three parts; the selection of the process type, the selection of the site the process happens, and the time required for the process to take place. The algorithmic steps involved in this type of KMC method are the following:^{168,181,182}

Step 1: Using a random number select the site at which the process takes place.

Step 2: Using a random number select the type of process happening at the selected site.

Step 3: Check if the transition selected is feasible at the selected site. If so, update the system accordingly. Otherwise, reject the event and return to Step 1.

Step 4: Calculate the time required for the transition to happen.

The selection of the site where the event occurs and the selection of the transition happening can be performed in any order. The method's efficiency depends on the ratio between the accepted and rejected events, as discussed in the rejection methods above. Due to the possibility of selecting an unfeasible event, the method is also referred to as the null-event.^{168,181}

First reaction method

The first reaction method belongs in the rejection–free family of the KMC simulations and combines the three steps described in the Random selection method in one. According to this KMC algorithm the next event executed is the one that happens at the shortest time. To determine what is the earliest event taking place from a list of transitions, the

algorithm scans all possible events and calculates the time required for every possible a-to-b transition to happen, identifying the one with the shortest time-value. The time of occurrence ($t_{a \rightarrow b}$) for each individual a-to-b transition is calculated by Eq. (2.17):¹⁶⁸

$$t_{a \rightarrow b} = t - \frac{1}{r_{ab}^{\text{KMC}}} \ln(u) \quad (2.17)$$

where,

t = the current simulation time,

r_{ab}^{KMC} = the rate constant for the a-to-b transition,

u = a random number uniformly distributed

This algorithm is also called a Discrete Event Simulation (DES). For large systems consisting of many transitions, the calculation of all the time transitions at each simulation step can come at a significant computational cost and significantly slow the simulation. A way of reducing the computational cost is by assuming that the outcome of an executed event has no influence on a second transition and thus retain the random time calculated for the second transition until (1) the secondary transition takes places, or (2) the number of particles/reactants for this secondary transition changes, due to another process taking place, or (3) another change in the system happens that forces the transition rate of the secondary process to change (e.g. local temperature change).¹⁶⁸

Direct method – Gillespie's algorithm

The direct method is another rejection-free algorithm used to simulate the M-equation. It requires the selection of two random, uniformly distributed random numbers u_1 and u_2 between 0 and 1, $u_1, u_2 \in [0,1]$. One of the selected numbers is used to select the event that takes place and the second is used to determine the time increment due to the selected transition. The algorithm steps involved during this type of KMC simulation are the same as those presented in subsection 2.1.8.2.

In 1977 Daniel Gillespie proposed a variation of the direct method algorithm in order to describe the distribution of N chemical species, which could interact through M specified reaction channels, while being confined in a fixed volume V . The motivation behind the studies performed was the inability of the reaction-rate equations, which provide information about the population levels in a deterministic way, to predict the fluctuations observed in some cases. With the algorithm he constructed, he was able to treat the time evolution of a homogeneous chemical system as a discrete stochastic process rather than a continuous deterministic one.¹⁸³

The proposed algorithm involved the selection of two random numbers, one to select the reaction pathway j_{exec} and one to calculate the time required until the next event τ . The difference between the algorithm he proposed, and the direct method algorithm is related to the selection of the event j_{exec} . Instead of following the Step 3 of the rejection-free procedure discussed in 2.1.8.2, he scaled the stochastic reaction-rate constants with the population of species available to react. This product describes the probability of occurrence per unit time and is called propensity.

In order to select the executed event, one needs to create a list of all possible events (j_{max}), define the transition rate constants (r_j^{KMC}) for each event j , and calculate the propensity of each event (w_j). In diffusive systems, where all transitions involve jumps of particles from one voxel to another, the propensity of an event is defined as the product of the rate constant and the state vector, which holds information regarding the population of particles in the corresponding voxel. As a next step, all the individual propensities are summed to give w_{tot} :

$$w_{\text{tot}} = \sum_{j=0}^{j_{\text{max}}} w_j \quad (2.18)$$

where, $w_0 = 0$, and j_{max} is the total number of events taking place in the system. A random number u_1 is then selected and multiplied by the w_{tot} calculated. A loop is then

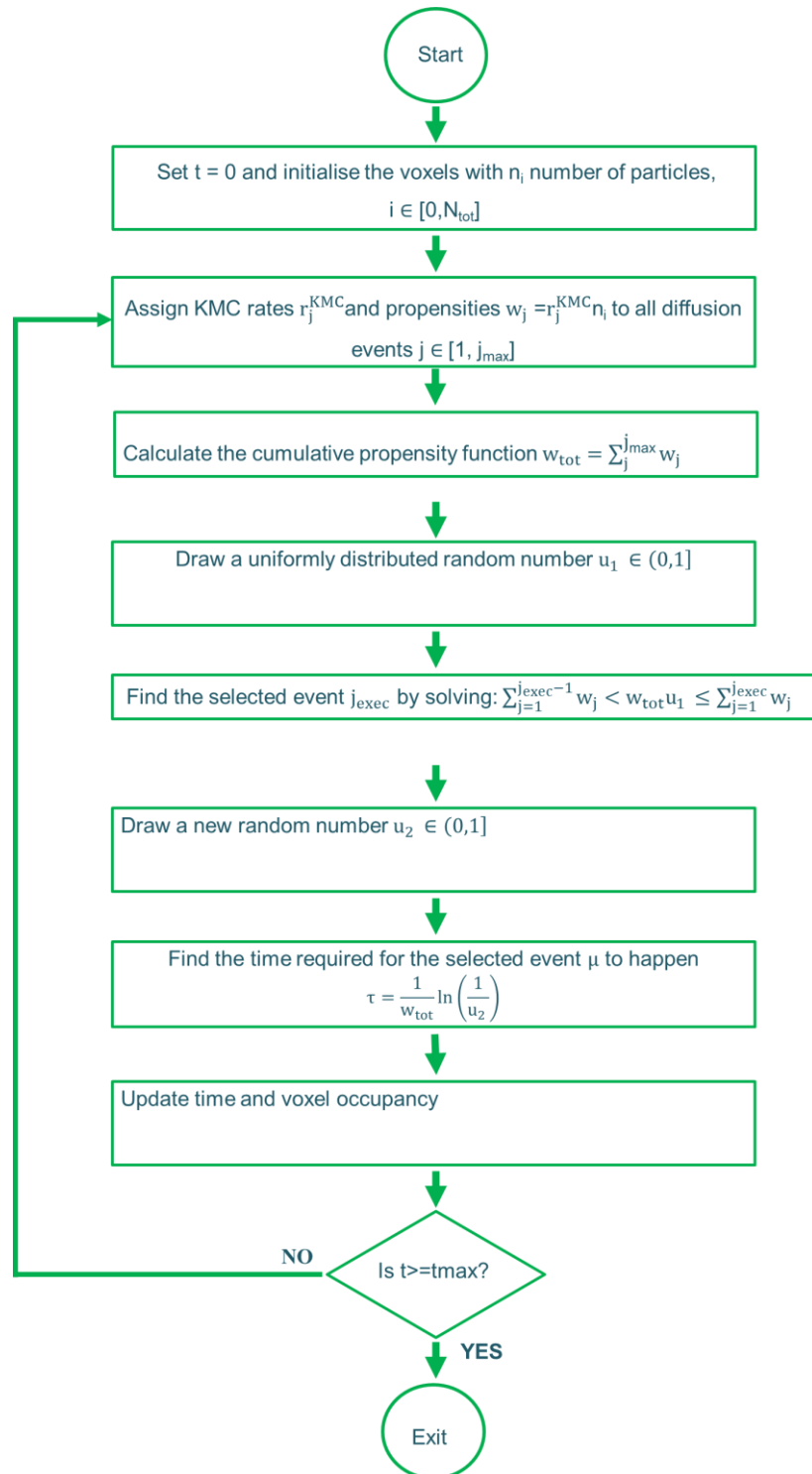
initiated and the list containing all the rates, defined in the previous step, is scanned. There are different ways to scan the list of rates. The simplest and less efficient is to go through the list of all possible events in a linear manner. The random event j_{exec} for which the following inequality holds true, is chosen to be the event that will take place.

$$\sum_{j=0}^{j_{\text{exec}}-1} w_j \leq u_1 \times w_{\text{tot}} < \sum_{j=0}^{j_{\text{exec}}} w_j \quad (2.19)$$

As Eq. (2.19) dictates, the probability of selecting an event is proportional to its rate. Since Gillespie's method is meant to be rejection free, the non-realizable events shouldn't be sampled and then rejected. To achieve this, they are assigned zero probability and therefore, do not contribute in the calculation of w_{tot} .¹⁴⁶ The time required until the next transition to happen (τ) is calculated by the following expression, where u_2 is the second random number selected.^{146,156}

$$\tau = \frac{\ln(u_2)}{w_{\text{tot}}} \quad (2.20)$$

As a final step, the system needs to get updated. Both the time and the occupancy at each position need to change accordingly, in order to reflect the occurrence of the randomly selected event j_{exec} . Afterwards, the process is repeated for the configuration created until the maximum simulation time is reached. The reader is referred to Gillespie's publications for more information regarding the calculation of the stochastic reaction-rates constant.^{183,184} Figure 2.5 shows a schematic of the algorithm he used, to which is referred to as the Gillespie's algorithm for what follows.

Figure 2. 5: Gillespie's algorithm.¹⁸³

More efficient selection algorithms

It is evident that although the linear search algorithm is simple and easy to code, it can be very time consuming for systems consisting of many possible events j . To overcome

this challenge and allow KMC simulations to be as fast as possible, various alternative event selection algorithms have been proposed. To evaluate and classify them according to the run time required, the big O notation can be used. For simplicity, let us assume that in the linear search algorithm, the total number of events j_{\max} is equal to M . Thus, the time required for the event selection through a linear search protocol is $O(M)$.¹⁸⁵

A more time efficient way of scanning through the list of propensities $\{w_j\}$, is by applying the binning search method, proposed by Maksym.¹⁸⁵ According to this protocol, the list of propensities can be divided in several subsets S_j . Assuming that each subset is a list containing m propensities out of the total M found in the main set, M/m subsets will be generated. Eq. (2.21) shows how the propensities are mapped into the subsets S_j .¹⁸⁵

$$S_j = \sum_{i=1+(j-1)m}^{jm} w_i, \quad j = 1, \dots, [M/m] \quad (2.21)$$

The search for the executed event is then divided into two steps; (1) search through the various subsets S_j (bins), and (2) after you select the bin containing the executed event, scan through the bin's elements to find the event j_{exec} . The time required for the first part of the scan is proportional to the number of bins (M/m) and can be expressed as $O(M/m)$. The time required for the second part of the search, depends on the number of propensities assigned in the bin (m), and can be expressed as $O(m)$. Following this scheme, the time required per simulated event is $O(M^{1/2})$. Blue et al., referred to Maksym's method as a two-level search scheme and suggested that better asymptotic behaviour can be obtained by constructing K -level schemes, with $K > 2$. According to this K -level scheme, the lowest level is identical to Eq. (21) with a slight change in notation:¹⁸⁵

$$S_j^{(2)} = \sum_{i=1+(j-1)m}^{jm} w_i, \quad j = 1, \dots, [M/m] \quad (2.22)$$

The higher levels are defined recursively according to Eq. (2.23).¹⁸⁵

$$S_j^{(k)} = \sum_{i=1+(j-1)m}^{jm} S_i^{(k-1)}, \quad (2.23)$$

$$j = 1, \dots, \left\lceil \frac{M}{m^{(k-1)}} \right\rceil, \quad k = 3, \dots, K$$

The total search time is $O(KM^{1/K})$. For a given M the best asymptotic time behaviour is obtained by using the largest feasible K , namely, the one for which there are only two propensities in each partial sum ($M^{1/K} = 2$).¹⁸⁵ The data structure is then a binary tree, similar to the one presented in Figure 2.6 by Gibson and Bruck.¹⁸⁶

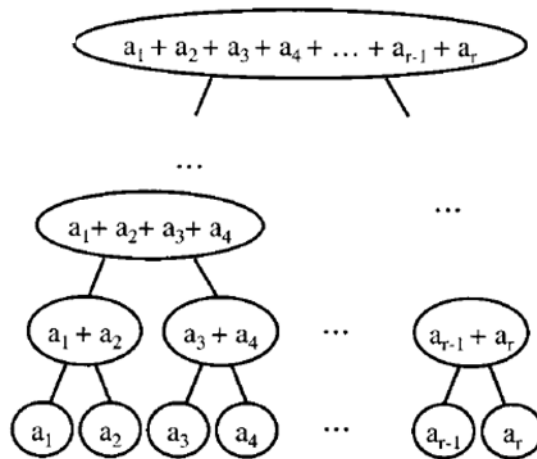


Figure 2. 6: Binary tree data structure used to store propensities, noted as a_r . For each partial sum there are only two assigned partial sums – propensities. Reproduced from Gibson and Bruck.¹⁸⁶

Blue et al.,¹⁸⁵ also compared the computational time required per event, when simulating a solid-on-solid model of epitaxial growth on a simple $N \times N$ lattice. For their comparison they considered $K=2,3,4,5$, and a binary tree implementation. Figure 2.7 presents the results they obtained. To help the reader, the K -level has been noted in each curve. The linear selection algorithm was implemented in this research study, except for the work discussed in Chapter 4, where the binary tree algorithm was applied.

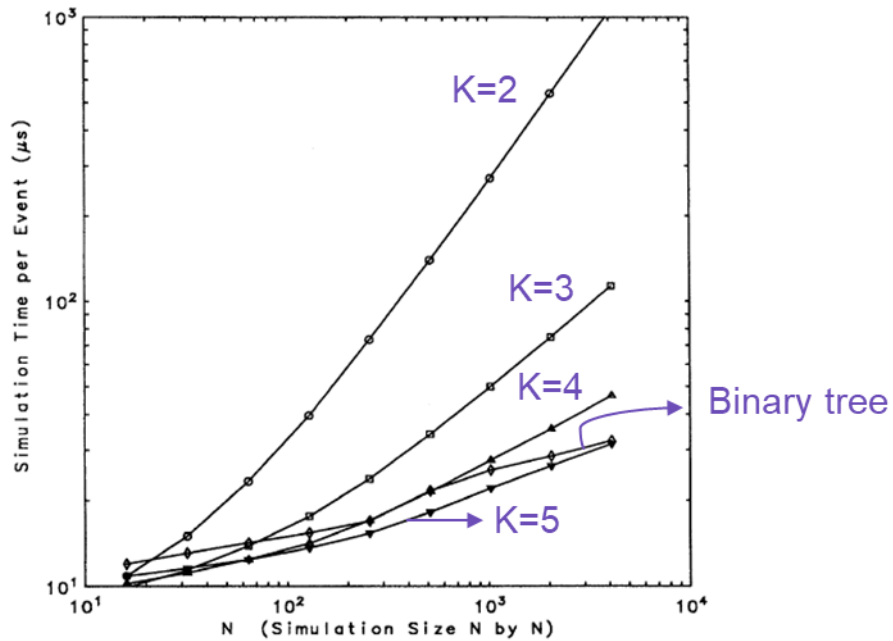


Figure 2. 7: Log-log plot of the time required per event for different search schemes, reproduced and modified by Blue et. al.¹⁸⁵ K=2 (circles), K=3 (squares), K=4 (triangles pointing up), K=5 (triangles pointing down), and binary tree (rhombus). Reproduced and modified from Blue et al.¹⁸⁵

Selection of the random number generator

One of the main assumptions made to enable the use of the Markov property is the memoryless transition between the states. Thus, the KMC algorithm has to exhibit the same property. In subsection 2.6, a mathematical description of how to determine the KMC rates, while correctly capturing the dynamics of the system and hence the Markov property was discussed. The necessity of an "efficient" uniform random number generator (u.r.n.g) emerged in subsection 2.8, where the algorithmic steps required for the implementation of the KMC algorithm were listed, including the selection of two random numbers, which define the event selected and the time required for the transition. The objective of a uniform random number generator is to produce samples of any given size that are indistinguishable from samples of the same size from a $U(0, 1)$ distribution.¹⁸⁷

A suitable u.r.n.g should be fast (small CPU times), in order to minimise the computational cost of the KMC algorithm, and have a long period, to ensure there is no correlation or bias in the process of selecting events. As an example, the minimal standard generator of Park and Miller has period of $2^{31}-1$ (approx. $10^{9.333}$). Considering that Monte Carlo algorithms require random numbers in the order of 10^{15} , this period is very short and makes this u.r.n.g unsuitable. While in most KMC applications, including those discussed in this research study, uniformly distributed random numbers are required, in many cases, random numbers from other distributions, such as the normal or exponential, are needed. If the routines for generating random deviates from nonuniform distributions use exact transformations from a uniform distribution, their quality depends almost solely on the quality of the underlying uniform generator.¹⁸⁷ An excellent review of some of the most important random number generators was reported by L'Ecuyer.¹⁸⁸ For this research study, the Mersenne Twister MT19937 is selected as a suitable u.r.n.g, due to its long period $2^{19937} - 1$ (over 10^{6001}), which is safely larger than the maximum number of events simulated per run of the KMC algorithm.¹⁸⁹

Summary

This chapter provided an overview of the KMC method. Initially the first ever type of Monte Carlo simulation (MC), the Metropolis algorithm was discussed. Starting from an initial state the system evolved towards its final state via importance sampling, where equilibrium is reached. After this point, the algorithm maintains the system at the equilibrium ensemble, regardless of the additional repetitions of the algorithm. The KMC algorithm, first reported as the N-fold way was the outcome of an effort to speed-up the MC simulations.

To achieve an accurate and computationally efficient implementation of the KMC method the Markov property needs to be satisfied together with the microscopic reversibility. The accuracy on determining the transition rates and the selection of time increments are also vital. Various approaches can be implemented to determine the transitions rates,

such as statistical mechanical frameworks (transition state theory and harmonic-transition state theory), density functional theory (DFT), the nudge elastic band (NEB), or analysis of molecular dynamics simulation trajectories. The selection of the most appropriate method depends on the characteristic timescales of the system of interest.

The backbone of the KMC simulations is the Master Equation, which is a differential form of the Chapman-Kolmogorov equation. KMC algorithms are implemented to solve the M-equation when numerical solutions are not applicable. There is a variety of KMC algorithms, mainly divided into three categories; the rare event selection method, the rejection method, and the rejection free method, each having its own limitations and advantages. The main difference between these three forms of KMC is the way the event executed is selected. It is frequently observed that the rejection method is not very computationally efficient. In this research study Gillespie's direct method is used to simulate the diffusive systems. Gillespie's method is a form of a rejection free algorithm, in which the non-realizable events are assigned zero propensity (probability of occurrence per unit time)

Moreover, it is observed that for systems with a large amount of transition events, the KMC algorithm spends a significant portion of time scanning through the list of calculated propensities in order to select the event executed. The solution to this shortcoming is to implement a more efficient selection algorithm. The simplest and most time-consuming method is the linear search method, while the most efficient is binary tree implementation.

Finally, it is important to understand the requirements of the system and accordingly decide on the most appropriate random number generator. For every computational step two random numbers need to be selected, and in order to ensure that there is no correlation or bias in the process of selecting events, a random number generator with sufficiently long period needs to be selected.

Algorithm construction, validation, and application in 1D networks

In Chapter 2, Gillespie's algorithm which simulates reaction networks, was introduced. To stochastically simulate diffusive processes using Gillespie's direct method, the sample space needs to be discretised (meshed) in a lattice. Transport can be then simulated as a random walk of molecules which "hop" from one mesh point to another. This chapter is organised in two parts; Part I shows the reproduction of Gillespie's KMC algorithm, when applied to reaction networks, and describes the modifications made in the algorithm, in order to simulate 1D diffusive processes. Reproducing Gillespie's data was essential for the construction of an accurate KMC model and was the starting point for this research study. In Part II the produced 1D KMC algorithm, for diffusive events, is validated against the analytical solution of the 1D diffusion equation, and then used to reproduce MD data obtained for slit micropores in two-phase systems. The results obtained in the second part have been published in JCP **147**, 134703 (2017) and provide a novel way of simplifying and accelerating a 3D two-phase system into a 1D single phase one.

KMC algorithm construction– Part I

In his work, Daniel Gillespie¹⁸³ performed computational studies for five different systems while using the direct KMC algorithm he proposed. The first two systems investigated, deal with simple reaction networks, while the remaining three describe systems with more complicated behaviour. Appendix A provides a brief description of the systems, the conditions and the sampling scheme Gillespie used. Based on this information, a KMC code was constructed in order to reproduce the results Gillespie reported.¹⁸³ For every system investigated in Appendix A, the results obtained by the developed KMC model were compared against the results reported by Gillespie and the deterministic solution of the M-equation. The agreement between the results obtained from the constructed KMC model and Gillespie's findings was satisfactory and therefore, the validity of the KMC constructed model was established.

From reactive to purely diffusive systems

A probabilistic model is a quantitative description of an experiment-phenomenon, whose outcome is uncertain. In every probabilistic model one needs to define the possible outcomes, by specifying a sample space and a probability law through which probabilities will be assigned to the possible outcomes. Looking at the surface of a rock sample, from a probabilistic point of view, and the possible positions one molecule could occupy over time one could argue that the sample space is continuous and infinite, as shown in Figure 3.1 This representation would create tremendous computational difficulties, in terms of the computational power required for such off-lattice simulations, and the level of detail needed to describe the probability of each point. Moreover, in such a sample space the probability of a molecule to be found at a specific position with infinite precision is close to zero. The idea behind the LKMC model is to discretise the sample space and create finite domains, subsets of the sample space, in which a molecule can be found. In this case there is no need to assign probabilities to individual points; one can instead

determine the probability law for these subsets, which are referred as voxels in this document.

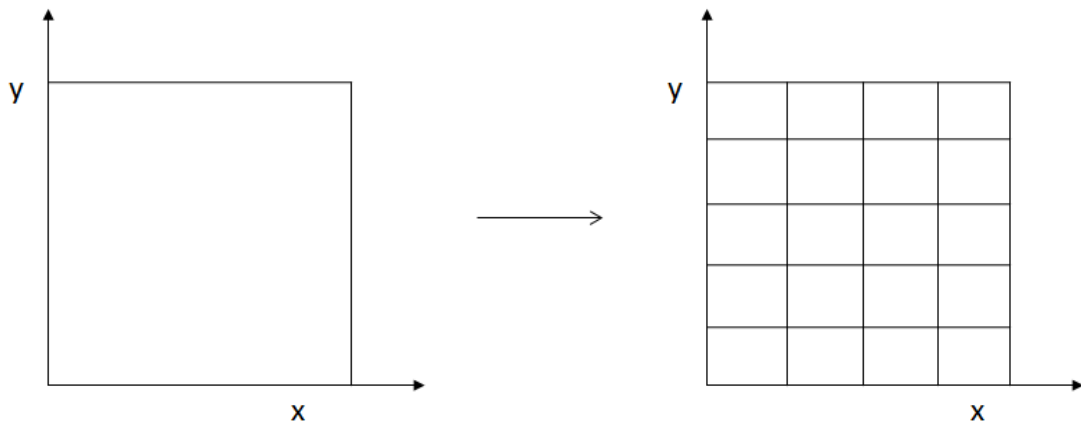


Figure 3. 1: Representation of the 2D sample space in an off-lattice (left) and on-lattice (right) lattice system.

Gillespie's algorithm was modified to simulate diffusive events. Earlier studies by Flamm et al.,¹⁵¹ implemented a lattice Kinetic Monte Carlo (LKMC) method to study diffusive-adhesive events, for systems subject to external fields. In this research study, the movement of molecules from one voxel to another (jumps) was treated as possible reaction pathways. As a first step, all possible pathways (jumps) need to be determined, and then all rates, through which the transitions take place, need to be defined. The possible pathways a molecule can follow, while it diffuses in a 1D domain with periodic boundaries and N square voxels is $2N$. For a closed and non – reactive system, with reflective boundaries (non – periodic) where the population of molecules remains constant, the possible pathways are reduced by two and are $2N – 2$. Further information regarding the calculation of possible pathways in 2D and 3D systems, is provided in Chapters 4 and 5.

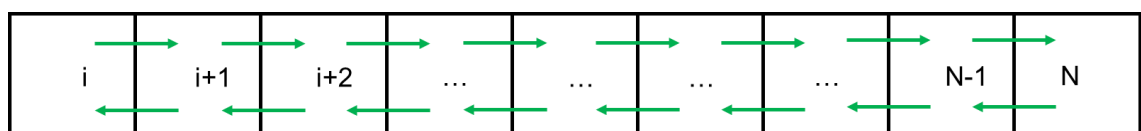


Figure 3. 2: Representation of the possible pathways in a 1D domain with reflective boundaries. For N square voxels there are $2N - 2$ possible moves a molecule can make.

However, identifying the possible pathways and determining the transition rates is not enough in order to build an accurate and efficient model. Two additional parameters need to be defined; the sampling frequency (sampling time-step) and the number of independent simulations performed to calculate the system properties. To develop a strategy for selecting these two parameters for any given system, a simple 1D lattice consisting of three square voxels, denoted as Left (L), Middle (M) and Right (R), was considered. The boundaries of this domain were reflective and hence there were four possible moves (jumps) a molecule could perform. Each one of these pathways was assigned an index $i \in [1,4]$ and a transition rate constant $k(i)$, as shown in the Figure 3.3.

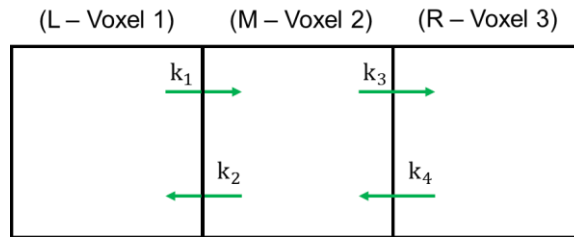
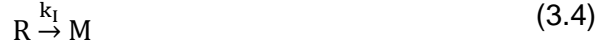


Figure 3. 3: Representation of a simple 3 voxel lattice. The possible pathways with rates $k(i)$, $i \in [1,4]$, are noted as green arrows.

For this simple exercise, it was assumed that there was only one type of species in the system and a matrix $X(j, t)$ was defined, in which $j \in [1,3]$ and $t \in [0, t_{\max}]$, in order to monitor the population of molecules in each voxel. Since there were no reactions taking place in the system and the boundaries of the lattice were closed, the population of molecules remained constant at all times and equal to X_{tot} . The four pathways were divided in two categories; jumps towards the middle voxels, with rate k_I (k_1, k_4) and jumps from the middle voxel, with rate k_{II} (k_2, k_3). Due to the simplicity of the system, the four potential movements were expressed as reaction-type equations:



Since there are four possible transitions that can take place during each simulation event, four propensities were required:

$$a_1 = k_I X(1, t) \quad (3.5)$$

$$a_2 = k_{II} X(2, t) \quad (3.6)$$

$$a_3 = k_{II} X(2, t) \quad (3.7)$$

$$a_4 = k_I X(3, t) \quad (3.8)$$

From a deterministic point of view, the population of molecules in the middle voxel ($X(2, t)$) over time, could be expressed as:

$$\frac{dX(2, t)}{dt} = k_I X(1, t) + k_I X(3, t) - 2k_{II} X(2, t) \quad (3.9)$$

Since $X_{\text{tot}} = X(1, t) + X(2, t) + X(3, t)$ Eq. (3.9) becomes:

$$\frac{dX(2, t)}{dt} = k_I X_{\text{tot}} - X(2, t)(k_I + 2k_{II}) \quad (3.10)$$

The solution of this differential equation is:

$$X(2, t) = c_0 \exp[-t(k_I + 2k_{II})] + \frac{k_I X_{\text{tot}}}{k_I + 2k_{II}} \quad (3.11)$$

Since the mathematical description of the system is complete, the transition rates k_I and k_{II} , as well as the population X_{tot} need to be defined. The values selected here for these parameters are arbitrary and have no physical meaning. It is assumed that $k_I = 0.005\text{s}^{-1}$

and $k_{II} = 0.003s^{-1}$ and that there are 100 molecules in the system, placed on the left voxel initially.

The first parameter investigated is the sampling frequency. To obtain a general idea of how fast the transitions between the voxels take place, a simulation was performed to obtain the time between two successive transitions of any kind (τ). Samples were taken every 0.1s and the number of events taking place between two consecutive samples was recorded. Figure 3.4 presents the frequency of events happening during each interval.

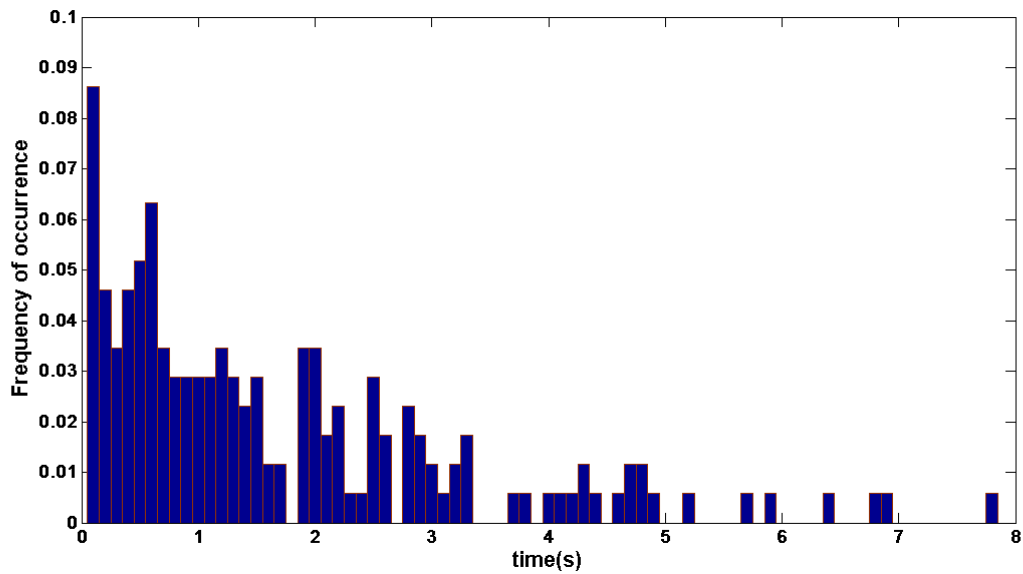


Figure 3. 4: Frequency of event occurrence for different time intervals. The y-axis represents the time required for a transition to happen. Each bar represents a 0.1s and $0 \leq t \leq 8s$.

As shown in Figure 3.4, there are events that happen rapidly, in less than 1 second and some less frequent events. For this simulation run, the minimum, the maximum and the mean reported times required for the transitions to take place were $t_{\min} = 7.85 \times 10^{-4}s$, $t_{\max} = 10.59s$, and $\bar{t} = 1.73s$, respectively. To identify a suitable sampling scheme, the population of molecules in the middle voxel was simulated using three different sampling time-steps; $dt_{\text{sample1}} = 0.02s$, $dt_{\text{sample2}} = 1.73s$ and $dt_{\text{sample3}} = 5s$. Figure 3.5 presents the molecular density in the middle voxel, as predicted by the KMC algorithm (top panel) and the deterministic model, for $0 \leq t \leq 300s$, and the number of events taking place in-

between the samples (bottom panel). The size of the voxels was 1(nm) x 1(nm) x 1(nm) and sample was taken every 0.02s.

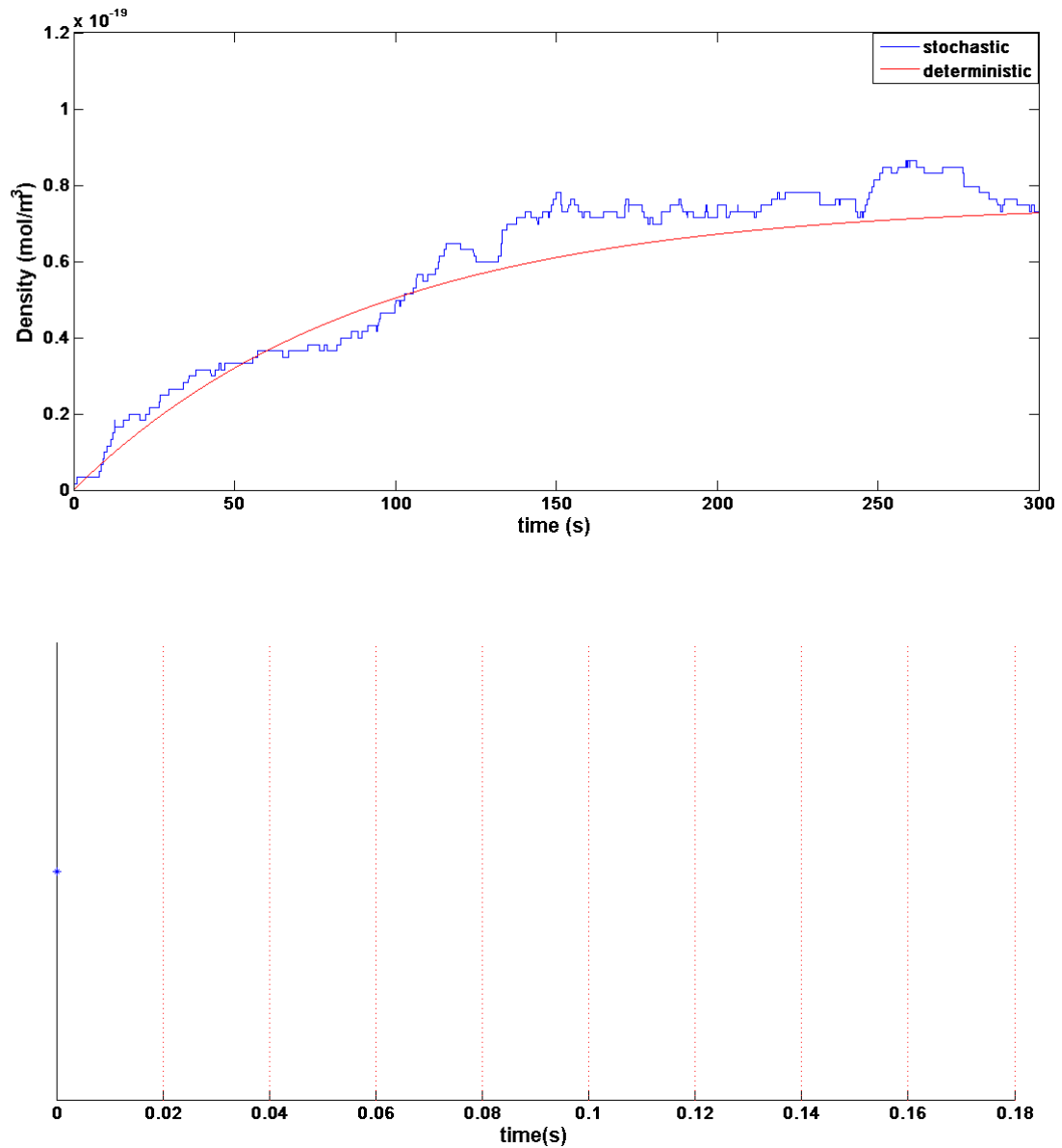


Figure 3. 5: The time evolution of the population in the middle voxel as predicted from the stochastic and the deterministic approach for $0 \leq t \leq 300s$ (top panel) and $dt_{\text{sample}} = 0.02s$. Representation of the samples taken, represented by red dashed lines and the occurrence of events, presented as asterisks (bottom panel).

As shown Figure 3.5, the sampling time-step was very small. Hence, the state of the system was being reported several times before a new transition happens. This sampling approach is not necessarily mistaken however, it negatively affects the efficiency of the

approach and is not a recommended practice. The same analysis was repeated when the sampling time-step was $dt_{\text{sample2}} = 1.73\text{s}$ and the results are summarised in Figure 3.6.

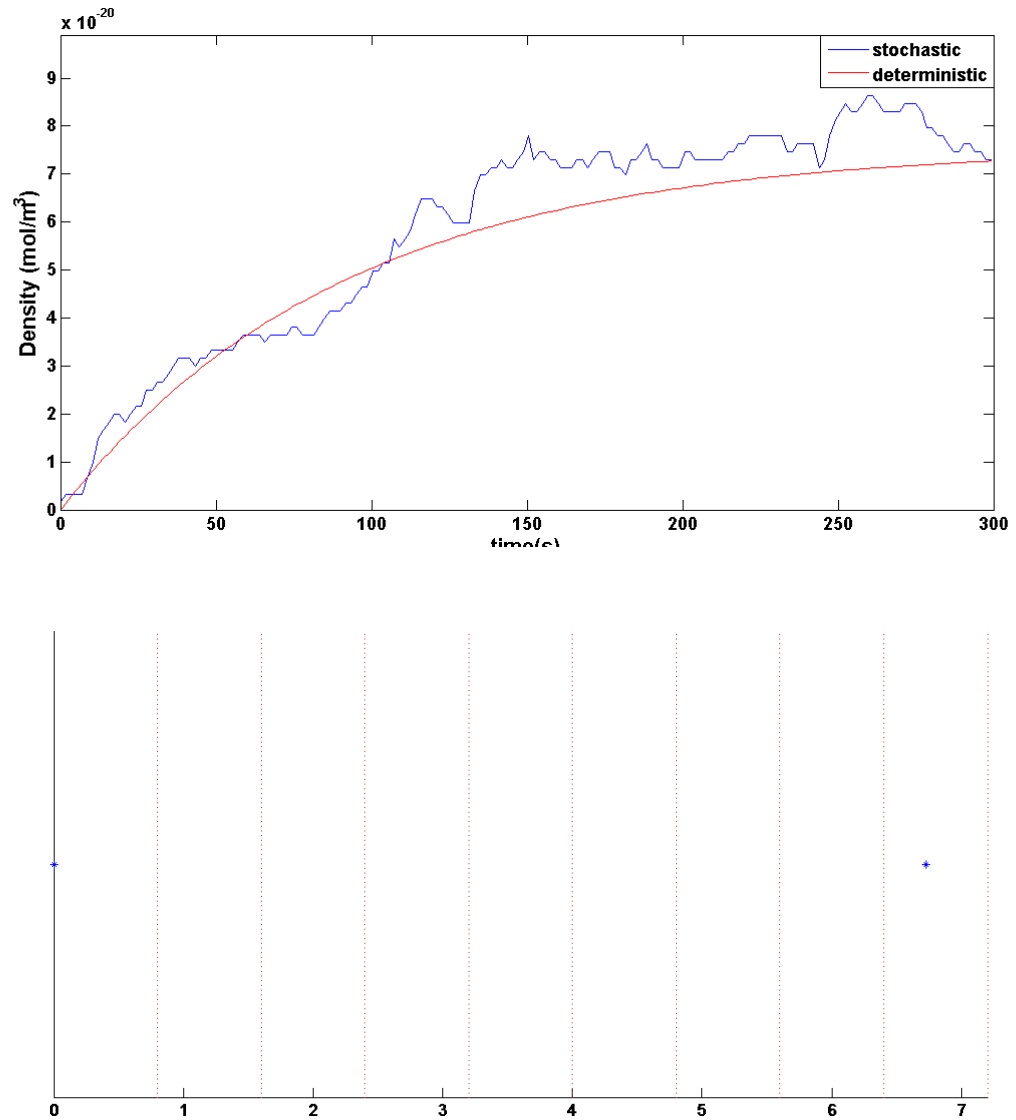


Figure 3. 6: The time evolution of the population in the middle voxel as predicted from the stochastic and the deterministic approach for $0 \leq t \leq 300\text{s}$ (top panel) and $dt_{\text{sample}} = 1.73\text{s}$. Representation of the samples taken, represented by red dashed lines and the occurrence of events, presented as asterisks (bottom panel).

By implementing this sampling time-step many data points were collected however, less than before. In Figure 3.7, the same analysis was carried out for a $dt_{\text{sample}} = 5\text{s}$.

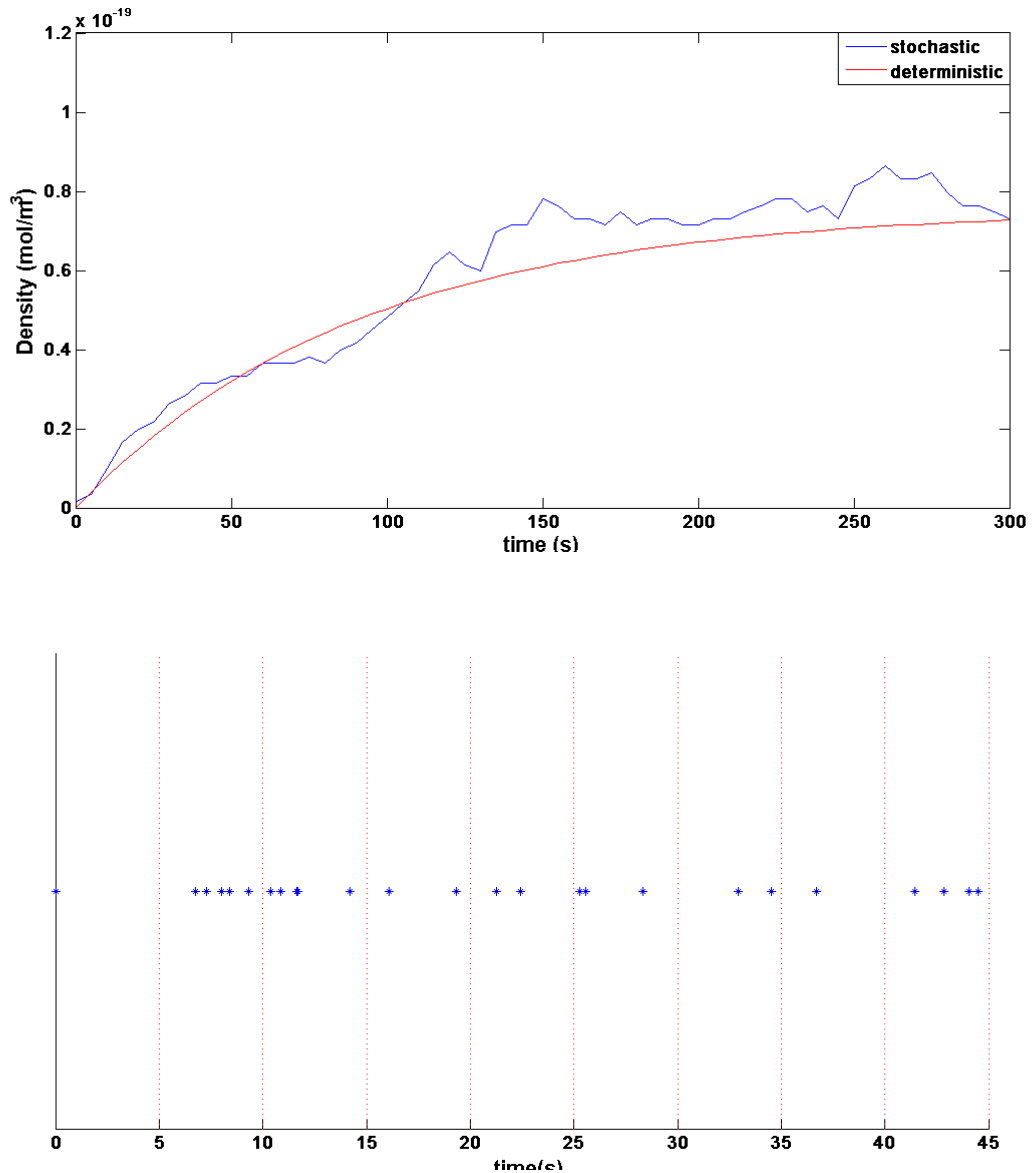


Figure 3. 7: The time evolution of the population in the middle voxel as predicted from the stochastic and the deterministic approach for $0 \leq t \leq 300\text{s}$ (top panel) and $dt_{\text{sample}} = 5\text{s}$. Representation of the samples taken, represented by red dashed lines and the occurrence of events, presented as asterisks (bottom panel).

With this sampling time-step, several transitions take place between two consecutive events, and as a result, the density plot presented in Figure 3.7 seems smoother, compared to the previous ones. However, since the total time of analysis has remained the same (300s), the number of samples taken is significantly reduced, and the results obtained may suffer significant uncertainties. Hence, a balance between the number of samples taken and the sampling frequency needs to be reached. Nevertheless, the

sampling scheme followed in each system/simulation should be as detailed as required. For the analysis that follows, which aims to prove the validity of the KMC algorithm for the diffusive systems, any sampling time-step between 1.73s and 5s can be selected.

The second parameter of interest is the number of independent runs required for the stochastically acquired data to resemble those obtained by following a deterministic approach. To this end, the number of independent runs performed was gradually increased, by a factor of 10, and the mean value of the population, $\bar{X}(2, t)$, was calculated at equilibrium ($t \geq 220\text{ns}$). The selected sampling time-step was $dt_{\text{sample}} = 2.5\text{s}$. According to the central limit theorem (CLT) the standard deviation of a random variable X with p.d.f $p_s(X)$ calculated for a number of independent runs v , $p_{s,x}(X_1, X_2, \dots, X_v)$ should satisfy the scaling relation $\sigma(p_{s,x}(X_1, X_2, \dots, X_v)) = \frac{C}{\sqrt{v}}$, where C is a constant and v is the number of averages taken at each time.¹⁶³ The results obtained follow the trend expected by the CLT and are presented in Figure 3.8.

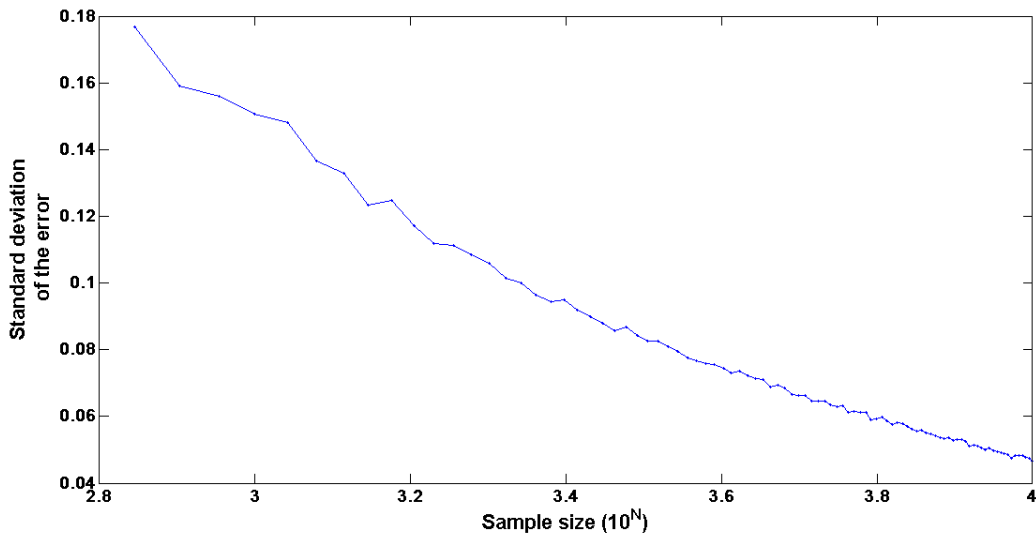


Figure 3. 8: Correlation between the increasing sample size and the standard deviation of the error between the stochastic and deterministic model. The sample size increased by a factor of 10 in each simulation run.

Figure 3.8 validates the accuracy of the KMC algorithm developed and can be used to determine the number of independent runs required, based on the desired standard error

value. Another way to validate the developed KMC algorithm, is to compare it against the predictions of the diffusion equation. The diffusion equation is a partial differential equation which describes concentration fluctuations in a material undergoing diffusion. The equation can be written as:

$$\frac{\partial \rho(\mathbf{r}, t)}{\partial t} = \nabla \cdot (D(\rho(\mathbf{r}, t), \mathbf{r}) \nabla \rho(\mathbf{r}, t)) \quad (3.12)$$

Where, $\rho(\mathbf{r}, t)$ is the population density in the location $\mathbf{r} = (x, y, z)$ and $D(\rho(\mathbf{r}, t))$ is the collective diffusion coefficient for density ρ and location \mathbf{r} . If the diffusion coefficient is constant and doesn't depend on the density the equation reduces to the following linear expression:

$$\frac{\partial \rho(\mathbf{r}, t)}{\partial t} = D \nabla^2 \rho(\mathbf{r}, t) \quad (3.13)$$

Under the assumption of an isotropic 1D diffusion on the x-direction, Eq. (3.13) becomes equivalent to Fick's second law.

$$\frac{\partial C(x, t)}{\partial t} = D \frac{\partial^2 C(x, t)}{\partial x^2} \quad (3.14)$$

In order to solve Eq. (3.14) two boundary conditions (BC) and one initial condition (IC) must be determined. For the IC, one needs to define the initial distribution of molecules in a finite domain with total length L at $t = 0$:

$$C(x, 0) = f(x) \quad \forall x \in [0, L] \quad (3.15)$$

Assuming that the boundaries of the domain are reflective, leading to zero flux, the BC for the left ($x = 0$) and the right ($x = L$) boundary can be expressed by the following equations:

$$\frac{\partial C(x, t)}{\partial x} = 0 \quad x = 0, \forall t \quad (3.16)$$

$$\frac{\partial C(x, t)}{\partial x} = 0 \quad x = L, \forall t \quad (3.17)$$

A non-trivial 1D analytical solution of Eq. (3.14), which satisfies both the IC and the two BC described above is:

$$C(x, 0) = \frac{1}{2} C_0 \sum_{n=-\infty}^{\infty} \left[\operatorname{erf}\left(\frac{h + 2nL - x}{2\sqrt{Dt}}\right) + \operatorname{erf}\left(\frac{h - 2nL + x}{2\sqrt{Dt}}\right) \right] \quad (3.18)$$

where $C(x, t)$ is the spatially and temporarily varying concentration, C_0 is the initial concentration of molecules and $-h \leq x \leq +h$ is region in which the molecules were initially confined.

To compare the predictions obtained by the KMC algorithm against the analytical solution of the 1D diffusion equation, a 1D domain consisting of 100 voxels in total was considered. All of the voxels were equidistant squares with characteristic length $l = 0.1\text{nm}$. The matrix was homogeneous and hence the diffusion coefficient was constant for the whole domain, during the time of the analysis. The value of the diffusion coefficient was arbitrarily chosen to be $D = 1.8 \times 10^{-9} \text{m}^2/\text{s}$. According to Chubynsky and Slater, the results obtained by solving the M-equation should be in agreement with the solutions of the continuum equations for slowly decaying modes.¹⁹⁰ Since the matrix was homogeneous and the diffusion coefficient remained constant, the transition rate of a diffusive jump between two neighbouring sites was defined as the ratio of the diffusion coefficient on the x-direction to the size of the voxel l . This relationship was derived in Chapter 2:¹⁷⁶

$$r^{\text{KMC}} = \frac{D}{l^2} \quad (3.19)$$

To achieve a slow diffusion, which would resemble a Boltzmann distribution, a population of 2125 molecules was distributed over the first 25 voxels at $t = 0$. Both the KMC algorithm and the continuum equation, can predict the concentration of molecules over time and over place ($C(x, t)$). Hence, the predictions of these two methods were compared by sampling over time and over space. The system was allowed to diffuse for a total time of $0.1\mu\text{s}$ and four samples were collected; at $t_0 = 0$, which is the initial

configuration of our system, at $t_1 = 2\text{ns}$, at $t_2 = 9\text{ns}$, and at $t_{\text{max}} = 0.1\mu\text{s}$. While sampling over space, two voxels were selected, the 30th and the last one (100th) and the concentration of molecules inside them over time was monitored. The concentration was expressed in number of molecules/ m^3 . The data collected are presented in Figure 3.9.

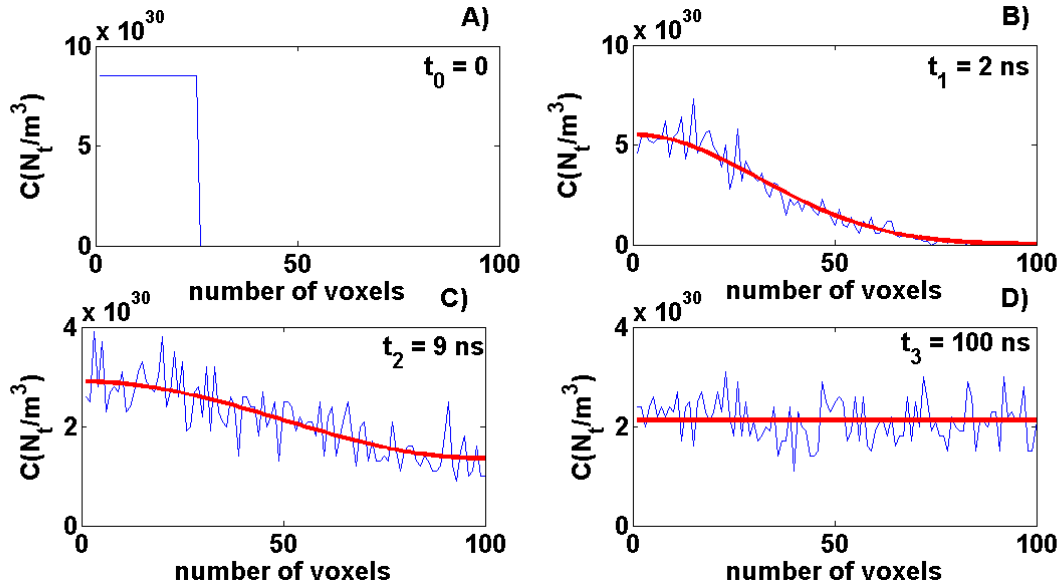


Figure 3. 9: Snapshots of concentration profiles at $t_0 = 0$ (panel A), $t_1 = 2\text{ns}$ (panel B), $t_2 = 9\text{ns}$ (panel C) and $t_3 = 0.1\mu\text{s}$ (panel D), as predicted by the KMC algorithm (blue line) and the 1D diffusion equation (red line).

The agreement between the stochastic and the deterministic model is satisfying. At the beginning of the simulation all molecules were distributed equally over the first 25 voxels. Once the system was let free to diffuse, the species started migrating to the neighbouring voxels (panel B and C) until equilibrium was reached (panel D). At equilibrium, the population was evenly distributed throughout the domain. Figure 3.10 presents the time evolution of the concentration profiles for two selected voxels.

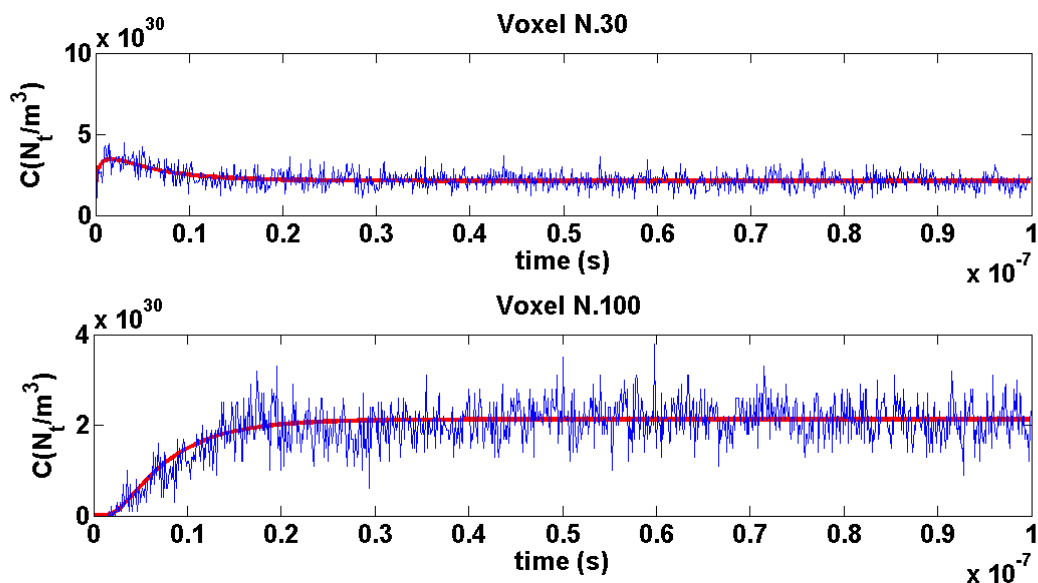


Figure 3.10: Concentration profile of the 30th and 100th voxel as a function of time. The blue line corresponds to the stochastic approach and the red line represents the solution of the 1D equation.

Since the 30th voxel is closer to the region where the molecules were initially distributed, less time is required to get occupied. On the other hand, the 100th voxel, which is the last voxel of the domain, stays empty at the beginning of the simulation. However, after approximately 20 nanoseconds the system gets equilibrated. In both Figures 3.21 and 3.22 the blue line corresponds to the KMC prediction and the red one is the solution of the diffusion equation.

In Part I of this chapter the constructed 1D KMC algorithm was a successfully validated against the analytical solution of the diffusion equation, for a homogeneous system with reflective boundaries. As a next step, the model was applied to simulate more complicated systems. In Part II of this chapter, the further development and validation of the KMC model is described. The stochastic model is validated against the MD study published by Phan et al.,⁸⁸ Three different pores, made of silica, MgO, and alumina were filled with water and methane to form the systems investigated. The size of the pores was 1 nm and the results obtained (methane flux, substrate permeability, and mean first

passage times) are used to compare the 1D KMC model against the MD findings reported by Phan et. al.⁸⁸

A KMC approach to study fluid transport in 1D pore networks – Part II

Abstract

The mechanism of fluid migration in porous networks continues to attract great interest. Darcy's law (phenomenological continuum theory), which is often used to describe macroscopically fluid flow through a porous material, is thought to fail in micro-channels. Transport through heterogeneous and anisotropic systems, characterised by a broad distribution of pores, occurs via a contribution of different transport mechanisms, all of which need to be accounted for. The situation is likely more complicated when immiscible fluid mixtures are present. To generalise the study of fluid transport through a porous network, a stochastic KMC model was developed. In the lattice model implemented for this study, the pore network is represented as a set of connected finite volumes (voxels), and transport is simulated as a random walk of molecules, which "hop" from voxel to voxel. In this study, fluid transport simulations along an effectively 1D pore is discussed. The KMC model was implemented to quantify the transport of methane through hydrated 1D micropores, in which case atomistic MD simulation results were reproduced. The model was then used to study flow through 1D pore networks, where it was able to quantify the effect of the pore length and the effect of the network's connectivity. The results are consistent with experiments, but also provide additional physical insights. Extension of the model in 2D and 3D will be useful to better understand fluid transport in shale rocks, topics that are covered in Chapters 4 and 5, respectively.

Introduction

The economic success related to shale gas production in the United States has generated great interest worldwide. The combination of horizontal drilling and hydraulic fracturing has provided access to large volumes of unconventional oil and gas, which were previously uneconomic to produce^{18,19}, to the point that shale gas has become one of the most important energy resources for the United States.⁵

Shale formations seem ubiquitous. For example the Bowland Shale Formation has been identified as the most promising shale gas play in the UK.^{10–12} However, economically producing shale gas in commercially relevant quantities has proven to be highly challenging. One of several unknowns, at present not fully understood, is which rock features contribute the most to gas transport during the various production steps; the microfractures, the existing pores and/or the hydraulic fractures depending on production stages. Transport of fluids through shale rocks is complicated because of the chemical heterogeneity of the pores, the low conductivity, the lack of a pore connectivity of significant extent, and reduced pore width, often in the nanometer scale.¹⁹¹

Considering that permeability depends on a number of factors, such as pore characteristics, chemical composition, and transport mechanisms, an approach that accounts for all these factors at low computational cost is required. This study investigates how the pore characteristics and the pore network connectivity affect the transport properties of light hydrocarbons in hydrated micropores with different chemical composition by performing KMC simulations. Methane is selected as it comprises the main component of natural gas. Phan et al.,⁸⁸ reported the transport properties of methane in three different 1 nm wide slit-shaped pores filled with water. In these molecular simulations models for silica, magnesium oxide and alumina were used as solid substrates and the diffusion coefficient of methane inside the pores was obtained by performing molecular dynamics MD simulations⁸⁸ in the canonical ensemble at 300 K. The three pores were filled with water are considered representative of minerals found in the subsurface.⁸⁸ KMC simulations, for the systems considered by Phan et al.,⁸⁸, were conducted to validate the stochastic model. Then, the validated KMC model is implemented to investigate the effect of the pore length and the pore network connectivity on methane transport.

The remainder Part II of this chapter is organised as follows. Section 3.2.3 provides the theoretical background under which the KMC algorithm is implemented. In Section 3.2.4 the physical systems considered by Phan et al.,⁸⁸ are described, together with the

methodology implemented to construct the 1D KMC lattice in order to represent-imitate them. This section also describes the methodology followed for the calculation of the KMC rates. In Section 3.2.5 results on flux, permeability and Mean First Passage Time (MFPT) through a few single pores are presented. The effect of the pore length and the network connectivity are also being investigated.

Theoretical background

KMC seeks to use state-to-state transition rates to simulate trajectories of the stochastic "wandering" of a system around the state space.¹⁴⁶ To this end, the KMC implementation requires rate constants that capture the probability per unit time of such state-to-state transitions.¹⁴⁶ A sequence of such transitions constitutes a sample path or trajectory, whose statistics follow the so-called Master equation (M-equation) that governs the dynamics of the system. The M-equation provides the means to describe a system in a "holistic" way, as it gives the time course of the probability of finding the system in a certain state at a given time:¹⁶³

$$\frac{dP_i(t)}{dt} = - \sum_{j \neq i} r_{ij}^{\text{KMC}} P_i(t) + \sum_{j \neq i} r_{ji}^{\text{KMC}} P_j(t) \quad (3.20)$$

The M-equation describes the system evolution as a balance of probabilities ($P_i(t)$ and $P_j(t)$) multiplied by the kinetic constants r_{ij}^{KMC} and r_{ji}^{KMC} , respectively, which quantify the propensity of an event, or, in other words, its probability of occurrence per unit time. It accounts for all the inflows from states j to states i minus the outflows from states i towards states j . Despite its simplicity, the M-equation can hardly be solved. To solve the M-equation Instead, a KMC algorithm can be employed to simulate sample paths (trajectories) and estimate statistical properties of interest.¹⁴⁶

A KMC algorithm can be implemented to address both surface (solid state) and bulk diffusion problems. The mathematical basis of the M-equation is the same but conceptual differences exist. Solid state problems can be described by a state vector x and a time

coordinate t , where x represents local minima on a potential energy surface (PES), and the M-equation describes the transition from one such local PES minimum state to another.¹⁹² Diffusion is an activated process and the kinetic constants that describe such transitions depend on the energy barrier between two states. In the case of bulk diffusion problems, the state vector x represents the population of species inside a region of a certain energy level. The kinetic constants depend on the diffusivity of the species considered and can be calculated through diffusion coefficient constants.¹⁹³

Microscopic reversibility (i.e. detailed balance) needs to be satisfied for any connected pair of states i and j . This implies the following relationship between rates $r_{i,j}^{\text{KMC}}$ (forward process) and $r_{j,i}^{\text{KMC}}$ (reverse process):^{146,168,183}

$$r_{i,j}^{\text{KMC}} P_i^0 = r_{j,i}^{\text{KMC}} P_j^0 \quad (3.21)$$

The reader is reminded that P_i^0 and P_j^0 are the probabilities of finding the system at state i and j , respectively, at equilibrium, as described in Chapter 2. The features of the KMC algorithm were first described by Young and Elcock in 1966.¹⁹⁴ Early implementations of the KMC algorithm were reported by Bortz et al.,¹⁶¹ and Gillespie, who utilised a rejection-free method known as the direct method.¹⁸³ In this study, the direct method is implemented to describe diffusion as a function of jumps between neighbouring voxels. The movement of molecules from one voxel to others is treated as a possible transition pathway. Firstly, all the possible pathways are identified and then the rates through which the transitions take place are determined. The possible pathways a molecule can follow, while it diffuses in a 1D domain with periodic boundaries and N square voxels is $2N$, as discussed in Part I of this chapter (see Figure 3.13).

The algorithm requires the selection of two random, uniformly distributed numbers u_1 and $u_2 \in [0,1]$. The Mersenne Twister MT19937 was implemented as the uniform random number generator (u.r.n.g).¹⁸⁹ One of the selected numbers, u_1 , is used to determine the event that takes place and the second, u_2 , is used to calculate the time

increment due to the selected transition. A detailed description of the direct method, including the event selection process and the time tracking is provided in Chapter 2 of this research study.

Simulation models and methodology

3.2.4.1 Model system

Each system considered here comprises of three types of voxels regions (Region 1, Region 2 and Region 3), two fluid species (methane and water), and two fluid phases. Each Region is described as a collection of different voxels, as it is discussed later. In all cases two bulk areas surround the pore (Region 1), two layers of liquid water lay outside both sides of the pore (Region 2) and a slit pore is filled with water (Region 3). Water molecules are in liquid phase while methane molecules are in gas phase. As methane migrates through the pore, it first solvates in the liquid water phase and then it diffuses. Interfaces separate the bulk and the pore space. The three different regions, through which methane migrates, are presented in the schematic is shown in Figure 3.11, which corresponds to a silica slit-pore filled with water, and methane molecules occupying both bulk regions. In the KMC lattice each Region is composed of voxels. Each voxel is assigned a forward and a backward diffusion rate. In Figure 3.11 the transition rates at the interfaces are presented.

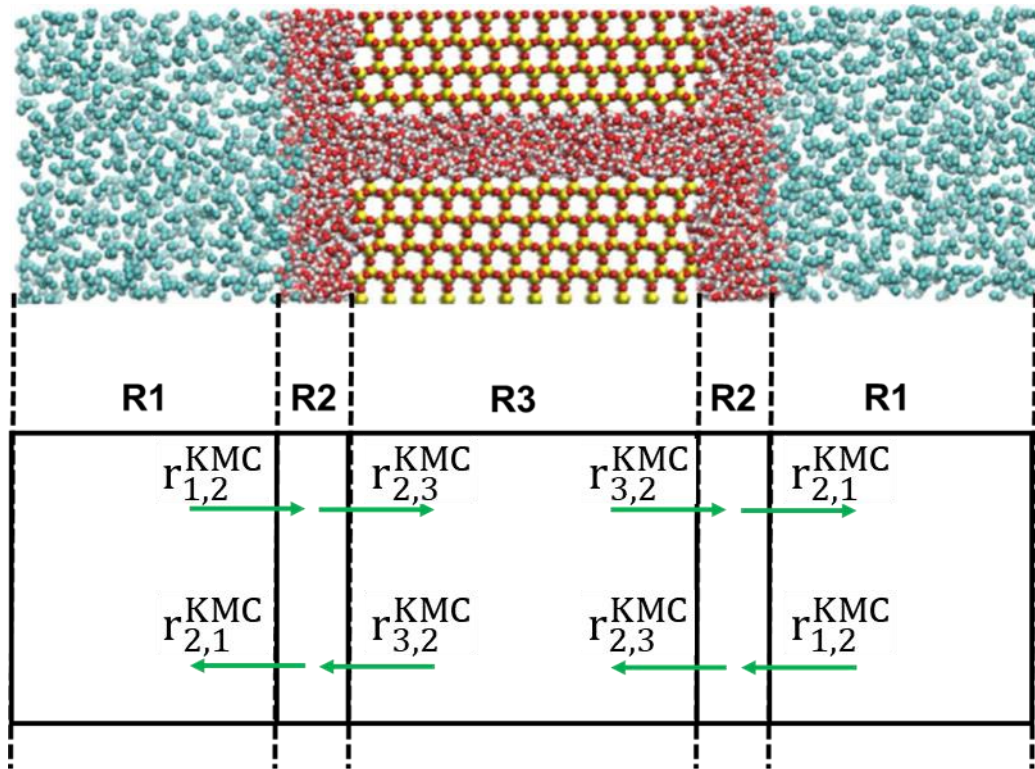


Figure 3. 11: Representation of our simulated system and the transition rates at the interfaces. Region 1 (R1) corresponds to the bulk methane reservoirs, Region 2 (R2) symbolises the layer of water formed outside of the pores and Region 3 (R3) represents the silicon oxide pore.

For the KMC model, the diffusion rates within the three regions and the transition rates at the interfaces between them, need to be defined. To determine the transition diffusion rates for our KMC lattice the following were considered; (1) the diffusion coefficient of methane in the water layer outside the pores, (2) the diffusion coefficient of methane inside the hydrated pores, (3) potential of mean force profiles, and (4) methane density profiles. Potential of mean force profiles (PMF) and methane density profiles were used to assign the transition rates at the interfaces. These data were reported by Phan et al.,⁸⁸

The rates that describe the back and forth transitions between neighbouring voxels inside each individual region, are equal, due to microscopic reversibility. To calculate the KMC rates inside the hydrated pore and the water layer the expression derived in Chapter 2, and implemented in Part I of this chapter was used:¹⁷⁶

$$\Gamma_{\text{Region}}^{\text{KMC}} = \frac{D}{l^2} \quad (3.22)$$

where D is the self-diffusion coefficient of methane. The diffusion coefficients of methane in the various hydrated pores were obtained by Phan et al., and are summarised in Table 3.1. The diffusion coefficient of methane inside the water layer is set to $1.8 \times 10^{-9} \text{ m}^2/\text{s}$.⁸⁸ The methane molecules diffuse first through the layer of water outside the pore, where the water molecules are able to move freely. However, once they enter the hydrated pores, the adsorbed water molecules are firmly attached to the surface and create an additional transport barrier that further hinders methane transport. To calculate the transition rate at the interfaces, the energy barriers obtained from the PMF profiles were used, as reported by Phan et al.⁸⁸ Then, Boltzmann's distribution expression was applied to define the probability of occupancy in Regions 2 and 3. The energy barriers considered here correspond to the maximum height (difference between maxima and minima) of two subsequent PMF curves and are reported in Table 3.1. These energy barriers represent the transport barrier inside the pores. The probability of occupancy in Regions 2 and 3, (p_2' , and p_3' respectively) resulting from these energy barriers can also be found in Table 3.1.

Table 3. 1: Diffusion coefficient of methane and energy barriers (ΔF), as obtained from Phan et al.,⁸⁸ and probability of occupancy in Regions 2 and 3 for the three substrates considered.

Material	$D_t \times 10^{10}$ (m^2/s)	ΔF (kcal/mol)	p_2'	p_3'
SiO₂	7.82	1.2	0.895	0.105
MgO	5.51	1.6	0.946	0.054
Al₂O₃	3.26	1.3	0.911	0.089

From the density profiles of methane and water presented in Figure 3.12, the methane population inside the water layer and the gaseous phase was determined. Table 3.2 summarises the estimated thickness of the water layer and the probability of occupancy

in each Regions 1 and 2 (p_1'' , and p_2'' respectively) for each system. The probabilities obtained from the PMF and density profiles were normalised and used to describe the transition rates at the interfaces. Table 3.3 summarises the probability of occupancy at Regions 1 (p_1), 2 (p_2) and 3 (p_3) for the methane molecules in each system. The transition rates $r_{1,2}^{\text{KMC}}$, $r_{2,1}^{\text{KMC}}$, $r_{2,3}^{\text{KMC}}$ and $r_{3,2}^{\text{KMC}}$ are calculated as:

$$r_{1,2}^{\text{KMC}} = p_2 \times r_{\text{Region2}}^{\text{KMC}} \quad (3.23)$$

$$r_{2,1}^{\text{KMC}} = p_1 \times r_{\text{Region2}}^{\text{KMC}} \quad (3.24)$$

$$r_{2,3}^{\text{KMC}} = p_3 \times r_{\text{Region3}}^{\text{KMC}} \quad (3.25)$$

$$r_{3,2}^{\text{KMC}} = p_2 \times r_{\text{Region3}}^{\text{KMC}} \quad (3.26)$$

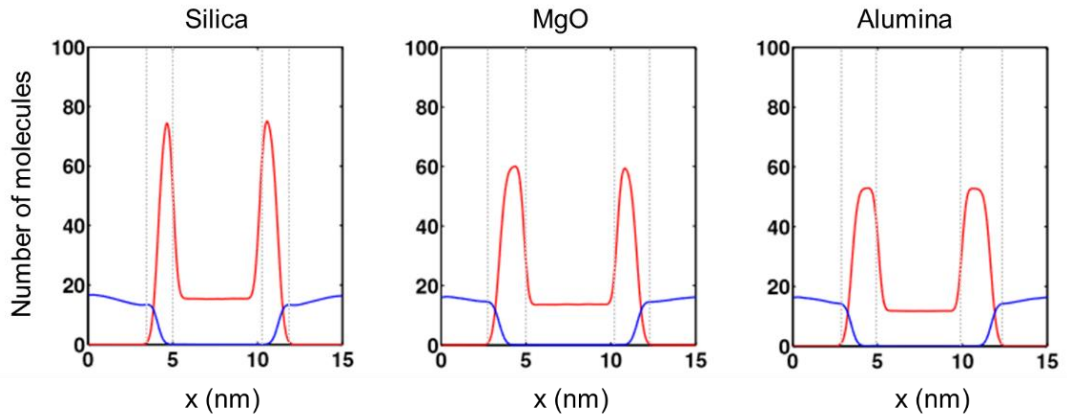


Figure 3. 12: Density profiles of water (red) and methane (blue) molecules inside 1nm wide slit-shaped pores. The dashed grey lines denote the borders of the water layer (region 2). Reproduced from Phan et al. ⁸⁸

Table 3. 2: Length of the water layer formed outside of the three pores and the probability of occupancy between regions 1 and 2.

Material	Length of water layer (nm)	p_1''	p_2''
SiO₂	1.63	0.724	0.276
MgO	2.12	0.770	0.230
Al₂O₃	2.28	0.767	0.233

Table 3. 3: The probability of occupancy between Regions 1, 2 and 3.

Material	p₁	p₂	p₃
SiO₂	0.709	0.270	0.020
MgO	0.760	0.227	0.012
Al₂O₃	0.748	0.227	0.024

As a final step, the KMC lattice was constructed. Because water is considered stagnant, the most appropriate way to represent the MD system is to create a 1D lattice and consider only one type of species, methane, effectively undergoing 1D transport along the direction parallel to the pore. To construct the lattice, the size and the number of the voxels need to be defined. To select the size each voxel must be bigger than the mean free path of the molecules, as there is no physical meaning in selecting voxels smaller than the mean distance the molecules can travel. Each Region contains a different number of voxels. Region 1 is represented by a single voxel, assuming the gaseous methane to be well mixed. The number of voxels selected to represent Regions 2 and 3 is decided according to the length of the regions (from the MD study) and the voxel size. The methane particles move from one voxel to a neighbouring voxel, located along the x-direction, following a 1D trajectory. An example of the lattice used to perform these calculations (in this regard for the silicon oxide pore) is presented in Figure 3.13. Further information regarding the lattice implemented for all three substrates is shown in Table 3.4. The number of particles inserted in Region 1 for each substrate depends on the density of the systems (from the MD study) and the size of the voxels.

Table 3. 4: Description of the lattice implemented for the KMC model.

Parameter	System		
	SiO ₂	MgO	Al ₂ O ₃
Region 1 dimensions (x,y,z) (nm)	1.6×0.4×0.4	2.12×0.42×0.42	2.30×0.46×0.46
Region 2 dimensions (x,y,z) (nm)	1.6×0.4×0.4	2.12×0.42×0.42	2.30×0.46×0.46
Region 3 dimensions (x,y,z) (nm)	5.2×0.4×0.4	5.09×0.42×0.42	4.60×0.46×0.46
Voxel size	0.4×0.4×0.4	0.42×0.42×0.42	0.46×0.46×0.46
Number of voxels in Region 1	1	1	1
Number of voxels in Region 2	4	5	5
Number of voxels in Region 3	13	12	10
Number of particles in Region 1	3	8	8

3.2.4.2 Flux calculations

Methane molecules in gas phase were inserted in one of the bulk areas (feed), resulting in a pressure rise. The other bulk area (permeate) was kept empty throughout the simulations, yielding a pressure that remains approximately 0. Once the methane molecules cross the slit pore and enter the permeate region, they are deleted and immediately added back into the feed region. Hence, the pressure drop across the substrates was maintained constant. The boundaries of the system were reflective. The cumulative number of particles that cross the permeate region, were reported every 30 ns, and averages were obtained from 100 independent simulations. Replicating the simulations as such, results in smooth profiles with minimum fluctuations. Starting from

$t = 0$, the system was allowed to progress for 30 ns, during which time a counter reports the number of molecules crossing the pore. After 100 simulations the system was left to diffuse for another 30 ns. This procedure was repeated until a total simulation time of 720 ns was reached. The flux was determined by counting the number of molecules crossing the pore (Q_t) over time:

$$J = \frac{\Delta Q_t / \Delta t}{A} \quad (3.27)$$

In Eq. (3.27), J is the molar flux of methane, $\Delta Q_t / \Delta t$ is the slope of the fitted line (cumulative number of molecules vs. time), A is the cross-sectional area available for gas permeation, perpendicular to the direction of the diffusion. An example of the lattice used to perform these calculations (in this regard for the silicon oxide pore) is presented in Figure 3.13.

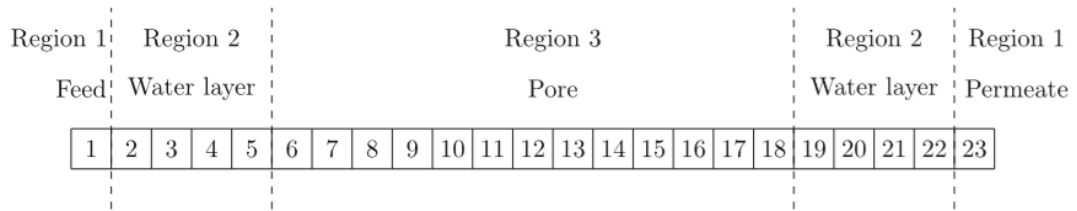


Figure 3. 13: The KMC lattice implemented for the silicon oxide flux calculations. Reproduced from Apostolopoulou et al.¹⁴⁰

3.2.4.3 Permeability calculation

The membrane permeability K was calculated as:

$$K = \frac{Jl}{p_1 - p_2} \quad (3.28)$$

where J is the molar flux of methane from the KMC calculations, l is the length of the pore, p_1 is the pressure applied in the feed phase, p_2 is the pressure applied in the

permeate region ($p_2 = 0$). In this calculation the pressure drop remains constant. At most 5% of the molecules in the feed volume escaped to the pore voxels (i.e., Region 2).

3.2.4.4 Mean First Passage Time (MFPT)

Useful information regarding the transport in a porous medium can be obtained by the calculation of the MFPT. For MFPT calculations, silicon, magnesium and aluminium oxide 40 nm long pores were considered. A methane molecule was placed in the middle of the pore and it was allowed to move towards any direction (forwards and/or backwards). However, to avoid re-crossings the propensity of the methane molecule hopping from the middle voxel, voxel No. 86, as shown in Figure 3.14, to its right neighbour (voxel No. 87) was set to zero, so that the molecule is not allowed to cross the middle of the pore. The molecule's trajectory was monitored throughout the simulation. The molecule was allowed to exit the pore and cover an additional distance of approximately 1.5 nm in the water layer. The MFPT reflects the average time required for a particle to reach a specific position inside the pore. For MFPT calculations, silicon, magnesium and aluminium oxide pores 40 nm long were considered.

In the beginning of the KMC simulation, a methane molecule was placed in the middle of the pore (voxel No. 86), as shown in Figure 3.14. To monitor the molecule's trajectory as it exited the pore, 1000 independent simulations were performed. The KMC lattice used for these calculations was symmetric and the analysis is focused on the x_a direction. Starting from voxel No.86, the first time, at which the molecule visited each neighbouring voxel sequentially (i.e. voxel No.85, voxel No.84, etc.), was recorded, until it reached voxel No.1. By averaging these "first times" the MFPT were obtained as a function of distance from the centre of the pore. Whenever the molecule attempted to cross the centre of the pore, by moving into voxel No.87, the simulation was terminated and discarded. The size of the voxels used to simulate the layer of water (Region 2) had

dimensions $0.25(\text{nm}) \times 0.5(\text{nm}) \times 0.5(\text{nm})$. The voxels used to represent the pore (Region 3) had dimensions $0.5(\text{nm}) \times 0.5(\text{nm}) \times 0.5(\text{nm})$.

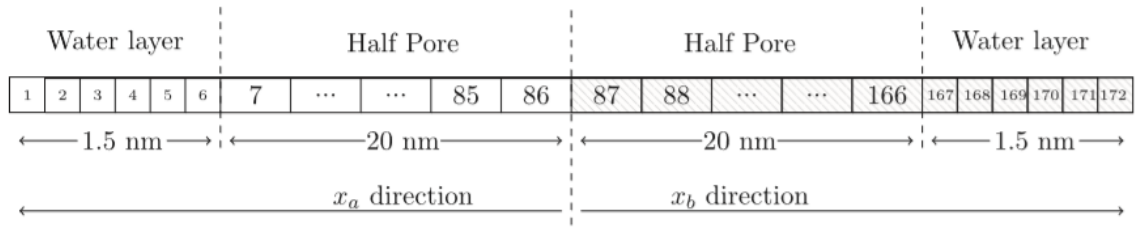


Figure 3. 14: The KMC lattice implemented for the MFPT calculations. The methane molecule is initially placed in voxel No.86 and moves towards voxel No.1. Movement towards direction x_b is disabled. Reproduced from Apostolopoulou et al.¹⁴⁰

3.2.4.5 Heterogeneous pore networks

The proposed KMC model was used to investigate the transport properties in heterogeneous pore networks, aiming to assess how the flux observed through the substrates is affected by the length and the connectivity of the pores. To understand how the pore size affects molecular flux, a lattice similar to the one described in Figure 3.13 is used. The size of the water layer formed outside of the pores is kept the same. To obtain better statistics, the density of methane particles in the bulk region is increased. The particle flux is expected to gradually decrease, as the length of the pore is increased, while keeping the pressure drop constant. The effect of the pore connectivity on flux was quantified, starting by a long pore surrounded by water and two bulk regions containing methane (as in Figure 3.11). As a next step, two disconnected pores with half the length of the original pore are used in place of the single long pore. These pores are also surrounded by bulk regions of water layers. Afterwards, the length of the pores is reduced by half, yielding four pores, also disconnected. The pore networks studied (type 1, type 2, and type 3) are illustrated in Figure 3.15.

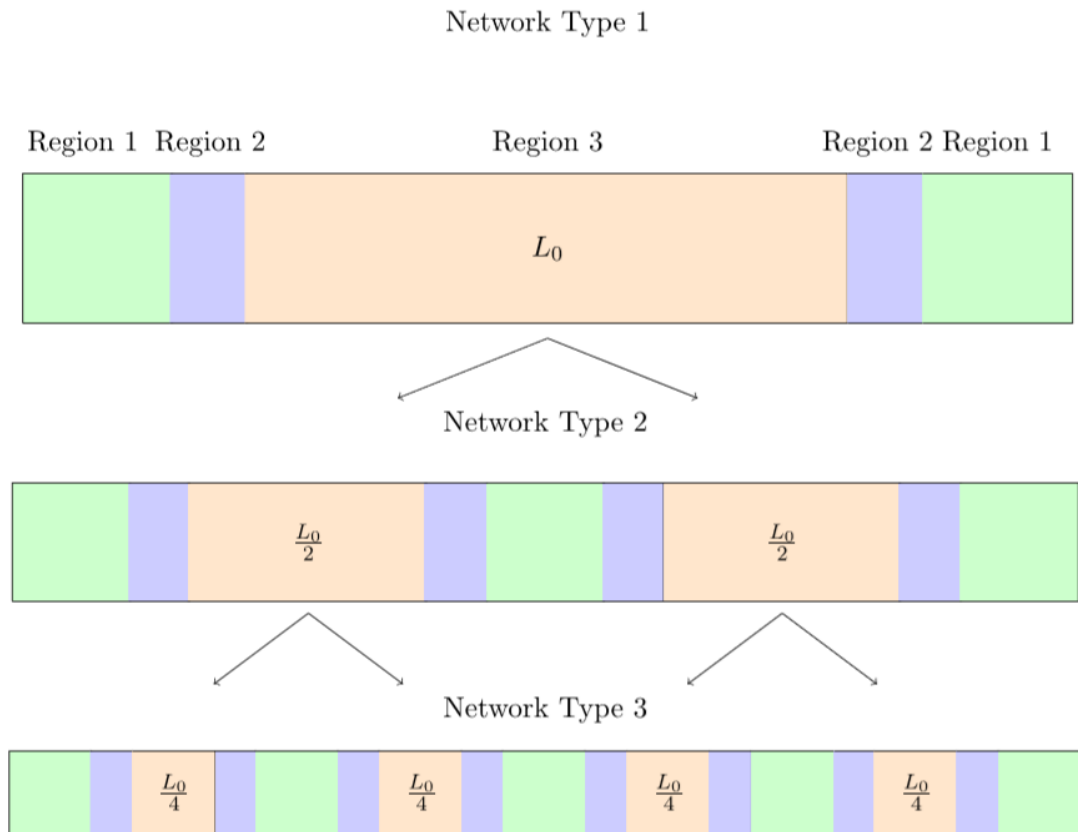


Figure 3. 15: Representation of the network design used to calculate the molar flux. The light green colour corresponds to the gas methane region, the light purple denotes the water layer outside of the pore and the orange voxels represent the pore. Reproduced from Apostolopoulou et al.¹⁴⁰

Results and discussion

3.2.5.1 Flux and permeability through single pores

A 1D lattice was implemented to represent the three slit-shape micropores studied using MD simulations by Phan et al.,⁸⁸ Information regarding the construction of the 1D lattice is provided in Table 3.3 and it refers to Figure 3.13, for the case of the silica pore. Region 1 corresponds to the bulk area where methane molecules are in gas phase, Region 2 represents the water layer found on both sides of the pore and Region 3 describes the hydrated pore. Plots of the cumulative number of molecules as a function of time obtained for every system are presented Figure 3.16. A straight line is fitted to these data

to calculate the slope of the linear plots. From the slope, Eq. (3.27) is used to calculate the flux of methane molecule.

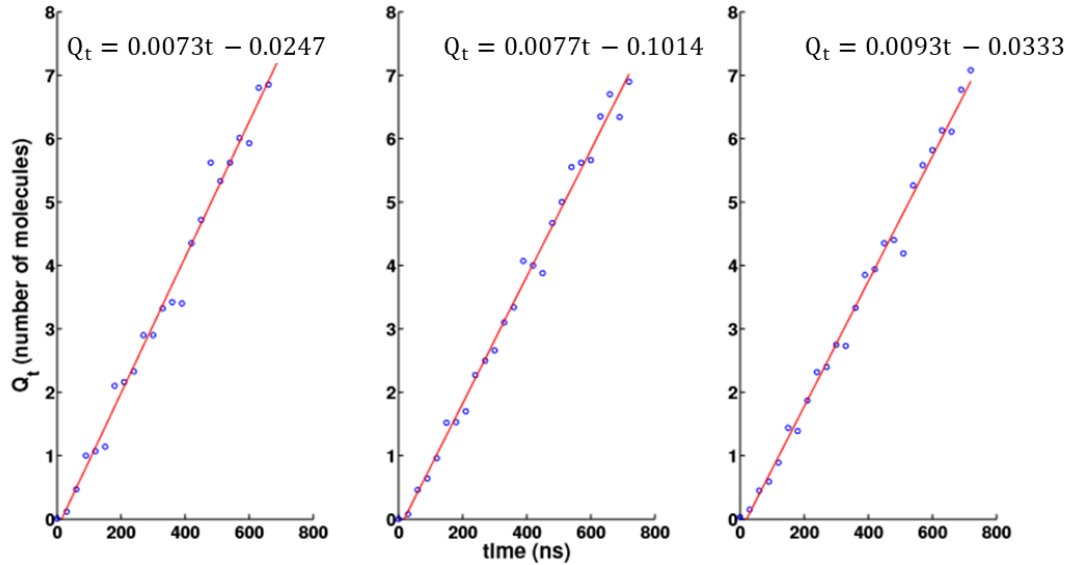


Figure 3. 16: Cumulative number of methane molecules (Q_t) in the permeate region (blue dots) as a function of time for the hydrated silica slit-shaped pore (left panel), the magnesium oxide (middle panel) and the aluminium oxide pore (right panel). The red line corresponds to a least-squares fitted line.

The results obtained by the KMC model are presented in Table 3.5. For validation purposes, the values obtained by the stochastic model are compared against those reported by Phan et al.⁸⁸ The results are presented in Figure 3.17.

Table 3. 5: Flux and permeability calculations obtained by the KMC model

Material	Flux J (mol/m ² s)	Permeability K (mol/msMPa)
SiO ₂	74.76 ± 1.42	$(5.38 \pm 0.11) \times 10^{-9}$
MgO	71.83 ± 1.26	$(3.05 \pm 0.05) \times 10^{-9}$
Al ₂ O ₃	75.91 ± 1.27	$(2.04 \pm 0.03) \times 10^{-9}$

The flux observed through the three pores is similar. However, the permeability varies. The silicon oxide pore is the most permeable, followed by the magnesium oxide one and the alumina oxide. These trends are in quantitative agreement with the MD results

reported by Phan et al.⁸⁸ According to Phan et al., the formation of molecular cavities within the water-filled pores is observed close to the pore walls. The cavities observed are more pronounced in the case of the silica pores, followed by the ones observed in the magnesium oxide and aluminium oxide pores. These structures promote the passage of methane molecules through the hydrated pores and increase the methane diffusivity.⁸⁸

Performing 100 independent KMC simulation runs for the silica, magnesium oxide and aluminium oxide pores required just 32.9s, 63.6s and 83.1s, respectively. Comparison between KMC and MD results from the two simulations is presented in Figure 3.17. To calculate the error bars shown in Figure 3.17 100 independent simulations were performed and the standard deviation for the flux and permeability were calculated. The standard deviation of the mean is divided by the square root of the sample size to obtain the standard error of the mean, which is reported in Figure 3.17.

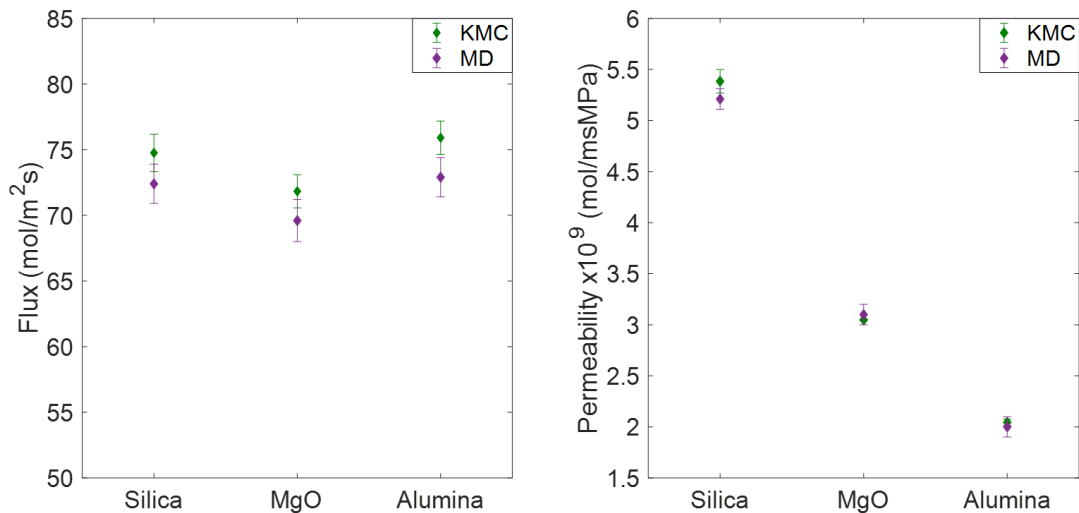


Figure 3. 17: Results obtained implementing the KMC model presented here versus MD simulations by Phan et al.,⁸⁸ for flux (left panel) and permeability (right panel). The results obtained from both methods are presented with error bars.

3.2.5.2 Mean First Passage Times (MFPTs)

The MFPT profiles shown in Figure 3.18 were obtained for the three substrates by implementing the KMC algorithm. As expected from the diffusion coefficients that

describe methane transport inside the slit-shaped pores, transport inside the silicon oxide pores is the fastest. Methane moves slowly inside the alumina oxide pores, for which the MFPT is almost three times slower compared to than that obtained in the silicon oxide pore. The results obtained from the KMC model are in agreement with the ones reported by Phan et al.,⁸⁸ as shown in Figure 3.18. It is worth repeating that, the computational effort associated with the KMC approach is significantly smaller than that of the MD approach. The CPU times required were 48.9s, 48.8s, and 51.3s for the simulations performed on the silica, magnesium and aluminium oxide pores, respectively, when the KMC model was implemented. The nodes used to perform these simulations on the supercomputer consisted of 2 Intel Xeon E5-2683 v4 cores in total and 128 GB total RAM.

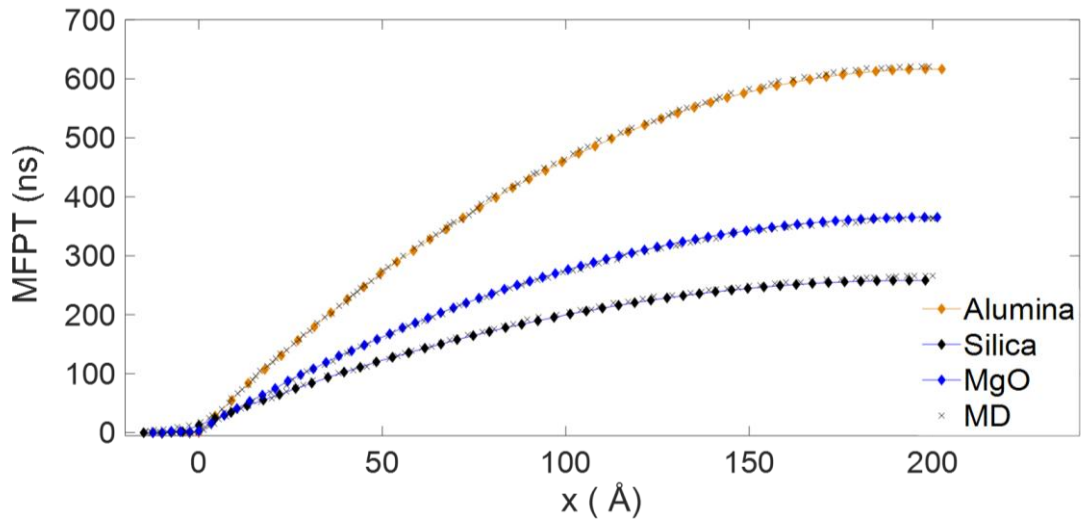


Figure 3. 18: Mean First Passage Time profiles of 40 nm wide pores as obtained by KMC calculations and Phan et al.,⁸⁸(MD).

3.2.5.3 Flux versus pore length

Since the KMC model quantitatively reproduces the results obtained from the MD simulations, it can be used to quantify how certain pore characteristics affect permeability. To elucidate the effect of the pore length on the observed flux, systematic KMC simulations were conducted. To improve the statistics, the number of particles inserted in the feed area was increased to 100. The results are shown in Figure. 3.31

(left panel) where the calculated flux is plotted against the pore length for the three different substrates. For these calculations the pore length was increased from 4 to 25 nm for all three substrates. As expected, as the pore length increases, the flux decreases. The rate of flux decrease is expected to be similar for all substrates. To investigate this hypothesis, the % flux decrease was calculated, and the results obtained were plotted as a function of the pore length. The results shown in Figure 3.19 (right panel) are indicative of the qualitative validity of the KMC model.

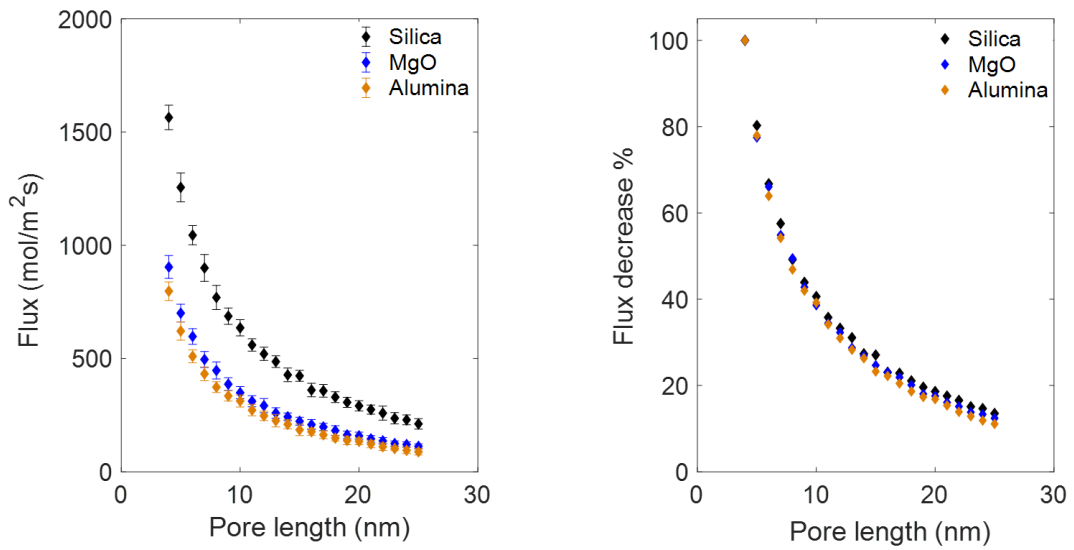


Figure 3. 19: Effect of the pore length on membrane flux (left panel) and the effect of pore length on the % of flux decrease as calculated from KMC simulations (right panel). The flux obtained for the different pore lengths is reported with error bars.

To quantitatively prove the accuracy of the KMC model Eq. (3.29), an analytical expression that describes the relationship between the observed flux and the membrane thickness, is employed.¹⁹⁵

$$J = \frac{L_m(L)RT}{L} \ln \frac{x_b}{x_p} \quad (3.29)$$

In Eq. (3.29) L is the membrane thickness, $L_m(L)$ is the mass transport coefficient, x_b is the mole fraction at the feed-membrane interface and x_p is the mole fraction at the membrane-permeate interface. As the pore length increases some of the molecules will

occupy positions inside the membrane, thus decreasing the driving force for transport. To balance this effect, the population of methane molecules inside the pore was monitored during the simulation and the number of feed molecules was adjusted as required in order to maintain a constant pressure drop. This adjustment keeps the x_b and x_p mole fractions in Eq. (3.29) constant.

It is assumed that the mass transfer coefficient linearly decreases as the pore length increases, since the conditions under which these simulations take place are kept constant. The relationship between the mass transfer coefficient and the pore length can then be described as:

$$L_m(L) = c_1 L + c_2 \quad (3.30)$$

The constants c_1 and c_2 are fitting parameters obtained from fitting two KMC data points. Eq. (3.30) is then used to calculate the expected flux for each pore length. The comparison between the KMC model and Eq. (3.30) is quantitative as shown in Figure 3.20.

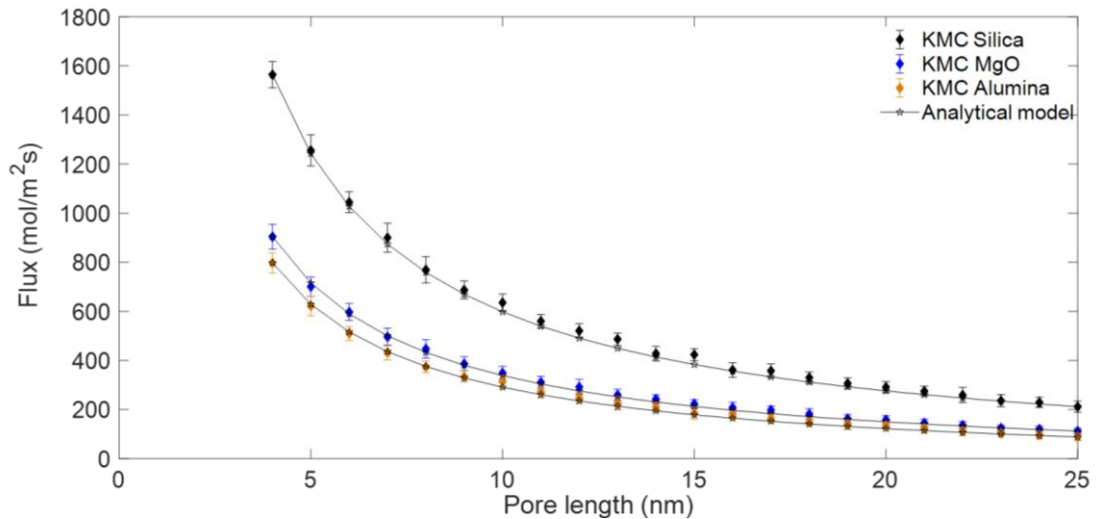


Figure 3. 20: Comparison between the KMC model and analytical expressions for the effect of pore length on the observed flux.

3.2.5.4 Effect of pore connectivity

Changing the pore network connectivity essentially alters the number of interfaces present in the system (see diagrams in Figure 3.15). Assuming that the resistance to diffusion is due to the pore length and the interfaces, the analysis below investigates whether these two effects equally hinder the gas transport, or whether a rate-limiting step is reached.

The effect of pore connectivity on the overall pore network's flux was quantified by simulating three 1D pore networks, shown in Figure 3.15. The first one consisted of a single long pore (4 nm). This pore was cut in half and the newly generated pores (2 nm) were surrounded by water layers and vapour bulk areas. These two pores were then cut in half to generate the third system. The flux observed for the three pore networks is reported in Figure 3.21. The results show that the fluxes in each of the 1D pore networks decrease as the number of interfaces increases, suggesting that the rate-limiting step in these pore networks is provided by the entrance of methane into the water-filled pores.

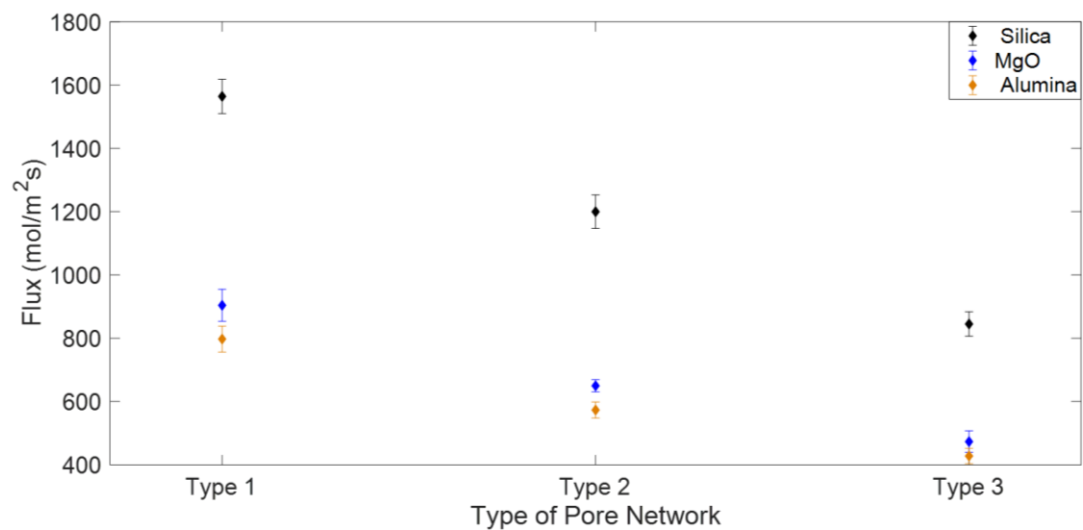


Figure 3. 21: Fluxes calculated for 1D pore networks with different pore connectivity (see Figure 3.15 for description of Type 1, 2, and 3 networks).

Figures 3.32 and 3.33 show that the pore length and the pore network connectivity are equally important in determining the flux. The observed flux decrease is similar whether the pore length increases by 1 nm (from 4 nm to 5 nm and from 5 nm to 6 nm) or the pore network becomes more disconnected (from Type 1 to Type 2 and from Type 2 to

Type 3). It is observed that the percent decrease in flux due to the interfaces added follows a similar trend for all three substrates.

Conclusions

In the first part of this chapter, a KMC algorithm was produced in order to reproduce results obtained by using a similar model for reaction networks. The results obtained by the produced code were in quantitative agreement with those report by Gillespie. Small fluctuations were observed. It was proved that these fluctuations are a result of the systems' unstable behaviour and the lack of performing a number of independent simulations to obtain the mean values.

Gillespie's algorithm, reproduced for validation purposes, was then modified in order to simulate a diffusive process. The constructed KMC algorithm was implemented to simulate diffusion in a homogeneous closed system with reflective boundaries. The results obtained from the stochastic approach, were validated against the analytical solution of the diffusion equation in 1D. The agreement between the stochastic and deterministic approach was satisfactory.

In the second part of this chapter, a lattice-based KMC model was developed to study fluid transport through 1D slit-shaped pores with different chemical composition. The substrates analysed represent main components of the inorganic material found in shale rocks. The proposed model was used to quantify how the presence of disconnected micropores affect the permeability of a heterogeneous domain.

The chemistry of the pores was found to affect the transport behaviour of gas methane molecules, as expected from previously reported studies. The hydrated silicon oxide micropores exhibit the highest permeability, followed by the permeability observed in hydrated magnesium and aluminium oxide pores. The agreement between the KMC model and MD simulations is quantitative, however, the computational times are significantly reduced when using the KMC model. The model was then used to provide insights regarding the contribution of the pore network characteristics in the transport

behaviour. It was found that both the pore length and the network connectivity play a significant role on gas migration.

From the simulations presented in Part II, it was also observed that the chemical composition of the substrates affects the absolute values of the flux observed for all pore lengths and type of networks, but it does not affect the behaviour of the systems (rate of flux decrease). The 1D KMC model developed for this study can be considered as a bottom-up approach that can be used to address mesoscopic problems. Any type of designed or natural network can be simulated, as long as the kinetic (diffusion constants) and thermodynamic (barriers due to the interfaces) properties are provided. The kinetic and thermodynamic properties used in Part II, together with the methodology followed for the calculation of the transition rates, can be applied to any type of pore networks and provide insights regarding the significance of the chemical composition and pore features to the resulting transport properties, provided gas transport occurs via diffusion. The KMC model should be extended towards the simulation of realistic 2D and 3D pore networks at the mesoscopic scale. Such studies will contribute to a better understanding of the diffusion encountered in shale rocks and potentially assist the formulation of strategies to maximise the natural gas or oil recovery.

KMC algorithm extension to 2D; Studies in synthetic pore networks and shale samples

In Chapter 3, the construction and validation of the 1D KMC model, to simulate diffusive systems, is discussed. The overall aim of this research study is to develop and apply stochastic methods to simulate fluid transport in shale rocks and other pore networks that exhibit similar properties. Since the pore networks found in shales are often complex, synthetic networks can be implemented to individually access the impact of each pore network property on the transport of fluids. This chapter is divided in two parts; Part I details the development of a 2D KMC algorithm and its application on synthetic 2D pore networks to elucidate the effects resulting from pore size distribution, the impact of micro- and macropores, and the effects of anisotropy on the predicted matrix permeability. The 2D KMC model is also implemented to estimate the permeability of a shale sample obtained from the Eagle Ford formation. Throughout Part I, the 2D KMC model is being compared against deterministic models that have been extensively used in the literature for the calculation of network permeability and recommendations are provided on the optimal conditions under which each method can be used. The results obtained from Part I are published in the *Int J Coal Geol*, **205** (2019) 140-154. Part II presents the outcome of a collaborative project with Halliburton's production and enhancement team that took place as an internship in 2017. During this collaboration the 2D KMC model was used to investigate the effect of man-made microfractures and proppants on the permeability improvement. The matrix permeability calculated in Part I was used as an input for the matrix permeability. The laboratory work presented in Part II, was carried out by Halliburton and the results were presented during the SPE Oil and Gas Symposium that took place in Oklahoma on the 9th-10th of April and published as a conference paper with ID SPE-195220-MS.

Estimating permeability in shales and other heterogeneous porous media: Deterministic vs. stochastic investigations – Part I

Abstract

With increasing global energy demands, unconventional formations, such as shale rocks, are becoming an important source of natural gas. Extensive efforts focus on understanding the complex behaviour of fluids (including their transport in the sub-surface) to maximise natural gas yields. Shale rocks are mudstones made up of organic and inorganic constituents of varying pore sizes (1-100nm). With cutting-edge imaging technologies, detailed structural and chemical description of shale rocks can be obtained at different length scales. Using this knowledge to assess macroscopic properties, such as fluid permeability, remains challenging. Direct experimental measurements of permeability supply answers but at elevated costs of time and resources. To complement these, computer simulations are widely available, however, they employ significant approximations, and a reliable methodology to estimate permeability in heterogeneous pore networks remains elusive. For this study, permeability predictions obtained by implementing two deterministic methods and one stochastic approach, using a KMC algorithm, are compared. This analysis focuses on the effects resulting from pore size distribution, the impact of micro- and macropores, and the effects of anisotropy (induced or naturally occurring) on the predicted matrix permeability. While considering multiple case studies, recommendations are provided on the optimal conditions under which each method can be used. Finally, a stochastic analysis is performed to estimate the permeability of an Eagle Ford shale sample using the KMC algorithm. Successful comparisons against experimental data demonstrate the appeal of the stochastic approach.

Introduction

Global primary energy consumption has been increasing slowly but steadily during recent years – 1% during 2016, 0.9% during 2015, 1% during 2014 – compared to a

10-year average yearly increase of 1.8%.¹⁹⁶ To meet these energy demands, in addition to developing renewable energy sources, the focus is on optimising the processes to recover hydrocarbons from the subsurface.¹⁹⁷ Nevertheless, our understanding of fluid transport within heterogeneous rocks typically identified in shale formations remains limited because of the rocks' complex texture.¹⁹⁸ Experimentally measured properties of shale rocks (i.e., porosity, chemical composition, pore size distribution (PSD), and wettability) vary greatly.¹⁹⁹ Estimating the permeability of porous media will not only assist toward improved production rates but will also minimise potential risks associated with the technologies currently implemented to stimulate shale formations. Predicting reliably medium permeability requires (1) selecting the appropriate transport model to quantify the physical properties that microscopically dictate fluid transport and (2) implementing effective methods to predict the system's macroscopic behaviour. While many physical properties for shale samples have been reported (PSD, mineralogy, organic content), not much progress has been made on combining these datasets to yield useful information regarding permeability.

Understanding the behaviour of fluid transfer through porous rock formations, in particular, permeability has been in the spotlight for many years.²⁰⁰ Cutting-edge imaging techniques provide detailed structural and chemical analysis of materials at different length scales,²⁰¹ but incorporating this knowledge systematically into models that can predict macroscopic properties remains challenging. Experimental methods can supply the necessary information, but this practice is often costly, time consuming, or even impractical.²⁰² On the contrary, computer simulations are cost effective, but are often limited in terms of accuracy or availability of computational resources;²⁰³ therefore, a balance among the levels of detail needed, the accuracy expected, and the computational cost should be determined. In this work, three approaches are implemented and compared to predict permeability of complex pore networks representing those identified in shale rocks. It is important to highlight that all computational approaches can fail to predict the overall permeability of highly

heterogeneous systems, compared to experiments, because of the uncertainty associated with the exact value of the properties assigned to each domain, as well as with uncertainties related to the extent and connectivity of the three-dimensional (3D) pore network.

This work compares two deterministic methods, EMT and a simplified renormalisation technique, and the developed stochastic KMC algorithm. The analysis focuses on pore size and network connectivity; pore sizes that follow log-normal distributions are considered and it is assumed that 'local' permeability coefficients depend solely on pore size. Further, networks with low, medium and high anisotropy are considered to obtain an estimate for the media permeability. The same pore mapping is also used to evaluate the three methods and identify applicability ranges of each approach, using a detailed understanding of the physical mechanisms responsible for the differences observed. Finally, the KMC approach is applied to predict the permeability of a shale rock sample.

The remainder Part I of this chapter is organised as follows: Section 4.1.3 provides the mathematical formulation of the three methods and describes the simulation set-up used. Section 4.1.4 describes the systems investigated, while Section 4.1.5 presents the results obtained while using synthetic networks and an actual shale sample. A summary of the main findings of this study is provided in Section 4.3.

Methods

4.1.3.1 Effective Medium Theory (EMT)

Kirkpatrick generalised the EMT from heterogeneous continuous systems to networks of conducting elements. He proposed a general formalism for inhomogeneous, disordered lattices, described by a range of conductances g_x , where x is the index of a cell or element in the network ($x = 1, \dots, X$, with X being the total number of elements). These conductance values follow a probability distribution function $p(g)$. Assuming no spatial correlation among the g_x values, the implicit mathematical relation involving the effective

g_m , the local conductances g_x , and the coordination number z , which characterises the lattice, is:

$$\left\langle \frac{g_m - g_x}{[(z/2 - 1)g_m + g_x]} \right\rangle = 0 \quad (4.1)$$

Considering a lattice, Eq. (4.1) can be solved numerically by Eq. (4.2), where φ_x describes the ‘significance’ of conductance g_x in the calculation of the effective g_m :

$$\sum_{x=1}^X \varphi_x \frac{g_m - g_x}{[(z/2 - 1)g_m + g_x]} = 0 \quad (4.2)$$

The EMT approach is indicated as ‘Method I’ in what follows. For this work Kirkpatrick’s formalism is implemented, initially used to describe networks of conductances, for calculating the equivalent permeability for a lattice-based pore network (i.e., a site percolation problem). In this study, k_{eff} is the effective matrix permeability and $k_{i,j}$ the permeability coefficients, as shown in Figure 4.1 and explicitly stated in Eq. (4.3).

$$\sum_{j=1}^{N_C} \sum_{i=1}^{N_R} \varphi_{i,j} \frac{k_{\text{eff}} - k_{i,j}}{[(z/2 - 1)k_{\text{eff}} + k_{i,j}]} = 0 \quad (4.3)$$

In Eq. (4.3), N_R is the number of matrix rows, N_C is the number of columns. The coordination number z is kept constant and equal to 4,²⁰⁴ as rectangular two-dimensional (2D) networks are considered. Building on the work on KMC discussed in Chapter 3, the term “voxel” refers to a single cell of a matrix representing a pore network. For Eq. (4.3), the frequency term $\varphi_{i,j}$ acts as a weighting factor on the permeability coefficient $k_{i,j}$. The weight of $\varphi_{i,j}$ represents the pore volume fraction represented by each voxel. In the matrices generated, the voxels are considered to contain the same volume of pores, and hence all $\varphi_{i,j}$ have the same weight:

$$\varphi_{i,j} = \frac{1}{N_C \times N_R} \quad (4.4)$$

4.1.3.2 Simplified renormalisation method

The simplified renormalisation method is indicated as 'Method II' in what follows. The description by Naraghi et al.,¹⁰² for a 2D matrix is followed to calculate the effective rock permeability using Method II:

$$k_{UB} = \frac{N_R}{N_C} \frac{1}{\sum_{i=1}^{N_R} \frac{1}{\sum_{j=1}^{N_C} k_{i,j}}} \quad (4.5)$$

$$k_{LB} = \frac{N_C}{N_R} \sum_{j=1}^{N_C} \frac{1}{\sum_{i=1}^{N_R} \frac{1}{k_{i,j}}} \quad (4.6)$$

$$k_{eff} = \sqrt{k_{LB} k_{UB}} \quad (4.7)$$

In Eqs. (4.5 – 4.7) $k_{i,j}$ is the permeability of the pores represented by voxel (i, j). According to these equations, the flow direction is vertical (top to bottom), and zero cross flow is imposed. Figure 4.1 provides a schematic of the calculation of k_{LB} and k_{UB} .

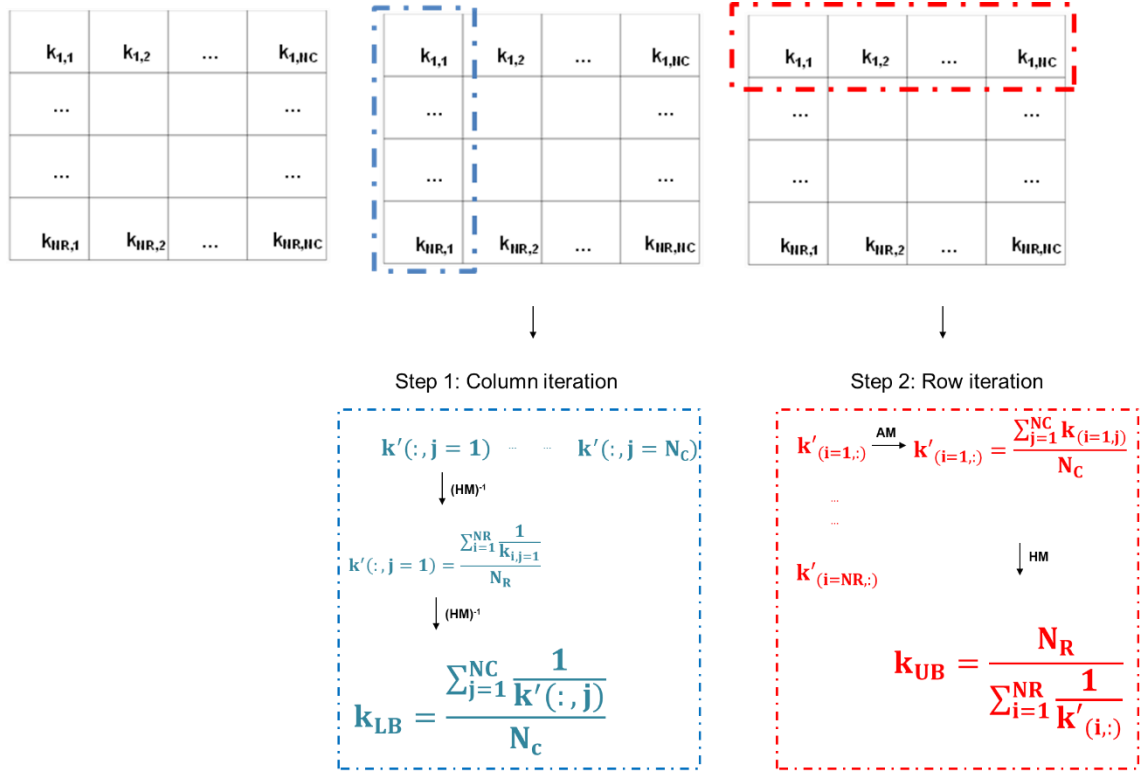


Figure 4. 1: Schematic of simplified renormalisation Method algorithm; (left) matrix considered and the voxels' IDs; (middle) process for calculating k_{LB} ; (right) process of calculating the k_{UB} ; AM stands for arithmetic mean and HM for harmonic mean. Eq. (4.7) calculates the effective matrix permeability.

4.1.3.3 Stochastic KMC approach

The KMC approach is indicated as 'Method III' in what follows.

KMC algorithms are designed to simulate stochastic realisations of the Master Equation.¹⁸³ For this work, the previous 1D lattice-based KMC algorithm, applied to a 2-phase system, is extended to 2D by increasing the number of possible moves a particle can make. For the 1D model a particle can either move to the left or to the right voxel at each algorithmic step, while when implementing a 2D approach it can also access the voxels above and below its initial position. In the 2D approach, only 1-phase systems of methane at supercritical conditions are considered (see Table 4.2). Using this 2D algorithm, the molecular trajectories are monitored and the overall permeability of a rock

sample is calculated. The Mersenne Twister MT19937 uniform random number generator was used to obtain sequences of random numbers.¹⁸⁹

The computational efficiency of the KMC algorithm is strongly dependent on the matrix mesh as the computational cost to select each KMC step scales with the number of possible events. For a $N \times N$ matrix with $z=4$, there are $4 \times N \times N$ possible events at each step. Note that for implementing the 1D KMC model to a matrix consisting of N voxels, the number of possible events would be $2 \times N$, which is $1/2N$ less, compared to the 2D KMC model. For a rather small system consisting of few voxels (i.e. $N < 50$), the computational time required for a 1D KMC model could be several seconds, while for an equivalent 2D model several minutes would be required. Other factors that challenge the computational efficiency of the KMC algorithm is the size of the system (number of particles) and the distribution of the KMC rates¹⁵². Considering that the latter factors depend on the investigated system, and hence can be rarely optimised, the computational efficiency of the KMC algorithm is usually improved by selecting a more efficient event selection algorithm. Event selection can be performed in a linear or branching manner, with the latter making use of binary tree representations, a topic covered in Chapter 2 (see Section 2.9);¹⁸⁶ for efficiency purposes, the latter approach is implemented in this study. The validation of the branching method and the computational savings achieved are reported in subsection 4.1.5.1.

4.1.3.4 Parameters selection

To directly compare results obtained when Methods I, II, and III are implemented, all system properties are kept constant, including permeability coefficients. This is straightforward when either the EMT or renormalisation methods are implemented, because the permeability coefficients are parameters in Eq. (4.3) and Eqs. (4.5 – 4.7). When the KMC approach is utilised, the permeability coefficients, $k_{i,j}$, expressed in m^2 or Darcy for Methods I and II, should be translated into KMC rates, expressed in s^{-1} , to simulate stochastic realisations of Eq. (4.8). To achieve this, Darcy's⁶⁸ and Fick's²⁰⁵ law

are combined in the following relation (see 4.9) to relate diffusion coefficients $D_{i,j}$, in m^2/s , and permeability, in m^2 .

According to Darcy's law, the flow J between two points in a 1D system is related to the pressure difference ΔP and distance Δx between them using the permeability k [(mol m)/(s m^2 MPa)]:

$$J = -k_{i,j} \frac{\Delta P}{\Delta x} \quad (4.8)$$

where J is the molecular flux per surface area ($\text{mol}/\text{s m}^2$), Δx is the distance between the two points (m), and ΔP is the difference in pressure across the specimen (MPa).

In a similar manner, Fick's law expresses the proportionality between the molecular flux and the concentration gradient:

$$J = D_{i,j} \frac{\Delta C}{\Delta x} \quad (4.9)$$

where $D_{i,j}$ is the diffusion coefficient (m^2/s) in voxel i,j , and ΔC is the difference in concentration between two points (mol/m^3).

For a 1D system, one can combine these two fundamental equations (Eqs. 4.8 and 4.9) and obtain a relationship between diffusivity and permeability:

$$D_{i,j} = \frac{k_{i,j} \Delta P}{\Delta C} \quad (4.10)$$

where ΔP is the pressure difference applied to the system and ΔC is the fluid concentration difference (see the description in subsection 4.1.3.6). With Eq. 4.11, assuming that either the diffusion coefficient or the permeability coefficient is known, one calculates the other upon applying a concentration gradient. The validation of Eq. (4.11) is provided in subsection 4.1.5.2.

To convert the permeability expressed in (mol m)/(s m^2 MPa) to the most commonly used permeability unit of m^2 , one needs to multiply the permeability coefficients $k_{i,j}$ in

Eqs. (4.8) and (4.11) by the fluid viscosity μ (MPa s), divide by the molecular concentration (mol/m³), and then calculate the KMC transition rates r_{KMC} using Eq. (4.12):¹⁴¹

$$r_{i,j}^{\text{KMC}} = \frac{D_{i,j}}{\delta^2} \quad (4.11)$$

In Eq. 4.12, δ is the voxel size (m). The KMC rate for each transition depends on the permeability coefficient of the neighbour/final destination. The assumption implicit in Eq. (4.11) is that the fluid transport from voxel to voxel takes place without encountering any thermodynamic barrier. For Eq. (4.11), $D_{i,j}$ is the diffusion coefficient as calculated using Eq. (4.10), and δ is the distance between the centres of two consecutive voxels. It is assumed that when a transition takes place, the effective distance covered by the particles equals δ . An example of the methodology followed to calculate the effective matrix permeability using Methods I, II, and III, is provided in the subsection that follows (see 4.1.3.5), where it is further demonstrated that all three methods produce equivalent effective matrix permeability values when a homogeneous network is considered, thus suggesting that further manipulation of the results (e.g., within the Smooth Field Approximation),²⁰⁶ is not necessary.

4.1.3.5 Assigning permeability coefficients for Methods I, II, and III

This section discusses the methodology followed for calculating the effective matrix permeability using EMT, simplified renormalisation, and KMC. As a first step, the lattice needs to be constructed; Figure 4.2 shows a 5x5 dual-permeability lattice. The green/pink voxels correspond to low-/high-permeability pores (1 and 100 nD, respectively). To calculate the effective matrix permeability, Figure 4.2 is converted into a permeability array (Table 4.1).

1	2	3	4	5
6	7	8	9	10
11	12	13	14	15
16	17	18	19	20
21	22	23	24	25

Figure 4. 2: Fictitious 5x5 lattice with the numbers representing the voxel ID; green-coloured voxels are assigned with permeability of 1nD, pink ones with 100 nD.

Table 4. 1: Voxel IDs and array of the corresponding permeability coefficients, as defined by Figure 4.2.

Voxel colour ID	Permeability (nD)	Voxels' number in lattice
Pink	100	1,7,13,19, 25
Green	1	2-6, 8-12, 14-18, 20-24

To calculate the effective matrix permeability, the weight of each contribution need to be determined. For this example, assuming that all contributions have the same weight, one defines $\varphi=0.04$ for each voxel. By applying Eq. (4.3) and Eqs. (4.5 – 4.7), the effective matrix permeability can be determined using Methods I and II, respectively.

To implement the KMC method, the rate of each transition needs to be determined. For a 2D lattice constructed by square voxels (Figure 4.3), there are four possible transitions that enable the particles to “jump” from one voxel to a neighbouring one. The KMC rate for each transition depends on the permeability coefficient of the neighbour/final destination. Figure 4.3 shows red arrows representing the KMC rates for the transitions

from a low- to high-permeability voxel, and the blue arrows indicate KMC rates that apply for transitions from a high- to low-permeability voxel. There are no arrows at the lattice boundaries because of the nonperiodic boundary conditions implemented; all boundaries are reflective, and the KMC rates/propensities of transitions through boundaries are set as zero.

For the last initialisation step, the initial distribution of particles should be defined. The protocol used for this study has all particles to be initially placed on top of the matrices considered.

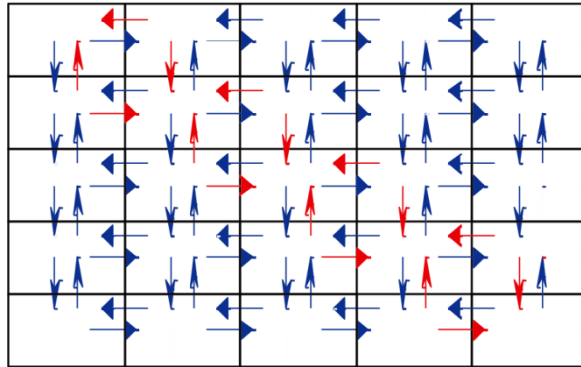


Figure 4. 3: KMC rates for the dual-porosity 5×5 lattice. Red arrows represent transitions from low- to high-permeability regions, and blue arrows indicate KMC rates for jumps between low-permeability regions.

4.1.3.6 Simulation set-up

2D pore networks (matrices) are constructed, each containing N_C columns and N_R rows along the x- and y- axis. The voxels in the matrix are cubic, but they can be considered effectively square, since the depth dimension is significantly smaller than the other two dimensions. The transport within the system can only occur on the xy plane, because the thickness along the z-axis is assumed to be negligible for a narrow cylindrical pore. It is assumed that the particles within voxels are well mixed.

To estimate the effective matrix permeability using Methods I and II, permeability coefficients were assigned to each voxel, and Eq. (4.3) and Eqs. (4.5 – 4.7) were

implemented, respectively. The assigned permeability coefficients were calculated based on the methodology proposed by Coppens²⁰⁷ and Naraghi et al.:¹⁰²

$$k_{i,j} = \frac{\eta M}{RT\rho_{av}} \frac{\theta}{\tau} (\delta'^{D_f-2}) D_{k_{i,j}} + k_{D_{i,j}} \left(1 + \frac{b_{i,j}}{P}\right) \quad (4.12)$$

$$b_{i,j} = \left(\frac{8\pi RT}{M}\right)^{0.5} \frac{\eta}{R_{i,j}} \left(\frac{2}{\alpha_{i,j}} - 1\right) \quad (4.13)$$

$$\alpha_{i,j} = 1 - \log(1 + Kn_{i,j}^{0.7}) \quad (4.14)$$

$$D_{k_{i,j}} = \frac{2R_{i,j}}{3} \left(\frac{8RT}{\pi M}\right)^{0.5} \quad (4.15)$$

In Eqs. (4.12 – 4.15) η is the gas viscosity, M is the molar mass, R is the ideal gas constant, T is the temperature in Kelvin, ρ_{av} is the average gas density, θ is the rock porosity, τ is the tortuosity, $R_{i,j}$ is the pore radius of the voxel (i,j), D_f is the fractal dimension of the pore surface, Kn is the Knudsen number, D_k is the Knudsen diffusion coefficient in a smooth cylindrical pore, k_D is the Darcy permeability, and δ' is the ratio of normalised molecular size to local average pore diameter. Here, it is assumed that the pores are smooth, so that $D_f = 2$; this would have to be adjusted for fractal pores. Once the properties of the diffusing gas are calculated, the diffusion coefficient is determined solely from the pore diameter.

For the lattices of the 2D pore networks generated the size of the voxels is constant. It is assumed that multiple pores can occupy a voxel and that these pores are highly connected. As a result, each voxel has an effective permeability that could be simplified by having a single pore with a corresponding effective radius. This effective radius is an input value in Eq. (4.12).

In the developed 2D KMC model, physical properties that represent supercritical methane are considered, as summarised in Table 4.2, together with the rock

characteristics. Note that the critical temperature of methane is 190.6 K at 4.6 MPa.²⁰⁸ The rock total organic content (TOC) shows the % volume of the organic matter and is used to construct the shale network (see subsection 4.1.4.4). Initially, a number of particles corresponding to a methane concentration C , are placed at the top of the matrix, while the rest of the system is empty. The particle concentration C at the top of the matrix is maintained constant at all times during the simulations. The amount of particles needed for the simulations is determined by knowing the voxels' volume and the methane density. Since the KMC matrix requires an area in which the particle concentration is constant, a row above the top row of the matrix is added. As this is a computational requirement for implementing the KMC model, the properties of this row are not taken into consideration when implementing Methods I and II.

The left and right matrix boundaries are reflective, while the bottom one is open: once the particles reach the bottom boundary, they can either exit the matrix or move to other neighbouring voxels. Because of the initial configuration selected, the particles on average move through the matrix along the vertical direction, from the top to the bottom boundary. A counter is used to track the number of particles leaving the matrix from the bottom boundary during the simulation. Once a particle leaves the matrix, it is deleted from the simulation. Effectively, this particle can be thought of as entering a large empty voxel at the bottom of the domain. To set this up in the KMC simulation an 'absorbing' row is added to the bottom of the matrix. The properties of this absorbing row are not used for Methods I and II.

Table 4. 2: Input parameters used for the permeability simulations for all three methods.

Parameter	Value
CH ₄ Temperature (T)	300 K
CH ₄ Pressure (P)	10 MPa
CH ₄ Concentration (C)	4685.9 mol/m ³
Rock Porosity (θ)	10%

Rock Tortuosity (τ)	2
Rock volumetric (TOC)	12%

A constant pressure and concentration difference is maintained during the simulation by following the protocol described in Chapter 3. To analyse the results, the number of particles leaving the domain ΔQ at constant time steps Δt is monitored. The time step selected depends on the configuration used. The slope of the linear fits is used to calculate the molecular flux J :

$$J = \frac{\Delta Q}{\Delta t A N_A} \quad (4.16)$$

where A is the cross-sectional area available for the particles to leave the matrix. The matrix effective permeability (Method III) is calculated using Darcy's law:

$$k_{\text{eff}} = -\frac{J\Delta x}{\Delta P} \quad (4.17)$$

where Δx is the matrix length, disregarding the top and bottom rows, added for computational requirements. The pressure drop is obtained by subtracting the pressure at the bottom (0 MPa) from the pressure at the top of the matrix (10 MPa). In this study, it is assumed that the macroscopic flow follows Darcy's law, while allowing for Knudsen diffusion to occur within voxels containing narrow smooth pores, as described in Eqs. (4.12 – 4.15).

Systems investigated

4.1.4.1 Model networks to test sensitivity to pore size distribution

The general consensus is that deterministic methods, such as Methods I and II, provide accurate predictions when the properties investigated follow a narrow log-normal distribution. Thus, a log-normal distribution (μ , σ^2) of pore sizes is considered in this study. The distribution's μ is kept constant ($\mu = 1.57$ on the logarithmic scale), but sigma

(σ) varies between 0.1 and 1 (Figure 4.4). While increasing sigma, the proportion of micropores (0-2 nm), mesopores (2-50 nm) and macropores (>50 nm)²⁰⁹ changes. Pore classification follows IUPAC guidelines.²⁰⁹

Methods I, II, and III were used to predict the effective medium permeability. For each σ value 10 pore networks were generated. Note that this number (10) is selected as it is small, and therefore requires reasonable computational resources, but sufficient to ensure that the permeability values calculated for the various sigma scenarios have confidence intervals that do not overlap, even when 99.9% confidence level is selected. Further discussion on the results obtained using this confidence level follows in subsection (4.1.5.4). Because Method III is stochastic, 10 independent KMC simulation runs are performed for each pore network. Note that completing one KMC simulation run requires significant computing time (several minutes), while deterministic methods require only a few seconds on a modern desktop computer. A 10 x 10 matrix was used for each sigma value considered and the voxels used to create the matrix had dimensions 100 x 100 x 1 nm. Using a 10 x 10 matrix is advantageous considering the computational time required for the KMC simulations but can sometimes generate not representative networks. To ensure that all networks simulated were representative of the PSD selected, the PSD of each potential network were plotted against the target PSD and those deviating were rejected. This was a time consuming, but necessary process.

A stochastic algorithm assigned pore sizes into the matrix voxels, according to the PSD selected, and Eq. (4.13) was used to calculate the permeability of each voxel. Since the number of stochastic realisations generated is small (10), Monte Carlo (MC) sampling was implemented over the PSDs to generate the stochastic realisations, as suggested by Naraghi et al.,¹⁰² However, to generate a larger number of stochastic realisations, more computationally efficient algorithms should be implemented. For example, First-Order Reliability Approach (FORM) can produce realisations similar to those obtained with MC sampling significantly faster.^{210,211} Another way to produce stochastic realisations is via geostatistical simulation, a method widely used in the petroleum

industry for characterising heterogeneous reservoirs that allows generation of many equally probable realisations which can be post-processed to quantify and assess uncertainty. For instance, Karacan et al., implemented sequential Gaussian simulation (SGSIM) and sequential Gaussian co-simulation (co-SGSIM) techniques to generate stochastic realisations of coal.²¹² In this study (subsections 4.1.4.1 and 4.1.4.4) a previously reported stochastic MC sampling technique was implemented, to generate the 2D pore networks^{102,213,214}, but also a stochastic method (Method III) was used to simulate the fluid transport of the gas particles (KMC) through the generated pore networks. The time step used for the KMC sampling was set at 100 ns. Once all simulations were completed, the average of the effective permeabilities was calculated $\langle k_{\text{eff}}(\sigma) \rangle$ for each sigma value. These effective permeability values are compared against results obtained from Methods I and II. The error bars for KMC calculations were calculated using Eq. (4.18):

$$\text{Error} = \frac{\text{STD}(k_{\text{eff}}(\sigma))}{\sqrt{n}} \quad (4.18)$$

In Eq. (4.18), $\text{STD}(k_{\text{eff}}(\sigma))$ is the standard deviation of the values obtained in each individual KMC run for a given PSD, and n is the number of observations (10 for the simulations previously discussed).

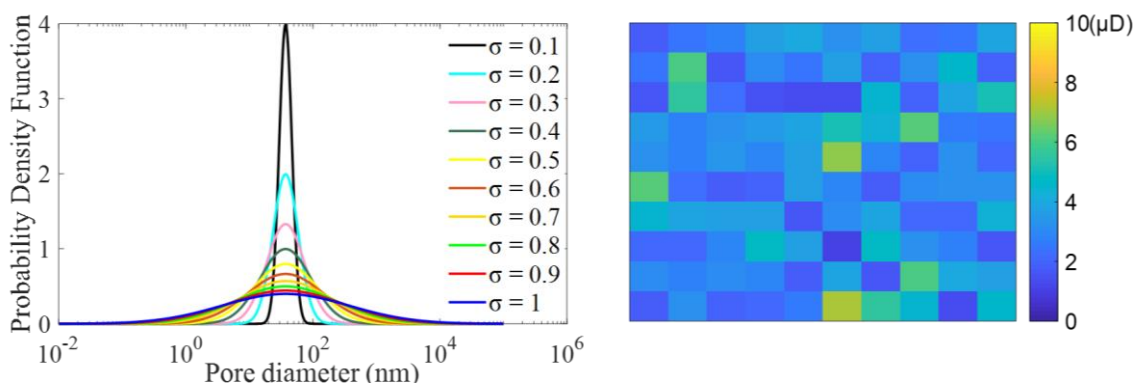


Figure 4. 4: (Left): Log-scale PSDs considered in this study analysis. In all cases the distribution's μ , is 37.15 nm, while sigma ranges between 0.1 and 1. (Right): Example of spatial arrangement of the permeability coefficients for sigma=0.1.

4.1.4.2 Model networks to test sensitivity to micro- and macropores

It is commonly accepted that Methods I and II provide satisfactory predictions when the proportion of low-permeability pores is low, in general $< 50\%$ and the system is sufficiently far from the percolation threshold. To assess how the differences among predictions obtained by implementing Methods I, II, and III change as the proportion of low-permeability pores vary, three pore-networks were generated, in which the volume proportion of low-permeability pores is 25%, 50% and 75%, respectively. Note that, as a simplification, each voxel is assumed to contain an equal pore volume, and that all the pores within a voxel are considered to be of the same size. In other words, each voxel represents a region containing only micro-, meso-, or macropores. Each voxel contains different numbers of perfectly conducting pores resulting in an equal pore volume per voxel.

The pore networks considered in this subsection are dual-permeability systems, generated within two scenarios: (1) a system comprising only micropores and mesopores; or (2) a system of mesopores and macropores. The micropores considered have a 1 nm diameter, yielding a permeability coefficient of 15 nD (note that the pore size determines the permeability; refer to Eq. 4.12). Mesopores and macropores were assumed to have diameters of 10 nm and 100 nm, respectively. The correspondent permeability coefficients are 0.3 μ D and 17 μ D and the dual permeability 10 x 10 matrix networks consisted of 100 voxels, each with dimensions of 500 x 500 x 1 nm.

Figure 4.5 shows the networks generated; note that in the pore networks of Figure 4.5 there is no distribution of pore diameters: there are only three possible values for these diameters, capturing micro-, meso- or macropores. Panels a, b, and c show the spatial arrangement of the micro- and mesopores for 25%, 50% and 75% micropores, respectively; panels d, e, and f show the arrangement of macro- and mesopores. The KMC sampling step was 5 ns and 50 ns for systems (1) and (2) respectively.

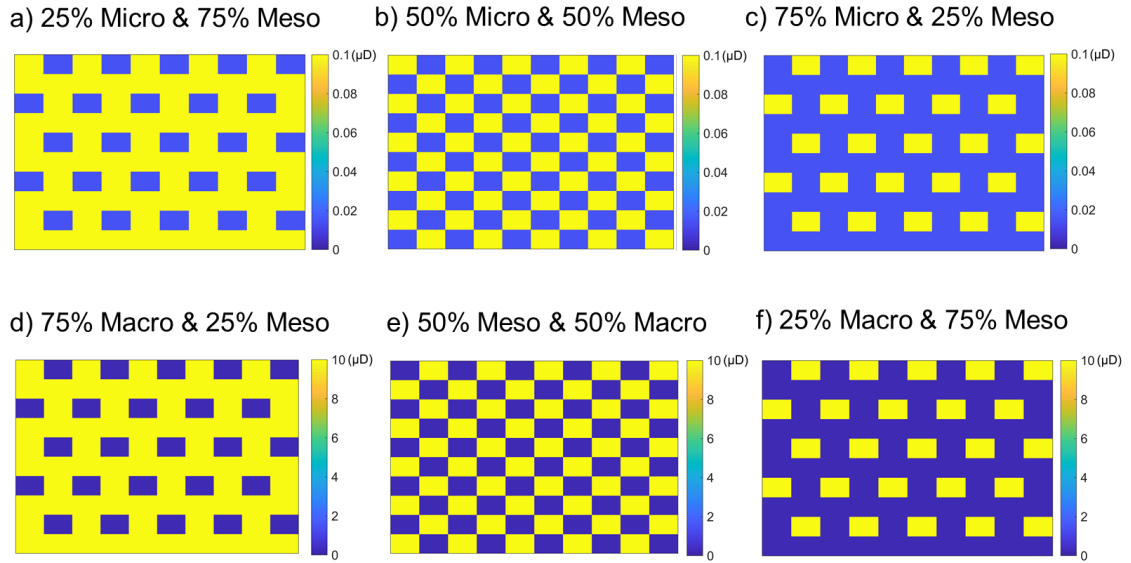


Figure 4. 5: Networks consisting of micro- and mesopores (a-c) and macro- and mesopores (d-f). The colour bars show the permeability coefficients assigned, in μD .

4.1.4.3 Model networks to test sensitivity to anisotropic distributions

Methods I and II are expected to face difficulties in differentiating between isotropic or anisotropic distribution of pores within a network, while it is likely that the stochastic KMC approach has the ability to differentiate between permeability along different directions within an anisotropic network. In shale rock samples, evidence confirms that permeability is indeed anisotropic.³⁶ To quantify the sensitivity of the methods considered here to the anisotropic distribution of pores, dual-permeability matrices were created, in which the proportion of the low and high-permeability voxels is kept constant (25% and 75%, respectively), but these components are spatially distributed in four different configurations. Figure 4.6 shows that the low-permeability values are aligned (A) horizontally; (B) vertically; (C) in a grid; and (D) both horizontally and vertically. The low and high-permeability pores are characterised by 15 nD and 0.3 μD permeability coefficients, respectively. For each configuration, 3 independent KMC simulation runs were conducted. The matrix size used for all four cases was 10 x 10, the voxel dimensions were 500 x 500 x 1 nm, and the sampling time step was 5 ns.

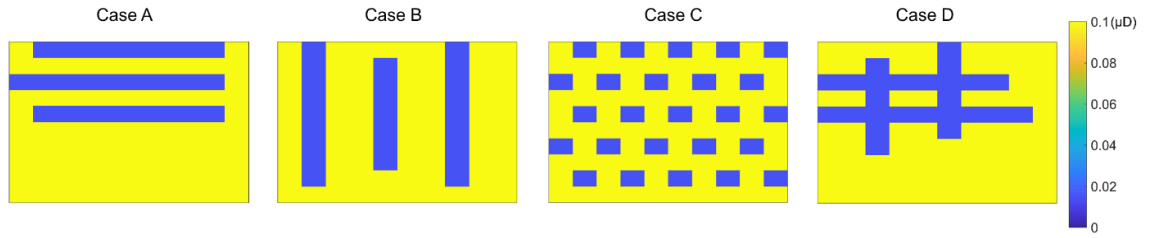


Figure 4. 6: Dual-permeability networks with different anisotropic distributions. Cases A and B exhibit high anisotropy and cases C and D have low and moderate anisotropy. The colour bars show permeability coefficients in μD .

The degree of anisotropy of each system was quantified by implementing covariance matrix analysis, as described by Ringnér and Bui et al.^{215,216} The unit cells considered for the covariance matrix analysis had periodic boundary conditions in all directions, and when the particle crossed a boundary, its new position was equal to the position in the unit cell plus the unit cell vector along the direction of the crossing. The initial position of the particle was randomised 100 times. The particle was not allowed to start from the same initial position more than once. From each initial position 200 independent runs were performed; hence, 20,000 independent runs were conducted for each configuration. The position of a single particle after 50 ns was obtained and the final position of the particle on the x and y direction was plotted against its initial origin.

Based on obtained trajectories, the covariance matrix was calculated, along with its eigenvectors and eigenvalues. The eigenvectors revealed the direction of the principal axis while the eigenvalues established the degree of variance for the data in that direction. The differences observed in the estimated eigenvalues are indicative of the degree of anisotropy. Additionally, the diffusion coefficient in the x and y directions, and in the xy plane was calculated by considering a single methane particle, whose trajectory was monitored for a total of 5 μs to obtain its MSD. The D_x , D_y and D_{xy} coefficients were calculated using Einstein's relation, on the basis of the calculated MSDs:

$$D_x = \frac{1}{2} \lim_{t \rightarrow \infty} \frac{\langle |x_i(t) - x_i(0)|^2 \rangle}{t} \quad (4.19)$$

$$D_y = \frac{1}{2} \lim_{t \rightarrow \infty} \frac{\langle |y_i(t) - y_i(0)|^2 \rangle}{t} \quad (4.20)$$

$$D_{xy} = \frac{1}{4} \lim_{t \rightarrow \infty} \frac{\langle |\mathbf{r}_i(t) - \mathbf{r}_i(0)|^2 \rangle}{t} \quad (4.21)$$

where $\langle |\mathbf{r}_i(t) - \mathbf{r}_i(0)|^2 \rangle$ is the MSD in the xy-plane and $\mathbf{r}_i(t) = (x_i(t), y_i(t))$. Covariance matrix analysis and diffusivity analyses were performed using KMC.

4.1.4.4 Experimental shale sample

A realistic pore network was also considered in this study. Naraghi et al.,¹⁰² applied King's simplified renormalisation method on the scanning electron microscope (SEM) image of an Eagle Ford shale sample, presented in Figure 4.7. Light grey areas represent inorganic components, and dark grey represents organic components. Naraghi et al.,¹⁰² segmented the image and determined the probability distribution of the organic block's size, referred to as "patch size" in their work. The patch size distribution is a normal Gaussian distribution with a mean of 5 μm and a sigma of 1 μm . To assign permeability coefficients within organic and inorganic components, Naraghi et al., used PSD data obtained from Brunauer, Emmett, and Teller (BET) measurements. They assumed that organic and inorganic components follow distinct log-normal PSDs and reported the distributions' means and standard deviations. It is assumed that the μ and sigma of the distributions, expressed on the log-scale, are 0.63 and 0.18 for the organic component, and 1.57 and 0.44 for the inorganic matter, respectively. These values are slightly different compared to those reported by Naraghi et al., but produce PSDs that closely match those reported by the authors. Naraghi et al., first generated a model pore network by assigning organic and inorganic components and then distributed pore sizes within the two components, while sampling from the appropriate distribution. The permeability coefficients were calculated using Eq. (4.13), and the effective network permeability was estimated using Method II.

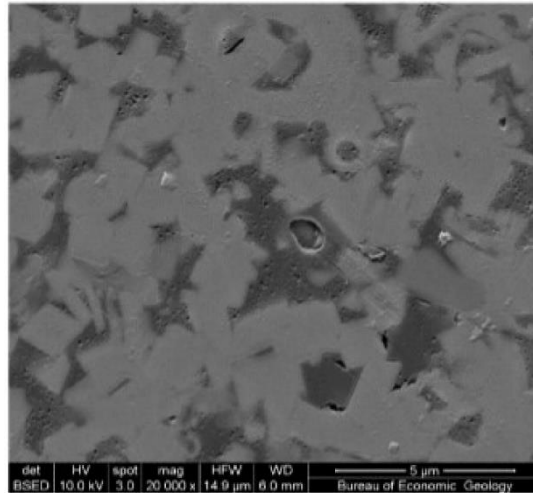


Figure 4. 7: SEM image of an Eagle Ford sample, reproduced from Naraghi et al.¹⁰² Dark grey regions correspond to organic matter and light grey to inorganic.

The experimental SEM image, presented in Figure 4.7, was used to calculate the effective matrix permeability using Methods I, II, and III, but to also generate additional equivalent networks. Following the approach by Naraghi et al., organic patches were distributed within the inorganic matter to generate the matrix for the 2D KMC model. The volumetric TOC was used to condition the total amount of organic pores assigned within the matrix and the pore sizes within the organic and inorganic matter were assigned according to the reported distribution properties. In this study, the effective matrix permeability of the organic and inorganic matter was separately calculated to reduce the computational load of the KMC simulations; similar calculations were not necessary using Model I and II.

To calculate the effective organic and inorganic permeability, 10 matrices consisting of 10 x 10 voxels in each case were generated, with voxel dimensions of 20 x 20 x 1 nm and 350 x 350 x 1 nm for the organic and inorganic matter, respectively. The effective permeability mean and error bars from all three methods for both components were calculated and then these 'effective' organic and inorganic permeability values were used to construct the dual permeability network, which represents the rock of Figure 4.7. To

calculate the permeability of the dual permeability network, a 15×15 matrix consisting of $1 \mu\text{m} \times 1 \mu\text{m} \times 1 \text{nm}$ voxels was considered.

To consistently compare Methods I, II, and III to calculate the network's effective permeability, the organic and inorganic permeabilities obtained from the previous step were used as input. The KMC sampling time step was 1 ns for all calculations (organic, inorganic, dual-permeability), and 10 independent KMC runs were performed for each dual-permeability configuration. Using the KMC method, the confidence interval of the results obtained was also calculated, for 99.9% confidence level, to ensure that using 10 stochastic realisations for the organic, inorganic and network permeability provides enough statistics to draw meaningful conclusions, especially when the KMC data are compared against experiments.

Results and discussion

Validation of the branching algorithm

At each step of the KMC simulation, an event is selected and executed, resulting in the occupancy at each voxel changing while the simulation progresses; therefore, the propensities need to be updated over time (propensity is defined as the product of the KMC rate and occupancy at each voxel). For the classic KMC algorithm description (linear event selection), after each event execution, the list of all propensities is scanned and updated; however, because only one particle transitions at each simulation step for our protocol, not all propensities change after the execution of an event. The branching algorithm implemented in this study, identifies which voxels are affected by the event being executed, and it updates only the propensities associated with these voxels. For systems consisting of many voxels (>50), implementing the branching algorithm results in significant computational savings. To test and validate the branching algorithm

implemented in the 2D KMC model, a 100×100 2D uniform lattice with the permeability 0.1 μD was generated.

Using the same sequence of random numbers, the KMC algorithm was executed twice. The first time the selection of transition events taking place at each time follows the linear selection algorithm (this approach is mentioned as “classic algorithm”) and the second time, the branching algorithm was implemented. As a next step, the ID of the event selected in both cases is reported and the events selected from each selection algorithm are compared against each other to determine if the event selected is the same in both simulations. A value of “0” is assigned when there is agreement between the two algorithms and a value of “1” whenever a different event is being selected; Figure 4.8 shows the values assigned over time. It is evident that for the 3,000 events sampled, there was always agreement between the events selected using the two different algorithms.

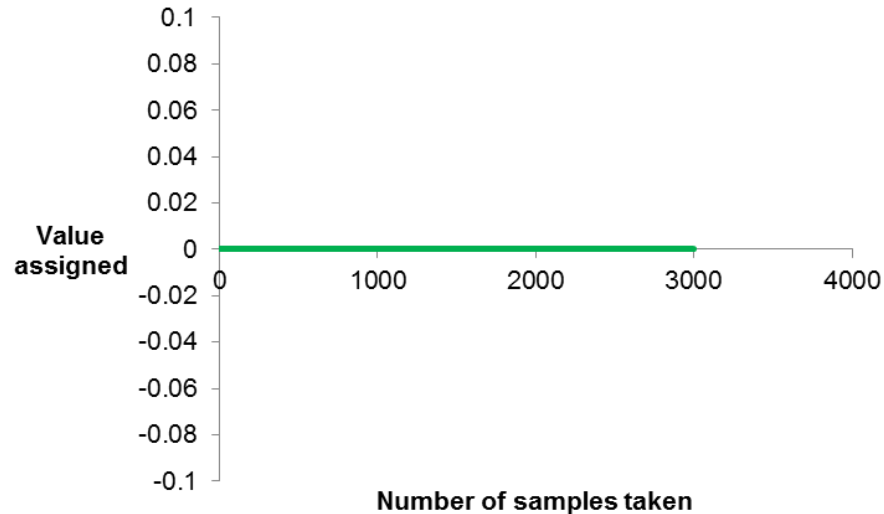


Figure 4. 8: Validation of the branching algorithm. When the value=0, there is agreement between the two algorithms implemented in terms of the event selected at each time.

To quantify the computational savings achieved by implementing the branching algorithm vs. the classic one, the CPU time necessary for each algorithm, to identify and execute the event at each step, was monitored. Figure 4.9 shows the CPU time

necessary for the branching algorithm in purple. Evidently, the computational demand is smaller compared to the CPU time necessary using the linear search algorithm (classic approach).

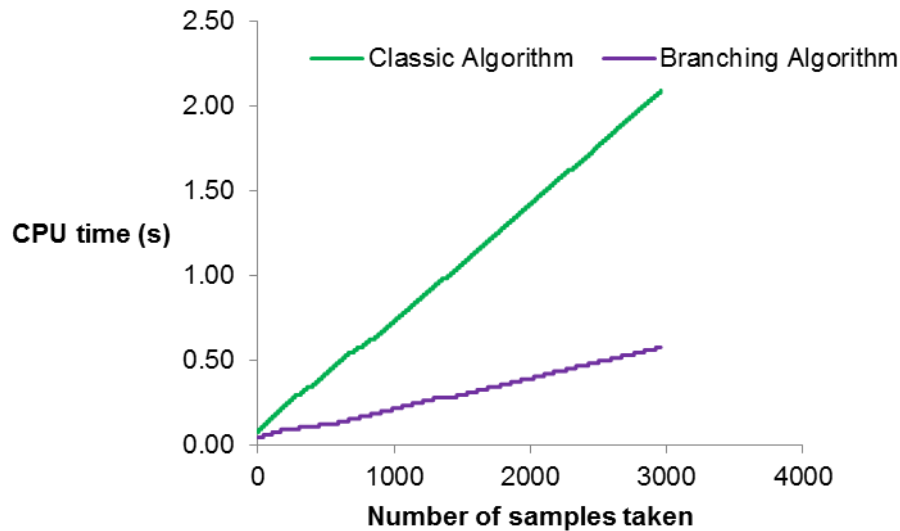


Figure 4. 9: Computational savings when implementing the branching algorithm in a 100×100 lattice.

Calculation of the permeability coefficient from diffusivity

To validate Eq. (4.11), a 2D homogeneous lattice was generated and a fixed permeability value (target permeability) was set. The system was not periodic; instead, the bottom boundary was maintained open, and the particles were initially loaded at the top of the matrix. Once they reached the bottom, the particles could exit the lattice by being “deleted” from the system. The particle concentration at the top boundary was kept constant during simulations. With this simulation setup, a pressure differential (high pressure at the top, zero pressure at the bottom) that acted as a driving force for the particles’ motion, was created. The number of particles exiting the lattice over time was monitored, allowing for the calculation of the molecular flux J . From J , using Eq. (4.17), the effective matrix permeability was calculated. Note that for Eq. (4.11) to stand true, Eq. (4.17) needs also to be valid and vice versa.

The sampling time step depends on the diffusivity and the lattice size. The appropriate sampling step for the systems considered in this study, is determined following a trial and error approach, as discussed in Chapter 2. However, for the systems analysed in this chapter, the appropriate sampling step needs to also result in a linear relationship between particles leaving the lattice and total time. Since molecules are loaded at the top of the matrix, time is required for them to diffuse, reach the bottom boundary, and eventually leave the matrix. If the total time of the simulation is too short, it is possible that zero molecules have left the matrix and the flux calculated is zero. As the total simulation time increases, the flux increases in a non-linear manner, until steady state is reached. This is when the observed relationship between the number of particles leaving the system and time is linear. As a consequence, the sampling frequency needs to account for this delay. The ideal scenario is to use two different sampling schemes, one prior- and one post- steady state. However, determining the exact time steady state is reached, while the simulation is in progress, can be tricky. In this study, a constant sampling step was implemented for all systems investigated. The selected time step resulted in (1) a linear flux curve and (2) kept the number of total samples collected to a minimum, since oversampling, as discussed in Chapter 2, results in unnecessary computational burden.

The permeability calculated using the KMC approach is compared against the permeability set up initially (target) as well as the permeability predicted using the EMT and the simplified renormalisation methods. The target permeability calculated using either one of the two deterministic methods implemented was always identical to the target permeability imposed; Figure 4.10 (panel A) shows the outcome for the KMC simulations, and the KMC lattice used for the validation of Eq. (4.11) (panel B). The same process was repeated using 10 different target permeability values. At each round of simulations, the target permeability was decreased by 10% of the original value, see Table 4.3 for further details.

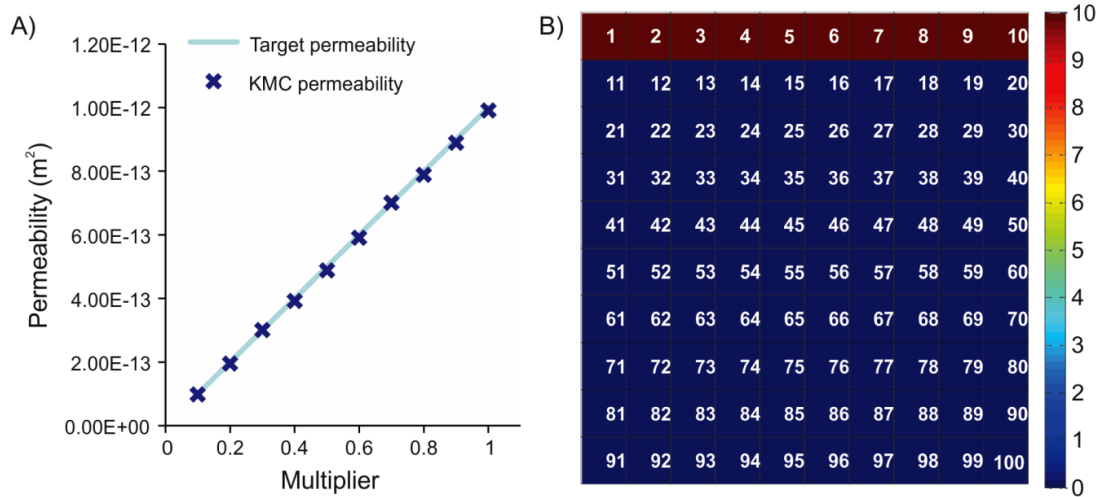


Figure 4. 10: A) comparison between the target permeability used as an input for the calculation of the KMC rates and the calculated effective matrix permeability at the end of the simulations. The results provide the validation of the proposed process. B) representation of the KMC lattice used for the validation process. The colour bar indicates the number of particles for the initial configuration.

Table 4. 3: List of the target permeability coefficients used as an input during our validation process.

Multiplier	Target Permeability (m ²)
1	1.00E-12
0.9	9.00E-13
0.8	8.00E-13
0.7	7.00E-13
0.6	6.00E-13
0.5	5.00E-13
0.4	4.00E-13
0.3	3.00E-13
0.2	2.00E-13
0.1	1.00E-13

Pore size distribution effects

Figure 4.4 shows that for the PSDs considered, in which the mean was kept constant, as sigma increased, the amount of both micro- and macropores present in the sample increased. The proportion of the micro-, meso- and macropores for the different sigma values was monitored, and the effective matrix permeability for each distribution using Methods I, II, and III was computed. Figure 4.11 shows the results; A) shows the absolute results from the three approaches, in terms of matrix effective permeability; B) shows the percent deviation of the deterministic Models I and II compared to the stochastic calculation (Model III); and C) shows the analysis of the PSD in terms of % structural composition due to micro-, meso-, and macropores.

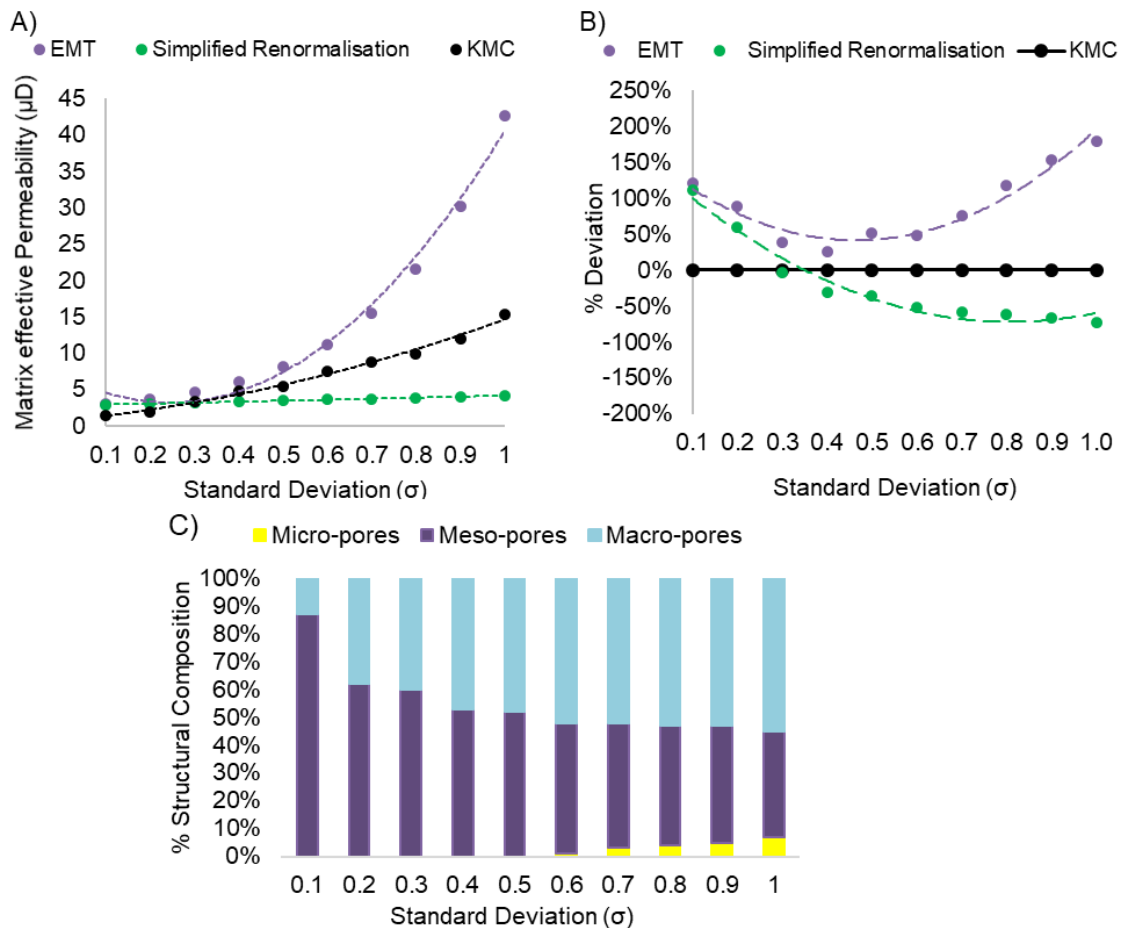


Figure 4. 11: (A) Comparison of the three methods used in this study as a function of the distribution's sigma; KMC error bars are estimated to be smaller than the size of the marker. (B) Percent deviation of the deterministic models compared to the stochastic calculation. (C) Percent of volume comprised of micro-, meso- and macropores in each system shown in (A). Lines in (A) and (B) are guides to the eye. The matrices simulated here are isotropic with PSDs shown in Figure 4.4.

When σ ranged between 0.1 and 0.2, the majority of the pore volume consisted of mesopores, yielding an isotropic network with a high proportion of low-permeability pore volume (only macropores are considered to be high-permeability pores in our analysis). Both deterministic methods overestimated the effective network permeability, compared to the KMC. This result agrees with expectations based on literature, because the high-permeability component (macropores) represents a low fraction of the respective pore networks, and the deterministic Models I and II are expected to over-estimate the contribution of high-permeability pores under the conditions tested.

When σ ranged between 0.3 and 0.4, there was good agreement among all three methods. Figure 4.11 – C shows that the volume fraction of macropores in the samples continuously increased as σ increased; for σ greater than 0.4, such pores accounted for the majority of pore volume in the system. At these conditions, the deterministic methods are expected to be accurate, and indeed the results obtained show small deviations compared to predictions based on the stochastic KMC approach, reinforcing these observations reinforce our hypothesis that the stochastic KMC method can yield accurate predictions for effective medium permeability.

When $\sigma=0.5$, the pore network still contained only meso- and macropores; however, there were 1% fewer mesopores (by volume) and 1% more macropores compared to the network characterised by $\sigma=0.4$. In this scenario, the results obtained demonstrate that Method I (EMT) significantly over-estimated the permeability, compared to both Methods II and Method III, suggesting that the EMT approach is highly sensitive to the presence of high-permeability components. Further, both Methods II and III predicted increases in effective permeability because of the increased amount of macropores in the system, but the effect was moderate.

When σ ranged from 0.6 to 1.0, the pore networks contained significant amounts of micro-, meso- and macropores. For $\sigma=0.6$, micropores accounted for 1% (by

volume) of the pores in the network and macropores for 52% (by volume). Method I predicted rapid increases in the effective permeability as sigma increased, which increasingly diverged from the KMC predictions, confirming the high sensitivity of EMT to high-permeability pores in the network. Method II yielded effective permeability predictions that were lower compared to those obtained by the KMC algorithm. It was actually observed that for PSDs with sigma larger than 0.3, Method III (KMC) predicted an effective permeability between those predicted by Method I and by Method II. This is due to the EMT's sensitivity to macropores and to the zero cross-flow assumption implicit in Eqs. (4.5 – 4.7), which describe Method II.

For distributions with sigma between 0.7 and 1, the volume fraction of mesopores dropped, while the volume fraction of micro- and macropores increased. The EMT continued to predict very high effective matrix permeability, while the simplified renormalisation (Method II) yielded a permeability lower than that obtained using Method III. The effective permeability predicted by Method I was up to ~10 times larger than that predicted by Method II, based on this case study. Even though the volume of micropores present in the network increased when sigma was larger than 0.7, both Methods II and III predicted an increased permeability as sigma increased. This is because, as the distributions of the pores in the networks became broader the generated networks contained larger macropore volumes as well.

Uncertainty and confidence intervals

To calculate the confidence interval of the mean in the KMC stochastic simulations Eq. (4.22) was implemented:

$$\langle x \rangle \pm z \frac{s}{\sqrt{n}} \quad (4.22)$$

In Eq. (4.22), $\langle x \rangle$ is the mean value obtained from averaging the KMC simulation data, z is the confidence coefficient, s is the standard deviation and n is the sample size. For confidence intervals with 99.9% confidence level, the confidence coefficient value is

4.1437. Because the number of independent stochastic simulations performed for each realisation in subsection 4.1.5.3 is small (10), to calculate the value of s the standard deviation of the population was used (instead of the standard deviation of the sample).

Figure 4.12 shows the results obtained using the KMC model for the network described in subsection 4.1.4.1 when the sigma value of the PSD is 0.1. Using a Monte Carlo sampling method, 10 stochastic realisations of equiprobable networks were generated. For each stochastic realisation, 10 independent KMC runs were performed. The x-axis shows the ID of the stochastic realisation and the y-axis the mean value of the permeability calculated through the 10 independent KMC runs. The error bars indicate the confidence interval for 99.9% confidence level for each stochastic realisation.

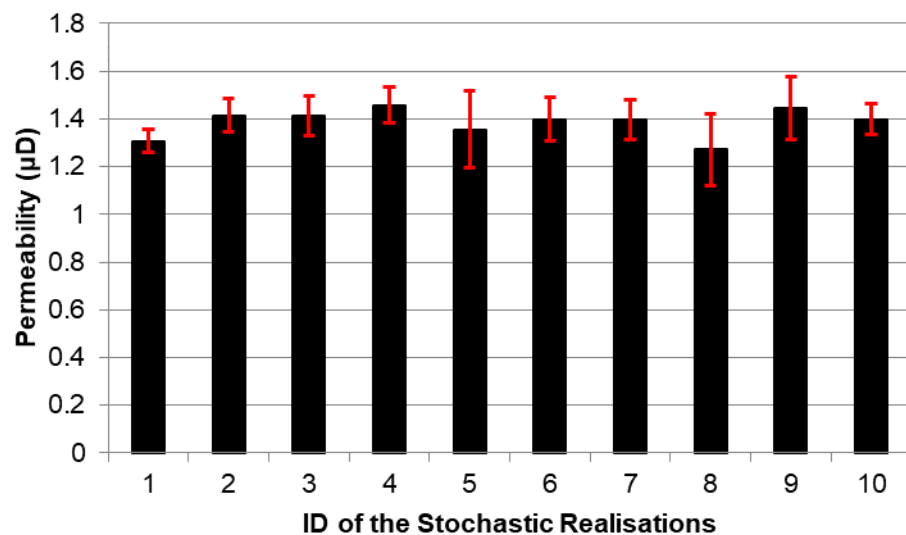


Figure 4. 12: Mean and confidence intervals of 10 independent KMC runs for each stochastic realisation. The network (Section 3.1) has log-normal PSD with $\mu=37.15$ nm and $\sigma=0.1$.

Figure 4.12 shows that all confidence intervals overlap. Therefore, calculating the mean permeability using 10 stochastic realisations provides reliable and reproducible estimates. However, it is expected that as the sigma value increases and the PSDs become broader, the variability/heterogeneity of the systems increases. To test whether

using 10 realisations can still capture the heterogeneity of the networks generated, the same analysis was performed for all 10 networks mentioned in subsection 4.1.4.1.

The mean permeability calculated from all 10 stochastic realisations was computed for each sigma value together with the confidence intervals, using Eq. (4.22) and 99.9% confidence level. The results are presented in Figure 4.13. As expected, all different sigma values result in different effective permeability values. Although, the confidence intervals increase slightly, as the PSDs become broader, they still remain narrow giving acceptable estimates for every sigma value with no overlaps between the various networks with 99.9% confidence intervals. Therefore, the risk of the mean permeability values presented laying outside of the confidence intervals (Type I error) is $\leq 0.1\%$.

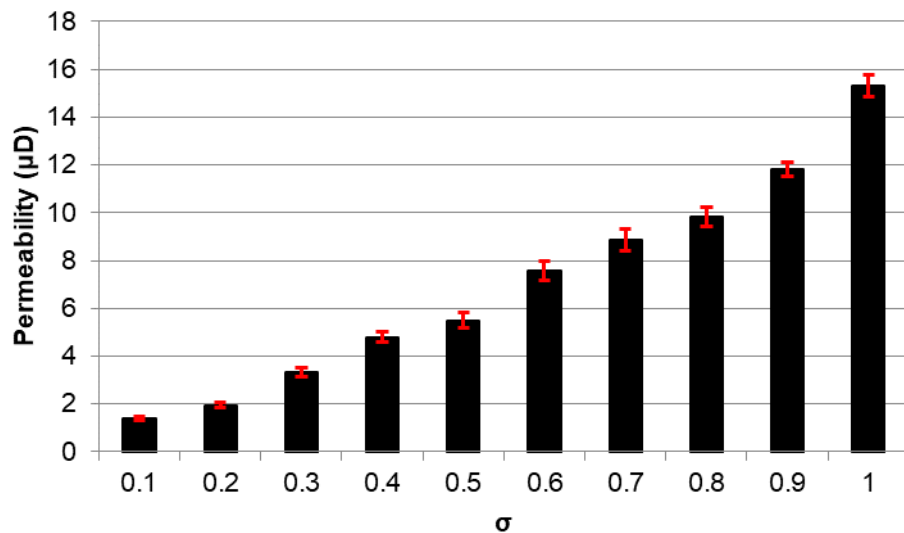


Figure 4. 13: Mean permeability values calculated using the KMC method for the networks described in subsection 4.1.4.1. The error bars represent the confidence intervals for 99.9% confidence level.

Micro- vs. macropore effects

The preceding investigation exhibits the sensitivity of the EMT on macropores. To quantify the methods' sensitivity on micropores, a sensitivity analysis was performed for all three methods, using dual-permeability networks consisting of micro- and mesopores, and meso- and macropores, respectively (Figure 4.5). The results obtained are reported

in Figure 4.14, in which A) and B) depict the effect of micro- and macropores to the effective matrix permeability, respectively.

Initially, the effect of micropores was quantified, Figure 4.14 – panel A. When 25% of the pore volume was micropores and the rest were mesopores, KMC and EMT methods yielded effective permeabilities in excellent agreement with each other. This is expected, considering the amount of the relatively low-permeability component is low for these networks. It is perhaps surprising that Method II underestimated the effective matrix permeability by almost half. This is due to the assumption of zero cross-flow, which likely does not hold when the pore network of Figure 4.5 – a, is considered, coupled with a pressure difference imposed along the top-bottom direction.

When the proportion of micropores volume increased from 25% to 50%, the network's connectivity was effectively reduced. As a result, the zero cross-flow assumption became acceptable, and Model II predicted an effective permeability that agreed well with what KMC predicted. All models yielded effective permeability values that were lower than those for the matrix with 25% micropores volume, which is expected. The fact that Methods II and III yielded predictions in excellent agreement with each other suggests that the KMC approach provides realistic estimates of the matrix permeability, since the network of interest had poor connectivity in the direction of flow. It is not surprising that Method I (EMT) over-estimated the effective permeability compared to the other two approaches, as EMT fails when the system is close to the percolation threshold. When the micropores account for 75% of the pores in the sample, by volume, Fig. 4.5 – c, both deterministic Methods I and II overestimated the effective matrix permeability.

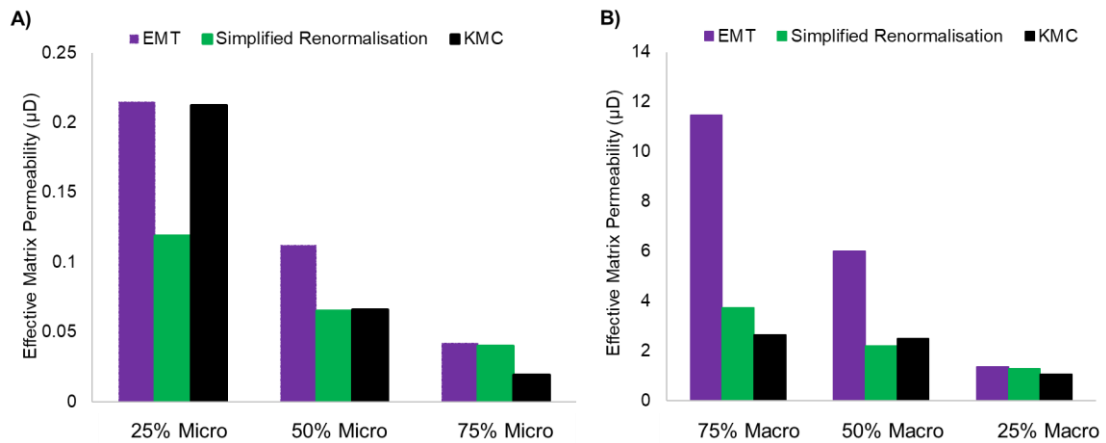


Figure 4. 14: Sensitivity analysis on the pore type in dual-permeability networks (Figure 4.5) with varying component % volume amount; (A) shows results for the network consisting of micro- and mesopores; (B) for the network with meso- and macropores.

Considering the effect of macropores (Figure 4.5, d – f, pore networks), the results (Figure 4.14 – panel B) suggest that there is a satisfactory agreement between the predictions by Methods III (KMC) and II (simplified renormalisation) for most of the cases. When 75% of the pore volume was macropores, in the dual permeability network (Figure 4.5 – panel d), both deterministic methods were highly sensitive to the presence of high-permeability pores, with Method I (EMT) significantly overestimating the effective permeability. The sensitivity of EMT to high-permeability coefficients was further evidenced by the extent of the over-prediction. When the % volume content of macropores was equal to that of mesopores, (Figure 4.5 – panel e), the EMT method overestimated the permeability, while Methods II and III were in satisfactory agreement. More specifically, the KMC's prediction lies between the two analytical methods, validating the previous observation for sigma 0.5 where the % of meso- and macropores was almost equivalent. The gap between the predictions of the EMT and the two other methods became smaller as the % of high-permeability components decreased. For 25% macropores (Figure 4.5 – panel f), the deterministic methods provided a slightly overestimated value for the matrix's permeability. In that case, the KMC's prediction was lower because the 25% of macropores present in the system were not well connected.

The same behaviour was observed for the case of 25% micro- and 75% mesopores, where the deterministic methods predicted values almost identical, but higher than the KMC's estimation, validating the reliability of the KMC methodology, as it accounts for the network's connectivity.

Anisotropy effects

The networks considered for the previous analysis probe the sensitivity of the three methods to micro- and macropores. In all pore networks considered so far (Figure 4.5) pore sizes were distributed uniformly within the networks. To quantify the effect of anisotropic distribution of the pores, dual-permeability networks containing 25% volume micropores and 75% volume mesopores were considered. Four configurations were generated (Figure 4.6 Cases A – D) and in all of them, the flow direction was along the y-axis. The effective matrix permeability using Methods I, II, and III was calculated, and Figure 4.15 shows the results.

To further assess the effect of anisotropic pore distribution, the diffusion coefficient of a particle representing a single methane molecule along the x and y directions was calculated, as well as its 2D diffusion coefficient in the xy plane (results in Figure 4.15). Figure 4.16 presents covariance matrix analysis results to test whether diffusion coefficients and measures of anisotropy can provide insights for the network's effective permeability.

The results in Figure 4.15 show that Method I (EMT) did not capture the anisotropic distribution of the pores within the network. This is expected, considering that EMT neglects the network structure. Method II (simplified renormalisation) exhibited some effects, because of the connectivity of the pores in the network, but the predicted changes in the effective medium permeability can be considered negligible. These observations are in stark contrast with the results obtained by the stochastic Method III (KMC), whose results exhibited high sensitivity to the anisotropic distribution of the pores.

The enhanced reliability of Method III is because KMC allows fluid transport to occur along both x and y directions.

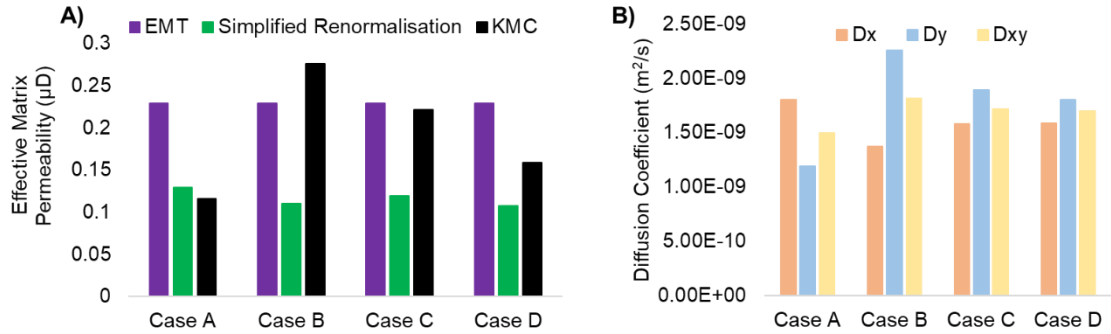


Figure 4. 15: Effective matrix permeability calculation using the three methods for networks with varying anisotropy (left) and diffusivity analysis in the x and y directions and the xy plane (right).

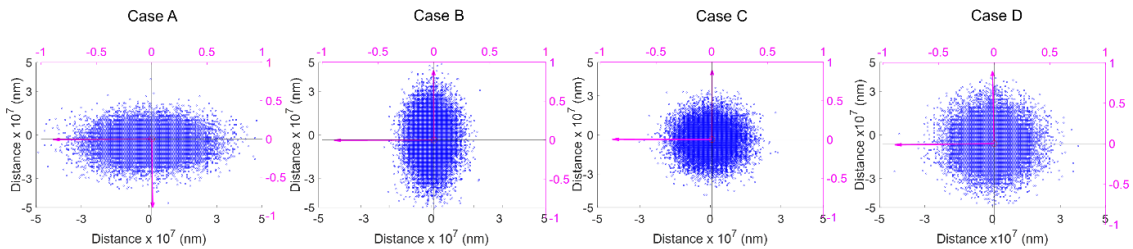


Figure 4. 16: Covariance matrix analysis of the anisotropic networks. Black x-axis shows the first principal component and the black y-axis the second. The purple arrows are vectors showing the preferential diffusion direction.

For the Figure 4.6 – Case B pore network, the voxels containing the micropores were aligned in the y direction, resulting in Method II predicting lower permeability than that predicted by Method III. For the KMC simulation, the vertical bars formed by voxels containing micropores added a kinetic barrier to the system, resulting in the fluid molecules diffusing through the network and physically “avoiding” the low-permeability pathways. Because the micropores were aligned along the flow direction, the fluid molecules were not forced to pass through them, as opposed to the situation represented

by the network presented in Case A where Methods II and III predicted similar permeability. Further, the results obtained demonstrate that Methods I and III are in good agreement for Case C, which is expected, because the pore network considered in this representation is homogeneous. The lowest matrix permeability predicted with the KMC approach corresponds to the Case D network in Figure 4.6. For this system, both x and y directions exhibited anisotropy; however, 2% by volume of mesopores were surrounded by micropores, and therefore contributed little to the matrix effective permeability. While KMC was able to account for this effect, both Methods I and II failed to do so.

According to the diffusion coefficient calculated on the xy plane (see right panel of Figure 4.15), the following trend was observed, exhibiting the diffusivity in descending order: Case B > C > D > A. For the diffusion coefficient calculated along the y direction, the same trend was observed. The effective matrix permeability calculated by the KMC method agrees with this order; however, note that considering the diffusion coefficients alone can lead to false predictions. For instance, the bars corresponding to Cases C and D in Figure 4.15, right, were similar; however, the corresponding KMC-predicted matrix permeability significantly varied because of the isolated mesopores identified in Case D. Covariance matrix analysis was unable to capture this difference, as can be seen in Figure 4.16. The results for Cases A and B highlight the anisotropy on the x and y direction, respectively, while Cases C and D resemble almost isotropic patterns. These observations were confirmed by the molecular trajectories and the % of difference for eigenvalues (Figure 4.16) calculated to be 51%, 64%, 16% and 13% for cases A, B, C, and D, respectively. It is evident that both diffusivity coefficients and covariance matrix analysis are not able to predict the low network connectivity represented by Case D.

Finally, it should be pointed out that predictions obtained by Methods I and II could be improved, especially for the case of anisotropic networks, by implementing formulations of Methods I and II specifically derived to model anisotropic systems. For example, the Smooth Field Approximation could be applied to enable the EMT to account for the

concentration difference imposed.^{72,206} Further developments have been proposed to modify Methods I and II and enable them to predict the properties of anisotropic networks.^{217–220} Implementing these approaches is beyond the scope of this work, which is to quantify the deviations of Methods I and II when applying them to heterogeneous and/or anisotropic pore networks, against the stochastic approach. It should be acknowledged that while in the networks considered here anisotropic features were introduced by design; in realistic networks it is not always possible to understand whether the pore networks are heterogeneous or anisotropic, because often only 2D visualisations such as those of Figure 4.7 are available.²²¹ Under such circumstances, deciding whether to implement deterministic approaches becomes complex. Because the results obtained are expected to be more likely applicable to practitioners, Methods I and II were implemented in their original formulation, with understanding that existing and more appropriate deterministic models could be applied to better capture the anisotropy and heterogeneity of the investigated systems.

Permeability estimation for a shale sample

The insights obtained in terms of the reliability of deterministic and stochastic methods are focused on model problems and well-defined networks; hence, realistic networks need to be examined in order to assess the applicability of the three methods to samples of industrial interest, which consist of an organic and inorganic constituent randomly configured. To obtain the effective organic, inorganic, and matrix permeability the methodology described in subsection 4.1.4.4 was followed.

Figure 4.17 shows a sample of the organic (left), inorganic (middle), and matrix networks (right) generated stochastically. The left panel shows the permeability distribution within the organic matter, middle shows permeabilities assigned with the inorganic matter, and right reports a matrix network considered. For the latter dual-permeability network, the orange blocks represent organic matter and the purple ones the inorganic pores.

Tables 4.4 and 4.5 show the permeability prediction results obtained and the experimental data for the Eagle Ford formation. Note that the experimental permeability strongly depends on the conditions selected (temperature and pressure).

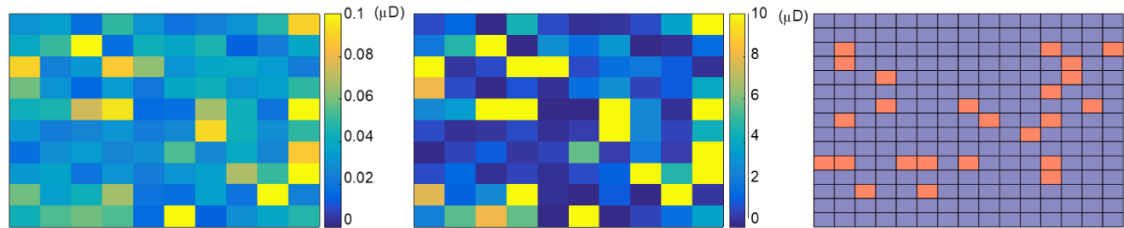


Figure 4. 17: Example of the permeability distribution within the organic matter (left), permeability distribution of the inorganic matter (middle) and the distribution of organic matter in the inorganic matrix (right). The colour bars represent permeability coefficients in μD .

Table 4. 4: Permeability calculation of the organic and inorganic matter, and the effective network permeability using EMT, simplified renormalisation and KMC methods. Error bars for matrix permeability calculation for Methods I and II are based on the minimum, maximum and average permeability using Eq. (4.18). The uncertainty assigned to the KMC calculation represents the confidence interval (99.9%).

Methods	Organic	Inorganic	Matrix
EMT	$0.05 \pm 0.01 \mu\text{D}$	$2.5 \pm 0.13 \mu\text{D}$	$1.46 \pm 0.03 \mu\text{D}$
Simplified renormalisation	$0.05 \pm 0.01 \mu\text{D}$	$1.43 \pm 0.07 \mu\text{D}$	$0.38 \pm 0.02 \mu\text{D}$
KMC	$0.08 \pm 0.02 \mu\text{D}$	$1.56 \pm 0.35 \mu\text{D}$	$1.11 \pm 0.15 \mu\text{D}$
Experiments	N/A	N/A	$0.1-0.6 \mu\text{D}^{50,222,223}$

As expected from the previous observations for broad log-normal PSDs (Figure 4.11), EMT over-estimated the permeability for the inorganic constituent compared to both Methods II and III. However, for the organic component, all three methods agree, because the PSD is narrow. For the matrix permeability, the EMT predicts the largest

permeability, simplified renormalisation predicts the smallest, and KMC predicts a value that lies between those from the two deterministic methods.

The matrix permeability predicted is compared against the values reported by Naraghi et al.,¹⁰² for the same SEM image. Using Method II with 40 stochastic configurations, those authors predicted the permeability to be 0.28 μD ; implementing the same approach, an effective matrix permeability of 0.38 μD was calculated instead. The difference might be because of the slightly higher mean values (μ) assumed in for the organic and inorganic PSDs in this study, the reduced number of configurations considered, or the methodology followed to calculate separately effective organic and inorganic permeability before characterising the dual-permeability network. However, the two predictions can be considered proximate.

More importantly, the predicted matrix permeability is compared against experimental data. While varying the confining stress applied to an Eagle Ford plug sample, Peng and Locks measured permeabilities between 0.1 and 0.6 μD ;²²³ other experimental studies^{50,222} report values within the same range. The effective matrix permeability predicted using Method I was significantly larger than these values, while Method II yielded a reasonable estimate (0.38 \pm 0.02 μD). For the networks considered for Figure 4.17 (right), the KMC prediction deviated substantially from experimental data and multiple reasons could explain this. For instance, in the model implemented, the rock porosity was considered constant (10%) over the 10-network ensemble, while, in reality, this is a variable quantity and is generally less than 10%. Adsorption phenomena were not considered, but only Knudsen diffusivity was accounted for. The analysis performed is based on a single SEM image, which exhibits low anisotropy. It is possible that the sample used for the experiments was anisotropic, while only an average permeability value was reported.³⁶ Because the KMC approach is affected by assumptions made about network connectivity and anisotropy, these simplifications might have affected the KMC predictions.

Further, it is possible that the deviation between KMC predictions and experimental data is because of the underlying assumption about the pore networks. So far, the assumption that the narrow pores (1-10 nm) in the shale sample correspond to organic matter micropores was followed, attributing the larger pores to the inorganic matter. This assumption might not be realistic; actually, recent absorption studies on clays demonstrate that the inorganic constituent comprises pore sizes of 1 to 10 nm.²²⁴ Loucks et al.,²²⁵ reported that organic matter particles generally range between 5 and 75 nm in length. Taking these observations under consideration, the permeability coefficients in Table 4.4 were used, as calculated by the KMC method, to generate networks where the organic matter is the high-permeability component (1.56 μD), and the inorganic matter the low-permeability one (0.08 μD). The effective matrix permeability calculated from 10 independent stochastic simulation runs using 10 different configurations with the KMC method yielded an effective matrix permeability of 0.36 μD with a confidence interval of ± 0.15 μD (Table 4.5). This falls within the experimental range of permeability reported, suggesting that the stochastic KMC approach could be a viable option for predicting permeability of shale rock samples. It is expected, however, that 3D representations of the model will be much more reliable. For completeness note that Table 4.5 shows that Methods I and II also predict permeability values that are consistent with the experimental observations. This is not unexpected, considering that Figure 4.7 suggests that the shale sample considered here is rather isotropic. A more stringent discrimination among the three methods could be attained when data for an anisotropic sample are available. Moreover, the results obtained show that despite the heterogeneity of the systems (organic, inorganic, dual-permeability network) using 10 realisations for the KMC model can provide effective network permeability with confidence intervals that is within the range of the experimental data, when the organic matter is considered to be the high-permeability component.

Table 4. 5: Permeability calculation of the organic and inorganic matter, and the effective network permeability using EMT, simplified renormalisation and KMC methods. The organic matter is the high-permeability component. The uncertainty assigned to the KMC calculation represents the confidence interval (99.9%).

Methods	Organic	Inorganic	Matrix
EMT	2.5±0.13 μD	0.05±0.01 μD	0.29±0.02 μD
Simplified renormalisation	1.43±0.07 μD	0.05±0.01 μD	0.15±0.01 μD
KMC	1.56±0.35 μD	0.08±0.02 μD	0.36±0.15 μD
Experiments	N/A	N/A	0.1-0.6 μD ^{50,222,223}

A Kinetic Monte Carlo study to investigate the effective permeability and conductivity of microfractures within unconventional reservoirs – Part II

Abstract

Estimating the effective permeability and microfracture (MF) conductivity for unconventional reservoirs can be challenging and Part II of this chapter investigates the potential of the stochastic approach to provide a possible solution. The KMC method, used to estimate the matrix permeability of a shale sample in Part I, is now implemented to evaluate the unpropped and propped MF conductivities during laboratory testing. During those experimental procedures, MFs were propped with ultrafine particles (UFPs). KMC simulations form the basis of the method used to estimate effective permeability of the system. The KMC approach is used to evaluate the effect of various parameters influencing the conductivity of laboratory-created MFs. The case studies considered investigate the conductivity improvement of a manmade MF as a function of the MF width, the UFP (proppant) concentration, and the leakoff area widths. The leakoff area is due to the UFP flow perpendicular into a secondary or adjacent MF zone (2nd MF) penetrating the face of an opened MF during flow testing under stress. For the laboratory-prepared non-propped and propped MF samples, the effective MF width was determined to have the greatest effect on the MF conductivity, which increased by two orders of magnitude in the presence of the UFPs. The remaining two factors—proppant concentration and length of 2nd MFs—helped improve the effective MF conductivity in a linear manner. Insights obtained from this study can be used to optimise fracturing designs by including UFPs and to create strategies for maximising hydrocarbon recovery during development of unconventional resources where MFs are opened during stimulation treatments.

Introduction

Unconventional resource plays, particularly resource shales, development has grown significantly during the previous ten years. Although production from shale gas began in the 1820s⁶⁰, the interest and scale of investment has only increased substantially during the previous decade. The US Energy Information Administration (EIA) estimates that during 2017, approximately 16.86 trillion cubic feet (Tcf) of dry natural gas was produced from shale resources within the US, which was approximately 62% of the total US dry natural gas production, while approximately 4.67 million barrels of crude oil per day (BOPD) were produced directly from shale (tight) oil resources within the US, which was approximately 50% of the US crude oil production.⁷ This production increase has been fuelled using horizontal well drilling and hydraulic fracturing. Compared to conventional reservoirs, unconventional reservoirs are typically characterised as highly anisotropic, heterogeneous, and highly laminated, having ultralow permeability, and containing varying quantities of natural fractures.^{226,227} Taking advantage of these resources despite these challenges, increasing the fracture-to-shale contact area, referred to as “fracture complexity”, is essential for successful developments of unconventional reservoirs.⁶⁰ Fracture complexity results from interactions of hydraulic fractures with natural fractures, MFs, bedding planes, faults, and pre-existing planes of weakness within the rock matrix. Characterising natural fractures, MFs, and planes of weakness can often be extremely difficult, considering their heterogeneity.²²⁸ Natural fractures can be closed or mineralised – plugged, can provide planes of weakness, and are rarely productive until opened and connected with a hydraulic fracture.⁶⁰ When opened and connected, Gale²²⁹ observed that flow through natural fractures at higher stress levels is much larger than through induced fractures because natural fractures tend to be much stiffer than induced fractures. Therefore, creating, exploiting, and accessing these complex fracture systems could potentially be the difference between an economic and uneconomic well. To take advantage of fracture complexity, it is important to understand the distribution and characteristics of the natural fractures, MFs, faults, and bedding planes and how

they affect the overall effective permeability of the reservoir. Studies demonstrate that these natural fractures and induced MFs vary in widths from as little as 1 to approximately 10 microns and lengths between 10 and 250 microns.^{96,230,231} Many natural fractures and MFs are left unpropped, due to their size, which is undesirable. This challenge caused the development of the UFPs implemented in this study, developed to access the MFs.²³² These UFPs have sufficient mobility to access the MFs without bridging or settling out and sufficient strength to withstand high-closure stresses. Calvin et al.,^{227,233,234} and Nguyen et al.,²³⁵ documented successfully the use of the developed UFPs in field applications.

During a field study, 11 wells were treated from three different drilling pads where direct offset wells on each pad were used for comparison.²³⁶ Figure 4.18 shows the normalised cumulative production observed in this study, comparing wells treated with and without UFPs. For this example, only a small quantity of UFPs was included at the pad fluid segment of each fracturing stage, yet the results demonstrate a marked improvement with cumulative production. The change in character between the gas and oil cumulative production curves was a result of condensate dropout, as this was a retrograde condensate reservoir.²³² Changes in relative permeability because of condensate dropout caused the flattening of the condensate cumulative production, but a significant increase for total condensate cumulative production between the wells treated and not treated with UFPs is the result of significantly more exposed fracture surface area resulting from the UFPs.

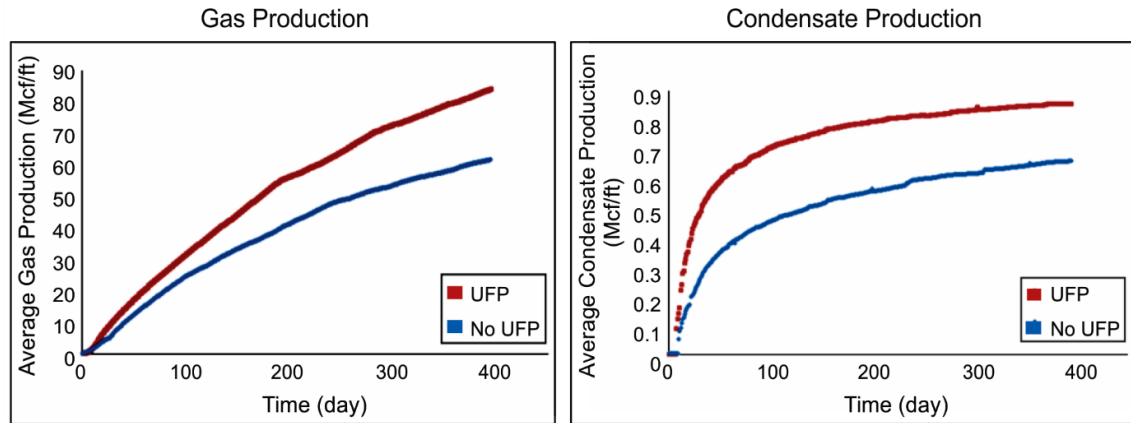


Figure 4. 18: Results of UFPs within the condensate portion of the Barnett Shale field that exhibit normalised cumulative production for an 11 well program on three pads using direct offset wells for comparison; UFPs were used for 5 of the 11 wells. Reproduced by Dahl et al.²³⁶

A production history match was performed on two direct offset wells: one with and one without UFPs. A comprehensive earth model was created within this region, making it possible to map reservoir quality and create probable distributions of natural fractures based upon image logs run and interpreted for each horizontal well within the region. This information was used to create a fully compositional reservoir simulator with unstructured gridding to perform production history matches (see Figure 4.19). For this case, a good history match was achieved on these two wells by simply including the natural fractures within the well where UFPs were used and not including conductive natural fractures within the well where UFPs were not used. The additional increase for the UFP well is attributed to using UFPs compared to the well without UFPs.²³²

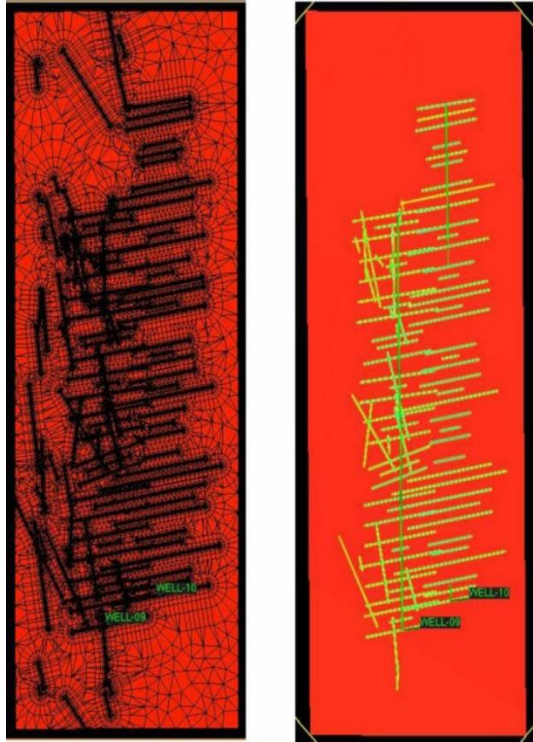


Figure 4. 19: Reservoir setup for production history matching and analysis for two direct offset wells: Well 9 with UFPs and conductive natural fractures and Well 10 with no UFPs and no conductive natural fractures. (Left) unstructured gridding used for the simulation; (right) pressure distribution within the reservoir after 242 days. Reproduced by Dahl et al.²³⁶

From the promising field result observed, it was theorised that additional work was essential to understand natural fractures and MFs and the effect of UFPs on the conductivity of natural fractures and MFs. This study presents a method for estimating the effective permeability and MF conductivity in unconventional reservoirs using the developed 2D KMC model, described in Part I of this chapter. Fluid transport is a three-dimensional (3D) process; however, for computational efficiency purposes, the 3D space is often assumed to be a collection of identical two-dimensional (2D) slices, and this implementation is followed in this work.

Materials and methods

To estimate the permeability and conductivity of MFs, the workflow was divided into two complimentary parts: laboratory and modelling work. The laboratory work, performed by Halliburton's flow enhancement team, consisted of performing a series of tests to

determine the effects of UFPs on the conductivity of MFs. Concurrently, the modelling work, performed by me, focused on developing a model to estimate the permeability of systems containing propped or unpropped MFs. Results from the laboratory work were used to validate the computational model and evaluate the effect of various parameters on the effective permeability and conductivity of the MFs.

Laboratory sample preparation

Outcrop samples from Eagle Ford and Marcellus formations were used by preparing 1 in. diameter cores for the laboratory experiments. The cores were cut into a 2 in. length sample and then cut lengthwise into two halves using a saw and oil to replicate a MF. (Saw and oil were used to reduce variability for surface asperities and to help prevent damage to the core from water exposure while cutting the core.) After splitting the core, the two halves were realigned along their axial edges to help ensure perfect alignment with the small saw mark grooves formed during processing, and a perfluoro-alkoxy polymer resin tape around the core reinforced their placement. The core halves were properly labelled to indicate top and bottom as well as left and right.

After sample preparation, the (unstimulated) core was installed into the conductivity measurement core system to determine the initial conductivity of the crack between the reassembled core halves. The closure (confining or annular) pressure on the core was slowly increased from 1,000 to 2,000 psi and then by 2,000-psi increments until 8,000 psi was reached (outlet backpressure was set to 500 psi). Conductivity or effective permeability measurements were determined at each confining pressure using an aqueous solution of a 1-gal/1,000-gal clay control additive, and all initial conductivity measurements were performed at room temperature.

After initial conductivity of the (unstimulated) split core was determined, the core was disassembled, and one of the faces of the two halves was treated with a solution containing a predetermined amount of UFPs to be studied (see Figure 4.20). To treat the core face, the two halves were placed on a flat surface and positioned side by side, flat surface facing up. UFPs were placed into a test vial and suspended within acetone,

forming a slurry. The test vial was manually swirled, and the slurry was transferred by bulb syringe to the core to treat one fracture face. During transfer, the acetone was periodically allowed to dry to help prevent the UFPs from spilling over the edge. Care was taken that all UFPs were transferred from the test vial onto the fracture face to help ensure an accurate UFP concentration was represented. Once all UFPs were transferred to one of the core halves and acetone evaporated, they were carefully reassembled and wrapped in perfluoro-alkoxy polymer resin tape.

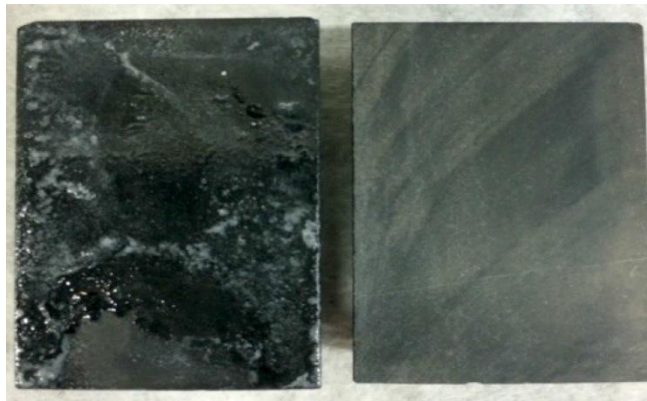


Figure 4. 20: Sawed Marcellus core after one half was treated with 0.001 lbm/ft² of UFPs. Reproduced from Inyang et al.²³⁷

The treated core was then reinstalled into the core system to determine final conductivity or effective permeability of the MFs stimulated with a known amount of UFPs. The confining pressure on the core was slowly increased from 1,000 to 2,000 psi and then by 2,000-psi increments until 8,000 psi was reached (backpressure was set to 500 psi). Conductivity measurements were determined at each confining pressure using an aqueous solution of a clay control additive (1-gal/1,000-gal), and all final conductivity measurements were performed at room temperature.

Methodology used to determine the effect of fracture width

To investigate the effect of fracture width on permeability, a 11 × 10 lattice consisting of 1-mm square voxels was considered. Figure 4.21 shows an induced fracture,

representing a MF that was formed vertically and can potentially channel proppants, placed at the middle of the lattice.

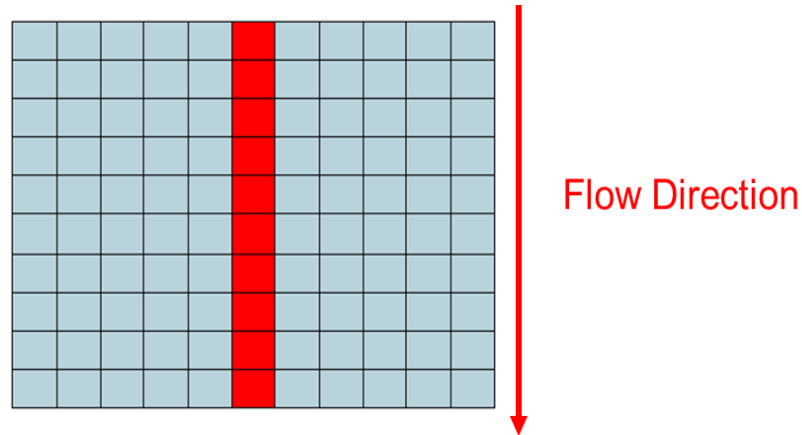


Figure 4. 21: 11 × 10 × 1 mm KMC lattice; each lattice voxel is 1 × 1 × 1mm. The cyan voxels represent the low permeability rock matrix and the red ones an induced MF. Permeability of the cyan voxels (refer to Table 4.5) is calculated following the previously described process. Reproduced from Inyang et al.²³⁷

Shortly after the fracture has been generated within the field, it is expected to be relatively wide, yielding high conductivity. Because of the stress applied within the formation, the fracture is expected to shrink over time; thus, different MF widths (w_f) were explicitly considered and investigated, including 0.5, 0.1, 0.01, and 0.001 mm. The permeability of the red voxels in Figure 4.21, which correspond to areas within the fracture, was calculated by Eq. (4.23), inspired by Buckingham's equation for flow through slit fractures. Eq. (4.23) was applied to each red square voxel individually, with the understanding that it is a simplification and could be replaced by a more appropriate and complex model:

$$k_{\text{fracture}} = \frac{w_f^2}{12} \quad (4.23)$$

Methodology used to determine the effect of UFPs concentration

During a hydraulic fracturing treatment, a mixture of water, chemicals, and proppants are injected; in a resource shale rock, this will often generate MFs. After the MFs have been generated, UFPs are pushed and channelled to the created 2nd MFs within the rock, due

to the pressure build-up. Figure 4.22 shows the lattice used to simulate the effect of the proppant concentration on the permeability improvement. The cyan voxels represent the rock matrix, the red voxels represent induced MFs, and the yellow regions exhibit the 2nd MF zone. The effect of proppant concentration on permeability was quantified by considering a specific 2nd MF zone of 1 mm and a homogeneous proppant distribution. The fracture width was 0.01 mm, and the rock matrix permeability was 0.36 μD (refer to Table 4.5).

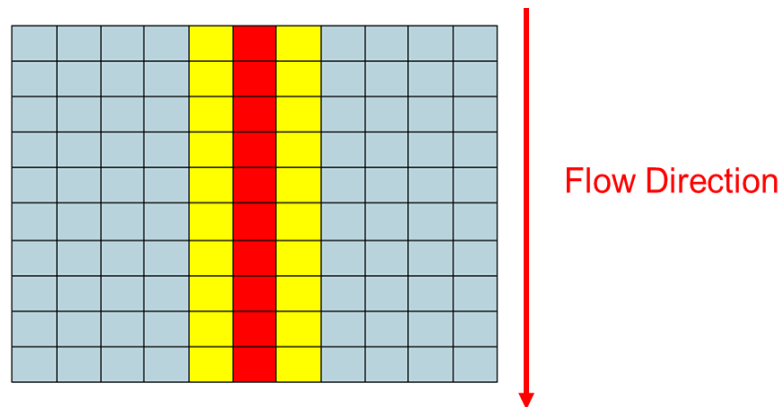


Figure 4. 22: KMC lattice used to investigate the effect of the proppant concentration. The blue voxels represent the rock matrix, the red voxels represent the induced MFs, and the yellow regions are 2nd MFs where proppants were homogeneously distributed. Reproduced from Inyang et al.²³⁷

The proppant concentration within the yellow regions is a parameter difficult to measure and monitor experimentally. To simulate the presence of proppants in the 2nd MFs within the rock matrix, the conceptual model from Figure 4.23 was considered.

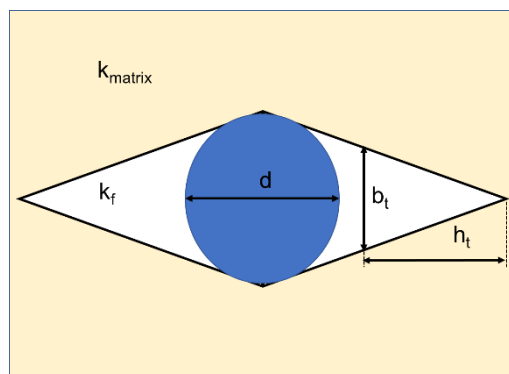


Figure 4. 23: Conceptual model used to represent the effect of a single proppant particle (blue sphere) within a compact rock matrix, where h_t is height and b_t is the base of the generated triangle corresponding to void space. Permeability of the void space and the compact rock matrix are denoted as k_f and k_{matrix} , respectively. Reproduced from Inyang et al.²³⁷

A proppant particle or small number of proppant particles can create a void space resembling a triangle with height h_t and base b_t . Assuming d is the diameter of proppant $h_t = d$ and $b_t = 0.7d$, the open area generated by an isosceles triangle is $A = 0.35d^2$. Because each voxel is $1 \times 1 \times 1$ mm, the maximum proppant concentration that could be accumulated within the leakoff zone was calculated. The proppant diameter was 50 μm , and the maximum proppant concentration per voxel was calculated to be 7 proppants/ mm^2 . For the purpose of this study, three proppant concentrations were considered: low (1 proppant/ mm^2), medium (4 proppants/ mm^2), and high (7 proppants/ mm^2). The total void area generated because of the proppants was calculated, and the square root of the value was used to represent the overall effective fracture width (w_f) maintained by the proppants. This assumption allowed the simplification of the complex proppant-MF system. Instead, the void area, maintained by the presence of the proppants, was considered to be an evident MF of effective width w_f , where fluid flow was unobstructed and non-tortuous. The permeability of these induced microfractures was calculated using Eq. (4.23). Figure 4.24 shows the resultant permeability distribution, which depends on the proppant concentration selected, for each system considered.

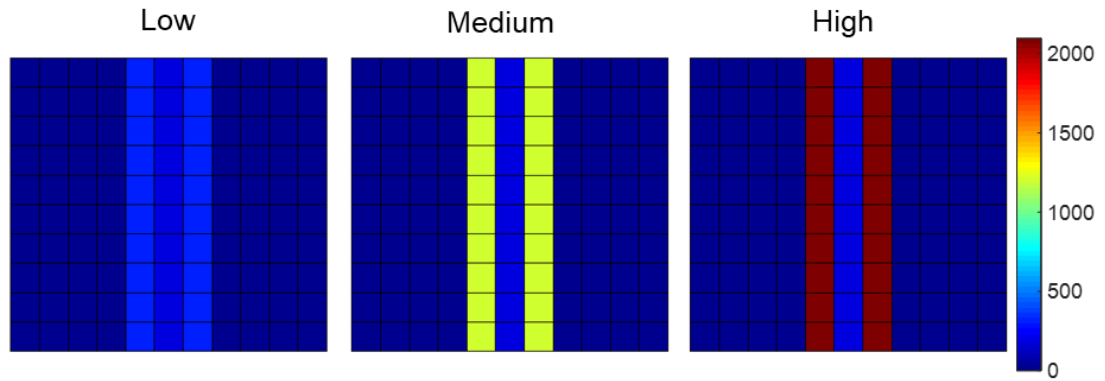


Figure 4. 24: Permeability distribution for the three systems considered. The colour bar displays the permeability in μD . For all three systems, an induced MF with uniform permeability is included. Reproduced from Inyang et al.²³⁷

Methodology used to determine the effect of the 2nd MF Zone.

Depending on pressure and velocity, fracturing fluid is injected, proppant particles can be transferred along different horizontal lengths inside the rock matrix. Therefore, perpendicular to the initially created propped MFs, some 2nd MFs can be formed; this region is termed 2nd MF zone. To investigate the effect of the 2nd MF (propped or unpropped) zone on the achieved permeability, three cases (Zones A, B, and C) were considered, as presented in Figure 4.25. Zone A extends 1 mm on both sides of the induced fracture, Zone B extends 2 mm, and Zone C is 3 mm in length on both sides of the primary MF fracture. The proppant concentration considered for these calculations was medium (4 proppants/ mm^2).

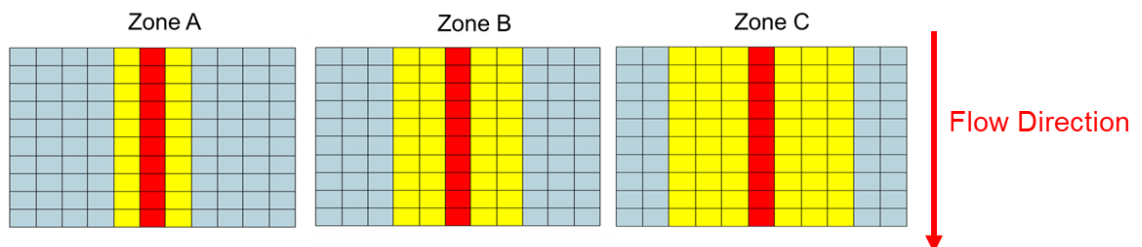


Figure 4. 25: Schematic of the three systems used to quantify the effect of the leakoff zone on the achieved permeability. Reproduced from Inyang et al.²³⁷

Representation of the experimental set-up in the KMC lattice

Analyses described provide insight on the impact of fracture width, proppant concentration, and the leakoff zone on the achieved permeability. Such insights can be used to optimise fracture design and/or proppant treatment technologies. However, a workflow that evaluates the performance of proppants when tested on actual samples is necessary. This section describes a proposed modelling approach to interpret the experimental testing data described in the fracture conductivity results section.

The first goal was to model the relationship between permeability and fracture width using an $11 \times 10 \times 1$ lattice consisting of $1 \times 1 \times 1$ mm voxels, similar to how Figure 4.21 was implemented. Additionally, seven fracture widths—0.001, 0.003, 0.006, 0.01, 0.03, 0.06, and 0.09 mm—were considered, and fracture permeability was calculated for each fracture width using Eq. (4.23). This permeability coefficient was assigned to all red voxels of Figure 4.21. It is widely accepted that even when low conductive fractures are introduced for ultralow permeability rock masses, the flow through fractures dominates. To test this assumption, eight matrix permeability values were considered for each of the seven fracture widths, resulting in a total of 56 KMC simulations. The matrix permeabilities considered were 0.05, 0.1, 0.5, 1, 5, 10, 50, and 100 μD . At the end of each simulation, the permeability obtained against the logarithm of the ratio of fracture width and matrix area was plotted, and a nonlinear regression for the two properties was performed. Next, the fitted equations were used to interpret experimental data and propose an empirical relationship between the MF width maintained and the MF conductivity measured.

Results and discussion

Fracture conductivity results

Figure 4.26 shows the comparison of experimental conductivity data for MFs of Eagle Ford and Marcellus cores (taken from outcrops) with and without UFP treatment. The

current study demonstrated that regardless of the formation and its properties, MFs stimulated with UFPs at a concentration as low as 0.001 lbm/ft² are more conductive compared to unstimulated MFs (control).

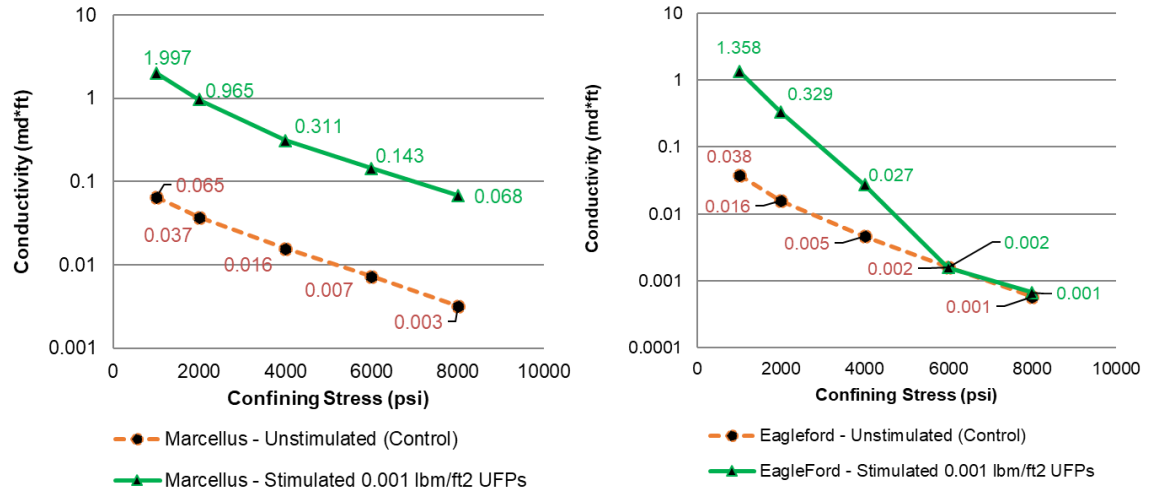


Figure 4. 26: Conductivity of MFs prepared from Marcellus (left) and Eagle Ford (right) cores with and without 0.001 lbm/ft² of UFP treatments.

Both Marcellus and Eagle Ford UFP-stimulated cores yielded two orders of magnitude higher conductivity compared to corresponding fractured but unstimulated cores. It is evident that there are differences to the degree of conductivity of MFs across different formations, which can be attributed to formation anisotropy, mineralogy, and rock mechanical properties.²³² However, because UFP performance on the conductivity of MFs for these cores resulted in increased conductivity, then it is important to keep these MFs open to contribute to the overall production of the reservoir. The results were incorporated within the KMC model along with proppant width and proppant in the 2nd MF zone.

Effect of fracture width

Table 4.6 shows the effective rock permeability measured while considering four fracture widths. For comparison purposes, the unfractured effective matrix permeability is included in Table 4.6. As expected, the presence of MFs creates a highly conductive

pathway for the gas molecules, resulting in a significant matrix effective permeability increase. Larger fracture widths result in a higher fracture permeability.

Table 4. 6: Effect of fracture width on effective matrix permeability

Fracture Width (mm)	Permeability (μD)
No fracture	0.36
0.001	2.77
0.01	26.52
0.1	265.48
0.5	1353

Effect of UFPs concentration

Table 4.7 shows the modelled results obtained and the effective permeability achieved without proppants for comparison. While permeability improves as the proppant concentration increases, the percent (%) increase achieved is significantly lower when compared against the model-calculated effect of fracture width from Table 4.6.

Table 4. 7: Effect of proppant concentration on permeability achieved.

Proppant Concentration	Permeability (μD)
No proppant	26.52
Low	28.96
Medium	37.08
High	70.53

Effect of secondary and/or adjacent MF (2nd MF) zone length

Table 4.8 shows model-calculated permeability achieved while considering Zones A, B, and C. Longer 2nd MF zones result in higher domain permeability; however, similarly to

the effect of proppant concentration, this factor's impact is moderate compared to the impact of fracture width.

Table 4. 8: Effect of the leakoff zone on permeability achieved.

2ndMF Zone	Permeability (μD)
Zone A	37.08
Zone B	40.80
Zone C	42.61

Proposed relationship for MF width and conductivity

The matrix permeabilities considered for the modelling approach are listed in subsection 4.2.3.5. The maximum percent difference for the calculated overall (rock mass and fracture) permeability was determined to be 3.6% when matrix permeability was considered to be 50 and 100 μD . This illustrates that considering matrix permeabilities approximately four orders of magnitude different will result in an extremely small difference of the overall calculated permeability. This is expected, considering that the permeability of the fractures is significantly higher compared to rock matrix permeability; therefore, transport through the fractures is dominant.

Figure 4.27 shows a typical plot obtained when considering rock mass permeability of 50 nD. The plot exhibits permeability calculated using the KMC method in μD as a function of the fracture width considered. During the experimental measurements, samples of different dimensions can be tested. With the computational approach, the matrix area should be factored to help ensure consistency between theory and experiments. Therefore, the KMC calculations were reported as per rock matrix area, making the obtained permeability-width relationships applicable, when core samples of varying dimensions are considered. In Figure 4.27 the term area corresponds to the rock mass area of the KMC lattice (cyan voxels).

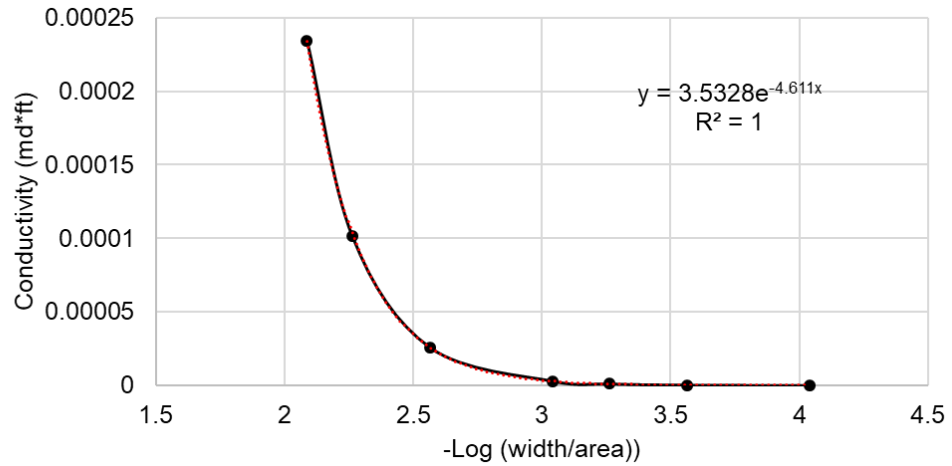


Figure 4. 27: Relationship between the fracture width maintained and the conductivity achieved for the case of 50-nD matrix permeability.

Analysis from Figure 4.27 was performed for all conductivities, and eight equations in total were obtained of the form $y = ae^{bx}$, where y represents the conductivity in md*ft, x the negative logarithm of the ratio width/area, and a and b are fitted constants with values $a = 3.5328$ and $b = -4.611$. These fitted constants do not have an implicit physical meaning and depend on the dataset used. However, they are utilised in order to predict the effective permeability as a function of the fracture width in the calculations that follow. All eight equations, derived using the KMC model, were used to analyse the conductivity values measured experimentally and to calculate the effective width maintained during the experimental procedure. The eight effective fracture widths calculated were used to obtain the average effective fracture width and calculate the corresponding error bars. Consequently, this methodology was then applied to the laboratory experimental data obtained for an Eagle Ford and a Marcellus sample before treatment (U) and after treatment (T) (refer to Figure 4.26 for further details); Figures 4.29 and 4.30 summarise the results, respectively.

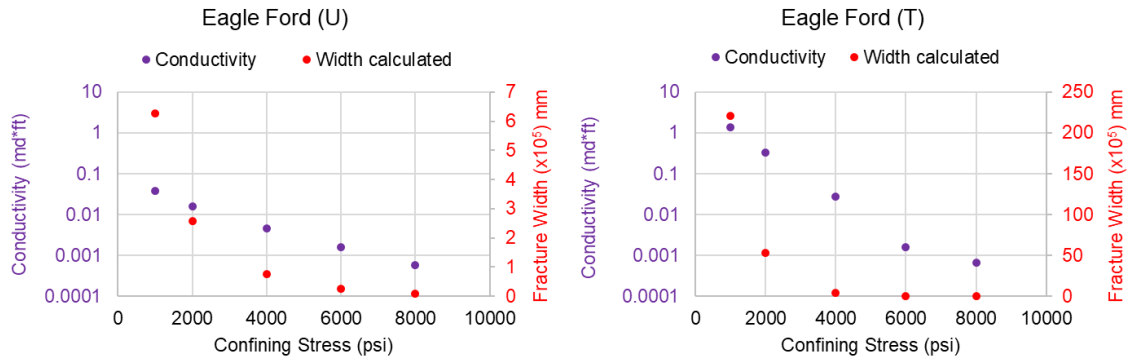


Figure 4. 28: Effective fracture width calculated for the untreated (U) and treated (T) Eagle Ford sample as a function of the confining stress experimentally applied. Purple represents the experimental data, and simulation results are red.

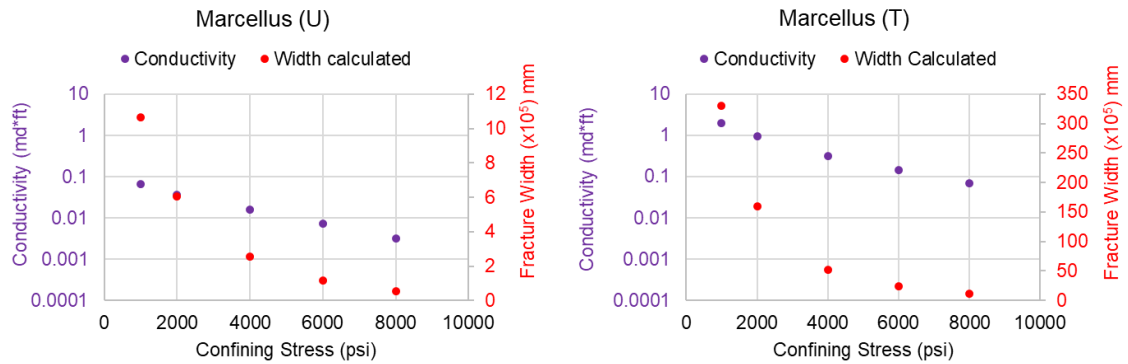


Figure 4. 29: Effective fracture width calculated for the untreated (U) and treated (T) Marcellus sample as a function of the confining stress experimentally applied. Purple represent the experimental data, and simulation results are red.

From the interpretation of these charts, it is apparent that Eagle Ford and Marcellus cores with UFP treatment (T) have much larger aperture sizes and therefore have much larger conductivity values at each of the confining stresses tested compared to the Eagle Ford and Marcellus cores having no UFP treatment (U), with the Marcellus cores performing slightly better. These charts provide direct evidence of the correlation that exists between the conductivity of these manmade MFs and their apparent MF widths, which further conveys how effective MF stimulation can significantly impact the overall productivity of a well.

Additionally, note that the conductivity of the manmade MFs appears to degrade linearly with increasing confining stress, whereas the width of the MFs appears to decay exponentially, regardless of UFP treatment. This response suggests that cores of the same outcrop have similar trends in response to increasing the confining stress.

Results of the KMC and the laboratory experiments demonstrate that MF width has the greatest influence on conductivity of the MFs compared to the other two factors investigated: proppant concentration and UFPs 2nd MFs perpendicular to the main MF. When maintaining a higher width, care should be taken to help ensure that UFPs used do not form a complete pack; rather, UFPs should form a partial pack while maintaining a high MF width. Results from a previous work demonstrated that UFPs migrated with leakoff after initial placement to form nodes that enhanced the conductivity of the MFs.^{232,235} Additionally, because the width and conductivities of these MFs can be estimated, these values can be introduced into a reservoir simulator to get improved distribution and properties of the MFs for production matching during reservoir simulations.

Conclusions

The first part of this chapter (Part I) deals with a thorough comparison between three approaches (two deterministic and one stochastic) to assess their ability, when evaluating the permeability of model pore networks. The EMT and simplified renormalisation methods were selected, within their original derivations, as deterministic models because of their simplicity. The results obtained using the deterministic models were compared against the developed 2D KMC algorithm that provided useful transport insights in the studies discussed in Chapter 3 (Part II), which were restricted to 1D pore networks. The pore networks considered in this chapter had varying PSDs; were mainly dual-permeability networks with different % content of micro-, meso-, and macropores; consisted of isotropic and anisotropic configurations; and one realistic network was designed to replicate the cross section of a shale rock sample.

The results obtained in Part I of this chapter both confirm observations from previous studies and provide new insights. The deterministic results were compared against KMC predictions, considering KMC to provide accurate estimations, and narrow log-normal distributions were identified to be ideal for applying the EMT and the renormalisation method. Both deterministic methods were sensitive to small changes in the amount of high-permeability pores rather than changes in the low-permeability ones. For broad distributions, the EMT always overestimated the network's permeability; the simplified renormalisation method provided low estimates because of the zero crossflow assumption while the KMC predictions were between the two. For networks with dual permeability, the simplified renormalisation method was suitable for cases of spatially uniform systems that had equal parts of the low- and high-permeability components. The EMT was suitable for mesoporous systems containing up to 25% of micro- or macropores without generating anisotropy to the flow direction (spatially uniform systems). For all other cases considered in this study, EMT overestimated the matrix permeability.

Based on the case studies considered here, among the approaches implemented, KMC is the most sensitive and reliable method because it responds to changes in both the low- and high-permeability values. For dual-permeability networks, KMC detected changes proportional to the components and provided an estimate that captured the matrix structural features. The most valuable feature of KMC, compared to the deterministic methods considered, is its sensitivity to anisotropy. KMC could be applied to low-connectivity networks and could quantify the effect of small-scale heterogeneities (e.g., local low connectivity). When the KMC was applied to predict the permeability of a shale sample for which one SEM image was available together with data on PSDs, the results were reasonably close to experimental data, when considering the organic matter to be the highly permeable portion of the matrix. The results obtained were also compared against experiments. Note that since there were no experimental data available corresponding to the shale SEM image considered for the computational

studies, literature resources were considered, where laboratory permeability experiments were conducted on Eagle Ford samples. As a result, the experimental permeability range used to compare the computational predictions obtained was broad. For the purpose of this comparative analysis, given the dataset available, using 10 stochastic realisations for the organic, inorganic and dual-permeability networks, the obtained KMC results were reasonably close to the experimental data, when considering the organic matter to be the highly permeable portion of the matrix. However, a narrower experimental range would require an increased number of stochastic realisations to be simulated, to ensure smaller confidence intervals for the KMC method and make the comparison between the two approaches statistically valid, at the expense of the computational resources needed. The method's accuracy can be improved by extending the analysis to more images of a plug sample so anisotropy and local heterogeneities are considered, accounting for the effect of adsorption and the true porosity. The disadvantage of KMC, compared to deterministic techniques, rests with the necessary computing time. The deterministic methods provided results in a few seconds while the computational cost of KMC ranged from minutes to hours.

In the second part of this chapter the KMC was applied to a process of industrial interest. During the hydraulic fracturing process small particles, referred to as proppants, are mixed with the hydraulic fracturing fluid and then injected into the rock formation. The role of proppants is to get channelled through the generated microfractures (MFs) and stay in place to prevent them from closing. The system containing proppants, MFs, and the impermeable rock matrix is very heterogeneous and anisotropic. Based on the study performed in Part I, KMC was found suitable to simulate transport through such systems, and it was therefore implemented to study the effect of proppants in gas transport.

Initially, the KMC model was used to simulate gas flow through synthetic systems. In those systems the effect of MFs width, proppant concentration, and leakoff zone were investigated separately. The results obtained from these systems provided an understanding of how these process design parameters impact the transport of fluids.

The effective MF width maintained was found to be the most important parameter for achieving fast gas transport. In fact, the relationship between the MF width and permeability showed an exponential positive correlation. Note that the permeability calculated corresponds to the system consisting of the low permeability matrix and the inserted MFs. The permeability assigned to the matrix was the value calculated in the first study of this chapter, corresponding to an Eagle Ford shale. The increase in the proppant concentration and leakoff zone were found to improve the permeability of the simulated system, but in a linear manner.

When the proppants are channelled through the MFs made on the rock fabric, all the three investigated parameters are present, enhancing the permeability of the rock. According to the initial analysis, the effect of the MF width has a significantly higher impact on the overall permeability achieved. Thus, it can be assumed to be the controlling parameter. From a design perspective, there are different types of proppants that can be used to treat shale formations. The ultrafine particles (UFPs) used to treat an Eagle Ford and Marcellus samples increased the MF conductivity by two orders of magnitude.

To determine which proppant is suitable for which formation, laboratory tests need to be carried out. Analysis of such experimental data can yield correlations between the MF conductivity improvement, the proppant type and the rock formation characteristics. However, there was no measure to describe the structural effect the UFPs have on the formation, besides post-treatment imaging techniques. To this end, the laboratory data obtained from Halliburton were analysed together with results from 56 KMC runs, and an empirical correlation between the MF conductivity and the MF width maintained due to the presence of the proppants was proposed. This methodology was used as a tool to evaluate the MF width maintained when a certain proppant type was used to treat a Marcellus and Eagle Ford sample. The empirical relationship proposed, derived from KMC and laboratory data, can be used for any formation with matrix permeability between 0.05 and 100 μD to conduct the same analysis.

KMC algorithm extension to 3D; Studies in single pores and pore networks

In this chapter, the KMC model is further extended to 3D and validated against analytical and computational data. The discussion is organised in two parts. In Part I, the developed 3D KMC model is implemented to describe the fluid transport in micro- to meso-scale slit-shaped porous materials. Firstly, it is demonstrated that atomistic molecular dynamics simulations for the self-diffusion coefficient of supercritical methane is reproduced, within a 10% uncertainty, by the stochastic approach. Then, the low computational cost of the KMC method allowed me to address a long-standing question in the porous materials community: at what pore sizes can the transport properties of confined fluids be described by their bulk counterparts? To answer this question quantitatively, slit-shaped pores of 5 different chemistries were considered, demonstrating that the answer is material-specific. In Part II, this new method is demonstrated and validated against analytical and computational results. The method is shown to be applicable in the investigation of fluid transport in pores of varying pore widths using as input molecular dynamics results for narrow pores. The second part of this chapter details the effect of four different pore network characteristics on the diffusivity of gases, while considering 3D pore networks. The characteristics of interest are those that significantly affect the permeability of rocks, namely the porosity, pore network connectivity, the pore throat width and pore chemistry. From the obtained results, recommendations on how possible technological approaches, involved in the hydraulic fracturing design, can be applied to maximise gas extraction are provided. Part I is the outcome of a fruitful collaboration with TAMUQ, who conducted the MD atomistic simulations, and the work is currently under peer review, while Part II is in preparation for submission.

Quantifying pore width effects on diffusivity via a novel 3D stochastic approach with input from atomistic molecular dynamics simulations – Part I

Abstract

The increased production of unconventional hydrocarbons emphasises the need of understanding the transport of fluids through narrow pores. Although it is well known that confinement affects structure and transport of fluids, it is not yet possible to quantitatively predict with confidence properties such as diffusivity as a function of pore width in the range of 1-50 nm. Such pores are commonly found in shale rocks, but also in a wide range of engineering materials, including catalysts. This study proposes a novel and computationally efficient methodology to obtain accurate diffusion coefficient predictions as a function of pore width for pores carved out of common minerals and engineering materials, such as silica, alumina, magnesium oxide, calcite and muscovite. Atomistic molecular dynamics (MD) simulations are implemented to quantify fluid structure and transport properties within 5 nm-wide pores, in particular, the diffusion coefficient within different pore regions. The data obtained for the diffusion coefficient are then used as input to the developed KMC model, developed to predict fluid transport in heterogeneous mesopores. The KMC model is used to extrapolate the fluid diffusivity for pores of increasing width. The stochastic approach is validated against atomistic MD simulation results obtained for wider pores. When applied to supercritical methane as a sample fluid, and for slit-shaped pores, the results suggest that the methodology implemented yields data that are within 10% of the atomistic simulation results, with significant savings in computational time. The proposed workflow, which combines the advantages of MD and KMC simulations, is used to generate a digital library for the diffusivity of gases as a function of pore chemistry and pore width and could be relevant for a number of applications, from the prediction of hydrocarbon transport in shale rocks to the optimisation of catalysts, especially when surface-fluid interactions significantly impact the transport properties.

Introduction

At present, the development and profitability of a shale play depends on its permeability, and computational methods can be implemented to calculate this parameter. The accuracy of such permeability calculations depends on several factors, most importantly on the quality of input data used to generate the pore networks. When implementing lattice-based stochastic or deterministic approaches, the transport properties assigned to the various pores and connections in the pore network must be carefully selected. Due to the significantly small scale of the pores often found in shale formations, but also in engineering materials such as catalysts, atomistic molecular dynamics and Monte Carlo simulations (MD and MC) have been widely used to quantify fluid transport through narrow pores as well as fluid structure and preferential adsorption.²³⁸ The atomistic simulations allow the user to define 1) the chemical composition of the pores, 2) their shape and size, 3) the fluids and mixtures used to fill the constructed pores, and 4) conditions such as temperature and pressure. For example, Sui et al., studied adsorption and transport of methane in dry and water-wet montmorillonite clays and found that the methane self-diffusion coefficient increases rapidly as the pore size increases.²³⁹ Vasileiadis et al., investigated the role of porosity on adsorption and transport of CH₄, C₂H₆, CO₂, and their mixtures, in over-mature type II kerogen under various temperature and pressure conditions.²⁴⁰ Wang et al., investigated the transport of supercritical methane in clay, calcite and organic matter as a function of pore size, pressure, and moisture.²⁴¹ Phan et al., calculated the permeability of methane through 1 nm-wide pores filled with water,⁸⁸ and Bui et al., identified the correspondent transport mechanisms by analysing the free energy landscape within various pores.²¹⁵

Apostolopoulou et al., recently implemented KMC simulations to study fluid transport across pore networks.²⁴² KMC methods can access long time scales (up to ms and in some cases h) and large spatial scales (nm to μm) at comparatively low computational expense.^{146,157} For example, the bottom-up 1D approach discussed in Chapter 3, 1) used

previously-reported MD data to inform the KMC model, 2) simplified a 3D, 2-phase system consisting of liquid water and methane into a 1D problem, and 3) obtained KMC transport data, using the KMC model, in quantitative agreement with atomistic MD simulations at a fraction of the computational cost.¹⁴⁰ The model was extended in 2D to analyse a 2D network, see Chapter 4, which was constructed using imaging data, previously reported, for an Eagle Ford shale sample, as well as PSDs.¹⁰² The transport model of Naraghi and Javadpour was used to assign transport properties to the various pores within the network.¹⁰² The KMC approach was validated both against deterministic models and experimental data. Could a stochastic approach based on the developed KMC model be used to upscale MD simulation results and predict fluid diffusivity in meso-scale pores when results are available for narrow pores?

This study addressed this question by developing a bespoke model that uses MD simulation findings as input to a KMC model framework. Slit-shaped pores are considered, carved out of five solid supports that resemble minerals typically found in the inorganic matter of shale formations. The fluid considered is supercritical methane. The MD simulations are conducted for pores of width 5 nm. Equilibrium NVT simulations yield density profiles, which are used to differentiate 'adsorbed' and 'bulk' methane layers within the pores. Then the diffusivity of methane in such areas is calculated, confirming that in the centre of the pores methane behaviour resembles that in the bulk. The data are used to construct and inform the developed 3D KMC model, which contains 3 distinct regions with substrate-specific transport properties. The stochastic simulations yield the effective diffusivity of methane as a function of pore width. The results are validated by reproducing independent atomistic MD simulations conducted in wider pores. The KMC model is then used to generate a digital library where methane diffusivity is quantified as a function of pore chemistry (within the 5 materials considered here) as well as of pore width (up to ~ 60 nm). Such digital libraries could be used to describe 3D networks consisting of pores with varying chemical compositions and PSDs. This is discussed in Part II of this chapter.

The remainder of this study is organised as follows. Section 5.1.3 describes the methods and algorithms implemented, from the atomistic simulations to the 3D KMC model used to predict diffusivity. Section 5.1.4 discusses the results obtained, from the data produced with atomistic resolution for supercritical methane in the model pores, to meso-scale KMC predictions of diffusivity, which yield the digital library, including the validations conducted. A summary of this study's findings, with a brief overview of possible applications of this bespoke approach, as well as of some of its limitations, are presented in subsection 5.1.4 and section 5.3.

Methodology

A series of equilibrium molecular dynamics (EMD) simulations were conducted to obtain the required input data and validate the developed 3D KMC model using 5 nm and 10 nm slit pores (in one case, a 25 nm pore was also used). This subsection describes, briefly, the models implemented to simulate the solid substrates and the force fields used to model methane and surface interactions. The discussion continues with information regarding the setup of the simulated systems and the algorithms utilised, with particular attention to the development and validation of the stochastic KMC model.

Solid supports

Slit-shaped pores obtained from five model materials: silica, alumina, MgO, calcite, and muscovite were considered. Details about the fabrication of the model materials have been reported elsewhere.^{243–250} All the non-bridging oxygen atoms on silica and alumina surfaces were protonated; MgO, muscovite, and calcite surfaces were not hydroxylated. The latter modelling choice is an oversimplification, as suggested by Bui et al.,²¹⁵ and Phan et al.,⁸⁸ but it allows us to understand, computationally, the effects of fluid-solid interactions on fluid transport under confinement. The substrates have a surface parallel to the X–Y plane of the simulation box. The X and Y dimensions of the substrates are shown in Table 5.1. Each pore was obtained by separating the solid substrates along

the Z direction, which is perpendicular to the X–Y plane. The Z dimension of the simulation box, which includes pore and substrate, is also presented in Table 5.1 for the silica, MgO, alumina, calcite and muscovite pores. These dimensions allowed to maintain the pore width at 5 nm in all the systems considered. To obtain pores with width 10 nm, the Z dimension was increased (see Table 5.1). The pore width was defined as the shortest centre-to-centre distance between surface oxygen atoms across the pore volume. One pore of width 25 nm made of calcite was also considered.

Table 5. 1: Simulation box dimensions used to simulate the 5 nm and 10 nm wide pores using five solid supports.

Substrate	Dimensions in nm			
	X	Y	Z (5 nm-wide pore)	Z (10 nm-wide pore)
Silica	5.20	10.10	8.30	13.30
MgO	5.50	10.40	7.50	12.50
Alumina	5.12	9.12	7.41	12.41
Calcite	4.86	9.00	9.90	14.90
Muscovite	4.73	7.35	8.50	13.50

Force fields

The force fields recommended by Bui et al.,²¹⁵ were implemented in this study. To simulate silica, MgO, alumina, and muscovite substrates CLAYFF was selected, while calcite was described using the force field developed by Xiao et al.,^{251,252} In the calcite substrate, calcium and carbon atoms were kept rigid, whereas the oxygen atoms were

allowed to move freely. In the other materials, silicon, aluminum, and oxygen atoms were held at fixed positions while the surface hydroxyl hydrogen atoms were allowed to vibrate. All atoms in MgO were kept rigid.

The transferable potentials for phase equilibria in the united atom formalism (TraPPE-UA) were implemented to model methane in all solid substrates, except calcite.²⁵³ To be consistent with Bui et al., the OPLS-UA forcefield was used to model methane in calcite.²⁵⁴ Nonbonded interactions were modeled by means of dispersive and electrostatic forces. The electrostatic interactions were described by the Coulombic potential, with long-range corrections treated using the particle mesh Ewald (PME) method.²⁵⁵ Dispersive interactions were modeled by 12–6 Lennard-Jones (LJ) potentials. The LJ parameters for unlike interactions were determined by Lorentz–Berthelot combining rules from the values of like components.^{256,257} The cut-off distance for all interactions was set to 1.4 nm. Long-range corrections were not applied; according to Siperstein et al., consistency in the cut-off radius is more important than the inclusion of long-range corrections to the energy.²⁵⁸

MD simulation set-up and algorithms

The simulation setup for the pores considered in this study mimics the one adapted by Bui et al.,²¹⁵ which was implemented to investigate the transport properties of methane molecules inside hydrated 1 nm-wide micropores. To directly compare results within the five different substrates, the overall methane density was kept constant at 0.01314 atoms/Å³ ~ 0.350 g/cm³ in all substrates investigated. To prepare systems with the desired fluid density, the slit-shaped pores surrounded by a bulk reservoir were simulated within a periodic simulation box. The pressure at the bulk reservoir regions was monitored using the density profiles and the Peng-Robinson equation of state, while simulating different amounts of methane, under the assumption that the methane in the bulk region behaves like a macroscopic fluid. The methane molecules were initially added to the reservoir. As the simulations progressed, some fluid molecules entered the

pore. Once the reservoir pressure for all substrates was constant, the molecules that had entered the five pores were counted. Then the reservoir was removed, and the desired amounts of methane were inserted to the 5 pores. It was necessary to introduce 3450, 3758, 3068, 2874, and 2284 methane molecules in the 5 nm-wide silica, MgO, alumina, calcite, and muscovite pores, respectively. For the 10 nm pores, exactly double the number of molecules just listed was used. For all solid substrates, the simulation box is periodic in the three directions. Thus, the pores are effectively infinite along X and Y dimensions. A representative simulation snapshot for the silica pore is shown in Figure 5.1.

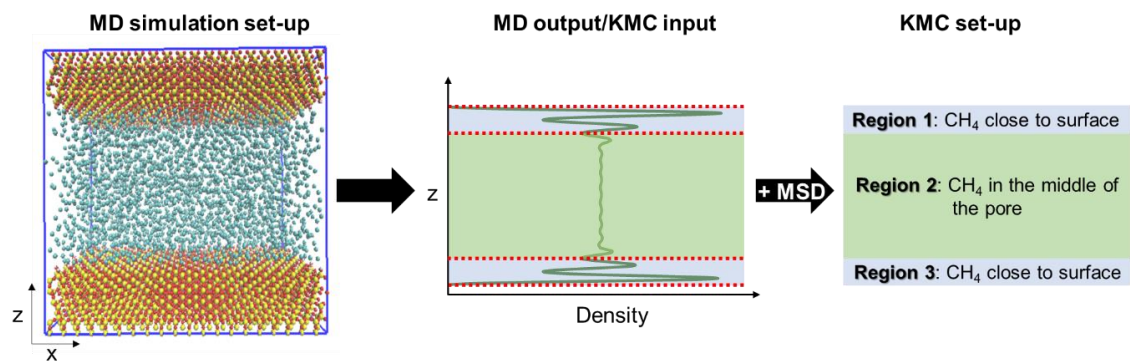


Figure 5. 1: Schematic of the MD simulation set up (left), the criteria for determining the 3 regions that describe the density of confined methane (middle), and a 2D slice of a typical 3D KMC simulation set up (right). In the left panel, for visualization purposes, the solid support is silica. The dashed red lines in the middle panel identify Regions 1, 2, and 3, and serve as guides to the eye.

EMD simulations were performed in the canonical ensemble (NVT) by maintaining constant number of particles (N), simulation volume (V) and temperature (T), using the package GROMACS, version 5.1.1.^{259,260} The temperature was kept constant at 300 K using 3 Nose-Hoover thermostats with relaxation time 100 fs.^{261,262} Two thermostats were used to control the temperature of the top and bottom solid surfaces, and one to keep the temperature of the methane constant. The leapfrog algorithm was used to solve the equations of motion with 1 fs time step.²⁶³ To equilibrate the systems, one NVT equilibrium simulation was conducted for 50 ns for each solid substrate. To confirm that equilibrium was reached, the convergence of methane's density profile was tested in

each system along the Z direction. Then, 3 ns NVT production runs were performed at 300 K for each system to collect our data. Following the same simulation protocol, 3 independent bulk methane simulations using 1638 CH₄ molecules and a cubic simulation box with side of 5 nm.

Once the EMD simulations were completed, analysis of the density profiles for methane in the direction perpendicular to the pore surface allowed to identify 3 regions within each of the pores: Region 1 (R1) and Region 3 (R3) are close to the solid surface; Region 2 (R2) corresponds to the middle of the pore (see Figure 5.1).

The data obtained from the 5 nm pores, were used as input for our KMC model to predict the diffusion of methane in slit pores of varying width, as detailed in subsection 5.1.3.4. The validity of the KMC predictions was tested against MD data obtained for methane within 10 nm - wide pores. In the case of calcite, as discussed in subsection 5.1.4.1, the diffusion was found to be anisotropic and the solid surface strongly interacted with the methane molecules. To test whether this increased fluid-surface interaction was accurately captured using the KMC model, a 25 nm-wide pore was also simulated using EMD simulations and an additional comparison between EMD and KMC was performed. Due to the high computational effort required for these simulations, other 25 nm-wide pores were not considered in this study. The procedures implemented to simulate 10 and 25 nm-wide pores are similar to those just described for the 5 nm pores.

To analyse the molecular trajectories obtained from the EMD simulations, calculations of density, diffusion coefficients, and radial distribution functions (RDFs) were performed. For the density analysis, bins of width 0.02 nm were used, and the number of molecules was counted as a function of the Z distance. From the density plots, Regions 1, 2, and 3 were identified (see Figure 5.1 for a schematic of the three regions within the pore). The trajectories within each region were used to calculate the diffusion coefficients for methane in all substrates. The diffusivity was calculated in the X (D_x), Y (D_y), Z (D_z) directions, and within the XY plane (D_{xy}). Also the overall (total) diffusivity (D_{xyz}) was

considered, using Einstein's relation, on the basis of the calculated mean square displacements (MSDs):

$$D_x = \frac{1}{2} \lim_{t \rightarrow \infty} \frac{\langle |x_i(t) - x_i(0)|^2 \rangle}{t} \quad (5.1)$$

$$D_y = \frac{1}{2} \lim_{t \rightarrow \infty} \frac{\langle |y_i(t) - y_i(0)|^2 \rangle}{t} \quad (5.2)$$

$$D_z = \frac{1}{2} \lim_{t \rightarrow \infty} \frac{\langle |z_i(t) - z_i(0)|^2 \rangle}{t} \quad (5.3)$$

$$D_{xy} = \frac{1}{4} \lim_{t \rightarrow \infty} \frac{\langle |\mathbf{r}_i^{\text{plane}}(t) - \mathbf{r}_i^{\text{plane}}(0)|^2 \rangle}{t} \quad (5.4)$$

$$D_{xyz} = \frac{1}{6} \lim_{t \rightarrow \infty} \frac{\langle |\mathbf{r}_i(t) - \mathbf{r}_i(0)|^2 \rangle}{t} \quad (5.5)$$

In Eqs. (5.4 – 5.5), $\langle |\mathbf{r}_i^{\text{plane}}(t) - \mathbf{r}_i^{\text{plane}}(0)|^2 \rangle$ and $\langle |\mathbf{r}_i(t) - \mathbf{r}_i(0)|^2 \rangle$ are the MSDs in the XY-plane and XYZ space, respectively, and $\mathbf{r}_i^{\text{plane}}(t) = (x_i(t), y_i(t))$, and $\mathbf{r}_i(t) = (x_i(t), y_i(t), z_i(t))$, respectively. The timescale for the diffusion coefficient calculations was 20 ps of simulation run time (which corresponds to 100 “frames” in the simulation). After these 20 ps, the $\mathbf{r}_i(0)$ was updated for all molecules. The process was repeated 150 times and the average diffusion coefficient value was obtained. To ensure that methane is at supercritical conditions, thermophysical data were used, considering the

density in Region 2, and the system temperature. It was confirmed that in the middle of the pore (Region 2) methane is at supercritical conditions.

3D Kinetic Monte Carlo validation

The KMC model, applied to 1D and 2D pore networks, is described in Chapters 3 and 4 and by Apostolopoulou et al.,^{140,242} The underlying model of the KMC simulation is the Master Equation (Eq. 5.6), which can be thought of as a “probability balance”.¹⁴⁶ The Master Equation expresses the rate of change for the probability $P_p(t)$ of finding the system in state p at time t , in terms of the probability influx from other states q , and the probability efflux toward these other states:¹⁶³

$$\frac{dP_p(t)}{dt} = - \sum_{q \neq p} W_{pq} P_p(t) + \sum_{q \neq p} W_{qp} P_q(t) \quad (5.6)$$

The generic Master Eq. (5.6) can be used to describe the diffusion of a particle from voxel A (x,y,z) to voxel B ($x,y+1,z$) as follows: in state q , voxel A has $n_A + 1$ particles and voxel B has $n_B - 1$ particles. The probability per unit time (propensity) for the aforementioned diffusion event to happen is given by the KMC rate for the A-to-B transition multiplied by the number of molecules in the A voxel, $n_A + 1$. If the transition is performed, the population in the A voxel will be n_A , while the number of particles in the B will be n_B , leading to state q .

To develop a 3D KMC model, the previously discussed 2D model was extended by increasing the number of possible moves a molecule can make from 4 to 6 (left, right, up, down, back, and forth). The computational efficiency of the KMC algorithm is strongly dependent on the matrix mesh, as the computational cost to select each KMC step scales with the number of possible events. Considering M to be the number of voxels, for an $M \times M \times M$ system, there are $6 \times M \times M \times M$ possible events at each step. The algorithmic steps implemented for the 3D KMC approach are summarised in Chapter 2 (subsection 2.8.1.5). The Mersenne Twister MT19937 uniform random number

generator was used to obtain sequences of random numbers needed for the selection of the event at each step and the calculation of the time required for the transition to happen.¹⁸⁹

The 3D KMC algorithm was validated against analytical and deterministic methods for a variety of systems. At first the model against the analytical solution of the diffusion equation, see Eq. (5.7), for a homogeneous system with non-periodic boundaries. Then, homogeneous systems with periodic boundaries were considered. At last, the KMC predictions were compared against MD data for three systems with increasing heterogeneity and mixed boundaries.

$$\frac{1}{D} \frac{\partial C}{\partial t} = \frac{\partial^2 C}{\partial x^2} + \frac{\partial^2 C}{\partial y^2} + \frac{\partial^2 C}{\partial z^2} \quad (5.7)$$

To compare the 3D KMC against the analytical solution of the diffusion equation, a 3 x 3 x 10 lattice was considered. The unit cell size was 1 nm and all boundaries were reflective. Molecules, 1350 in total, were uniformly distributed in a 3 x 3 x 3 cube from origin O (0,0,0), as shown in subsection 5.1.4.3, while the rest of the lattice remained empty. The diffusion coefficient in all voxels was set at 1 x 10⁻⁸ m²/s. The molecules were allowed to diffuse and the population in Voxel 5 (5,1,1) and Voxel 10 (10,1,1) was monitored as a function of simulation time. A sample was taken every 0.01 ns and the total simulation time was 10 ns. The average population over time in the 2 voxels of interest was obtained by performing 10 independent simulations. The equation of diffusion for a 3D system is shown in Eq. (5.7), where 0 ≤ x ≤ l_x, 0 ≤ y ≤ l_y, and 0 ≤ z ≤ l_z, D is the diffusion coefficient, and C(x,y,z) is the overall concentration of molecules. For certain types of initial and boundary conditions, the analytical solution of Eq. (5.7) is the product of the analytical solutions of the three one-spatial-variable problems (C_x(x, t), C_y(y, t), and C_z(z, t)), and hence Eq. (5.7) can be transformed into Eq.(5.8):²⁶⁴

$$C(t) = C_x(x, t) * C_y(y, t) * C_z(z, t) \quad (5.8)$$

For reflective periodic boundary systems, where the molecules are initially distributed in a well-defined region $-h_x \leq x \leq h_x$, $-h_y \leq y \leq h_y$, and $-h_z \leq z \leq h_z$ with concentration C_{0x} , C_{0y} , and C_{0z} , initially distributed in the X, Y, and Z dimension, respectively, the concentration distribution over time is described by:²⁶⁴

$$C_x(x, t) = \frac{1}{2} C_{0x} * \sum_{n=-\infty}^{n=+\infty} \left\{ \operatorname{erf} \left(\frac{h_x + 2nl_x - x}{2\sqrt{D_x t}} \right) + \operatorname{erf} \left(\frac{h_x - 2nl_x + x}{2\sqrt{D_x t}} \right) \right\} \quad (5.9)$$

$$C_y(y, t) = \frac{1}{2} C_{0y} * \sum_{n=-\infty}^{n=+\infty} \left\{ \operatorname{erf} \left(\frac{h_y + 2nl_y - y}{2\sqrt{D_y t}} \right) + \operatorname{erf} \left(\frac{h_y - 2nl_y + y}{2\sqrt{D_y t}} \right) \right\} \quad (5.10)$$

$$C_z(z, t) = \frac{1}{2} C_{0z} * \sum_{n=-\infty}^{n=+\infty} \left\{ \operatorname{erf} \left(\frac{h_z + 2nl_z - z}{2\sqrt{D_z t}} \right) + \operatorname{erf} \left(\frac{h_z - 2nl_z + z}{2\sqrt{D_z t}} \right) \right\} \quad (5.11)$$

To validate the accuracy of the 3D KMC model, the analytical solution of the diffusion equation (Eq.7) was obtained, which is the product of Eqs.(5.8 – 5.11), and the stochastic vs. analytical results were compared. It was found that the stochastic approach is in excellent agreement with the analytical solution of the diffusion equation (see subsection 5.1.4.3).

To test the 3D KMC model for systems with periodic boundary conditions, a 5 x 6 x 3 lattice was used, with unit cell size of 1 nm. The lattice was periodic in all directions and the diffusion coefficient was uniform along X, Y, and Z directions, with values ranging from 1.3 to 2.3 x 10⁻⁸ m²/s (target diffusivity). A single molecule was inserted in a random position and was let to diffuse. Its trajectory was monitored for 70 ns in total; samples were taken every 0.7 ns. For every value of the diffusion coefficient selected (target), 3 independent runs were performed. From the stochastic trajectories obtained, the diffusion coefficient of the particle was calculated and compared against the input diffusion coefficient (target). The results showed perfect agreement between the input and output diffusion coefficient values, providing further validation of the 3D KMC model.

In Chapter 4 the appeal of a 2D KMC model to quantify the effect of heterogeneity, within a pore network in terms of the effective permeability of the medium, was discussed. In this study the accuracy of the developed 3D KMC model is tested, while considering systems with strong fluid-surface interactions and increasing degree of heterogeneity. The 5 nm silica set up was used as a base case and the ϵ (epsilon) parameter that describes methane-silicon and methane-hydroxyl interactions was increased 5 and 25 times. The resulting force field is not realistic, but it works as an artificial system exhibiting strong surface-fluid attractions and high degree of heterogeneity. Methane molecules, 3000 in total, were used to fill each artificial system and the results obtained from all three cases are compared. The diffusion coefficient values, predicted from the EMD simulations within the three regions (R1, R2, and R3) using a set-up similar to the one presented in Figure 5.1, were used to assist this comparison. The overall (total) diffusion coefficient of methane was calculated using EMD simulations and the 3D KMC model. At the end, the coefficients obtained from the two methods were compared and the results were in excellent agreement. For each system 3 independent EMD runs were performed. The mean error was calculated using the standard error equation, shown in Eq. (5.12):

$$\overline{\text{Error}} = \frac{\text{STD}(D(i))}{\sqrt{n}} \quad (5.12)$$

where, STD is the standard deviation, $D(i)$ is the diffusion coefficient calculated at each independent run, and n is the number of independent runs. For these calculations, $i=[1,3]$ and hence $n=3$.

3D Kinetic Monte Carlo set-up

The developed 3D KMC model was set up to mimic the EMD slit pore described in Figure 5.1. The simulation boxes were periodic along X and Y directions and reflective along Z, to represent the presence of the pore slab. To set up the transition rates, r^{KMC} , required

to describe the probability of methane moving from one voxel to another within the simulation box, the kinetic barriers were considered consistent with the diffusion coefficients in Regions 1, 2 and 3, using Eq. (5.13):^{151,176}

$$r^{\text{KMC}} = -\frac{D}{l^2} \quad (5.13)$$

where D is the diffusion coefficient, and l is the voxel size. Thermodynamic barriers were not considered, as there are no pore entrance or exit effects in the present model. The diffusion coefficient values from the EMD simulations, for the 5 nm wide pores, were used as input for the stochastic KMC model's Region 1 and 3 (see Figure 5.1 for a schematic). These values are reported in Figure 5.5 (panel A) in subsection 5.1.4.1 for each solid support considered. The diffusion coefficient assigned to Region 2 in the stochastic model, was obtained from bulk EMD simulations: $1.91 \pm 0.08 \times 10^{-8} \text{ m}^2/\text{s}$. The error bars for all the input values used to feed the KMC model, were calculated by performing 3 independent EMD simulations for each system. To increase the accuracy and minimise the uncertainty of the stochastic model, the error bars calculated were incorporated when assigning the transition rates for the stochastic approach.

To predict the overall (total) methane diffusivity in large pores, the necessary voxels were added to Region 2. For all five substrates 35 different pore widths were considered. For each pore width, a single molecule was initially placed at a random position. The molecule was allowed to move freely through the simulation box for a total of 70 ns. A sample monitoring the position of the molecule was taken every 0.7 ns. This process was repeated 10 times, while starting the molecule from the same position. At the end of the 10th iteration, a different random position was selected for the molecule and 10 independent runs followed. For each pore width simulated 75 initial configurations were generated. The simulation protocol followed for the KMC simulations is presented in Figure 5.2. The confidence intervals obtained of the diffusion coefficient calculations were considered, while simulating different pore sizes for each substrate, and no overlap

was observed. Hence, this number of iterations and initialisations of the particle position allowed to obtain sufficient statistics for the calculation of the molecule's diffusivity.

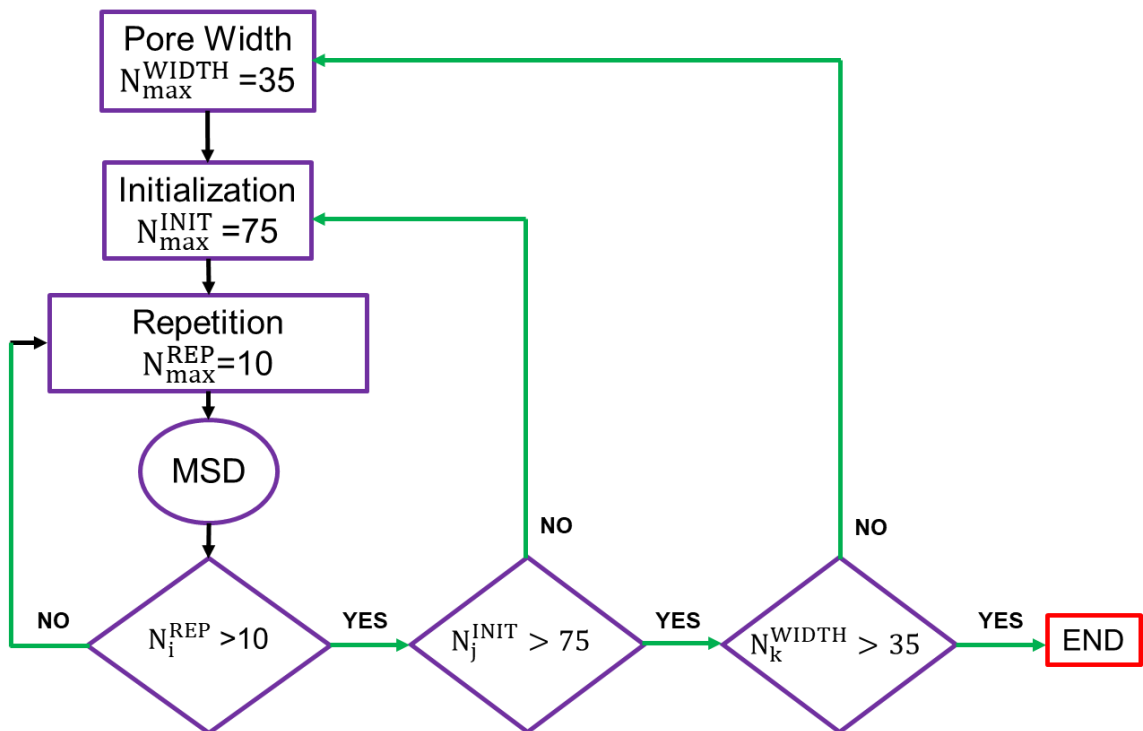


Figure 5. 2: Schematic of the KMC algorithmic steps performed to simulate methane diffusion through pores of varying widths.

Results and discussion

Data analysis

Density plots were obtained for methane inside the 5 nm and 10 nm-wide pores from EMD simulations. Using MATLAB, the density profiles were integrated, and the total amount of molecules was counted in all systems, to ensure less than 1% deviation between the number of molecules in Regions 1 and 3 for both 5 nm and 10 nm-wide pores, and to confirm that equilibrium was reached. From the density profiles, the extend of the three regions inside the pore was identified (see Table 5.2) together with the number of molecules counted in each. From the analysis of the density profiles, it was confirmed that the regions close to the pore surface (R1 and R3) do not change in thickness when the pore width increases. It was also ensured that the difference between

the number of molecules in Regions 1 and 3 was less than 5% for each pore-fluid system. The number of molecules adsorbed on the pore surface was found to remain approximately the same (within 5%) when the pore width is increased from 5 to 10 nm. The numbers of molecules found within each of the 3 regions within each substrate are reported in Table 5.2.

To characterise the structure of the adsorbed methane on each pore surface, the surface density of methane was plotted for the 5 systems, as shown in Figure 5.3. Methane molecules in the first and second adsorbed layer were considered for this analysis. In some of the substrates, methane shows evidence of patterning (silica, calcite, and muscovite), while in others the molecular distribution is close to uniform.

Figure 5.4 shows the density profiles obtained along the Z direction within the 5 nm (black line) and the 10 nm pores (blue line). From the analysis of the density profiles, it is confirmed that the density measured in the middle of all pores remains constant when the pore substrate is changed and when the width is increased.

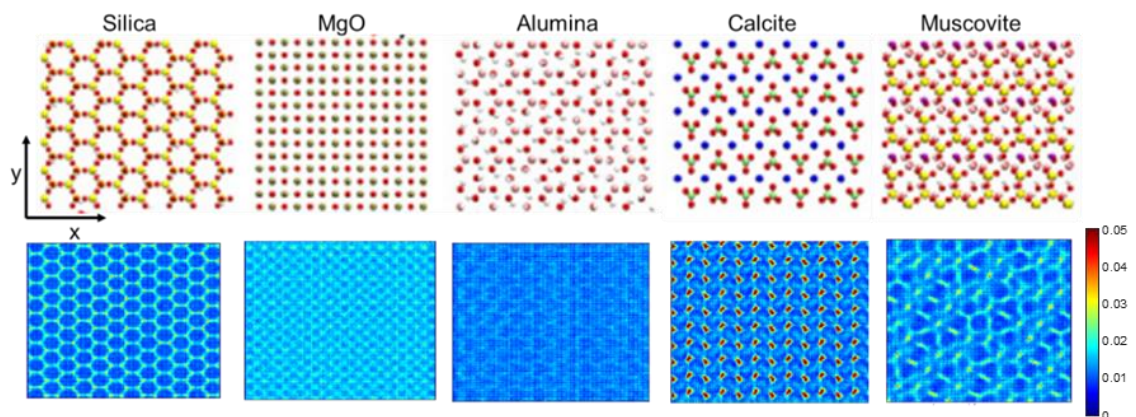


Figure 5. 3: Density of CH_4 close to the surface of the 5 substrates (bottom panel). The top panel shows the composition of the 5 solid supports, as reproduced by Bui et al.,²¹⁵ Colour code: Si=yellow, Mg= tan, Al=pink, K=purple, C=green, Ca=blue, O=red, and H=white.

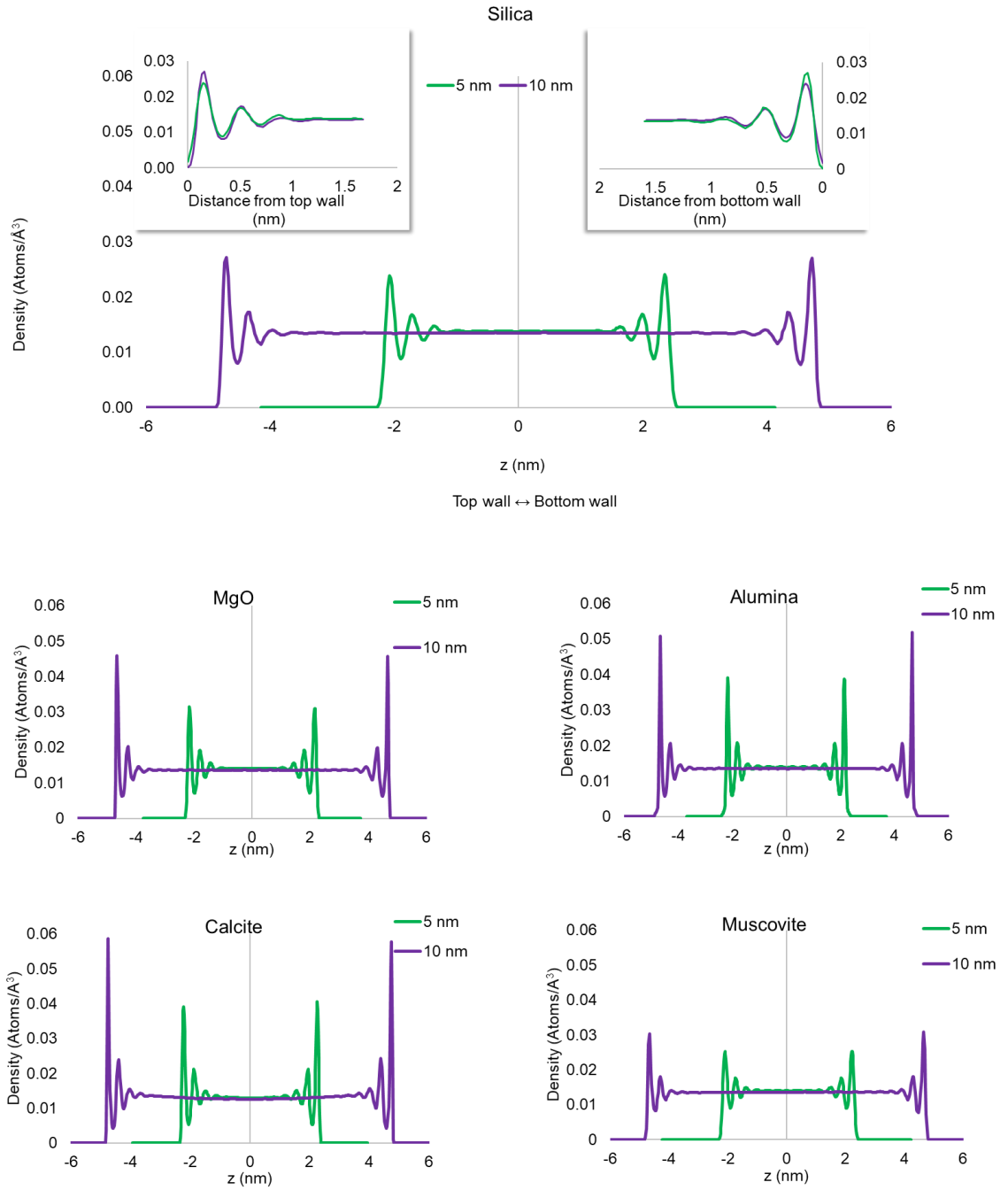


Figure 5. 4: Density profiles for the 5 nm pores (black lines) and the 10 nm pores (blue lines). The top panel (Silica) provides the comparison between the 5 nm and 10 nm density profiles as a function of the distance from the pore wall.

Table 5. 2: Comparison between the thicknesses of regions 1 and 3, the density (in atoms/nm³), and the number of molecules contained in all three regions formed, when considering slit pores of width 5 and 10 nm. The values reported for R1 & R3 represent the average of the two regions. The % difference between them is less than 5%, confirming the hypothesis regarding the non-changing properties in Regions 1 and 3.

Substrate	Length (nm)		Density (atoms/nm ³) Molecules			
	Regions 1&3		Regions 1&3		Region 2	
	5nm pore	10nm pore	5nm pore	10nm pore	5nm pore	10nm pore
Silica	0.70	0.70	13.8 506	13.7 505	12.9 2438	13.0 5890
MgO	0.64	0.64	14.8 543	14.2 520	12.6 2672	13.0 6476
Alumina	0.82	0.83	12.2 467	12.0 466	13.6 2134	13.4 5204
Calcite	0.63	0.62	16.4 451	16.8 456	12.1 1972	12.6 4836
Muscovite	0.74	0.72	15.0 385	14.9 372	12.4 1514	12.8 3824

Within each region, the self-diffusion coefficients were calculated as described subsection 5.1.3.3. Figure 5.5 summarises the results within 5 nm (panel A) and 10 nm pores (panel B). The error bars shown in panel (A) are obtained by calculating the standard error, see Eq. (5.12), from results obtained in 3 independent EMD simulations. Error bars for panel (B) are not available using the standard error formula, as shown in Eq. (5.12), since the simulations were performed only once to validate the 3D KMC model and not to be used as inputs. The diffusion coefficient close to the pore surface is lower than in the pore centre, where methane exhibits bulk-like behaviour. When considering the average values for the 5 nm wide silica, MgO, alumina, and muscovite pores, the diffusion coefficient in Region 2 is slightly lower than the bulk diffusion coefficient, which was calculated to be $1.91 \pm 0.08 \times 10^{-8} \text{ m}^2/\text{s}$ for CH₄ density of 0.01314 atoms/Å³ at 300 K. This is due to the slightly higher density observed in the middle of

these pores. For the case of calcite, the opposite behaviour was observed. This is due to the significantly stronger interaction between the fluid and the calcite surface, which yields a higher number of adsorbed molecules close to the pore surface, leaving the middle of the pore (Region 2) less crowded, as shown in Table 5.2. Since much fewer molecules are in Region 2, compared to the other substrates, a higher diffusivity in calcite's Region 2 was observed. When considering the error bars estimated for these diffusivity values, it is observed that all diffusion coefficient values, besides calcite's, for Region 2 agree with each other within the error bars. This observation confirms that the molecules found in Region 2 are beyond the range of interactions due to the surface, when the pores are at least 5 nm wide. Wang et al., reached a similar conclusion, for simulations conducted within 5.4 nm-wide slit-pores made of montmorillonite and calcite and filled with supercritical methane at various densities.²⁴¹ All methane densities considered by those authors were lower than the densities considered in our work.

The diffusion coefficient in Regions 1 and 3 for each substrate is similar, as expected. Moreover, the diffusion coefficient in the regions close to the pore remains almost constant when comparing 5 and 10 nm pores. This is expected, since the number of adsorbed molecules and the thickness of the adsorbed regions remains unaltered while increasing the size of the pore. Wang et al., also observed the mass density of the two adsorbed layers to remain unchanged when simulating supercritical methane confined in 1.8 and 5.4 nm wide calcite pores.²⁴¹ When considering pores of the same material, the results in this study show that the overall (total) diffusivity increases as the pore width increases. It is later discussed at which pore width the diffusivity of confined methane reaches values comparable to those found in the bulk. The hypothesis is that this increase in diffusivity with pore width is due to the relative increase of the Region 2 thickness when pore width increases. In fact, within Region 2 the diffusion coefficients are significantly higher compared to the areas close to the pore walls.

When considering the diffusivity across the whole substrate (Regions 1, 2, and 3), the D_x and D_y values calculated for silica, MgO, alumina and muscovite pores are very similar

– less than 1% different, which is an indicator of isotropic diffusion. The same behaviour is also observed when comparing the D_x and D_y values in Regions 1, 2, and 3 individually (see Figure 5.6). However, within calcite pores, the D_x and D_y values in Regions 1 and 3 are significantly different, approximately 33%, 40%, and 17%, when considering 5, 10, and 25 nm pores, respectively, as presented in Figure 5.7. In the middle of the pore, Region 2, the % difference between the D_x and D_y values is significantly smaller, as the effect of the surface is vanished. Similar anisotropic effects, in the region close to the calcite surface, were also observed by Bui et al.,²¹⁵ and Franco et al.,²⁶⁵ Bui et al., proposed an explanation for the anisotropic behaviour of methane in hydrated calcite micropores using free energy landscape calculations to further characterise the surface of the calcite pores, although in that case the pores were filled with water. They showed that, because of the structure of confined water, the path of minimum resistance for methane diffusion along the Y direction is a straight line, while the preferable path along the X direction is tortuous and zigzag-like.²¹⁵ Note that the determination of the X and Y directions is arbitrary; in the above comparisons X and Y directions are those shown in Figure 5.3. Franco et al., also observed the methane diffusivity along the Y direction to be higher than the diffusivity in the X direction close to the calcite surface for three pore widths.²⁶⁵ The results produced in this study agree with this observation, as shown in Figure 5.7.

To verify that the thermodynamic conditions inside all pores correspond to supercritical methane, thermophysical data were used, considering the density in Region 2, and the system temperature. Based on these data it was confirmed that methane in Region 2 is at supercritical conditions within all systems considered.

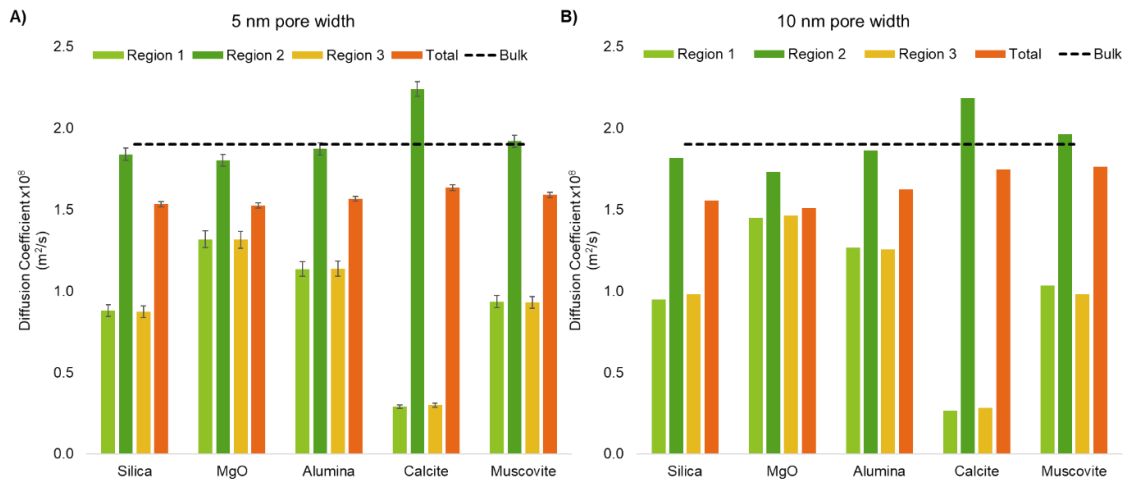


Figure 5. 5: Diffusion coefficient calculated in Regions 1, 2, and 3, as well as in the whole simulation box (Total). Panel (A) shows the results obtained for the 5 nm pores, and panel (B) shows the results for the 10 nm pores, respectively.

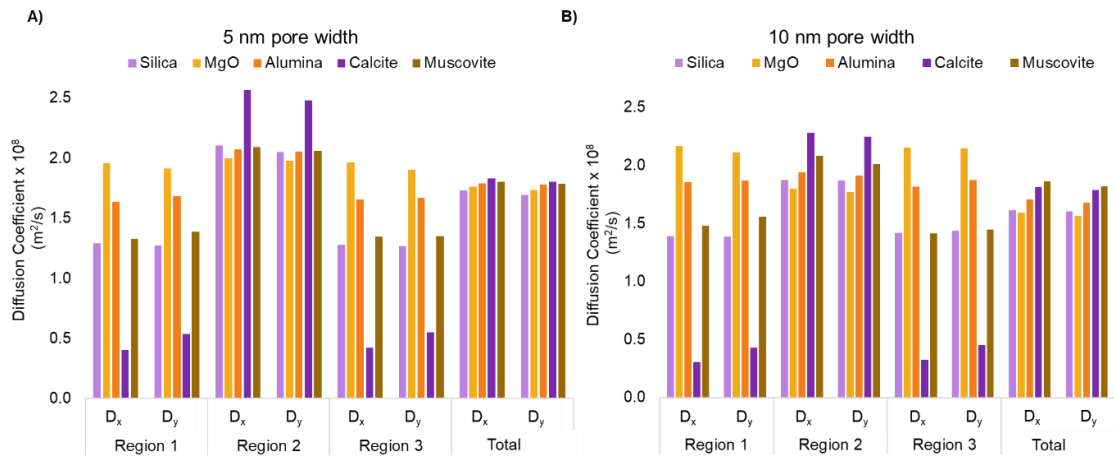


Figure 5. 6: Diffusion coefficients in the X and Y direction, calculated in Regions 1, 2, and 3, as well as in the whole simulation box (Total). Panel (A) shows the results obtained for the 5 nm pores, and panel (B) shows the results for the 10 nm pores, respectively.

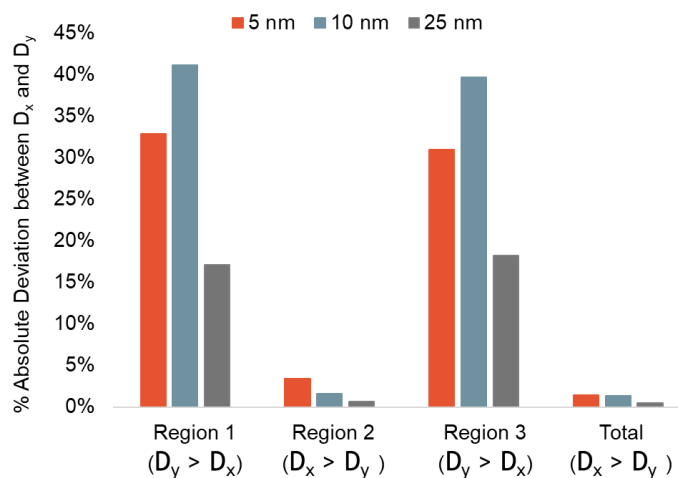


Figure 5. 7: Analysis of anisotropic diffusion in calcite. The y axis shows the % absolute deviation between D_x and D_y values measured in the three regions and the overall (Total) pore, using 3 different pore widths.

Model systems with exceptionally strong surface-fluid interactions

The analysis discussed above was also performed for the silica substrates when the force fields were modified to represent exceptionally strong surface-fluid interactions. In these model systems, the methane-silicon and methane-hydroxyl interactions were increased by 5 and 25 times, as described in subsection 5.1.3.4. Figures 5.8 and 5.9, compare the results obtained against those gathered for methane within the realistic silica substrate. Note that for the systems considered here, the number of molecules inserted in the pores was 3000. Figure 5.8 shows how the three systems compare in terms of density profiles (panel A) and RDF profiles (panel B). The comparison between the diffusion coefficients calculated in the three regions are reported in Figure 5.9 (panel C, panel D).

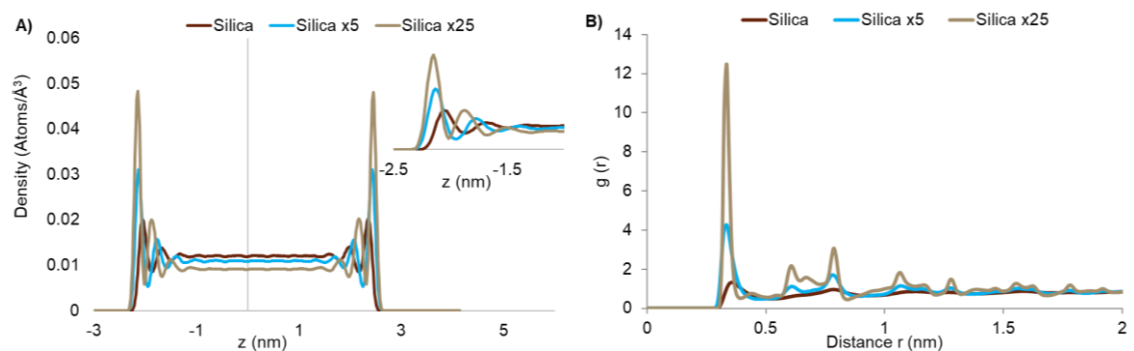


Figure 5. 8: Density (panel – A) and RDFs (panel – B) for the 3 systems used to represent systems with exceptionally strong solid-fluid interactions.

The effect of the strong surface interaction is evident from the density profiles and RDF plots, as shown in Figure 5.8. To further characterise the systems, Figure 5.10 presents the planar density profiles parallel to the pore surface for methane within the second adsorption layer. The adsorption layer is determined from the density profiles in Figure 5.8. The colour-bar has been kept constant to allow for visual comparison. According to panel (A), methane molecules preferably arrange in circles surrounding the oxygen atoms on the surface. As the interaction between surface and methane increases (panels

B and C), the amount of methane molecules occupying positions aligned with the oxygen atoms increases. This is probably because the maximum number of molecules that can occupy the peripheral positions surrounding the oxygen atoms has been reached, and additional molecules have to occupy positions that correspond to higher conformational energy.

In Figure 5.9, panel (A), the thickness of Regions 1 and 3 is presented, as calculated from the density plots. As the solid-fluid attraction increases, these regions narrow and the methane density in Regions 1 and 3 increases, which is in qualitative agreement with the 2D density profiles presented in Figure 5.10. On the contrary, the methane density in Region 2 decreases, as confirmed by the density profiles shown in Figure 5.8. As a result, the diffusivity of methane in the 3 regions is expected to significantly change as the solid-fluid interactions increase. The number of molecules in the 3 regions within these pores is summarised in Figure 5.9, panel (B). As the attraction between the surface and the fluid increases, the number of molecules adsorbed on the surface increases, leading to a reduced occupancy in the middle of the pore.

As the surface-methane attraction increases, the methane diffusion coefficient in Regions 1 and 3 was found to drop significantly, by almost one order of magnitude every time the solid-surface interaction increased by 5 times, while the diffusivity in Region 2 increases moderately. However, the overall (total) diffusivity was found to remain constant. To explain these observations, the hypothesis is that the following two effects cancel each other out: 1) decreased R1 and R3 thickness, with correspondingly decreased diffusivity, and 2) increased R2 thickness, with correspondingly increased diffusivity.

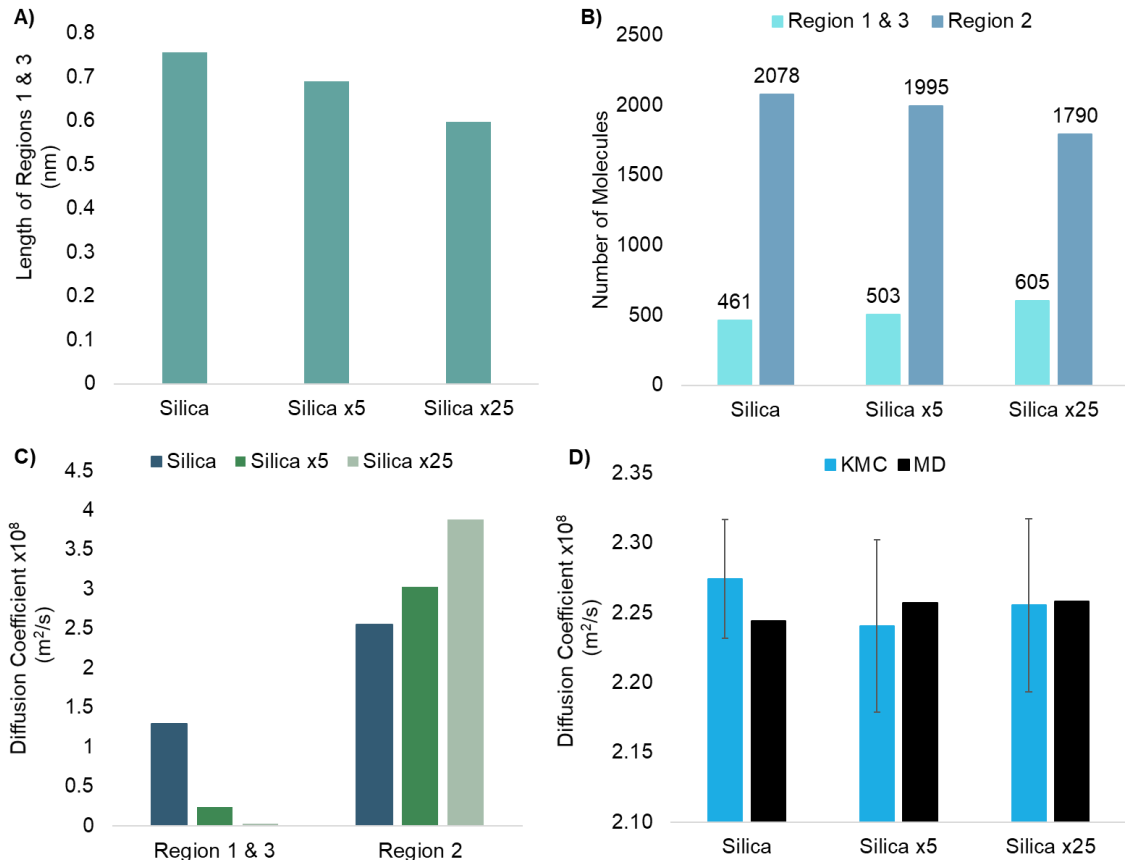


Figure 5. 9: Analysis of the surface interaction effect as a function of the physical extent of Regions 1 & 3 (panel A), number of molecules absorbed (panel B), diffusivity in Regions 1,2, and 3 (panel C), and overall (total) diffusivity predicted using EMD simulations and the KMC model (panel D).

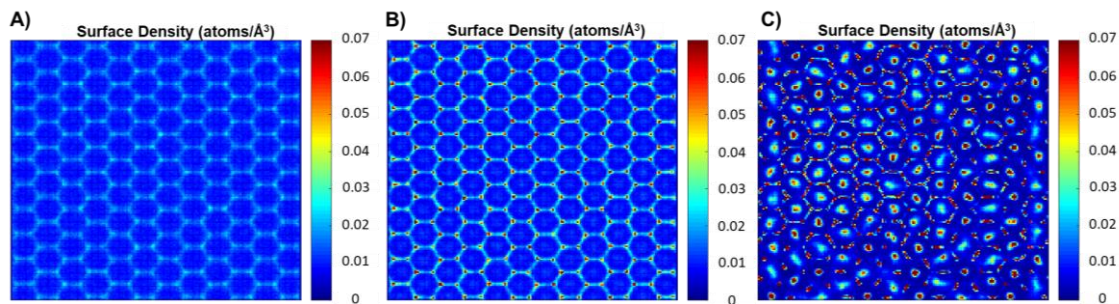


Figure 5. 10: Surface density profiles for the 3 silica-methane systems as a function of surface-methane interactions. Panel (A) shows the realistic silica surface, while panels (B) and (C) the surfaces that are 5 and 25 times more attractive, respectively. Methane molecules in the first and second adsorbed layer were considered for this analysis.

3D KMC model validation

The 3D KMC was validated against the analytical solution of the diffusion equation. To solve Eq. (5.8) and Eqs. (5.9-5.11), a system containing 10 columns (X direction), 3 rows (Z direction), and 3 slices (Y direction) was considered. All boundaries were reflective: once a molecule reached a boundary, it bounced back to the lattice. Molecules, 1350 in total, were distributed in the first third of the system, as shown in red in Figure 5.11, panel (A). The diffusion in all voxels within the KMC model was set to be $1 \times 10^{-8} \text{ m}^2/\text{s}$. The population in the 5th and 10th voxels was monitored over time, and Eqs. (5.8-5.11) were solved. The results obtained from the 3D KMC and those from the analytical equation are plotted in Figure 5.11 panels (B) and (C). Visual inspection confirms that there is satisfactory agreement. The stochastic approach shows fluctuations around the deterministic values. These fluctuations can be reduced by performing more independent runs and obtaining the average values.

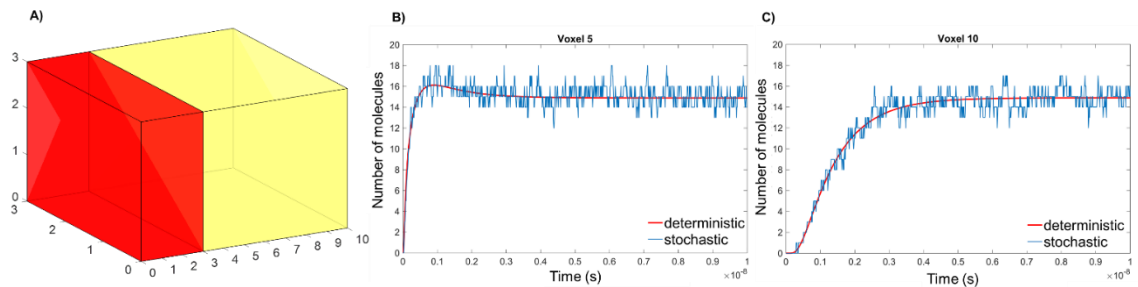


Figure 5. 11: (A) Representation of the 3D KMC non-periodic system. The red region represents the area where the molecules were initially distributed. The comparison between the analytical equation and the 3D KMC predictions for (B) Voxel 5 and (C) Voxel 10, respectively.

The 3D KMC model was also tested for a homogeneous and periodic system. In this case, 6 different systems were considered, consisting of 5 columns (X direction), 6 rows (Z direction), and 3 slices (Y direction). A single molecule was then inserted in the lattice and was let to diffuse. Samples were collected every 0.07 ns during a total of 70 ns of simulations. At the end of the simulations, the MSD from the trajectories was calculated, leading to the calculation of the diffusion coefficient. Each system was homogeneous

and the input (target) diffusion coefficient varied from 1.3×10^{-8} to 2.3×10^{-8} m²/s. Figure 5.12 presents the mean square displacements calculated from the 6 systems (panel A) and the comparison between the input (target) and calculated diffusion coefficient (panel B) when using the 3D KMC algorithm.

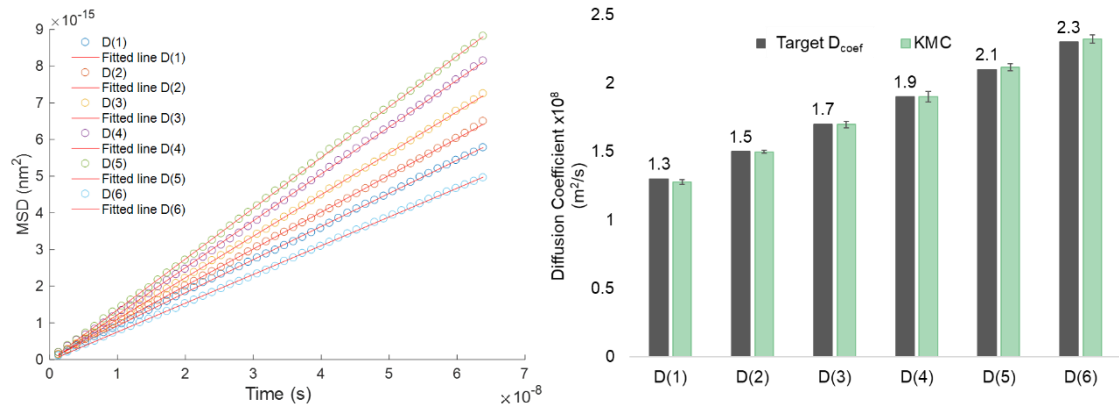


Figure 5. 12: Validation of the 3D KMC algorithm using a periodic system.

Finally, the effect of the unit cell size on the diffusion coefficient calculated was tested, when implementing the 3D MC approach. No statistically significant differences were observed when using smaller or bigger unit cell sizes. This confirms the validity of the 3D KMC model in representing periodic systems. To test the 3D KMC model in a heterogeneous system the 3 systems where the surface - fluid interaction was altered (see subsection 5.1.3.4) were considered. To set the diffusivity in Regions 1, 2, and 3 the values reported in Figure 5.9. were used. The algorithmic steps described in Figure 5.2 were also implemented, but for only 1 value of the pore width. From the trajectories obtained, the diffusion coefficient from 10 independent runs was calculated. The results are presented in Figure 9 panel (D), which shows agreement between the KMC and EMD approaches, validating the applicability of the KMC model in heterogeneous systems.

3D KMC predictions of supercritical methane diffusivity in pores

This subsection presents the results obtained using the 3D KMC on the slit pore systems, using as input the results from atomistic EMD simulations. Regions 1, 2, and 3 were spatially defined within the KMC lattice based on analysing density profiles such as those in Figure 5.4. The diffusion coefficient assigned to voxels within each region was the output of the EMD results of Figure 5.5. To predict the overall (total) diffusivity in pores of increasing width, the algorithmic steps described in Figure 5.2 were followed. Figure 5.13 presents the results obtained for the pores carved out of the 5 solid supports, for widths ranging from 3 to 60 nm. Note that the limit of the x-axis in the five panels shown in Figure 5.13 changes from one system to another. This is because of the protocol used to set up the 3D KMC systems, according to which the number of pore widths was the parameter used to determine the systems (35 pore widths for each substrate), together with the thickness of Regions 1 and 3, which differ among the substrates, as shown in Table 5.2. The KMC data points are shown as blue circles. The error bars calculated according to Eq. (5.12), considering 10 independent runs, are shown in red. The grey fitted line is used as a guide to the eye and the blue dashed line shows the diffusion coefficient of the bulk methane, as calculated from 3 independent EMD simulations in the bulk. It is helpful to remember that the density of the bulk methane is set to 0.01314 atoms/Å³ and the temperature is 300 K.

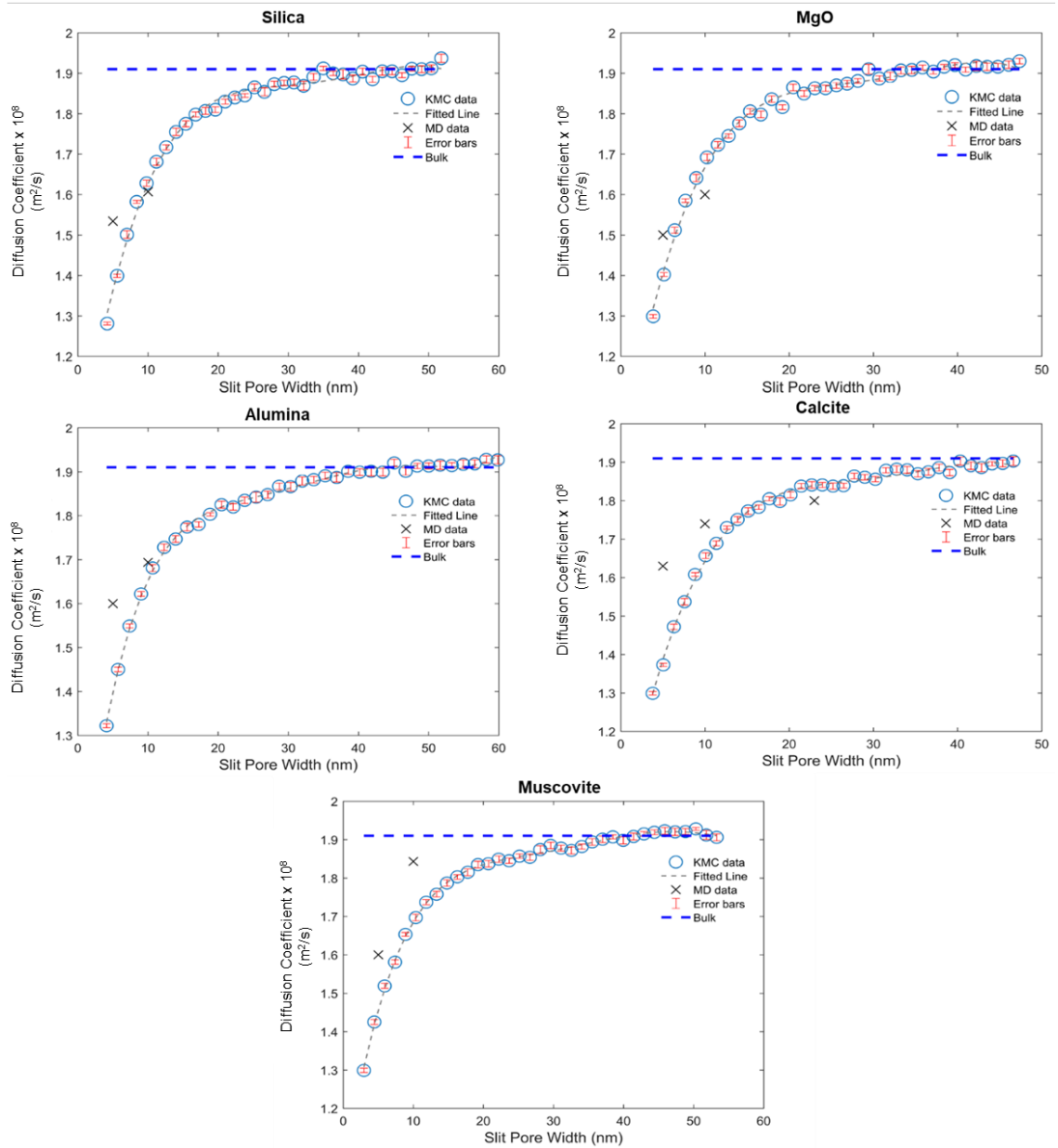


Figure 5. 13: Overall (D_{xyz}) diffusion coefficient as a function of the pore width for the 5 solid supports considered here for the whole pore. Comparison between KMC predictions and EMD data. Note that the deviation between KMC and MD data is less than 10%.

As the pore width increases, the diffusion coefficient of methane increases, until it reaches its bulk value, $1.91 \pm 0.08 \times 10^{-8} m^2/s$, in all of the pores considered. According to the results in Figure 5.13, the supercritical methane confined in MgO and silica slit-shaped pores exhibit bulk-like diffusivity when the pore width is slightly above 30 nm and 35 nm, respectively. Within the muscovite pores, supercritical methane reaches bulk

behaviour when the pore width is almost 40 nm. Within the alumina pores, this happens when the pore width is slightly wider than 37 nm, while in calcite the pore width required for supercritical methane to achieve bulk-like diffusivity is almost 50 nm. The hypothesis here is that this substrate-specific behaviour is due to the preferential distribution of methane in Regions 1 and 3, near the solid substrates. While comparing the surface density profiles within the first adsorbed layer, presented in Figure 5.3, the MgO substrate shows the most uniform methane distribution, with silica, alumina, and muscovite substrates following. However, calcite exhibits sites that strongly attract methane. In a few pores, notably within the silica one, the results seem to suggest that in some cases the diffusion coefficient for the confined methane can be larger than in the bulk. This is ascribed to numerical errors, which are quantified in what follows. It is noted that the datapoints that appear to have faster diffusion than bulk are, when the error bars are considered, consistent with bulk-like diffusion.

In the five panels of Figure 5.13, the diffusion coefficient data obtained by atomistic EMD simulations are also reported. For silica, MgO, alumina, and muscovite, there are 2 EMD data points, corresponding to the 5 nm and 10 nm pore widths. For calcite, an additional data point is reported, at 25 nm pore width. The deviation between EMD data and KMC predictions in all cases is less than 10%. For the 5 nm pores, the % deviation is 8.8%, 8.1%, 7.4%, 9.3%, and 4.5% for the silica, MgO, alumina, calcite, and muscovite, respectively, while for the 10 nm pores the % deviations values become -1.3%, -4%, -0.8%, 6.1%, and 7.9%, respectively. From the plots reported in Figure 13 and the % deviation calculated it appears that the 3D KMC predictions agree better with the EMD predictions as the pore width increases. This is because of the diffusion coefficient assigned to Region 2, during the set-up of the KMC model. As discussed in subsection 5.1.4.1, the diffusion coefficient calculated in the middle of the pores was very similar to the bulk value, yet not identical; calcite exhibited a higher diffusion coefficient in Region 2, compared to the bulk value, and for the rest of the substrates the diffusivity calculated was slightly lower. Therefore, it is expected that as the pore width increases, the diffusion

coefficient of methane in Region 2 converges to the bulk value, and the KMC input for the region becomes more accurate. This can be further confirmed by the case of the 25 nm calcite pore, where the difference between the EMD and the KMC values is -2.3%. These deviations are satisfactorily small and presumably could be further reduced if more independent EMD simulations were performed and more accurate inputs for Regions 1 and 3 were used to initiate the 3D KMC model, at the expense of increased demands on computational resources. The additional independent EMD simulations could also provide error bars and further aid the comparison between the two approaches. However, in pores smaller than 5 nm, each parallel pore wall may interact with fluid molecules adsorbed near both the opposite walls, causing strong deviations from bulk-like behaviour for the whole methane within the pore, even for those molecules in the middle of the pore. In this case, the accuracy of the KMC model is expected to worsen and the % deviation between the KMC and EMD simulation data will potentially exceed the 10% threshold.

It should be emphasised that using the 3D KMC model for estimating self-diffusion coefficient in pores with varying pore width provides accurate results at very low computational cost. For the 5 nm pores considered here, atomistic EMD simulations for 53 ns were performed for each solid support. The time required for these calculations, using a supercomputer, ranged between 30 and 42 hours; the time required for conducting atomistic EMD simulations within the 10 nm and 25 nm simulations was higher, as the number of molecules increased in those systems. By comparison, the time required for the KMC simulations, per substrate, was approximately 35 minutes on the supercomputer to predict self-diffusion coefficient in pores of 35 different pore widths. The nodes used to perform these simulations on the supercomputer consisted of 2 Intel Xeon E5-2683 v4 cores in total and 128 GB total RAM. For each pore width, 75 different initial configurations were tested in one simulation run, and 10 independent runs were performed, leading to a total of 26,250 simulations. This amount of simulations takes approximately 4 hours on a standard desktop computer, where it would be prohibitive for

the atomistic EMD simulations to be completed. Admittedly, transport models such as those discussed in subsection 5.1.2, could be used to generate digital libraries similar to those shown in Figure 5.13. However, to make those models applicable for the systems investigated, a certain number of parameters, usually obtained from EMD data, should be fitted to describe each substrate.²⁶⁶

A novel 3D pore network modelling approach to stochastically evaluate the impact of pore network geometry, chemistry and topology on fluid transport – Part II

Abstract

Fine-grained sandstones, siltstones, and shales have become increasingly important to satisfy the ever-growing energy demands, globally. Of particular current interest are shale rocks, which are mudstones made up of organic and inorganic constituents of varying pore sizes. These materials exhibit high heterogeneity, low porosity, varying chemical composition and low pore connectivity. Due to the complexity and the importance of such materials, many experimental, theoretical and numerical efforts attempt to quantify the impact of rock features on fluids diffusivity, and ultimately on permeability. It is becoming apparent that a successful approach should consider realistic 3D pore networks consisting of pore bodies that communicate via pore throats, which however requires prohibitive computational resources. To overcome current limitations, this study presents a rigorous protocol to stochastically generate synthetic 3D pore networks in which pore features can be isolated and varied individually. Using this protocol, the contribution of pore network's connectivity, porosity, mineralogy, and pore throat width distribution, on the diffusivity of supercritical methane is quantified. To conduct these calculations and simulate the fluid transport, the developed 3D stochastic KMC model, discussed in Part I of this chapter, is implemented. A sensitivity analysis is conducted to rank the significance of the various network's features on methane diffusivity. Connectivity is found to be the most important feature, followed by pore throat width distribution, and porosity. Based on such insights, recommendations are provided on possible technological approaches to enhance fluid transport through shale rocks and equally complex pore networks. These findings could be relevant for applications that make use of porous media, ranging from catalysis to radioactive waste management, from shale gas production to environmental remediation.

Introduction

In view of the growing demand for energy, production rocks that were once considered non-reservoirs, such as fine-grained sandstones, siltstones, and shales, are becoming increasingly important. These drastic changes have been enabled by technological advances in horizontal drilling and hydraulic fracturing, which permitted dramatic increases in hydrocarbon (gas and oil) production from shale formations.^{267–269} It is known that fluid flow and mass transport through rocks are controlled by pore networks' characteristics such as pore size distribution, pore connectivity, porosity, pore throat width distribution, and mineralogy.^{66,79,270,271} Current research focus includes attempts to determine which, out of these and other features, control fluid migration. For example, Sahimi described pore connectivity by an equivalent network of pore throats, i.e., the narrow passages through which fluids flow, and pore bodies, large voids that meet through the throats.²⁷² This feature of the porous media, frequently referred to as topology, pore throat connectivity, or coordination number, has been widely identified as one of the most important parameters that affect transport in many porous media, including shale rocks.^{273,274} According to Rabbani et al.,²⁷⁵ connectivity can be measured following either forward or backward methods: forward methods mainly involve 2D or 3D image analysis of core samples, followed by sophisticated morphological analysis and image processing to extract the network's coordination number;^{276,277} backward methods first quantify some macroscopic characteristics of the porous media, e.g., capillary pressure, porosity, or relative permeability, and then back-calculate the features of the underlying pore network model.^{278–282}

When applied to USA shale rocks, e.g., Barnett and Haynesville samples, such approaches revealed pore networks with low connectivity.²⁸³ Similar results have been reported for UK samples from the Bowland, and it is now generally assumed that most shale formations consist of poorly connected pore networks. Moreover, it is common that during hydraulic fracturing, due to the large pressure gradients applied and in-situ stress

alterations, part of these poorly connected networks crush and the connectivity further reduces.^{284,285} To support this possibility, Davudov et al.,²⁸⁶ identified connectivity loss as the main mechanism controlling permeability reduction in shale samples. From a modelling perspective, the effect of pore network connectivity on permeability can be quantified by modifying selected parameters within the permeability models used. Few examples include Civan's²⁸⁷ modified Kozeny–Carman (KC) permeability model, and Pape's²⁸⁸ model, which is derived from fractal theory. The aim of this study is to explore an alternative method of quantifying the effect of connectivity on fluid transport, by implementing a stochastic approach to generate pore networks with desired properties and quantify methane gas diffusion within these materials.

In addition to connectivity, other materials properties are important in this quest. For example, the porosity of a porous medium, defined as the volume fraction of its voids.²⁸⁹ Porosity affects permeability so strongly,^{290,291} that Archie proposed a porosity-permeability relationship, derived for sandstones, limestones and muddy sands, which predicts a tenfold increase in permeability, if porosity is increased by 3%.²⁹² Because it has been suggested that porosity intrinsically depends on the microstructure of porous materials,²⁹³ a sensitivity analysis on the effect of macro and micro porosity on permeability was performed in Chapter 4. A plethora of published studies have also attempted to correlate the porosity of a formation to its permeability. Magara, e.g., proposed a log-derived permeability-porosity relationship to fit laboratory-based porosity-permeability data.²⁹⁴ Additionally, several modifications to the classic fractal theory²⁹⁵ have been proposed to better capture such relationship.^{296–298} Zhang et al.,²⁹⁹ utilised the theory of poroelasticity to derive this correlation, and Javadpour proposed a dynamic model to describe dynamic porosity and apparent permeability, taking into consideration the poromechanical processes that occur during reservoir stimulation.³⁰⁰ These authors also correlated permeability, porosity and formation depth using neural networks.³⁰¹ These efforts are justified by the fact that understanding the effect of porosity on

permeability is crucial in developing stimulation strategies and for the evaluation of shale formations profitability.

Pore size and pore throats are also certainly important. In conventional reservoir rocks, pore sizes and throats are relatively large, sufficiently so to store and deliver economic quantities of petroleum. On the contrary, pore throats in unconventional reservoirs are so small that they can limit hydrocarbons passage.³⁰² Nelson reported that the experimentally measured pore-throat sizes in samples from Devonian, Jurassic, Cretaceous, Pennsylvanian, and Pliocene shale formations range from 5 nm to 50 nm, although in some samples these values can reach 100 nm.³⁰² Other experimental studies also confirm this assessment.²⁸³ Zhang et al.,³⁰³ evaluated pore size distribution (PSD) and permeability of a tight reservoir, located in China, and reported that throat sizes are slightly positively correlated with permeability. On the other hand, Katsube et al.,³⁰⁴ found that the PSDs' mode significantly impact permeability for various Canadian shale samples. However, even these groups acknowledge that other material properties are likely to affect the relationships reported.

Another material property that is often considered important in determining fluid transport is the chemistry of the porous medium. This is quantified in terms of the mineralogy of the pore throats. It has been observed that in narrow, single pores, the pore throat surface interacts with the fluids, in some cases yielding kinetic barriers that hinder transport.^{241,265} This is more pronounced when the throat surfaces are charged and water is present, especially if two-phase systems are present.^{88,215,305} In Part I of this chapter, the developed 3D KMC model was implemented to generate digital libraries correlating gas diffusivity to the pore size for five solid substrates. In those single-pore systems, it was found that the solid substrate chemistry has little effect on gas diffusivity for pore widths larger than ~30 nm, although the effect can be large in smaller pores.

Although the importance of the pore network features has been excessively discussed in the literature, the classification of these features in order of importance remains

elusive. A rigorous systematic approach is employed here to generate 3D pore networks in which connectivity, porosity, PSD, and mineralogy are treated as variables and altered individually to quantify their impact on the transport of supercritical methane. The remainder of this study is organised as follows. Section 5.2.3 describes the protocols implemented to generate the pore networks, the systems investigated, and the stochastic 3D KMC model used to model supercritical methane transport. The results obtained are presented in Section 5.2.5, when the pore network features are altered separately. The sensitivity analysis is also reported to reveal the relative importance of the pore networks characteristics. Finally, a summary of the observations obtained, followed by recommendations to practitioners are provided in Section 5.3.

Methodology

Pore network features

As discussed above, in this study pore networks whose features are changed systematically are generated. The following subsections discuss how pore connectivity, network porosity, pore throat size distribution, and pore throat chemistry are changed systematically in the implementation of the developed 3D KMC model. In the 3D pore networks generated, the pores are of same size and are represented as binary variables; each voxel can either have a single pore or be empty. Similarly, pore connectivity is represented as a binary variable for a set of adjacent pores, i.e. the neighbouring voxels i and j can be either connected via a pore throat or not. The number of connections a voxel has with its neighbouring 6 voxels defines the connectivity, which is an integer variable with values between 0 and 6. The pore throats are slit shaped, have the same length and different widths.

Pore connectivity

According to Sahimi, the pores in natural porous media can be divided into two groups: the pore bodies, which comprise most of the porosity, and the pore throats, which are

narrow channels connecting pore bodies. To construct the pore networks considered in this study, both pore bodies and throats were employed. The connectivity level determines the number of connections between neighbouring pores, and therefore the number of pore throats in the network. The minimum number of throats per pore is 0, when the pore is not connected to any adjacent pores; the maximum is 6, when the pore is surrounded by neighbouring pores in all 3 dimensions and is connected with them all. The maximum number of connections is defined by the shape of the voxels implemented for the construction of the 3D KMC lattice. Since cubic voxels are used in this 3D KMC model, the maximum number of connections is 6. If a different mesh type is used to generate the 3D KMC lattice (ex. triangular or hexagonal voxels), the number of maximum connections will be different.

To make the generated pore networks realistic, log-normal distributions were used to determine the degree of connectivity. For each distribution, the mu and sigma values were specified. Sensitivity analysis is performed on both parameters separately.

The mu values considered were 2, 3, 4, 5, and 6. In these networks, the sigma value was kept constant at 1 (Figure 5.14A). Because connectivity is one of the most important parameters affecting fluid transport, an additional step was implemented to ensure that the simulations conducted were not biased by a poor choice of the connectivity via the mu parameter. To this end, two sets of networks were generated, five networks with low connectivity ($\mu=2$) and sigma ranging from 0.5 to 2.5 (shown in Figure 5.14B) and five networks with high connectivity ($\mu=5$) with sigma values also from 0.5 to 2.5 (Figure 5.14C). Sensitivity analysis is performed on these two sets separately.

The sigma parameters considered were 0.5, 1, 1.5, 2, and 2.5. In these cases, the mu value constant and equal to 2, and 5, for the low and high connectivity networks. As sigma increases, the heterogeneity of the system increases because the connectivity distribution becomes broader, and the pores with low connectivity coexist with pores that are highly connected and can easily transport fluids.

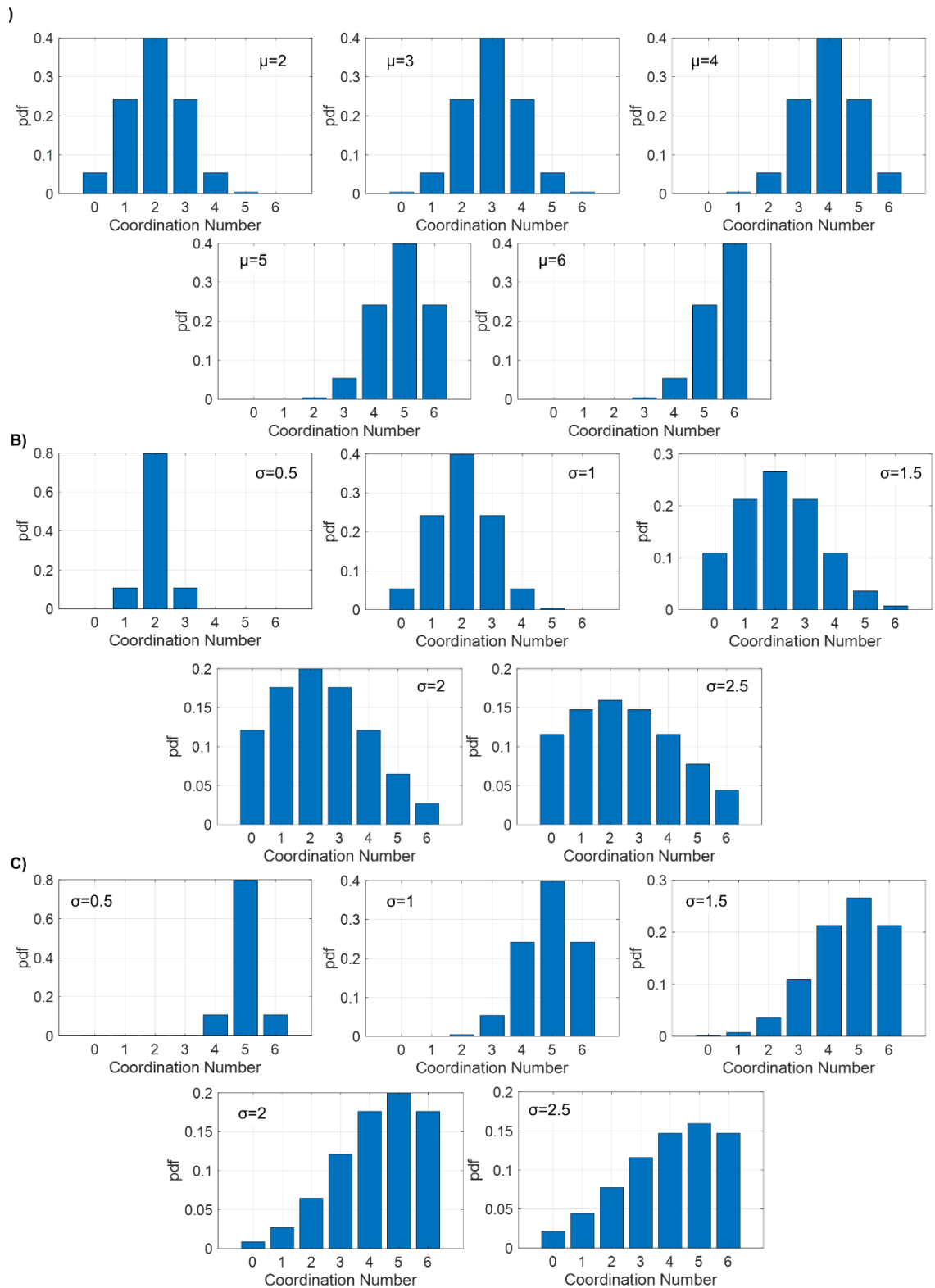


Figure 5. 14: Distributions considered for the networks' connectivity. A) Sigma=1 and constant, B) Mu=2, and constant, and C) Mu=5, and constant.

Porosity

To quantify the effect of porosity on fluid diffusion, pore networks on increasing porosity were considered: 5%, 10%, 15%, 20%, 25%, 30%, 35%, 40%, 45%, and 50%. These porosity values, when multiplied by the total number of voxels in the 3D KMC lattice, yield the number of pores present in the network. The pores are randomly inserted in the pore network. To ensure that the diffusivity calculated does not depend on the pore distribution, 5 configurations were generated for each porosity. The diffusion coefficient in each network was calculated to obtain the average, together with the uncertainty quantified using the standard error formula:

$$\overline{\text{Error}} = \frac{\text{STD}(D(i))}{\sqrt{n}} \quad (5.12)$$

In Eq. (5.12), STD is the standard deviation, $D(i)$ is the diffusion coefficient obtained for $i \in [1, n]$, and n is the number of 3D pore network considered for the calculation. Figure 5.15 shows an example of the pore networks with porosity 10%, 20%, 30%, 40%, and 50%. Figure 5.16 presents an example of three different pore networks with 25% porosity. For all networks presented in Figures 5.15 and 5.16, the connectivity of the networks is high ($\mu=5$).

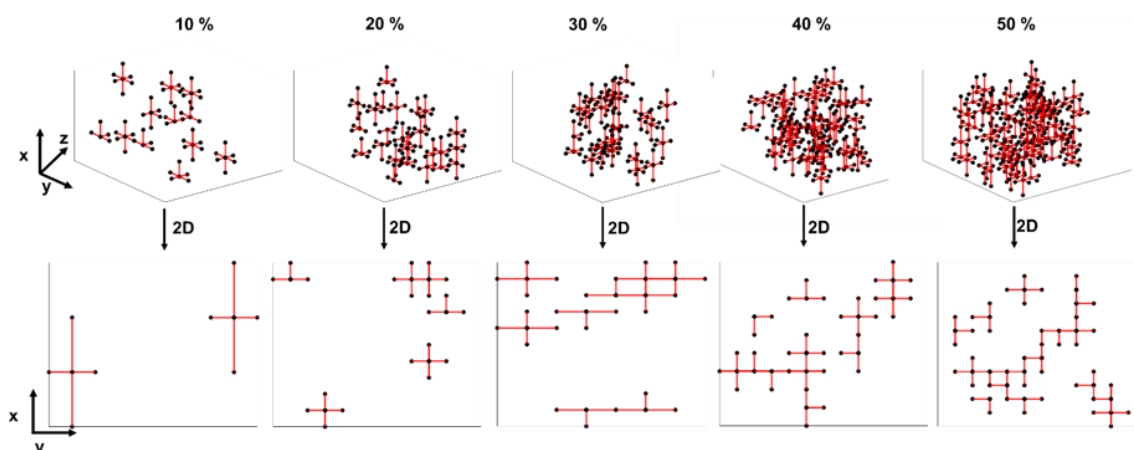


Figure 5. 15: Representation of the 3D and 2D pore networks generated while considering porosity values 10%-50%. As porosity increases, the cluster connectivity increases.

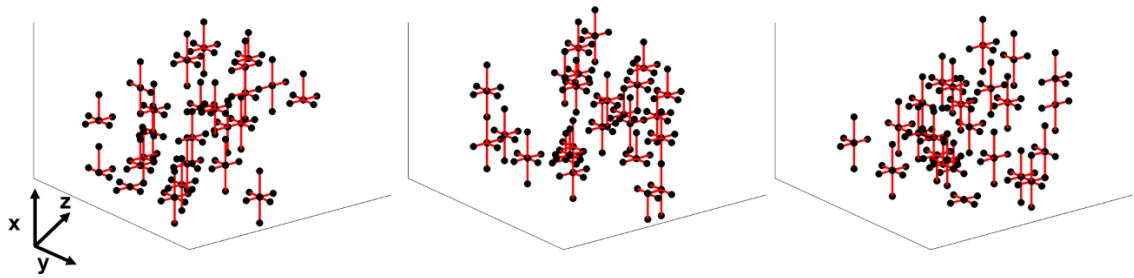


Figure 5. 16: Representation of three equivalent 3D pore networks with 25% porosity and high connectivity ($\mu=5$). For every porosity value considered, 5 equivalent networks were generated.

Pore throat Size Distribution (PSD)

As discussed in Chapter 4, in 2D pore networks, the pore size distribution was found to strongly affect permeability. In this study, a similar sensitivity analysis is performed on the effect of pore throat size distribution, while considering 3D networks. To be consistent with the literature, log-normal distributions were considered, which characterise shale rock formations.³⁰⁶ The impact of the distribution's μ and σ was investigated, within 10 systems. In the first five pore networks, σ is kept constant and equal to 1, while μ changes (5, 10, 15, 20, and 25 nm) (see Figure 5.17A). These μ values are relative low, as shales are characterised by a significant amount of microporosity.^{283,302} In the other five pore networks, μ is kept constant and equal to 25 nm, while σ changes (0.5, 1, 1.5, 2, and 2.50 nm). As σ increases, the distribution becomes broader and the level of heterogeneity in the pore networks increases (see Figure 5.17B).

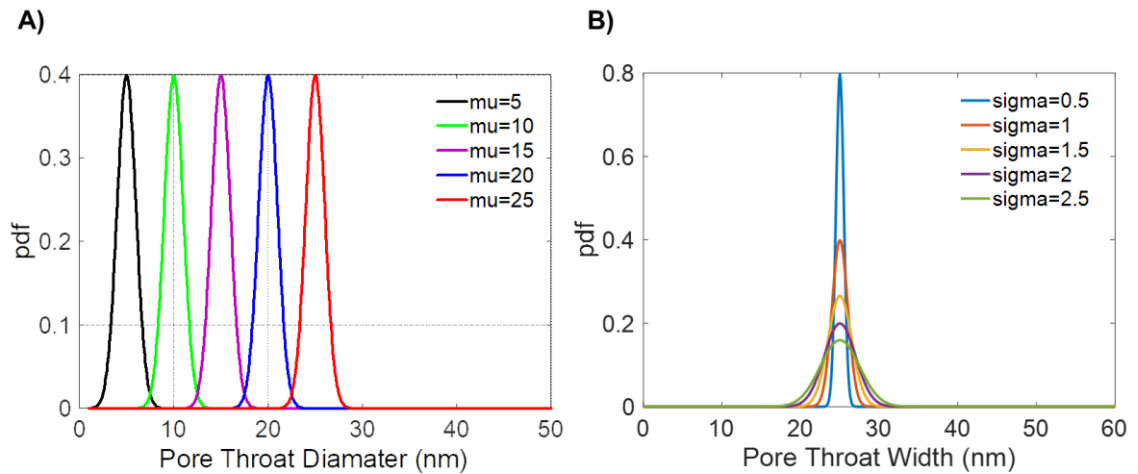


Figure 5. 17: Pore throat size distributions considered when (A) Sigma=1 nm and remains constant while mu changes, and (B) Mu = 25 nm and remains constant while sigma changes.

Pore throat chemistry

This study considers systems with varying mineralogy content, namely, silicon oxide (silica), magnesium oxide (MgO), aluminum oxide (alumina), calcite, and muscovite. These minerals closely resemble those found in the inorganic part of shale rocks.^{36,307,308} Five different compositions, shown in Table 5.3, were implemented. The composition of the pore throats was used, together with their size, to determine the diffusivity of supercritical methane. To assign diffusion coefficient values to the pore throat diameters for each substrate, the digital libraries produced in Part I of this chapter (see Figures 5.13 and 5.18) were used. Note that to generate these libraries, only supercritical methane was considered, as a pure fluid. If moisture was present, water would could fill (partially or fully) some of the pore throats, generating additional barriers to fluid transport. For the pore networks considered in subsections 5.2.3.1.1 – 5.2.3.1.3, the composition of pore throats was 100% silica.

Table 5. 3: The mineral composition of the five systems generated to investigate the impact of pore throat chemistry on the diffusivity of supercritical methane.

Mineral concentration	Silica	MgO	Alumina	Calcite	Muscovite
System 1	20%	20%	20%	20%	20%
System 2	10%	30%	20%	20%	20%
System 3	30%	20%	10%	20%	20%
System 4	20%	20%	10%	30%	20%
System 5	20%	20%	30%	20%	10%

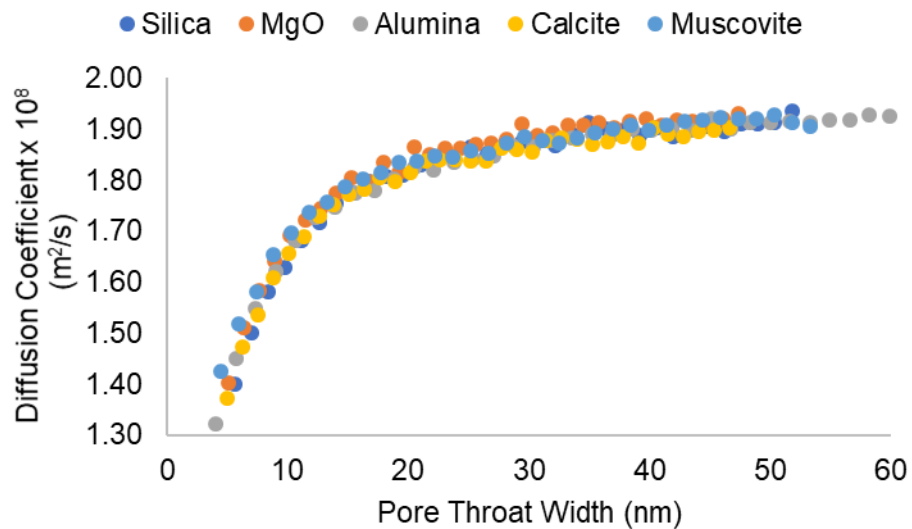


Figure 5. 18: Digital Libraries obtained from Part I of this chapter, presenting the relationship between the pore chemistry, the pore throat width, and the diffusivity.

Pore network generation – Algorithmic steps

Several sets of pore networks were generated, within each of which only one pore feature was changed, while the other parameters remained constant. The number of voxels in the simulation box was kept constant for the various pore networks. The simulation box is made by inserting 10 voxels in the x and y directions, respectively, and 5 voxels in the z direction. The boundaries of the lattice are open, making the lattice

periodic in all three dimensions. The outcome is a $10 \times 10 \times 5$ matrix, presented in Figure 5.19.

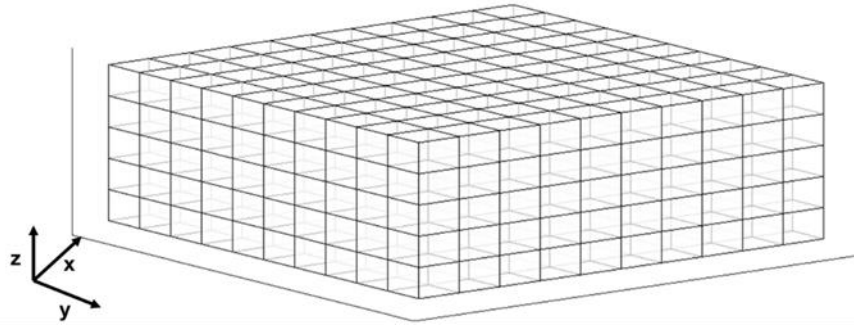


Figure 5. 19: Representation of the 3D KMC lattice containing 10 voxels in the x, and y dimensions, and 5 voxels in the z, yielding a 500-voxel lattice. All boundaries are periodic.

To construct the pore networks, the algorithmic steps presented in Figure 5.20 were followed. The first parameter selected is the matrix porosity, which defines the number of pores inserted in the lattice. All the pores have the same size and are assumed to act as reservoirs, where molecules preferably accumulate. These can be considered as well-mixed systems, where transitions happen fast and could resemble minima in a PES. On the other hand, the pore-to-pore throat transitions and vice versa are more difficult to take place and can be considered as rare events. To speed-up the 3D KMC simulations, only on the latter type of transitions is simulated. The positions of the pores are randomly assigned within the lattice, via the uniform random number generator. If a lattice voxel chosen in the routine is already occupied by a pore, a different position is selected for the new pore.

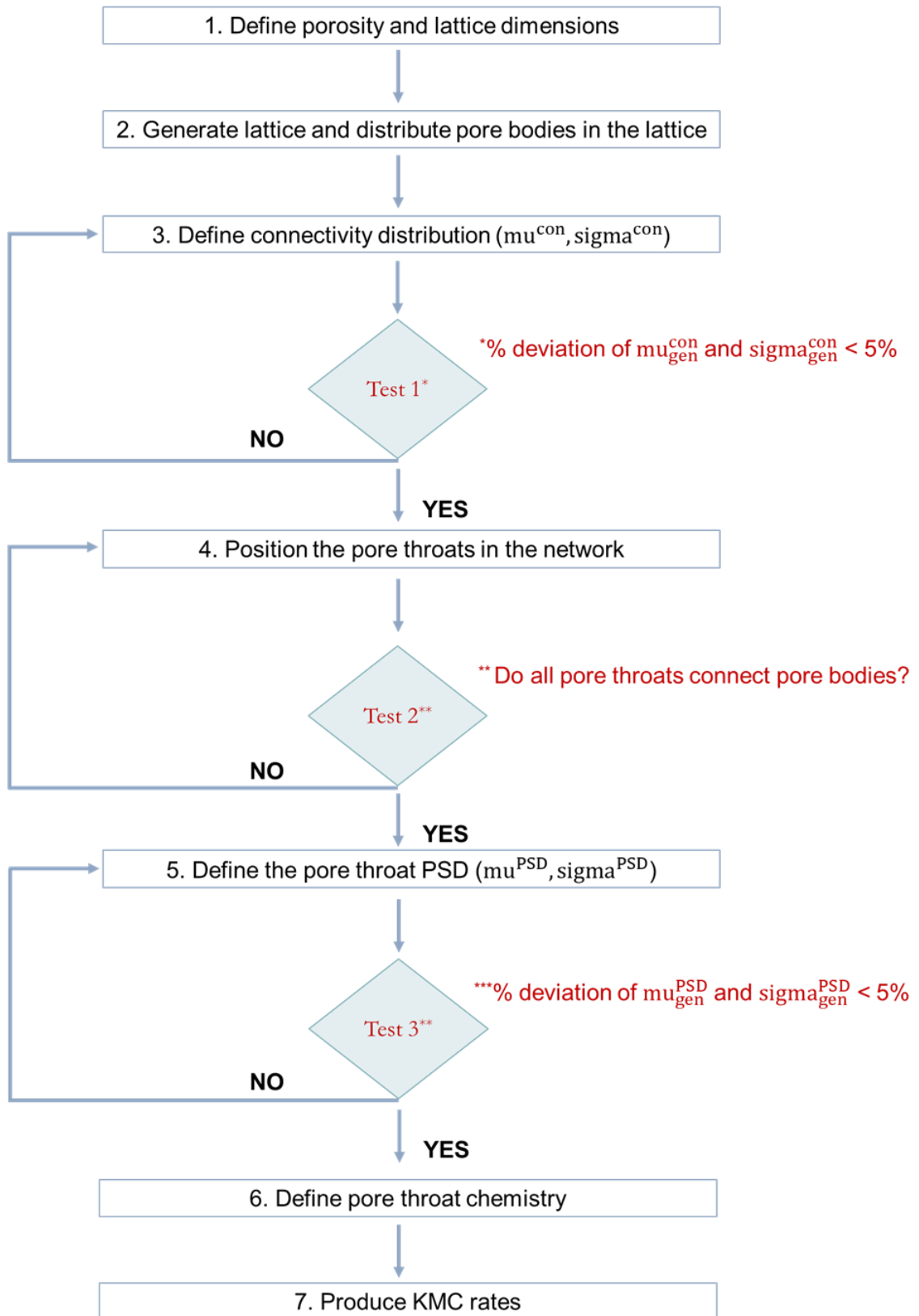


Figure 5. 20: The algorithmic steps implemented for the pore network generation using a stochastic approach.

Once all pores are placed in the lattice, the connectivity is needed to identify the pore throats. While sampling through a connectivity distribution, a list of connections is generated. To test whether the generated distribution of connectivity matches the target distribution, the μ and σ of the two distributions are analysed. The generated networks are accepted if the % deviation between these values is less than 5%, otherwise a new distribution needs to be generated. The number of elements in the produced list of coordination numbers, in other words the number of samples taken from the connectivity distribution, is equal to the number of pores in the network, as defined by the porosity value. At this stage, each pore has a maximum of 6 connections available. Once the list of connections has been identified, each pore is matched randomly with a coordination number. Depending on the coordination number selected, there are up to 6 possible KMC rates that can be determined for a given pore.

These rates define the direction a particle may follow travelling from that pore; towards the voxel on top, bottom, left, right, back, and forth. The direction of the jump is randomly selected, so that diffusion is equally probable in all three dimensions. Once the direction is defined, a test is performed to see if a pore is present in the neighbouring voxel. If the voxel is empty, a different direction is selected, etc. All connections must begin and end in a pore body, otherwise a new configuration of pore bodies is produced. The process is repeated until all connections are assigned to voxels containing pores and the appropriate number of neighbours surrounding them. However, using this methodology, a pore may be connected to a neighbouring voxel with zero connectivity. In that case, if a molecule ends up in this pore it remains “stuck” and is unable to transport anywhere else during the simulation. The process of assigning coordination numbers to pores is time consuming but necessary, especially when generating networks with low porosity and high connectivity.

Next, the width of the pore throats is determined. The pore throats are considered to be slit-shaped, and their diameter is dictated by a selected PSD. Stochastic sampling is implemented to sample through the target PSD and select the diameter of each pore

throat. To validate the network, the generated PSDs are plotted against the reference PSDs presented in Figure 5.17. The μ and σ values of the generated PSDs are also extracted and compared against the initial ones. If the % deviation between the produced and actual PSDs is less than 5%, the pore chemistry is assigned, which is an input parameter. According to the % of silica, MgO, alumina, calcite, and muscovite in the network, the number of pores made of these materials is specified. The last step of the algorithm is to assign the KMC rates across the network. To that ends, the digital libraries obtained from Part I of this chapter (as summarised in Figure 5.18) are utilised. Depending on the pore throat chemistry, the diffusion coefficient associated with the pore diameter selected from step 5, is obtained from the corresponding digital library. The diffusion coefficient values are then transformed to KMC rates using Eq. (5.13), as discussed in Part I of this chapter:^{151,176}

$$r^{\text{KMC}} = \frac{D}{l^2} \quad (5.13)$$

When all 7 algorithmic steps are completed, the generated list of KMC rates is used to inform the 3D KMC model.

3D KMC model for fluid diffusion

The KMC algorithm, as described in Part I of this chapter was implemented for the 3D pore network modelling presented in this study. The Mersenne Twister MT19937¹⁸⁹ uniform random number generator was utilised to produce the required random numbers, for the selection of the event and the calculation of the time required for the selected event to happen, at each iteration of the KMC algorithm.

To simulate diffusion, a single particle was randomly inserted in the lattice. To obtain accurate statistics, several independent runs are performed, as summarised in Figure 5.21. The initial position of the particle is randomised 75 times for each initial

configuration, 10 independent KMC runs are performed to compute the diffusion coefficient.

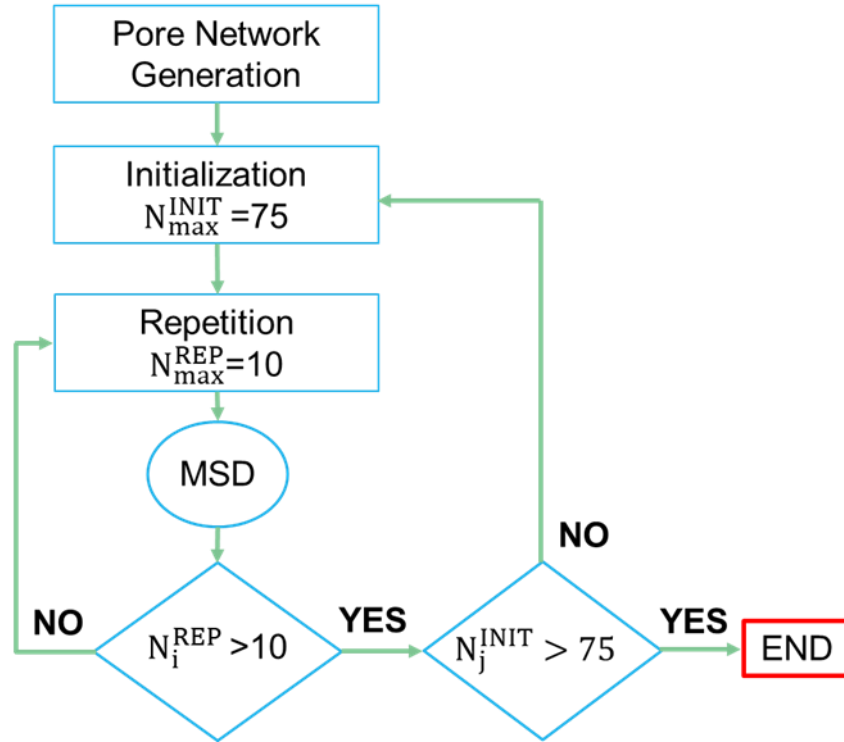


Figure 5. 21: Algorithm for 3D KMC independent runs

The particle trajectory was monitored and the mean square displacement (MSD) was calculated over time, which, coupled with the Einstein equation, see Eq. (5.5), yield the fluid diffusivity.

$$D_{xyz} = \frac{1}{6} \lim_{t \rightarrow \infty} \frac{\langle |\mathbf{r}_i(t) - \mathbf{r}_i(0)|^2 \rangle}{t} \quad (5.14)$$

In Eq. (5.5), $\langle |\mathbf{r}_i(t) - \mathbf{r}_i(0)|^2 \rangle$ are the MSDs in the XYZ space. The simulation time is 70 ns and a sample to monitor the particle's position is taken every 0.07 ns. From the 10 independent runs performed, the standard error was calculated using Eq. (5.12).

Results and discussion

Effect of network's connectivity

To quantify the impact of pore throat connectivity, 15 networks were generated with constant porosity (15%), chemical composition (silica), and pore throat size distribution ($\mu=25$ nm, and $\sigma=1$). The only parameter changing among these 15 networks was the connectivity level, also referred to as coordination number (see Figure 5.14 for details). In the first 5 networks, μ was increased incrementally, from 2 to 6, while σ was kept constant at 1. For the next 5 networks, connectivity was low ($\mu=2$) and σ was gradually increased from 0.5 to 2.5. For the last 5 networks, connectivity was high ($\mu=5$) and σ was from 0.5 to 2.5. Note that the pore throat widths are described via a size distribution, rather than a single value. Thus, when a pore is connected to several other pores, the slit pore throats used as channels have different widths. The smaller the widths are, the lower the likelihood of transition of molecules, due to the higher resistance to flow. Thus, when the molecules are given the option to choose between wide and narrow pore throat widths, it is expected that the fast transitions through the wider pore throats will be more frequent compared to those that are narrower.

Diffusion was calculated using the stochastic KMC method and analysing the molecular trajectories. Figure 22 – panel A presents the results obtained from the first 5 networks (increasing connectivity). An exponential increase in diffusivity is observed as the networks' connectivity increases. Indeed, when μ increases from 2 to 6, the diffusivity increases by almost 1 order of magnitude. This is expected for two main reasons. Firstly, as the connectivity increases, more pore to pore connections are available, yielding longer pathways. This is captured by the MSD obtained. Secondly, since more pathways are generated, the particles have more choices among pathways, which enables them to visit more of the material.

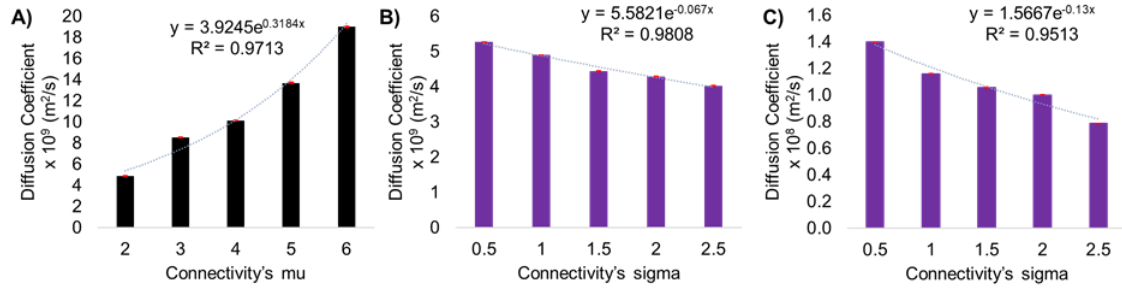


Figure 5. 22: Effect of the networks' connectivity on methane diffusivity. A - Results obtained when the networks' sigma value equals 1 and mu increases. B and C – Results for networks with low (mu=2), and high (mu=5) connectivity, respectively, with increasing sigma. The distributions representing the networks in A-C are shown in Figure's 1 A-C, respectively.

The 15 generated networks, presented in Figure 5.14, are assumed to exhibit an exponential relationship (according to Figure 5.22) between the pore network's connectivity and methane diffusivity that can be expressed as:

$$y = K_i e^{L_i x} \tag{5.15}$$

In Eq. (5.15), y is the diffusion coefficient (in m²/s), x is the value of the distribution's parameter (connectivity), K and L are constants, and i = 1, 2 and 3 for the networks presented in panels A, B, and C of Figure 5.22, respectively. According to the R² value calculated during fitting, the variance in the diffusivity is strongly associated to the variance in the network's connectivity characteristics. However, a linear or polynomial fitting could also be implemented, since there is sufficient evidence that the relationship between the network connectivity and diffusivity is explicitly exponential. In this work it is assumed that an exponential fitting is adequate. To allow for better comparison between panels A-C in Figure 5.14, the fitting is set exponential to all three figures. If a linear or polynomial fitting was to be employed, the values of the corresponding K and L are constants (quantitative measures) are expected to be different than those reported here, but the discussion regarding the trend observed (qualitative measures) are expected to be similar. The error bars calculated are shown in red. They are relatively small for all networks considered. Visualising the results obtained, together with the error bars, no

overlaps are observed, confirming that the number of independent runs selected for our calculations was appropriate.

In the remaining two sets of pore networks as the connectivity distributions become broader, pores that are poorly connected co-exist with others that are highly connected. It is not clear how these changes affect fluid transport. On one hand, the increase in the proportion of highly connected pores could promote fast diffusivity. On the other hand, more pores with low connectivity could yield the opposite effect. It is also likely that the results depend on the sensitivity of fluid transport on the existence of poorly- vs. highly-connected pore bodies.

For both low ($\mu=2$) and high ($\mu=5$) connectivity systems (Figure 5.14 – panels B and C, respectively), diffusivity is found to decrease as the sigma increases (Figure 5.22 – panels B and C). Considering that the diffusion coefficient reduces when the amount of pores with low connectivity is increased, and that the connectivity distributions considered are log-normal, it is concluded that the diffusivity is more sensitive to the presence of poorly connected pores. Comparing L_2 and L_3 values, calculated from the exponential trendline fitting (Eq. (5.15)), it is found that $L_2=0.07$ and $L_3=0.13$, suggesting that when the connectivity is high, the decrease in diffusivity due to increasing sigma is more pronounced. To better understand the reason behind this observation, the distributions presented in Figure 5.14 – panels B and C were investigated. When the connectivity is low ($\mu=2$), the number of highly connected pores increases as sigma increases. Contrary, when the connectivity is high, an increase in the sigma value results in the appearance of more poorly-connected pores. This confirms that low-connectivity pores have a more significant impact on diffusion, compared to high-connectivity ones. In practical terms, building from this observation, it is possible that when it is desired to increase diffusivity and permeability for a network characterised by high connectivity, applying techniques to increase the network's connectivity (i.e., generate secondary fractures in a reservoir) will result in modest improvements of the transport properties.

On the contrary, the same treatment will have much stronger beneficial effects when applied to a low-connectivity network.

Moreover, the coefficients L_1 (equal to 0.32), L_2 , and L_3 are indicative of how sensitive the diffusivity is when the networks' connectivity changes. Since L_1 is significantly higher than the absolute values of L_2 and L_3 it can be extrapolated that the diffusivity is more sensitive to changes in the network's connectivity (μ), rather than the degree of heterogeneity, caused due to the increase in the σ 's value.

Effect of porosity

To investigate the effect of porosity, two sets of pore networks were considered, one of which with low ($\mu=2$) and one with high connectivity ($\mu=5$). In each set of networks, 10 porosities were assigned, ranging from 5% to 50%. To obtain meaningful statistics, for each porosity 5 equivalent networks were generated, following the protocol described in Figure 5.20. In all cases, the pore throats that connect the pore bodies are made of silica and are characterised by pore width distribution described by $\mu=25$ nm and $\sigma=1$.

Figure 5.23 presents the mean values obtained for the diffusion coefficient, as a function of porosity, for the two network families. Panel A presents the results obtained when considering networks with low connectivity and panel B those with highly connected pore bodies. The results show that, for porosity from 5% to 30% there is no change in the diffusion coefficient calculated. However, a rapid, almost exponential increase is predicted when the porosity exceeds the 35% threshold. This trend is observed in pore networks with both low and high connectivity.

As the porosity of the system increases, more pore bodies are present within the system. Considering that the connectivity remains unaltered, the new additional pores provide the connections with their adjacent neighbours as described by the connectivity distribution curves. As the number of pores in the system increases, more pores become

interconnected, generating longer pathways. This is also shown in the 3D pore networks presented in Figure 5.15. As this higher effective connectivity due to increased porosity, appears, the initial plateau in calculated diffusivity transitions to a rapidly increasing function of porosity, as shown in Figure 5.23. Since the 3D lattices are periodic in all 3 dimensions, this 35% threshold is not expected to be strongly dependent on the representative elementary volume (REV) used to construct our systems. In fact, a similar threshold porosity value ($\sim 39\%$) was observed by Prasianakis et al.,³⁰⁹ who simulated an acidic aqueous mixture diffusing through a calcite mineral matrix, dissolving part of it, thus increasing the system's porosity. An exponential increase in permeability was observed when the 39% porosity threshold was reached. In agreement with those observations, the results obtained in this study suggest that the network's transport behaviour can be significantly improved when the porosity is artificially altered. However, the process of modifying the network's porosity utilising chemical reactions should be carefully planned, as the reaction by-products (mineral precipitation in Prasianaki et al.,'s case study) could clog the existing pore bodies thus reducing the network's connectivity, and fluid transport.

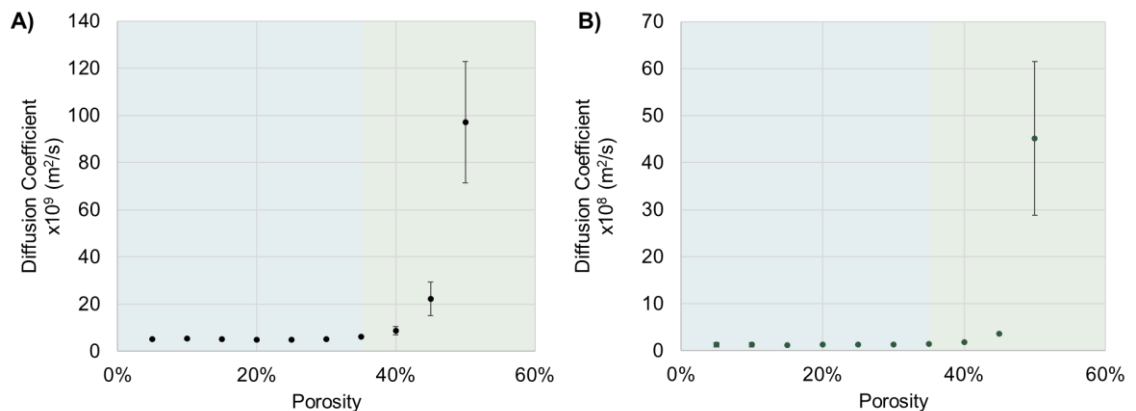


Figure 5. 23: Relationship between the networks' porosity and methane diffusivity for (A) low connectivity ($\mu=2$) and (B) high connectivity ($\mu=5$) networks. The error bars are calculated considering 5 equivalent pore networks for each porosity value and applying Eq. (5.12).

Effect of pore throats size distribution

For the investigation of the impact pore throat widths have on the diffusivity, 20 pore networks in total, were considered. In those networks, the pore throat size distribution was described via log-normal distributions. In the first 10 pore network sets the PSDs' sigma was kept constant and equal to 1, while the PSDs' mu was ranging between 5 and 25 nm. The network connectivity was low ($\mu=2$). The next 10 pore network sets consisted of PSDs with constant mu ($\mu=25$ nm), while sigma was in the range of 0.5-2.5. The connectivity of those networks was high ($\mu=5$). For consistency, the pore throats were all made of silica. Figure 5.24 – panel A presents the results obtained for the low connectivity systems and in Figure 5.24 – panel B presents those for the highly connected networks, respectively.

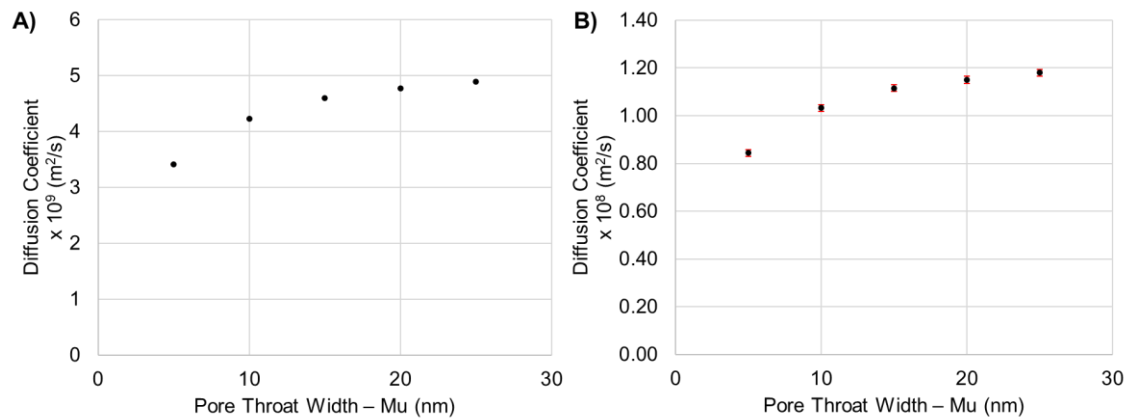


Figure 5. 24: Relationship between the pore throats width size distribution and methane diffusivity for (A) low connectivity and (B) high connectivity networks. For the mu of the pore throat widths, the distributions presented in Figure 5.17 – panel A are considered.

For both panels A and B in Figure 5.24, the results show that as the pore throat size distribution increases, the methane diffusion coefficient also increases. This is expected, since wider pore throats allow fluid to transport faster, as shown in Figure 5.18. The results in Figure 5.24 show that when the pore throats are narrow, increasing their size yields moderate increases in diffusivity, while the effect is less pronounced when the pore throats are wide (i.e., see the plateau in the datasets). This is a direct consequence of the relationship between diffusion coefficient and pore width, as observed for single

pores (see Figure 5.18). The practical implication of this observation is that once the pore throats have reached sizes of ~ 30 nm, further widening them has little effect on the overall diffusion coefficient of supercritical methane.

In Figure 5.24, the error bars as estimated by applying Eq. (5.12) are also reported. In panel A the error bars are smaller than the symbols, while in panel B they are slightly larger. Analysis of the errors shows no overlaps among results obtained for different pore throat size distributions, which confirms that the number of independent runs performed was sufficient to obtain statistically significant results. Comparing the results shown in panel A to those in panel B, an almost 2.5 times increase is observed, which is due to the change in the networks' connectivity. By observing the trend of the diffusivity increase, as a function of the pore throat width, it is observed that the connectivity of the network (low or high), affects the diffusivity in a similar manner, from a qualitative perspective.

The effect of changing the PSDs' sigma on the diffusivity calculated is quantified in Figure 5.25. It is expected that as the PSDs' sigma increases, narrow pore throat widths coexist with wider ones. Pore networks with low and high connectivity (results shown in panel A and B of Figure 5.25, respectively) were both considered. It is observed that the heterogeneity of the pore throat size distributions, i.e. the sigma value, has no impact on methane diffusion coefficient. This result is phenomenologically explained by the following observation: when particles have the option of diffusing to neighbouring pore bodies travelling across narrow or wide pore throats, they mostly prefer the pathways of lowest resistance, i.e., the wider pore throats. This is reinforced by the observation that the same trend is observed for both low and high connectivity pores, although the self-diffusion coefficients obtained in networks with high connectivity are larger than the others by, in general, a factor of almost 2.5. When the networks are highly connected, there are more possible pathways available for the particles to diffuse, and the proportion of the wider pore throats is considerably increased.

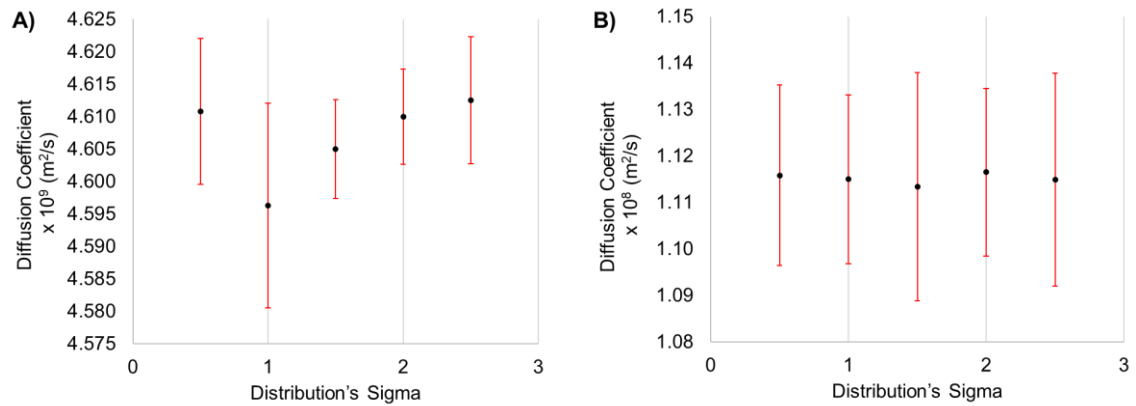


Figure 5. 25: Relationship between the pore throat width size distribution and methane diffusivity for (A) low connectivity and (B) high connectivity networks. For the sigma of the pore throat widths, the distributions presented in Figure 5.17 – panel B are considered.

Effect of pore throat chemistry

To investigate the effect of the chemistry of the pore throat widths, 2 sets of networks, each containing 5 pore networks, were generated. The first set contained networks with low connectivity ($\mu=2$), the second, high connectivity ($\mu=5$). The pore throats size distribution and the network porosity were kept constant. The composition of the pore networks in each of the 2 sets of 5 networks is shown in Table 5.3. The results obtained for the self-diffusion of methane, together with the error bars, are presented in Figure 5.26. The chemical composition of the pore throats seems to have little to no effect on the diffusion coefficient calculated. The same observation was reported by Ismail and Zoback, in which permeability measurements indicated that shale mineralogy does not have a strong effect on permeability.³¹⁰ Based on the results obtained, this observation could be explained considering the diffusion coefficients obtained in single pores of different widths (see Figure 5.18): when the pores are of width ~ 15 nm or wider, the chemistry of the solid substrate has little effect on the diffusion coefficient of supercritical

methane. This result could change when the composition of the fluid changes. For example, in hydrated pore networks (similar to those discussed Chapter 3), water molecules could accumulate near the pore throats, depending on the chemistry of the solid, yielding additional kinetic barriers to gas transport that are not explicitly considered in this study. It is worth noting that in Figure 5.26 no statistically significant difference is observed between the self-diffusion coefficients obtained in the networks with low and high connectivity (panels A and B, respectively). This is expected and validates the accuracy of the protocol followed to construct the various pore networks.

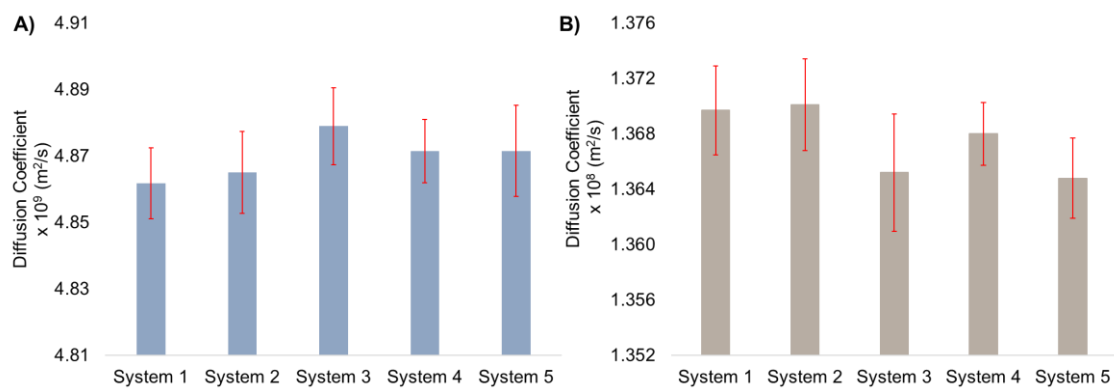


Figure 5. 26: The effect of pore throat chemistry on the self-diffusion coefficient of supercritical methane. Results for pore networks with low and high connectivity are shown in panels A and B, respectively.

Sensitivity analysis

This subsection presents an overview of the results obtained and discussed above, by performing a sensitivity analysis to determine the impact of connectivity, porosity and pore throat size distribution on the diffusion coefficient of supercritical methane within the various pore networks. To determine the contribution of each network feature on the output (methane diffusion coefficient), the % change in output is plotted as a function of the % change in network feature. In this analysis the effect of the spread (sigma) for the connectivity and pore throat width sizes is not considered, since it was found to have moderate to low significance on methane diffusivity. For the same reason, the effect of

the pore throat chemistry is also not considered in the sensitivity analysis. Because the analysis presented in subsections 5.2.4.1 – 5.2.4.3 quantifies how changes in pore network features promote or hinder diffusivity, only the absolute % change in output is considered here. Figure 5.27 presents the results obtained for pore networks with low (panel A) and high (panel B) connectivity.

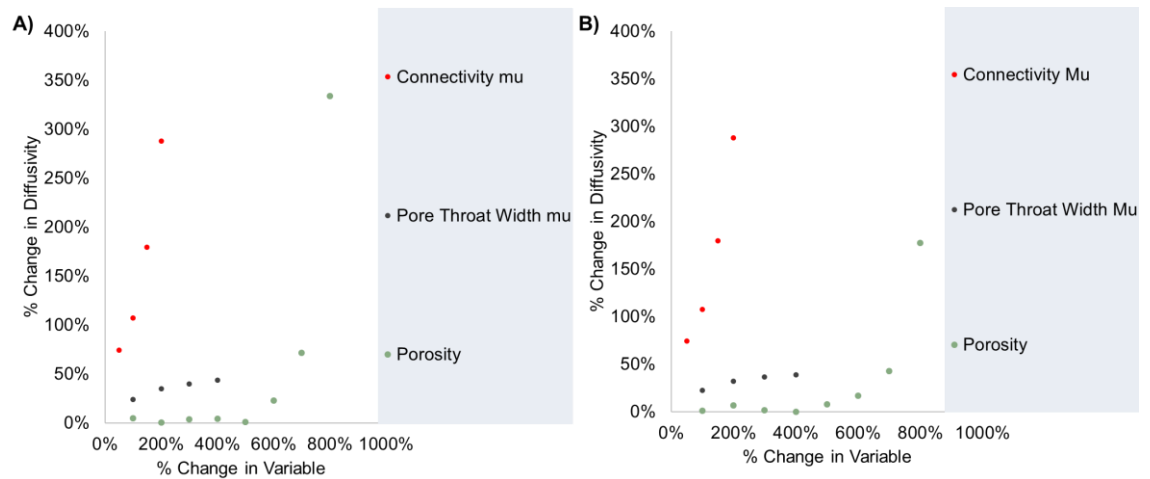


Figure 5. 27: Sensitivity analysis on the impact of connectivity, porosity, and pore throat width size distribution on methane diffusion coefficient. Results for pore networks with low and high connectivity are shown in panel A and B, respectively.

Comparing the results in panels (A) and (B), it is observed that the trends, and their magnitudes are consistent. It is found that: (1) changes in the pore networks connectivity have the greatest impact on methane diffusion; (2) changes in pore throat size distributions yield the second largest impact on methane diffusion, at least when the network feature changes for up to 400%; (3) changes in porosity have little effect on methane diffusion until changes in porosity are of at least 400%.

Considering the results shown in Figure 5.18 (methane diffusion coefficient in single pores as a function of pore width and pore chemistry), supercritical methane shows a self-diffusion coefficient within the pores that is bulk-like when the pore width is of at least 30 nm. To achieve a 700% change in the pore throat size distribution's μ , μ should be 40 nm. The diffusion coefficient of supercritical methane is expected to be

approximately 1.18×10^{-8} m²/s, for the case of the highly connected network, which corresponds to an almost 40% improvement in diffusivity. For 700% change in porosity, the % change in diffusivity is almost 45% and for higher porosity values the diffusivity exponentially increases. Thus, it can be assumed that the porosity and PSD ranking will remain the same if the analysis of the PSDs' μ was to be extended for $\mu > 25$ nm values.

From a practical perspective, these observations can be used to provide recommendations on how to increase the transport properties within a pore network, when the network's characteristics are known. Since connectivity is the most important parameter, any strategy aiming to increase this feature is expected to result in significant improvements in fluids transport. For example, during the hydraulic fracturing process, the creation of more dense secondary fractures could yield significant increases in production rates. This observation is consistent with field measurements during the development of the Wolfcamp and Spraberry formations.³¹¹ Improvements in the network's porosity are also expected to be beneficial, but only after the 'critical' threshold of ~30% porosity is reached. This is consistent with results reported by Prasianakis et al.,³⁰⁹ The pore throats size distribution is an important feature, but, in the case of unconventional reservoirs, it depends on factors that operators have no control of. However, this feature can be altered in engineering materials used for example in catalysis (e.g., zeolites). Finally, it is important to highlight that the synergistic alteration of both connectivity and porosity is expected to be the most impactful, as shown in Prasianaki's et al., study, where the chemically active agents were dissolving the rock matrix, resulting to a simultaneous increase in porosity and pore network connectivity.

Conclusions

In this chapter a, 3D KMC model was developed and used to perform two separate studies. In the first study (Part I), a methodology that synergistically implements atomistic equilibrium molecular dynamics (EMD) simulations and stochastic 3D kinetic Monte

Carlo (KMC) calculations was proposed and validated. The proposed methodology was used to predict self-diffusion coefficient for gases confined in pores as a function of pore width. In this study, slit-shaped pores were considered, but the methodology proposed can be applied to cylindrical or rough pores as well. Initially atomistic EMD simulations were conducted in pores of moderate width (5nm) and the representative data, obtained within 3 regions inside the pores, were used as input to inform the 3D KMC model. Then a sophisticated simulation protocol was implemented to obtain diffusion coefficients as a function of the pore width. The number of iterations and initialisations implemented in this protocol ensured that the KMC data obtained for the various pore widths were statistically different and not overlapping.

The proposed methodology acknowledges advantages and disadvantages of EMD and KMC approaches and implements each in the most efficient and impactful way. For instance, the EMD simulations provided detailed and accurate atomic-scale data, which are necessary for obtaining accurate KMC calculations, at the expense of long run times. Considering that the computational time required for the KMC simulations is significantly smaller than that required for EMD simulations, the KMC model was used to predict the diffusivity of methane in slit-shaped pores of increasing pore width. Comparing the KMC predictions to atomistic EMD simulations in pores of width 10 and 25 nm, it was found that the % deviation between the two methods is less than 10% for all cases considered here. Further, the combined EMD-KMC approach allowed for the quantitative description of the self-diffusion coefficient of confined supercritical methane as a function of pore width. The outcome of this study was a digital library that matches diffusivity to pore widths and pore chemistry at minimum computational cost. Within the pores considered, it was found that confinement reduces the methane diffusivity, and that bulk-like diffusivity is reached when the pore width is at least 30 nm, and in some cases more than 50 nm, depending on the pore chemistry. This digital library was used in the second study performed (Part II) to simulate 3D pore networks that contain pores with varying chemistry and pore sizes. It is expected that the methodology proposed, in Part I, can be

applied to study gasses at different densities and temperature conditions, as well as mixtures. While the approach is expected to be useful in improving our ability to predict gas permeability in shale samples, many applications that involve fluid transport across pore network, including catalysis, could benefit from the proposed methodology.

In the second part of this chapter, the developed 3D KMC model was implemented to determine the impact of four pore network characteristics on the transport of fluids. The characteristics considered are the pore network's connectivity, porosity, pore throat widths, and pore chemistry. The 3D pore networks generated consisted of pore bodies, pockets where molecules accumulate, connected via slit-shaped pore throats. To generate the 3D pore networks a rigorous protocol was followed.

For all the 3D pore networks generated for this study, the uncertainty of the mean values reported was calculated using a standard error formula. It was found that the results obtained together with the reported errors did not overlap for most of the case studies considered. This confirms that the number of independent runs selected for the stochastic calculations were appropriate to provide results that are statistically valid. The systems that yield overlapping results are those investigating the effect of pore chemistry and the pore throats distributions' variance in the diffusion coefficient of supercritical methane. This is because of the similar transport properties of the substrates considered, and the ability of molecules to select a low resistance pathway when the networks become highly heterogeneous.

It was also found that the pore network connectivity has a significant impact on the diffusivity of fluids. This is expected, since the increase in connectivity results in the generation of additional pathways for the molecules to diffuse. In fact, as the connectivity increases the transport of fluids accelerates exponentially. This means that if a low connectivity network was to be treated to improve its connectivity, the improvement in transport properties is expected to be significant. Porosity was also found to yield an exponential increase in methane diffusivity, after a threshold value (~35%) was achieved.

Similar observations have been reported in other computational studies, strengthening this argument. For low porosity values, the diffusion coefficient exhibited a slow increase with the increase of porosity. The hypothesis is that, for low porosity values, the pores may be connected, but the level of cluster connectivity is low. When considering pore throats with increasing width diameters, the calculated diffusion coefficient increased with a moderate rate initially, until a plateau was almost reached. This is probably due to the digital libraries considered to correlate the pore widths selected and the diffusion coefficient, when considering single pore throats. The sensitivity analysis revealed the connectivity to be the most important parameter that affects the diffusivity of fluids followed by the pore throat widths and finally porosity. The network connectivity and porosity are both characteristics that can be artificially altered. For example, during the hydraulic fracturing process, the creation of denser secondary fractures and treatment of the rock formation with chemically reactive compounds can increase the network's connectivity, and porosity respectively. However, a synergistic approach that combines the improvement of both features is expected to result the best outcomes, as long as these strategies are carefully planned, sustainable, taking into consideration their environmental effects.

Summary and future work

Summary and conclusions

In this research study, Kinetic Monte Carlo (KMC) is implemented as a stochastic approach to investigate the transport of fluids in porous media. Although KMC has been widely applied to address a number of surface diffusion-reaction problems, only a few studies have reported on the use of KMC to address mesoscopic transport in porous media. The media of interest in this research study are those that resemble shale rocks, which have a complex and heterogeneous structure and very low permeability. These formations contain large amounts of natural gas and have been widely exploited in the U.S, but not yet in the UK.

The first aim was to construct and validate a 1D KMC algorithm that simulates particle diffusion, and test whether it is suitable for fluid transport studies. In an effort to simplify a 3D two-phase transport problem in a 1D single phase one, previously studied using molecular dynamics (MD), it was evident that the KMC rates need to be carefully selected. From the studies undertaken in this thesis, different approaches were implemented towards the calculation of the transition rates, depending on the available input data. For example, in Chapter 3, density profiles together with potential of mean force calculations and diffusion coefficients, obtained from the literature, were used to calculate the KMC rates. From this initial study, KMC was found to be able to simulate fluid transport processed while certain advantages of the method emerged.

Then, the 1D KMC was extended to 2D and was implemented to calculate the effective matrix permeability of synthetic networks, shale sample, and rock samples that were treated with proppants. The 2D KMC was validated against analytical solutions of the 2D diffusion equation. To select the KMC rates, transport models from the literature were used to assign permeability coefficients in the voxels of the lattice. To convert these permeability coefficients into KMC rates, an equation was proposed and validated. The predictions obtained from the 2D KMC model were compared against those obtained

from two deterministic approaches. From a series of several synthetic networks and sensitivity analysis, recommendations were made on the optimal conditions under which each method should be used. The 2D KMC was then implemented to estimate the permeability of a shale rock sample and investigate the effect of proppants on the permeability improvement. An empirical correlation was generated that “translates” microfracture (MF) conductivity to fracture width maintained.

The 2D KMC was thereafter extended to 3D and implemented to generate digital libraries and perform pore network modelling studies. For the generation of the digital libraries, MD data were used as inputs. The outcome of this study was to obtain gas diffusivity as a function of the pore width at minimum computational cost. Single slit-shaped pores were considered consisting of minerals similar to those found in shales’ inorganic part. Then, the 3D KMC was employed to quantify the impact of four key pore network characteristics, including the pore chemistry, on the diffusivity of gasses. According to the results obtained, recommendations are provided on possible technological approaches to enhance fluid transport through shale rocks and equally complex pore networks.

The advantages of implementing KMC to simulate fluid transport are numerous. Firstly, the computation time required was significantly less compared to similar calculations conducted using MD simulations. Such KMC-MD comparisons were made in Chapters 3 and 5. However, to obtain accurate KMC rates, time consuming MD simulations need to be performed. As an effort to minimise the need of extensive MD simulations, which are often not available, a synergistic methodology was proposed in Chapter 5. This methodology acknowledges advantages and disadvantages of MD and KMC approaches and implements each in the most efficient and impactful way. The predictions made using this approach were in satisfactory agreement with results obtained from atomistic studies (MD) and the % deviation between the two methods was less than 10%.

Another advantage of the KMC is the ability to perform multiple independent runs and quantify the degree of uncertainty in the predictions. This is an essential step to (1) minimise the statistical noise, and (2) obtain results that are statistically valid. Moreover, since KMC simulations are significantly faster than MD calculations, multiple realisations of the pore networks can be constructed and simulated. When the analysis is based on a set of equivalent networks rather than a single one, uncertainties that may arise during the process of the networks' generation are minimised.

Although the KMC is significantly less time consuming, compared to MD simulations, it still requires a considerable amount of computing time, when compared to deterministic methods, such as the effective medium theory, or the simplified renormalisation technique. The computational efficiency of the KMC simulations strongly depends on the lattice size selected. When considering pore networks in which both the microscopic and mesoscopic features need to be simulated, such those found in shales, a very fine mesh needs to be created making the KMC challenging to implement. To address this issue two strategies were employed in this research study. The first was to optimise the event selection process, which is ultimately the most time-consuming step. The binary tree selection algorithm was employed in Chapter 4, replacing the linear selection one, resulting in significant computational savings. The second strategy was to implement multi-stage modelling. In Chapter 4, the shale rock, consisting of organic and inorganic matter, was simulated in two steps. In the first step the transport properties of the organic and inorganic matter were calculated and then used in the second stage of the analysis as input parameters. This multi-scale type of analysis furthered the applicability of the KMC, which can be now used as a tool to simulate fluid transport at different scales.

Proposed future work

The existing approaches for completion design and well space optimisation are inconclusive. Very recently, for example, Sen et al., reported that increasing well-spacing improves recovery after the 1st year of production, while Jaripatke et al., reported that tighter cluster spacing and shorter stage lengths improve productivity.^{311,312} Further, the

successful development of unconventional reservoirs using multi-stage hydraulic fracturing depends on multiple factors including geology and production practices/rock treatments (proppants, reactive fluids to partially dissolve the rock matrix, etc.), leading to un-foreseeable investment losses. To reduce financial risk, considering the intrinsic diversity of unconventional reservoirs, completion and production strategies should be customised for each formation, sometimes on a well-by-well case. This is a monumental challenge. Tackling this challenge, a user-friendly protocol is required to

- i. harmonise characterisation insights, recovery predictions and field-testing data to yield a reliable interpretation of the production potential;
- ii. seamlessly optimise completion design and production strategies to maximise unconventional's productivity, ideally on a well-by-well case.

Artificial Intelligence (AI) promises to revolutionise the technological landscape. Among various AI approaches, recent studies demonstrated that machine learning algorithms such as 2D and 3D convolutional neural networks (CNNs), using digitised rock samples as a training dataset, are able to predict permeability from image analysis alone.³¹³ As with other AI approaches, the quality of the predictions depend on the quantity and quality of the input data and the training label accuracy (known pore network characteristics). To this end, the proposed methodology should consist of the following development stages:

1. Development of a versatile and comprehensive digital library.
2. Implementation of the KMC approach in a multi-scale framework to predict permeability.
3. Calibration of an AI model to extend predictive capabilities.
4. Quantify recovery improvement due to completion design and treatment strategies.

In the first stage of the proposed methodology a diverse digital library needs to be constructed including geological information, physical properties, imaging data and permeability measurements for various formations. Additional data obtained from sample materials (e.g., ceramics, zeolites, concrete), as well as from custom-made 3D printed materials representative of unconventional formations could also be included in the digital library. These sample or custom-made materials would be beneficial, especially for the third stage of the proposed methodology, which is to train the AI model, as they have known pore network characteristics. This data will be categorised to generate a digital library. It is critical that the library must contain information on permeability at a variety of length scales, from that of the rock mass, to that of extensively fractured formations. Figure 6.1 summarises a proposed protocol that could be used for the multi-scale permeability modelling using the KMC. Once the AI model has been developed, trained, and tested, it can be used to systematically quantify the effects of various rock treatment technologies on the permeability improvement, such as reactive fluid stimulation, proppant loading and size effects.

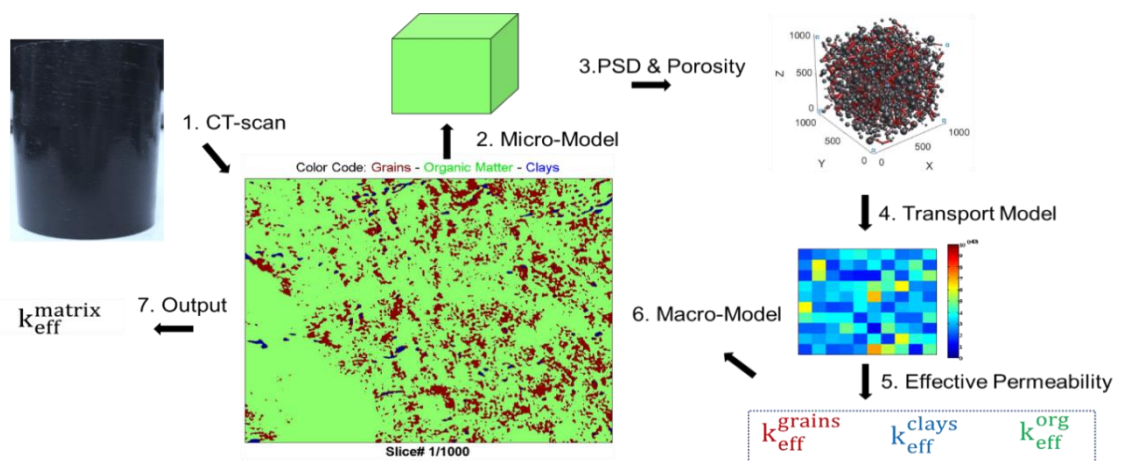


Figure 6.1: A stochastic approach to calculate matrix permeability using imaging, porosity and pore size distribution data.

The implementation of the KMC approach, combined with the development of the AI model could significantly speed-up the time required to perform case study runs. Thus, multiple scenarios can be considered by the user, who could quantify different stages

throughout the life of an asset (pressure depletion, proppant deactivation, rock dissolution, etc.) achieving a dynamic time-dependent evaluation of the reservoir's permeability. This could lead to optimisation of completion design and production strategies on a well-by-well case, which is essential for maximising unconventionals' productivity and reducing financial risks.

Appendix A

Validation of the KMC algorithm – Gillespie’s reaction networks

In his work, Daniel Gillespie¹⁸³ performed computational studies for five different systems while using the direct KMC algorithm he proposed. The first two systems investigated, deal with simple reaction networks, while the remaining three describe systems with more complicated behaviour. Appendix A provides a brief description of the systems, the conditions and the sampling scheme Gillespie used. Based on this information, a KMC code was constructed in order to reproduce the results Gillespie reported.¹⁸³ As an effort to compare the stochastic and the deterministic formalism, the deterministic reaction-rate equations together with the propensity expressions used in the KMC algorithm are reported for each system. Moreover, for every system investigated in Appendix A (Systems 1 – 5), the results obtained by the developed KMC model (blue colour – right panels) are compared against the results reported by Gillespie (left panels) and the deterministic solution of the M-equation (red colour – right panels). Further information regarding the calculation of the stochastic rate constants and their dimensionality can be found in Gillespie’s work.^{183,184} To be consistent with the notation used by Gillespie, the symbol a_i is used for the propensities, where i is the index representing the type of reaction-transition taking place.

System 1

The first system investigated, is a simple set of coupled chemical reactions, which describe the decay of species X to species Z, as shown in Eq. (A.1)



The reaction proceeds with a rate constant $c = 0.5 \text{ s}^{-1}$ and the initial population of the X species is 1000. Since there is only one type of reaction taking place in this system, only one propensity needs to be defined in the KMC algorithm, given by Eq. (A.2):

$$a_1 = cX \quad (\text{A.2})$$

For system 1 there was no sampling scheme implemented and hence all data points were saved and reported. Each time an event took place, the time and the population of the system were plotted. Moreover, due to the simplicity of the system, the population of X species can be predicted by solving the M-equation or by following the deterministic formulation, as expressed in Eq. (A.3):

$$X(t) = X_0 e^{-ct} \quad (\text{A.3})$$

Figure A.1 combines the results reported by Gillespie and the results produced by the developed KMC code. To validate his results, Gillespie reported the population of species X, as predicted by his KMC algorithm, against those obtained by solving the M-equation. In Figure A.1 (left panel) Gillespie's stochastic results are plotted together with a one-standard deviation envelope (shown in dashed lines), and a two-standard deviation envelope (shown as a continuous line). In a similar manner, the results obtained by the developed KMC algorithm (blue colour – right panel) were validated against the deterministic predictions (red colour – right panel).

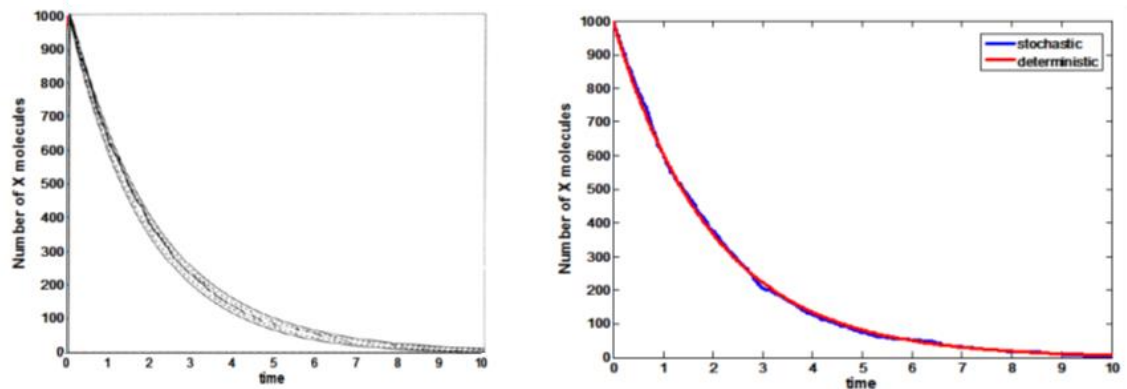


Figure A. 1: Comparison between Gillespie's data (left panel) and the KMC code data (right panel).

System 2

Another example of a simple reaction network can be described by the following set of reactions:



This system consists of 3 species; an ambulant reactant X, a product Z and a compound Y, which serves both as a reactant and as an intermediate product. The population of the X species is constant, either because the system is open to a large reservoir of X, or because the amount of X initially found in the system is so high, that its depletion during the reaction can be considered negligible. From a deterministic point of view, the reaction rate equation for species Y can be expressed by Eq. (A.6):

$$\frac{dY}{dt} = c_1XY - 2\left(\frac{c_2}{2}\right)Y^2 \quad (\text{A.6})$$

The two propensities required to describe the stochastic behaviour of this system can be calculated from Eq. (A.7) and Eq. (A.8) :

$$a_1 = c_1XY \quad (\text{A.7})$$

$$a_2 = c_2 \frac{Y(Y-1)}{2} \quad (\text{A.8})$$

The rate constants for this system are $c_1X = 5$ and $c_2 = 0.005$. Two different initial configurations were selected for this system; in the first one, the initial amount of Y species was 10 and in the second one the population was set at 3000. In both cases a sample was taken for every 10 reactions performed. In Figure A.2 the results obtained by the KMC model for the two initial configurations are compared against the results reported by Gillespie.

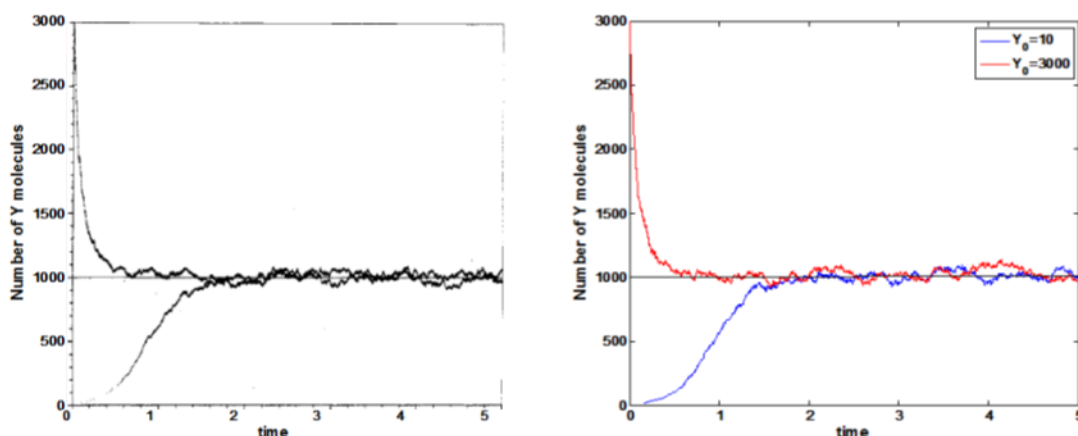


Figure A. 2: Comparison between Gillespie's data (left panel) and the KMC code data (right panel) for the second system. Two different initial configurations are shown for the population of Y species together with the deterministic steady state $Y_s = 1000$.

The agreement between the two KMC algorithms is satisfactory from a qualitative perspective. Differences between the numbers predicted do exist, but can be considered negligible, as the data plotted in both cases are obtained by performing a single KMC run. As discussed in Chapter 2, for every event simulated, two random numbers have to get selected. The random number generator used in both cases requires a starter number (seed) in order to get initiated. This starter number defines the sequence of random numbers produced by the u.r.n.g. Each starter number generates a unique sequence of numbers and every time this number is selected to initiate the u.r.n.g, the exact same sequence of numbers will be generated.

By changing the sequence of random numbers, one would expect a different KMC prediction. For instance, in system 2 there are two possible reaction pathways. If both pathways shared the same propensity, there would be 50% chance for each one to happen at each reaction event. By performing the same simulation for different starter numbers, and hence for different chains of generated random numbers, the pathway selected at a specific time $t(i)$ at each independent simulation might be different, however, the average frequency of the two pathways will always be the same. Hence by following a stochastic approach, it is expected to predict a feasible but uncertain

sequence of events. In order to minimise the uncertainty enclosed to the KMC predictions (stochastic noise), a sufficient amount of independent simulations is required.

System 3

Moving on to a system with more complex behaviour, Gillespie simulated the Lotka reactions, a set of coupled auto-catalytic reactions described by Eqs. (A.9 - A.11):



This set of chemical reactions exhibit remarkable dynamical properties. Species Y_2 behave as predators who reproduce by feeding on species Y_1 , which can be considered as the prey. The population of species Y_1 and Y_2 over time can be described from the following deterministic reaction-rate equations:

$$\frac{dY_1}{dt} = c_1XY_1 - c_2Y_1Y_2 \quad (\text{A.12})$$

$$\frac{dY_2}{dt} = c_2Y_1Y_2 - c_3Y_2 \quad (\text{A.13})$$

System 3 consists of three coupled reactions and hence, three propensities need to be determined in the KMC algorithm. These propensities are:

$$a_1 = c_1XY_1 \quad (\text{A.14})$$

$$a_2 = c_2Y_1Y_2 \quad (\text{A.15})$$

$$a_3 = c_3Y_2 \quad (\text{A.16})$$

The rate-constants of this system are $c_1X = 10$, $c_2 = 0.01$ and $c_3 = 10$. The population of species X remains constant throughout the simulation and the initial population of species Y_1 and Y_2 was 1000. Results are being reported for every 100 reactions

performed. Figures A.3 – A.5 depict the population level of species Y_1 and Y_2 for $0 \leq t \leq 10$ s and $0 \leq t \leq 30$ s.

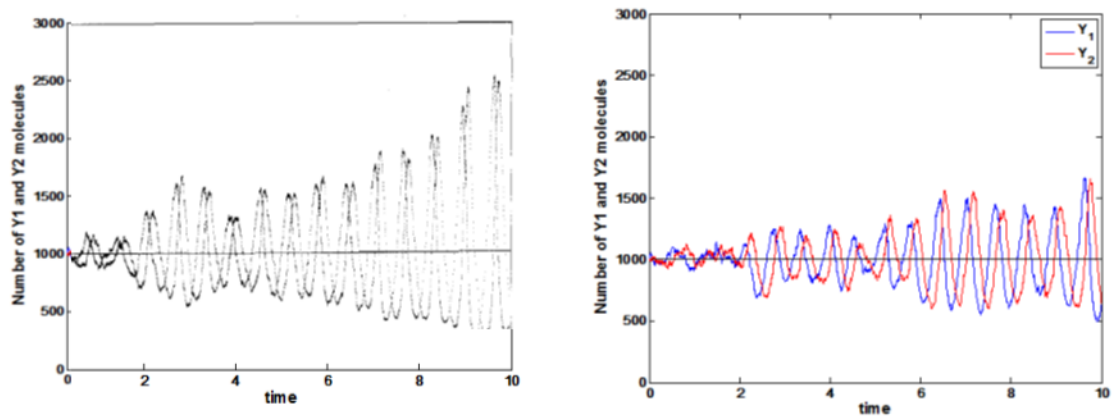


Figure A. 3: Comparison between Gillespie's data (left panel) and the KMC code data (right panel) for species Y_1 and Y_2 for $0 \leq t \leq 10$ s. The straight black line corresponds to the deterministic steady state $Y_{1s}, Y_{2s} = 1000$.

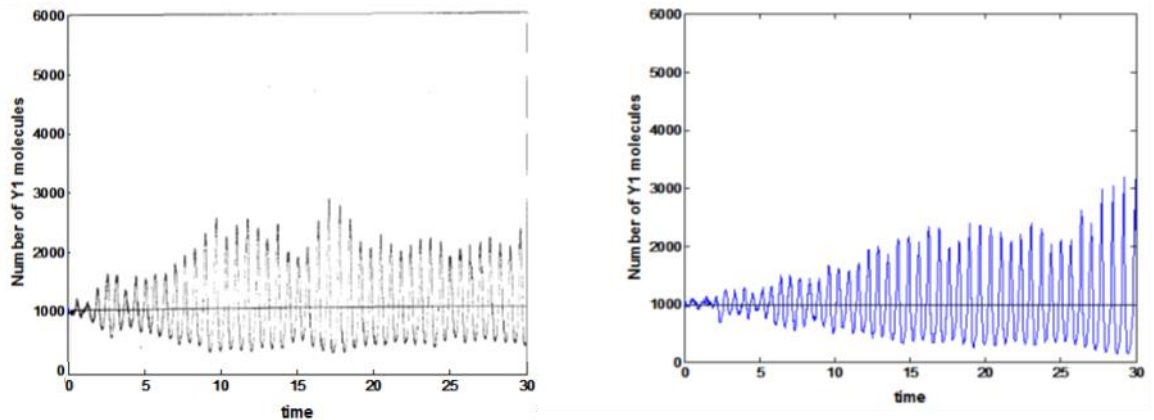


Figure A. 4: Comparison between Gillespie's data (left panel) and the KMC code data (right panel) for species Y_1 for $0 \leq t \leq 30$ s. The straight black line corresponds to the deterministic steady state $Y_{1s} = 1000$.

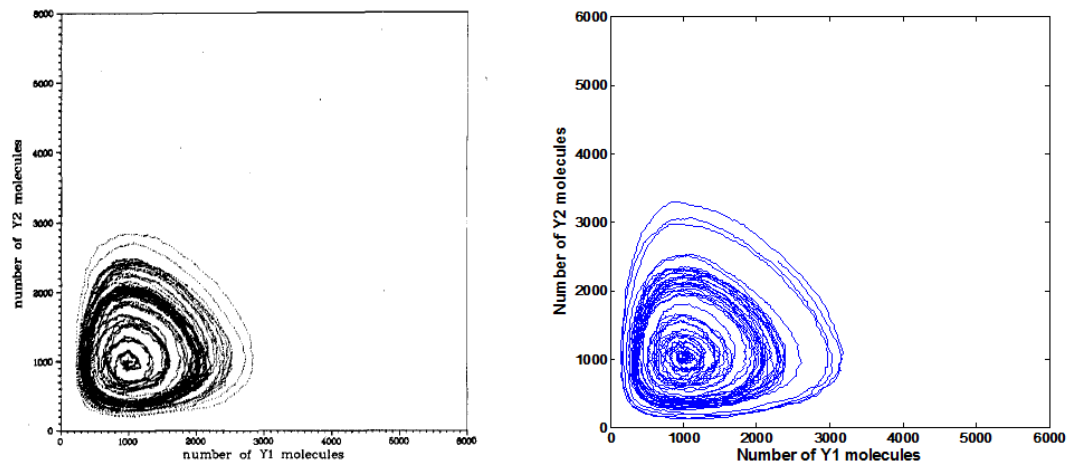


Figure A. 5: Comparison between Gillespie's data (left panel) and the KMC code data (right panel). The population of species Y_1 is plotted against the population of species Y_2 for $0 \leq t \leq 30$ s.

In Figures A.3 – A.5. differences between the two predictions are observed. At this point it is essential to prove that the disagreement observed is due to the starter numbers used and not due to an error in the developed KMC algorithm. Therefore, three additional independent simulations were performed. In each one a different starter number was selected to initiate the u.r.n.g. The population of species Y_1 for all four simulations are presented in Figure A.6.

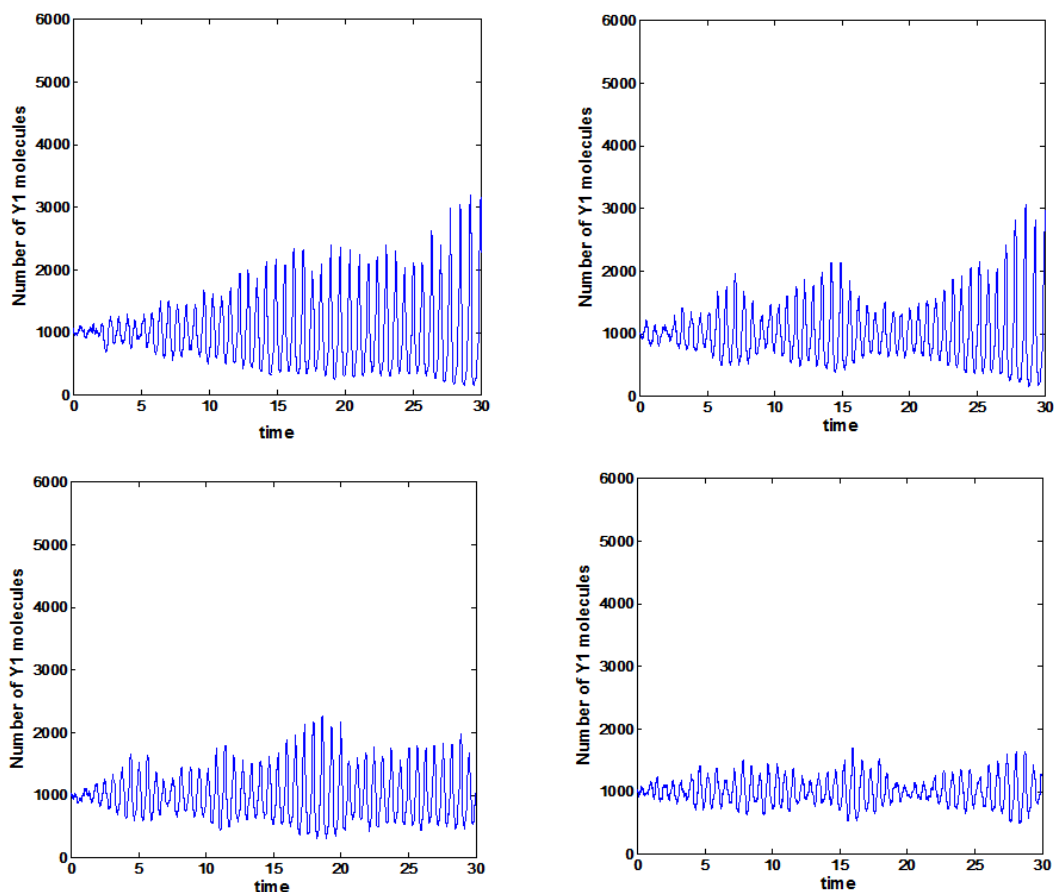


Figure A. 6: The population of species Y_1 as calculated by four independent KMC simulations for $0 \leq t \leq 30$ s, while using different starter numbers to initiate the u.r.n.g.

As expected, the different starter numbers yield different profiles for the population of Y_1 species. Since the set of reactions that apply for this system describe an auto-catalytic reaction, there are times when the population of Y_1 species (prey) is high, leading to a rise in the predator population. As a result, an increased consumption of Y_1 species is observed. However, this leads to a food shortage and hence a decrease of the predators, which permits the increase of the prey population. Clearly, it is a matter of time until a random fluctuation of the system leads to the extinction of the prey species Y_1 . Shortly after the prey extinction the predators should also disappear ($Y_1 = 0$, $Y_2 = 0$). Similarly, if the population of the predators is led to extinction, the population of species Y_1 should increase infinitely ($Y_1 = \infty$, $Y_2 = 0$). In order to test whether the KMC algorithm can

predict that behaviour, two independent KMC simulations were performed until these two states were observed. In Figure A.7, the population of species Y_1 and Y_2 are plotted against time, just before the extinction takes place.

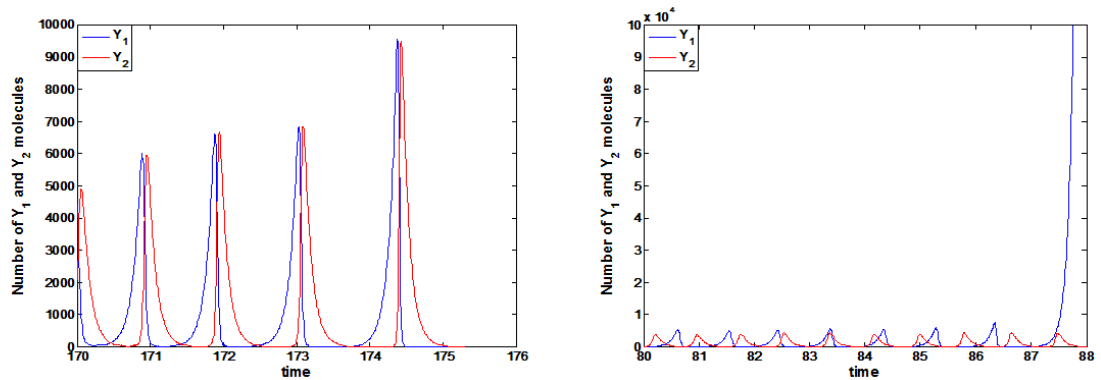


Figure A. 7: The population of species Y_1 and Y_2 in the case of mutual extinction (left panel) and in the case of species Y_2 extinction (right panel).

System 4

As Gillespie observed, the set of reactions in the Lotka model exhibited a neutrally stable oscillating behaviour. As a next step, he wanted to simulate a system with positively stable oscillations. The system he selected, comprises of two intermediate species Y_1 and Y_2 , two products Z_1 and Z_2 and two reactants X_1 and X_2 in abundant concentration. The system is described by the following set of reactions:



The deterministic rate-reaction equations that describe the evolution of species Y_1 and Y_2 over time are:

$$\frac{dY_1}{dt} = c_1 X_1 - c_2 X_2 Y_1 + \frac{c_3}{2} Y_1^2 Y_2 - c_4 Y_1 \quad (\text{A.21})$$

$$\frac{dY_2}{dt} = c_2 X_2 Y_1 - \frac{c_3}{2} Y_1^2 Y_2 \quad (\text{A.22})$$

The four propensities required to describe the four reaction pathways in the KMC algorithm are calculated by the following equations:

$$a_1 = c_1 X_1 \quad (\text{A.23})$$

$$a_2 = c_2 X_2 Y_1 \quad (\text{A.24})$$

$$a_3 = c_3 Y_2 Y_1 \frac{(Y_1 - 1)}{2} \quad (\text{A.25})$$

$$a_4 = c_4 Y_1 \quad (\text{A.26})$$

The reaction-rate constants selected for this system are $c_1 X_1 = 5000$, $c_2 X_2 = 50$, $c_3 = 0.00005$ and $c_4 = 5$ and the initial population of species Y_1 and Y_2 is 1000 and 2000, respectively. Figures A.8 and A.9 present the evolution of species Y_1 and Y_2 over the time interval $0 \leq t \leq 14$ s for every 100 reactions simulated. Figure A.10 shows the population of the two intermediate species against each other, for a slightly longer time interval $0 \leq t \leq 18$ s, for every 50 reactions occurred.

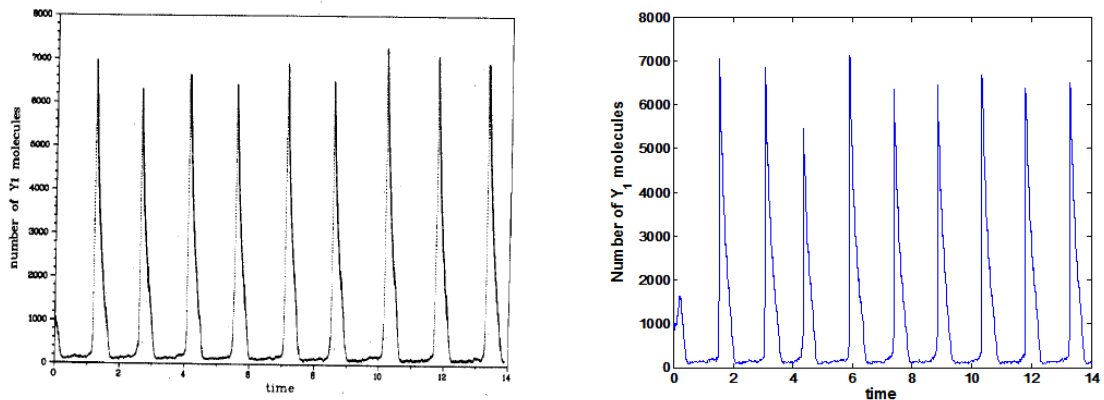


Figure A. 8: Comparison between Gillespie's data (left panel) and the KMC code data (right panel) for species Y_1 for $0 \leq t \leq 14$ s. Samples are exported for every 100 reactions simulated.

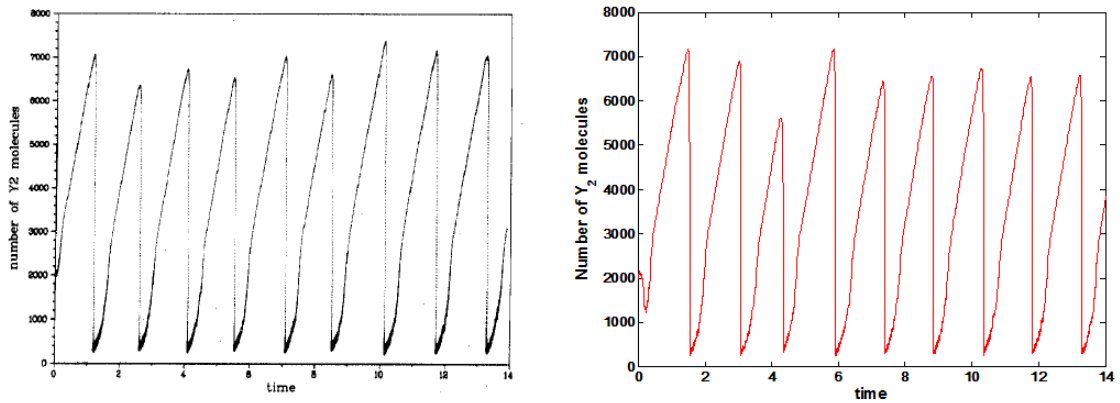


Figure A. 9: Comparison between Gillespie's data (left panel) and the KMC code data (right panel) for species Y_1 for $0 \leq t \leq 14$ s. Samples are exported for every 100 reactions simulated.

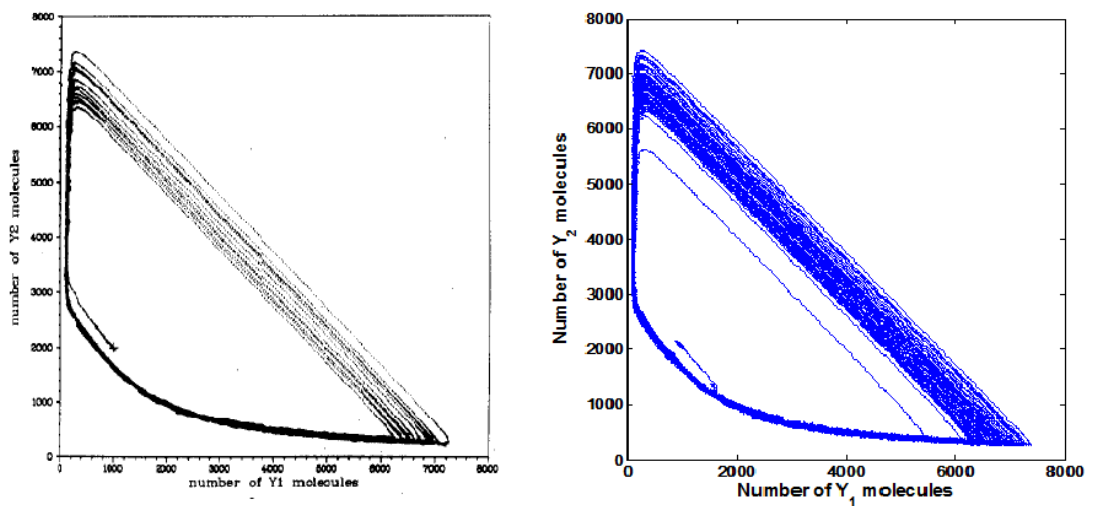
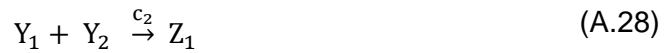


Figure A. 10: Comparison between Gillespie's data (left panel) and the KMC code data (right panel). The population of species Y_1 is plotted against the population of species Y_2 for $0 \leq t \leq 18$ s. Samples are exported for every 50 reactions simulated.

For this system small discrepancies were detected between the two algorithms. However, as previously discussed, the differences noticed can be attributed to the different starter numbers used.

System 5

The final system simulated in Gillespie's work resembles the 4th system and introduces a third intermediate species (Y_3) and a third reactant (X_3) at high and constant concentration. The reaction network corresponding to that model is as follows:



The deterministic reaction-rate equations that can be used in order to calculate the population of all three intermediate species are:

$$\frac{dY_1}{dt} = c_1 X_1 Y_2 - c_2 Y_1 Y_2 + c_3 X_2 Y_1 - c_4 Y_1^2 \quad (\text{A.32})$$

$$\frac{dY_2}{dt} = -c_1 X_1 Y_2 - c_2 Y_1 Y_2 + c_5 X_3 Y_3 \quad (\text{A.33})$$

$$\frac{dY_3}{dt} = c_3 X_2 Y_1 - c_5 X_3 Y_3 \quad (\text{A.34})$$

Assuming that the deterministic reaction rates of the first two equations are ρ_{1s} and ρ_{2s} and that the steady state values of the intermediate species are Y_{1s} , Y_{2s} and Y_{3s} , the reaction-rate constants for the five pathways can be expressed as:

$$c_1 X_1 = \frac{\rho_{1s}}{Y_{2s}} \quad (\text{A.35})$$

$$c_2 = \frac{\rho_{2s}}{Y_{1s} Y_{2s}} \quad (\text{A.36})$$

$$c_3 X_2 = \frac{\rho_{1s} + \rho_{2s}}{Y_{1s}} \quad (\text{A.37})$$

$$c_4 = \frac{2\rho_{1s}}{Y_{1s}^2} \quad (\text{A.38})$$

$$c_5 = \frac{\rho_{1s} + \rho_{2s}}{Y_{3s}} \quad (\text{A.39})$$

Since there are five possible reactions that can take place during each simulation event, five propensities need to be defined:

$$a_1 = c_1 X_1 Y_2 \quad (\text{A.40})$$

$$a_2 = c_2 Y_1 Y_2 \quad (\text{A.41})$$

$$a_3 = c_3 X_2 Y_1 \quad (\text{A.42})$$

$$a_4 = c_4 Y_1 \frac{Y_1 - 1}{2} \quad (\text{A.43})$$

$$a_5 = c_5 X_3 Y_3 \quad (\text{A.44})$$

The initial population of species Y_1, Y_2 and Y_3 is 500, 1000 and 2000 respectively, while the reaction rates are $\rho_{1s} = 2000$ and $\rho_{2s} = 50000$. By implementing these inputs in the KMC algorithm, the evolution of the three intermediate species over the time interval $0 \leq t \leq 6$ s, for every 100 reactions simulated is presented in Figure A.11.

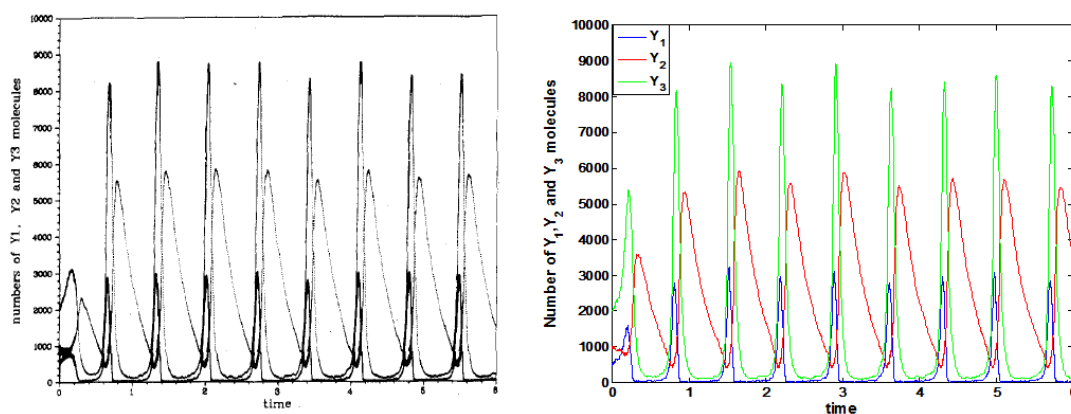


Figure A. 11: Comparison between Gillespie's data (left panel) and the developed KMC (right panel). The time evolution of species Y_1 , Y_2 and Y_3 is plotted for every 100 reactions simulated.

Similarly, the population of the intermediate species is being plotted for a shorter time interval. Figure A.12 shows the results obtained when samples are taken every 250 reactions.

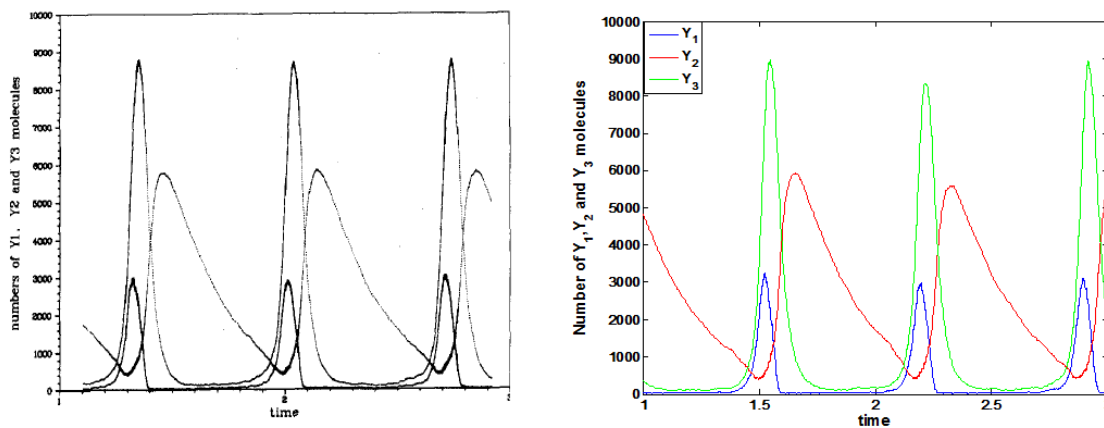


Figure A. 12: Comparison between Gillespie's data (left panel) and the KMC code data (right panel), over the time interval $0 \leq t \leq 3$ s. The time evolution of species Y_1 , Y_2 and Y_3 is plotted for every 250 reactions simulated.

In his paper Gillespie performed more simulations for these five systems. The variables in those simulations were the sampling step, the value of the reaction-rate constants and the availability of the X_1 , X_2 and X_3 reactants. These simulations were performed for

validation purposes, but the results are not reported here. With the data presented so far, the validity of the constructed KMC algorithm was established.

References

1. International Energy Agency. *Key Natural Gas Trends - Excerpt from: Natural Gas Information.*; 2016.
2. Hughes JD. Energy: A reality check on the shale revolution. *Nature*. 2013;494:307-308.
3. Sovacool BK. Cornucopia or curse? Reviewing the costs and benefits of shale gas hydraulic fracturing (fracking). *Renew Sustain Energy Rev*. 2014;37:249-264.
4. BP. *Statistical Review of World Energy*. Vol 68.; 2019.
5. Zendehboudi S, Bahadori A. Shale Gas Characteristics. In: *Shale Oil and Gas Handbook: Theory, Technologies, and Challenges*. Cambridge, MA, USA: Elsevier Inc.; 2017:27-79.
6. Cooper J, Stamford L, Azapagic A. Shale Gas: A Review of the Economic, Environmental, and Social Sustainability. *Energy Technol*. 2016;4(7):772-792.
7. EIA. *Annual Energy Outlook 2019 with Projections to 2050*. Vol 44.; 2019.
8. Statistics N. *Digest of UK Energy Statistics (DUKES): Natural Gas.*; 2018.
9. Lucking B, Pearce A. *Energy Trends: UK Gas, January to March 2019.*; 2019.
10. Fleming C, Hough E, Kemp S. Feasibility of ASD AgriSpec Analysis to Indicate Mineralogy of a Potential Shale Gas Reservoir from West Lancashire, UK. *Energy Procedia*. 2016;97:326-333.
11. Gross D, Sachsenhofer RF, Bechtel A, Pytlak L, Rupprecht B, Wegerer E. Organic geochemistry of Mississippian shales (Bowland Shale Formation) in central Britain: Implications for depositional environment, source rock and gas shale potential. *Mar Pet Geol*. 2015;59:1-21.
12. Miller CT, Dawson CN, Farthing MW, et al. Numerical simulation of water resources problems: Models, methods, and trends. *Adv Water Resour*. 2013;51:405-437.
13. Cooper J, Stamford L, Azapagic A. Sustainability of UK shale gas in comparison with other electricity options: Current situation and future scenarios. *Sci Total Environ*. 2018;619-620:804-814.
14. *Fracking UK Shale : Planning Permission and Communities.*; 2014.
15. Smith MB, Montgomery CT. Hydraulic Fracturing. In: Florida, USA: CRC Press; 2015.
16. Soeder DJ. Shale Gas Development in the United States. In: *Advances in Natural Gas Technology*. IntechOpen; 2012:1-28.
17. Cheng L, Jia P, Rui Z, Huang S, Xue Y. Transient responses of multifractured systems with discrete secondary fractures in unconventional reservoirs. *J Nat Gas Sci Eng*. 2017;41:49-62.

18. Vengosh A, Kondash A, Harkness J, Lauer N, Warner N, Darrah TH. The geochemistry of hydraulic fracturing fluids. *Procedia Earth Planet Sci.* 2017;17:21-24.
19. Vedachalam N, Srinivasalu S, Rajendran G, Ramadass GA, Atmanand MA. Review of unconventional hydrocarbon resources in major energy consuming countries and efforts in realizing natural gas hydrates as a future source of energy. *J Nat Gas Sci Eng.* 2015;26:163-175.
20. Li Q, Xing H, Liu J, Liu X. A review on hydraulic fracturing of unconventional reservoir. *Petroleum.* 2015;1(1):8-15.
21. Montgomery C. Fracturing Fluids. In: *Effective and Sustainable Hydraulic Fracturing.* IntechOpen; 2017:1-24.
22. Maule AL, Makey CM, Benson EB, Burrows IJ, Scammell MK. Disclosure of Hydraulic Fracturing Fluid Chemical Additives: Analysis of Regulations. *NEW Solut A J Environ Occup Heal Policy.* 2013;23(1):167-187.
23. Sarri F, Tatini D, Raudino M, Ambrosi M, Carretti E, Lo Nostro P. Electro-Responsive Green Gels for Lower Environmental Impact Shale Gas Extraction. *Energy and Fuels.* 2019;33(3):2057-2066.
24. Fink JK. Proppants. In: *Hydraulic Fracturing Chemicals and Fluids Technology.* Cambridge, MA, USA: Elsevier Inc.; 2013:205-216.
25. Liang F, Sayed M, Al-Muntasheri GA, Chang FF, Li L. A comprehensive review on proppant technologies. *Petroleum.* 2016;2(1):26-39.
26. Gleeson T, Moosdorf N, Hartmann J, Beek LPH van. Felt seismicity associated with shale gas hydraulic fracturing: The first documented example in Europe. *Geophys Res Lett.* 2014;41(9):1-7.
27. Vengosh A, Jackson RB, Warner N, Darrah TH, Kondash A. A critical review of the risks to water resources from unconventional shale gas development and hydraulic fracturing in the United States. *Environ Sci Technol.* 2014;48(15):8334-8348.
28. Driscoll FD. Groundwater and Wells. In: *Groundwater and Wells.* 2nd ed. Minnesota, USA: Johnson Screens; 1986:413-461.
29. Collell J, Galliero G, Gouth F, et al. Molecular simulation and modelisation of methane/ethane mixtures adsorption onto a microporous molecular model of kerogen under typical reservoir conditions. *Microporous Mesoporous Mater.* 2014;197:194-203.
30. Bai B, Elgmati M, Zhang H, Wei M. Rock characterization of Fayetteville shale gas plays. *Fuel.* 2013;105:645-652.
31. Gensterblum Y, Ghanizadeh A, Cuss RJ, et al. Gas transport and storage capacity in shale gas reservoirs - A review. Part A: Transport processes. *J Unconv Oil Gas Resour.* 2015;12:87-122.
32. Rezaee R, Rothwell M. Gas shale: Global significance, distribution, and challenged. In: *Gas Shale, in Fundamentals of Gas Shale Reservoirs.* Hoboken, NJ: John Wiley & Sons, Inc.; 2015:1-19.

33. Mendhe VA, Mishra S, Varma AK, Kamble AD, Bannerjee M, Sutay T. Gas reservoir characteristics of the Lower Gondwana Shales in Raniganj Basin of Eastern India. *J Pet Sci Eng.* 2017;149(45):649-664.
34. Wang Y, Zhu Y, Liu S, Zhang R. Pore characterization and its impact on methane adsorption capacity for organic-rich marine shales. *Fuel.* 2016;181:227-237.
35. Nykky A. Pores, porosity and pore size distribution of some Draupne Formation and Colorado Group shales and kerogens. 2014.
36. Backeberg NR, Iacoviello F, Rittner M, et al. Quantifying the anisotropy and tortuosity of permeable pathways in clay-rich mudstones using models based on X-ray tomography. *Sci Rep.* 2017;(June):1-12.
37. Mendonça Filho JG, Menezes TR, Mendonça JO, et al. Organic facies: palynofacies and organic geochemistry approaches. *Earth's Syst Process.* 2012:211-248.
38. Ross DJK, Marc Bustin R. The importance of shale composition and pore structure upon gas storage potential of shale gas reservoirs. *Mar Pet Geol.* 2009;26(6):916-927.
39. Rouquerolt J, Avnir D, Fairbridge CW, et al. Recommendations for the characterization of porous solids. *Pure Appl Chem.* 1994;66(8):1739-1758.
40. Chalmers GRL, Bustin RM. Porosity and pore size distribution of deeply-buried fine-grained rocks: Influence of diagenetic and metamorphic processes on shale reservoir quality and exploration. *J Unconv Oil Gas Resour.* 2015;12:134-142.
41. Sun J, Dong X, Wang J, et al. Measurement of total porosity for gas shales by gas injection porosimetry (GIP) method. *Fuel.* 2016;186:694-707.
42. Ma L, Fauchille A-L, Dowey PJ, et al. Correlative multi-scale imaging of shales: a review and future perspectives. *Geol Soc London, Spec Publ.* 2017;454(1):175-199.
43. Ma Y, Zhong N, Li D, Pan Z, Cheng L, Liu K. Organic matter/clay mineral intergranular pores in the Lower Cambrian Lujiaping Shale in the north-eastern part of the upper Yangtze area, China: A possible microscopic mechanism for gas preservation. *Int J Coal Geol.* 2015;137:38-54.
44. Sun H, Yao J, Cao Y, Fan D, Zhang L. Characterization of gas transport behaviors in shale gas and tight gas reservoirs by digital rock analysis. *Int J Heat Mass Transf.* 2017;104:227-239.
45. Eshghinejadfard A, Daróczy L, Janiga G, Thévenin D. Calculation of the permeability in porous media using the lattice Boltzmann method. *Int J Heat Fluid Flow.* 2016;1329(0):0-1.
46. Hudson JA. Permeability. In: *Elsevier Geo-Engineering Book Series.* Elsevier Inc.; 2006:231-252.
47. Klinkenberg LJ. The Permeability Of Porous Media To Liquids And

- Gases. *API Drill Prod Pract.* 1941:200-2013.
48. Chakraborty N, Karpyn Z, Liu S, Yoon H. Permeability evolution of shale during spontaneous imbibition. *J Nat Gas Sci Eng.* 2016;38:590-596.
 49. Meng M, Ge H, Ji W, Wang X, Chen L. Investigation on the variation of shale permeability with spontaneous imbibition time: Sandstones and volcanic rocks as comparative study. *J Nat Gas Sci Eng.* 2015;27:1546-1554.
 50. Nazari Moghaddam R, Jamiolahmady M. Fluid transport in shale gas reservoirs: Simultaneous effects of stress and slippage on matrix permeability. *Int J Coal Geol.* 2016;163:87-99.
 51. Gu Y, Ding W, Yin S, Wang R, Mei Y, Liu J. Analytical modeling of mercury injection in high-rank coalbed methane reservoirs based on pores and microfractures: A case study of the upper carboniferous Taiyuan Formation in the Heshun block of the Qinshui Basin, central China. *J Geophys Eng.* 2017;14(2):197-211.
 52. Zou C, Zhao Q, Dong D, et al. Geological characteristics, main challenges and future prospect of shale gas. *J Nat Gas Geosci.* 2017;2(5-6):273-288.
 53. Wang FP, Hammes U, Reed R, Zhang T, Tang X, Li Q. Petrophysical and mechanical properties of organic-rich shales and their influences on fluid flow. *AAPG Mem.* 2013;103(January):167-186.
 54. Clavaud JB, Mainault A, Zamora M, Rasolofosaon P, Schlitter C. Permeability anisotropy and its relations with porous medium structure. *J Geophys Res Solid Earth.* 2008;113(1):1-10.
 55. Marcus H. The permeability of a sample of an anisotropic porous medium. *J Geophys Res.* 1962;67(13):5215-5225.
 56. Lo T, Coyner KB, Toksöz MN. Experimental determination of elastic anisotropy of Berea sandstone, Chicopee shale, and Chelmsford granite. *Geophysics.* 2002;51(1):164-171.
 57. Vernik L, Liu X. Velocity anisotropy in shales: A petrophysical study. *Geophysics.* 2002;62(2):521-532.
 58. Sone H, Zoback MD. Mechanical properties of shale-gas reservoir rocks - Part 1: Static and dynamic elastic properties and anisotropy. *Geophysics.* 2013;78(5):D381-D392.
 59. Heng S, Guo Y, Yang C, Daemen JJK, Li Z. Experimental and theoretical study of the anisotropic properties of shale. *Int J Rock Mech Min Sci.* 2015;74:58-68.
 60. King GE. Thirty years of gas-shale fracturing: What have we learned? *SPE Annu Tech Conf Exhib held Florence, Italy, 19-22 Sept SPE-133456-MS.* 2010:88-90.
 61. Cipolla CL, Warpinski NR, Mayerhofer M, Lolon EP, Vincent M. The Relationship Between Fracture Complexity, Reservoir Properties, and Fracture-Treatment Design. *SPE Prod Oper.* 2010;25(04):438-452.

62. Britt LK, Schoeffler J. The Geomechanics Of A Shale Play: What Makes A Shale Prospective! *SPE East Reg Meet held Charlestone, West Virginia, USA, 23–25 Sept SPE-125525-MS*. 2009:1-9.
63. Avseth P, Mukerji T, Mavko G, Dvorkin J. Rock-physics diagnostics of depositional texture, diagenetic alterations, and reservoir heterogeneity in high-porosity siliciclastic sediments and rocks — A review of selected models and suggested work flows. *Geophysics*. 2010;75(5):75A31-75A47.
64. Sullivan KB, McBride EF. Diagenesis of sandstones at shale contacts and diagenetic heterogeneity, Frio Formation, Texas. *Am Assoc Pet Geol Bull*. 1991;75(1):121-138.
65. Dvorkin J, Walls J, Tutuncu A, Prasad M, Nur A, Mese A. Rock property determination using digital rock physics. *SEG Tech Progr Expand Abstr*. 2003:1660-1663.
66. Dullien FA. Single-Phase Transport Phenomena in Porous Media. In: *Porous Media: Fluid Transport and Pore Structure*. 2nd ed. Sab Diego, California: Academic Press, INC; 1992:237-313.
67. Shapiro A a., Wesselingh J a. Gas transport in tight porous media. *Chem Eng J*. 2008;142(1):14-22.
68. Brown GO. Henry Darcy and the making of a law. *Water Resour Res*. 2002;38(7):1-12.
69. Guo C, Xu J, Wu K, Wei M, Liu S. Study on gas flow through nano pores of shale gas reservoirs. *Fuel*. 2015;143:107-117.
70. Wood J, Gladden LF, Keil FJ. Modelling diffusion and reaction accompanied by capillary condensation using three-dimensional pore networks. Part 2. Dusty gas model and general reaction kinetics. *Chem Eng Sci*. 2002;57(15):3047-3059.
71. Roy S, Raju R, Chuang HF, Cruden BA, Meyyappan M. Modeling gas flow through microchannels and nanopores. *J Appl Phys*. 2003;93(8):4870-4879.
72. Kärger J, Douglas RM, Theodorou DN. Elementary Principles of Diffusion. In: *Diffusion in Nanoporous Materials*. Weinheim, Germany: Wiley-VCH Verlag GmbH & Co. KGa; 2012:1-24.
73. Song W, Liu H, Wang W, et al. Gas flow regimes judgement in nanoporous media by digital core analysis. *Open Phys*. 2018;16(1):448-462.
74. Falk K, Coasne B, Pellenq R, Ulm F-J, Bocquet L. Subcontinuum mass transport of condensed hydrocarbons in nanoporous media. *Nat Commun*. 2015;6:6949.
75. Yang B, Kang Y, You L, Li X, Chen Q. Measurement of the surface diffusion coefficient for adsorbed gas in the fine mesopores and micropores of shale organic matter. *Fuel*. 2016;181:793-804.
76. Wang W, Yao J, Sun H, Song WH. Influence of gas transport

- mechanisms on the productivity of multi-stage fractured horizontal wells in shale gas reservoirs. *Pet Sci.* 2015;12(4):664-673.
77. Flaconneche B. Transport properties of gases in polymers: Experimental methods. *Oil Gas Sci Technol D Ipf Energies Nouv.* 2001;56(3):245-259.
 78. Sander R, Pan Z, Connell LD. Laboratory measurement of low permeability unconventional gas reservoir rocks: A review of experimental methods. *J Nat Gas Sci Eng.* 2017;37:248-279.
 79. Chalmers GRL, Ross DJK, Bustin RM. Geological controls on matrix permeability of Devonian Gas Shales in the Horn River and Liard basins, northeastern British Columbia, Canada. *Int J Coal Geol.* 2012;103:120-131.
 80. Cui X, Bustin AMM, Bustin RM. Measurements of gas permeability and diffusivity of tight reservoir rocks: Different approaches and their applications. *Geofluids.* 2009;9(3):208-223.
 81. Tanikawa W, Shimamoto T. Comparison of Klinkenberg-corrected gas permeability and water permeability in sedimentary rocks. *Int J Rock Mech Min Sci.* 2009;46(2):229-238.
 82. Meredith PG, Main IG, Clint OC, Li L. On the threshold of flow in a tight natural rock. *Geophys Res Lett.* 2012;39(4):1-5.
 83. Dong M, Li Z, Li S, Yao J. Permeabilities of tight reservoir cores determined for gaseous and liquid CO₂ and C₂H₆ using minimum backpressure method. *J Nat Gas Sci Eng.* 2012;5:1-5.
 84. Loucks RG, Reed RM, Ruppel SC, Jarvie DM. Morphology, Genesis, and Distribution of Nanometer-Scale Pores in Siliceous Mudstones of the Mississippian Barnett Shale. *J Sediment Res.* 2009;79(12):848-861.
 85. Bhattacharya DK, Lie GC. Nonequilibrium gas flow in the transition regime: A molecular-dynamics study. *Phys Rev A.* 1991;43(2):761-767.
 86. Botan A, Ulm FJ, Pellenq RJM, Coasne B. Bottom-up model of adsorption and transport in multiscale porous media. *Phys Rev E - Stat Nonlinear, Soft Matter Phys.* 2015;91(3):1-10.
 87. Ozcan A, Perego C, Salvalaglio M, Parrinello M, Yazaydin O. Concentration gradient driven molecular dynamics: A new method for simulations of membrane permeation and separation. *Chem Sci.* 2017;8:3858-3865.
 88. Phan A, Cole DR, Weiß RG, Dzubiella J, Striolo A. Confined Water Determines Transport Properties of Guest Molecules in Narrow Pores. *ACS Nano.* 2016;10(8):7646-7656.
 89. Deuffhard P, Hermans J, Leimkuhler B, Mark AE, Reich S, Skeel RD. *Computational Molecular Dynamics: Challenges, Methods, Ideas.* New York, USA: Springer-Verlag Berlin Heidelberg; 1997.
 90. Berendsen HJC. *Computational Molecular Dynamics: Challenges, Methods, Ideas.*; 1999.

91. Phan A, Striolo A. Microporous and Mesoporous Materials Methane transport through hierarchical silica micro-mesoporous materials : From non-equilibrium atomistic simulations to phenomenological correlations. *Microporous Mesoporous Mater.* 2019;288:109559.
92. Akkutlu IY, Fathi E. Multiscale Gas Transport in Shales With Local Kerogen Heterogeneities. *SPE Annu Tech Conf Exhib Denver, 30 October–2 November SPE -146422-MS.* 2012.
93. Krishna R, Wesselingh JA. Review Article Number 50-The Maxwell-Stefan approach to mass transfer. *Science (80-).* 1997;52(6):861-911.
94. Javadpour F. Nanopores and apparent permeability of gas flow in mudrocks (shales and siltstone). *J Can Pet Technol.* 2009;48(8):16-21.
95. Wu K, Chen Z, Li X, Guo C, Wei M. A model for multiple transport mechanisms through nanopores of shale gas reservoirs with real gas effect-adsorption-mechanic coupling. *Int J Heat Mass Transf.* 2016;93:408-426.
96. Wu K, Li X, Wang C, Chen Z, Yu W. A Model for Gas Transport in Microfractures of Shale and Tight Gas Reservoirs. *AIChE J.* 2015;61(6):2079-2087.
97. Cao P, Liu J, Leong YK. Combined impact of flow regimes and effective stress on the evolution of shale apparent permeability. *J Unconv Oil Gas Resour.* 2016;14:32-43.
98. Song W, Yao J, Li Y, et al. Apparent gas permeability in an organic-rich shale reservoir. *Fuel.* 2016;181:973-984.
99. Darabi H, Etehad A, Javadpour F, Sepehrnoori K. Gas flow in ultra-tight shale strata. *J Fluid Mech.* 2012;710:641-658.
100. Malek K, Coppens MO. Pore roughness effects on self- and transport diffusion in nanoporous materials. *Colloids Surfaces A Physicochem Eng Asp.* 2002;206(1-3):335-348.
101. Tahmasebi P, Javadpour F, Sahimi M. Stochastic shale permeability matching: Three-dimensional characterization and modeling. *Int J Coal Geol.* 2016;165:231-242.
102. Naraghi ME, Javadpour F. A stochastic permeability model for the shale-gas systems. *Int J Coal Geol.* 2015;140:111-124.
103. Dagan G. Models of Groundwater Flow in Statistically Homogeneous Porous Formations. *Water Resour Res.* 1979;15(1):47-63.
104. Ph. Renard MG de. Calculating equivalent permeability: a review. *Adv Water Resour.* 1997;20:253-278.
105. Kerner EH, Bailey AC, Waterhouse N, Yates B, Mackenzie JK. The Elastic and Thermo-elastic Properties of Composite Media. *Proc Phys Soc Sect B.* 1956;69:808-813.
106. Bruggeman VDAG. Berechnung verschiedener physikalischer Konstanten von heterogenen Substanzen. *Ann Phys.* 1935;5(24).

107. Landauer R. The Electrical Resistance of Binary Metallic Mixtures. *J Appl Phys.* 1952;23(7):779-784.
108. Kirkpatrick S. Percolation and Conduction. *Rev Mod Phys.* 1973;45(4):574-588.
109. Kanellopoulos NK, Petrou JK. Relative gas permeability of capillary with various size distributions networks. *J Memb Sci.* 1988;37:1-12.
110. Davis HT. The Effective Medium Theory of Diffusion in Composite Media. *J Am Ceram Soc.* 1977;60(11-12):499-501.
111. Jiang J, Younis RM. A multimechanistic multicontinuum model for simulating shale gas reservoir with complex fractured system. *Fuel.* 2015;161:333-344.
112. Khatlb ZI, Vitthal S. The Use of the Effective-Medium Theory and a 3D Network Model To Predict Matrix Damage in Sandstone Formations. *Soc Pet Eng J.* 1991;(May):233-239.
113. Daigle H, Sreaton EJ. Predicting the permeability of sediments entering subduction zones. *Geophys Res Lett.* 2015;42:5219-5226.
114. Singh T, Kang D, Nair S. Rigorous calculations of permeation in mixed-matrix membranes : Evaluation of interfacial equilibrium effects and permeability-based models. *J Memb Sci.* 2013;448:160-169.
115. Bunde A, Dieterich W. Percolation in Composites. *J Electroceramics.* 2000;5(2):81-92.
116. King PR. The Use of Renormalization for Calculating Effective Permeability. *Transp Porous Media.* 1989;4:37-58.
117. Renard P, Loc'h G Le, Ledoux E, Marsily G De, Mackay R. A fast algorithm for the estimation of equivalent hydraulic conductivity of heterogeneous media. *Water Resour Res.* 2000;36(12):3567-3580.
118. Kelkar M, Perez G. Scaleup. In: Chopra A, ed. *Applied Geostatistics For Reservoir Characterization.* 1st ed. Texas, USA: Society of Petroleum Engineers Inc.; 2002:189-209.
119. Sondergeld CH, Ambrose RJ, Rai CS, Moncrieff J. Micro-structural studies of gas shales. *SPE Unconv Gas Conf 23-25 February, Pittsburgh, Pennsylvania, USA SPE 131771-MS.* 2010.
120. Boyer C, Kieschnick J, Suarez-Rivera R, Lewis RE, Waters G. *Producing Gas from Its Source.* Vol 18.; 2006.
121. Sondergeld CH, Newsham KE, Comisky JT, Rice MC, Rai CS. Petrophysical Considerations in Evaluating and Producing Shale Gas Resources. *SPE Unconv Gas Conf held Pittsburgh, Pennsylvania, USA, 23-25 Febr 2010 SPE 131768-MS.* 2010.
122. Josh M, Esteban L, Delle Piane C, Sarout J, Dewhurst DN, Clennell MB. Laboratory characterisation of shale properties. *J Pet Sci Eng.* 2012;88-89:107-124.
123. Heller R, Zoback M. Adsorption of methane and carbon dioxide on gas

- shale and pure mineral samples. *J Unconv Oil Gas Resour.* 2014;8(C):14-24.
124. Li J, Sultan AS. Permeability Computations of Shale Gas by the Pore-scale Monte Carlo Molecular Simulations. *Int Pet Technol Conf held Doha, Qatar, 6–9 December 2015 IPTC-18263-MS.* 2015:1-10.
 125. Chen C, Hu D, Westacott D, Loveless D. Nanometer-scale characterization of microscopic pores in shale kerogen by image analysis and pore-scale modeling. *Geochemistry, Geophys Geosystems.* 2013;14(10):4066-4075.
 126. He S, Jiang Y, Conrad JC, Qin G. Molecular simulation of natural gas transport and storage in shale rocks with heterogeneous nano-pore structures. *J Pet Sci Eng.* 2015;133:401-409.
 127. Bernsdorf J, Jaekel U, Zeiser T, et al. Numerical Simulation of Reaction-Diffusion and Adsorption Processes in Porous Media using Lattice Boltzmann Methods with Concurrent Visualisation. In: *Parallel Computational Fluid Dynamics 2002: New Frontiers and Multi-Disciplinary Applications.* Kansai Science City, Japan: Elsevier Inc.; 2002:233-240.
 128. Blunt MJ, Bijeljic B, Dong H, et al. Pore-scale imaging and modelling. *Adv Water Resour.* 2013;51:197-216.
 129. Angeles-Martinez L, Theodoropoulos C. A Lattice-Boltzmann scheme for the simulation of diffusion in intracellular crowded systems. *BMC Bioinformatics.* 2015;16(1):1-15.
 130. Okabe H, Blunt MJ. Prediction of permeability for porous media reconstructed using multiple-point statistics. *Phys Rev E - Stat Nonlinear, Soft Matter Phys.* 2004;70(6 2):1-2.
 131. Hazlett RD. Simulation of capillary-dominated displacements in microtomographic images of reservoir rocks. *Transp Porous Media.* 1995;20(1-2):21-35.
 132. Bakhshian S, Hosseini SA, Shokri N. Pore-scale characteristics of multiphase flow in heterogeneous porous media using the lattice Boltzmann method. *Sci Rep.* 2019;9(1):1-13.
 133. Raeini AQ, Bijeljic B, Blunt MJ. Generalized network modeling of capillary-dominated two-phase flow. *Phys Rev E.* 2018;97(023308):1-20.
 134. Boek ES, Venturoli M. Lattice-Boltzmann studies of fluid flow in porous media with realistic rock geometries. *Comput Math with Appl.* 2010;59(7):2305-2314.
 135. Akai T, Alhammadi AM, Blunt MJ, Bijeljic B. Modeling Oil Recovery in Mixed-Wet Rocks: Pore-Scale Comparison Between Experiment and Simulation. *Transp Porous Media.* 2019;127(2):393-414.
 136. Zhang X, Xiao L, Shan X, Guo L. Lattice Boltzmann simulation of shale gas transport in organic nano-pores. *Sci Rep.* 2014;4:4843.
 137. Germanou L, Ho MT, Zhang Y, Wu L. Intrinsic and apparent gas permeability of heterogeneous and anisotropic ultra-tight porous media. *J*

- Nat Gas Sci Eng.* 2018;60(October):271-283.
138. Tahmasebi P, Javadpour F, Sahimi M. Multiscale and multiresolution modeling of shales and their flow and morphological properties. *Sci Rep.* 2015;5(16373):1-11.
 139. Metropolis N, Arianna R, Marshall R, Teller A, Teller E. Equation of State Calculations by Fast Computing Machines. *J Chem Phys.* 1953;21(6):1087-1092.
 140. Apostolopoulou M, Day R, Hull R, Stamatakis M, Striolo A. A kinetic Monte Carlo approach to study fluid transport in pore networks. *J Chem Phys.* 2017;147(134703):1-10.
 141. Dai J, Seider WD, Sinno T. Lattice kinetic Monte Carlo simulations of defect evolution in crystals at elevated temperature. *Mol Simul.* 2006;32(3-4):305-314.
 142. Kolokathis PD, Theodorou DN. On solving the master equation in spatially periodic systems On solving the master equation in spatially periodic systems. *J Chem Phys.* 2012;137(034112):1-21.
 143. Comer J, Aksimentiev A. Predicting the DNA Sequence Dependence of Nanopore Ion Current Using Atomic-Resolution Brownian Dynamics. *J Phys Chem C.* 2012;(116):3376–3393.
 144. Vardavas R. Fluctuations and scaling in 1D irreversible film growth models . 2002.
 145. Stamatakis M, Vlachos DG. A graph-theoretical kinetic Monte Carlo framework for on-lattice chemical kinetics. *J Chem Phys.* 2011;134(21).
 146. Darby MT, Piccinin S, Stamatakis M. First principles-based kinetic Monte Carlo simulation in catalysis. In: *Physics of Surface , Interface and Cluster Catalysis.* 2nd ed. Bristol, UK: IOP Publishing, Bristol, UK; 2016:1-38.
 147. Alfonso DR, Tafen DN. Simulation of atomic diffusion in the Fcc NiAl system: A kinetic monte carlo study. *J Phys Chem C.* 2015;119(21):11809-11817.
 148. Fragkopoulos IS, Theodoropoulos C. Multi-scale modelling of electrochemically promoted systems. *Electrochim Acta.* 2014;150:232-244.
 149. Rai A, Warriar M, Schneider R. A hierarchical multi-scale method to simulate reactive-diffusive transport in porous media. *Comput Mater Sci.* 2009;46(2):469-478.
 150. Wang X, Faßbender J, Posselt M. Efficient calculation methods for the diffusion coefficient of interstitial solutes in dilute alloys. *Materials (Basel).* 2019;12(9).
 151. Flamm MH, Diamond SL, Sinno T. Lattice kinetic Monte Carlo simulations of convective-diffusive systems. *J Chem Phys.* 2009;130(9).
 152. Karayiannis NC, Mavrantzas VG, Theodorou DN. Diffusion of small molecules in disordered media : study of the efect of kinetic and spatial

- heterogeneities. *Chem Eng Sci.* 2001;56:2789-2801.
153. Stamatakis M. Kinetic modelling of heterogeneous catalytic systems. *J Phys Condens Matter.* 2015;27(1):013001.
 154. Battaile CC, Srolovitz DJ. Kinetic Monte Carlo Simulation of Chemical Vapor Deposition. *Annu Rev Mater Res.* 2002;32(1):297-319.
 155. Yang X, Hassanein A. Kinetic Monte Carlo simulation of hydrogen diffusion on tungsten reconstructed (0 0 1) surface. *Fusion Eng Des.* 2014;89(11):2545-2549.
 156. Voter A. Introduction To the Kinetic Monte Carlo Method. *Radiat Eff Solids.* 2007;235:1-23.
 157. Kratzer P. Monte Carlo and kinetic Monte Carlo methods. *Multiscale Simul Methods Mol Sci.* 2009;42:51-76.
 158. Bhanot G. The Metropolis algorithm. *Rep Prog Phys.* 1988;51:429-457.
 159. Owen B. Importance sampling. In: *Monte Carlo Theory, Methods and Examples.* Art Owen; 2013:3-40.
 160. Robert CP. The Metropolis – Hastings algorithm. In: *Monte Carlo Statistical Methods.* New York: Springer-Verlag; 1999:231-283.
 161. Bortz AB, Kalos MH, Lebowitz JL. A New Algorithm for Monte Carlo Simulation of Ising Spin Systems. *J Comput Phys.* 1975;17:10-18.
 162. Bulnes F, Pereyra V, Riccardo J. Collective surface diffusion: n-fold way kinetic Monte Carlo simulation. *Phys Rev E.* 1998;58(1):86-92.
 163. Van Kampen N. The Master Equation. In: *Stochastic Processes in Physics and Chemistry.* ; 2007:96-133.
 164. Marx D, Hutter J. Getting started: unifying MD and electronic structure. In: *Ab Initio Molecular Dynamics: Basic Theory and Advanced Methods.* Cambridge, UK: Cambridge University Press; 2009:11-84.
 165. Hänggi P, Talkner P, Borovec M. Reaction rate theory: 50 years after Kramers. *Rev Mod Phys.* 1990;62(2):250-341.
 166. McQuarrie DA. Classical Statistical Mechanics. In: *Statistical Mechanics.* New York: Harper and Row; 1973:113-121.
 167. Cramer CJ. Density Functional Theory. In: *Essentials of Computational Chemistry: Theories and Models.* 2nd ed. West Sussex, England: John Wiley & Sons, Inc.; 1996:249-301.
 168. Jansen APJ. *An Introduction to Kinetic Monte Carlo Simulations of Surface Reactions.* Berlin, Germany: Springer-Verlag Berlin Heidelberg; 2012.
 169. Neyertz S, Brown D. A trajectory-extending kinetic Monte Carlo (TEKMC) method for estimating penetrant diffusion coefficients in molecular dynamics simulations of glassy polymers. *Macromolecules.* 2010;43(21):9210-9214.
 170. Pandiyan S, Brown D, Neyertz S, Van Der Vegt NFA. Carbon dioxide

- solubility in three fluorinated polyimides studied by molecular dynamics simulations. *Macromolecules*. 2010;43(5):2605-2621.
171. Hanson B, Pryamitsyn V, Ganesan V. Computer simulations of gas diffusion in polystyrene-C60 fullerene nanocomposites using trajectory extending kinetic monte carlo method. *J Phys Chem B*. 2012;116(1):95-103.
172. Neyertz S, Brown D. Molecular dynamics study of carbon dioxide sorption and plasticization at the interface of a glassy polymer membrane. *Macromolecules*. 2013;46(6):2433-2449.
173. Hanson B, Pryamitsyn V, Ganesan V. Mechanisms Underlying Ionic Mobilities in Nanocomposite Polymer Electrolytes. *ACS Macro Lett*. 2013;2(11):1001-1005.
174. Mogurampelly S, Ganesan V. Effect of nanoparticles on ion transport in polymer electrolytes. *Macromolecules*. 2015;48(8):2773-2786.
175. Tien WJ, Chiu CC. Generic parameters of trajectory-extending kinetic Monte Carlo for calculating diffusion coefficients. *AIP Adv*. 2018;8(6).
176. Jansen APJ. *An Introduction To Monte Carlo Simulations Of Surface Reactions.*; 2008.
177. Andersen M, Panosetti C, Reuter K. A Practical Guide to Surface Kinetic Monte Carlo Simulations. *Front Chem*. 2019;7:1-24.
178. Margraf JT, Reuter K. Systematic Enumeration of Elementary Reaction Steps in Surface Catalysis. *ACS Omega*. 2019;4(2):3370-3379.
179. Schulze TP. Efficient kinetic Monte Carlo simulation. *J Comput Phys*. 2008;227:2455-2462.
180. Ruzayqat HM, Schulze TP. A Rejection Scheme for Off-Lattice Kinetic Monte Carlo Simulation. *J Chem Theory Comput*. 2018;14(1):48-54.
181. Chatterjee A, Vlachos DG. An overview of spatial microscopic and accelerated kinetic Monte Carlo methods. *J Comput Mater Des*. 2007;14(2):253-308.
182. Lukkien JJ, Segers JPL, Hilbers PAJ, Gelten RJ, Jansen APJ. Efficient Monte Carlo methods for the simulation of catalytic surface reactions. *Phys Rev E*. 1998;58(2):2598-2610.
183. Gillespie DT. Exact Stochastic Simulation of couple chemical reactions. *J Phys Chem*. 1977;81(25):2340-2361.
184. Gillespie DT. A general method for numerically simulating the stochastic time evolution of coupled chemical reactions. *J Comput Phys*. 1976;22(4):403-434.
185. Blue JL, Beichl I, Sullivan F. Faster Monte Carlo simulations. *Phys Rev E*. 1995;51(2):867-868.
186. Gibson MA, Bruck J. Efficient exact stochastic simulation of chemical systems with many species and many channels. *J Phys Chem A*. 2000;104(9):1876-1889.

187. Gentle JE. Quality of random number generators. In: *Statistics and Computing: Random Number Generation and Monte Carlo Methods*. 2nd ed. New York: Springer; 2003:61-88.
188. L'Ecuyer P. Uniform random number generators: a review. In: *Proceedings of the 1997 Winter Simulation Conference*. Vol 54. ; 1997:127-134.
189. Matsumoto M, Nishimura T. Dynamic creation of pseudorandom number generators. *Monte Carlo and Quasi-Monte Carlo Methods*. 2000;1(1):56-69.
190. Chubynsky M V., Slater GW. Diffusing diffusivity: A model for anomalous, yet Brownian, diffusion. *Phys Rev Lett*. 2014;113(9):1-5.
191. Ma L, Taylor KG, Lee PD, Dobson KJ, Doney PJ, Courtois L. Novel 3D centimetre-to nano-scale quantification of an organic-rich mudstone: The Carboniferous Bowland Shale, Northern England. *Mar Pet Geol*. 2016;72:193-205.
192. Cuppen HM, Karssemeijer LJ, Lamberts T. The kinetic Monte Carlo method as a way to solve the master equation for interstellar grain chemistry. *Chem Rev*. 2013;113(12):8840-8871.
193. Lee YK, Sinno T. Analysis of the lattice kinetic Monte Carlo method in systems with external fields. *J Chem Phys*. 2016;145(23):234104.
194. Young WM, Elcock EW. Monte Carlo studies of vacancy migration in binary ordered alloys: I. *Proc Phys Soc*. 1966;89(3):735-746.
195. Villaluenga JPG, Khayet M, Godino P, Seoane B, Mengual JI. Analysis of the membrane thickness effect on the pervaporation separation of methanol/methyl tertiary butyl ether mixtures. *Sep Purif Technol*. 2005;47(1-2):80-87.
196. BP. *Statistical Review of World Energy*. Vol 66.; 2017.
197. Kelkar M. Introduction. In: Patterson M, ed. *Natural Gas Production Engineering*. Oklahoma, USA: PennWell Books; 2008:1-25.
198. H.Schön J. Rocks—Their Classification and General Properties. In: *Handbook of Petroleum Exploration and Production*. 1st ed. Oxford, UK: Elsevier B.V.; 2011:1-16.
199. Sayed MA, Almontasheri GA, Liang F. Development of shale reservoirs : Knowledge gained from developments in North America. *J Pet Sci Eng*. 2017;157:164-186.
200. Mansfield P, Issa B. Fluid Transport in Porous Rocks . I . EPI Studies and a Stochastic Model of Flow. *J Magn Reson*. 1996;122(Series A):137-148.
201. Saif T, Lin Q, Butcher AR, Bijeljic B, Blunt MJ. Multi-scale multi-dimensional microstructure imaging of oil shale pyrolysis using X-ray micro-tomography , automated ultra-high resolution SEM , MAPS Mineralogy and FIB-SEM. *Appl Energy*. 2017;202:628-647.
202. Ling K, He J, Pei P, Han G, Zhang H. Determining the permeability of

- tight rock with gas transient flow. *J Nat Gas Sci Eng.* 2013;15:1-7.
203. Liu X, Bin YZ, Yu GJ. From molecular dynamics to lattice Boltzmann : a new approach for pore-scale modeling of multi-phase flow. *Pet Sci.* 2015;12:282-292.
 204. Redner S. Fractal and Multifractal Scaling of Electrical Conduction in Random Resistor Networks. In: Meyers RA, ed. *Mathematics of Complexity and Dynamical Systems.* New York: Springer; 2009:1858.
 205. Tyrrel HJ V. The Origin and Present Status of Fick ' s Diffusion Law. *J Chem Educ.* 1964;41(7):397-400.
 206. V. N. Burganos SVS. Diffusion in Pore Networks : Effective Medium Theory and Smooth Field Approximation. *AIChE J.* 1987;33(10):1678-1689.
 207. Coppens M. The effect of fractal surface roughness on diffusion and reaction in porous catalysts – from fundamentals to practical applications. *Catal Today.* 1999;53:225-243.
 208. Tsonopoulos C. Critical Constants of Normal Alkanes from Methane to Polyethylene. *AIChE J.* 1987;33(12):2080-2083.
 209. Sing KSW, Everett DH, Haul RAW, et al. Reporting Physisorption Data For Gas/Solid Systems with Special Reference to the Determination of Surface Area and Porosity. *Pure Appl Chem.* 1985;57(4):603-619.
 210. Sitar N, Cawfield D, Kiureghian A. First-Order Reliability Approach to Stochastic Analysis of Subsurface Flow and Contaminant Transport. *Water Resour Res.* 1987;23(5).
 211. Li Y, Leboeuf E, Basu P., Mahadevan S. Stochastic Modeling of the Permeability of Randomly Generated Porous Media. *Adv Water Resour.* 2005;28(8):835-844.
 212. Karacan CÖ, Olea RA. Stochastic reservoir simulation for the modeling of uncertainty in coal seam degasification. *Fuel(Lond).* 2015;148:87-97.
 213. Capek P, Vesely M, Bernauer B, et al. Stochastic reconstruction of mixed-matrix membranes and evaluation of effective permeability. *Comput Mater Sci.* 2014;89:142-156.
 214. Wu K, Van Dijke MIJ, Couples GD, et al. 3D stochastic modelling of heterogeneous porous media - Applications to reservoir rocks. *Transp Porous Media.* 2006;65(3):443-467.
 215. Bui T, Phan A, Cole DR, Striolo A. Transport Mechanism of Guest Methane in Water-Filled Nanopores. *J Phys Chem C.* 2017;121:15675-15686.
 216. Ringnér M. What is principal component analysis ? *Nat Biotechnol.* 2008;26(3):303-304.
 217. Zhang X, Wu Y. Effective medium theory for anisotropic metamaterials. *Sci Rep.* 2015;5(7892):1-7.
 218. Cherkaev OL and E. Effective medium approximations for anisotropic

- composites with arbitrary component orientation. *J Appl Phys.* 2015;114(164102):1-8.
219. Bernasconi J. Conduction in anisotropic disordered systems: Effective-medium theory. *Phys Rev B.* 1974;9(10):4575-4579.
 220. Preux C, Ravalec M Le, Enchéry G. Selecting an Appropriate Upscaled Reservoir Model Based on Connectivity Analysis. *Oil Gas Sci Technol Rev IFP Energies Nouv.* 2016;71(60):1-15.
 221. Wehr SD, Shaw JM. A Note on the Misuse of Area Images to Obtain Particle Size Information in Solid-Solid Systems. 2002;41(3):365-372.
 222. Tinni A, Fathi E, Agarwal R, Sondergeld C, Akkutlu Y, Rai C. Shale Permeability Measurements on Plugs and Crushed Samples. *SPE Can Unconv Resour Conf 30 October-1 November, Calgary, Alberta, CanadaSPE-162235-MS.* 2012:1-14.
 223. Peng S, Loucks B. Permeability measurements in mudrocks using gas-expansion methods on plug and crushed-rock samples. *Mar Pet Geol.* 2016;73:299-310.
 224. Kuila U, Prasad M. Specific surface area and pore-size distribution in clays and shales. *Geophys Prospect.* 2013;61:341-362.
 225. Loucks RG, Reed RM, Ruppel SC, Hammes U. Spectrum of pore types and networks in mudrocks and a descriptive classification for matrix-related mudrock pores. *Am Assoc Pet Geol Bull.* 2012;96(6):1071-1098.
 226. Soliman M, East L, Augustine J. Fracturing Design Aimed at Enhancing Fracture Complexity. *SPE Eur Annu Conf Exhib held Barcelona, Spain, 14-17 June SPE -130043-MS.* 2010:1-20.
 227. Calvin J, Grieser B, Bachman T. Impact of Microproppant on Production in the SCOOP Woodford Shale: A Case History. *SPE Unconv Resour Conf held Calgary, Alberta, Canada, 15-16 February SPE-185041-MS.* 2017.
 228. Han G. Natural Fractures in Unconventional Reservoir Rocks : Identification , Characterization , and its Impact to Engineering Design. *45th US Rock Mech Symp San Fr California, 26-29 June ARMA-11-509.* 2011:509-514.
 229. Gale JE. Effects of fracture type (induced versus natura) on the stress-fracture closure-fracture permeability relationships. *23' US Symp Rock Mech Berkeley, California, 25-27 August ARMA 82-290.* 1982:290-298.
 230. Apaydin OG, Ozkan E, Raghavan R. Effect of Discontinuous Microfractures on Ultratight Matrix Permeability of a Dual-Porosity Medium. *SPE Reserv Eval Eng SPE-147391-PA.* 2012;15(04):473-485.
 231. Zhou Z, Abass H, Li X, Teklu T. Experimental investigation of the effect of imbibition on shale permeability during hydraulic fracturing. *J Nat Gas Sci Eng.* 2016;29:413-430.
 232. Cortez-Montalvo J, Inyang U, Dusterhoft R, Hu D, Apostolopoulou M. Laboratory evaluation of apparent conductivity of ultra-fine particulates.

- SPE/AAPG/SEG Unconv Resour Technol Conf Houston, Texas, 23-25 July URTeC-2902308-MS*. 2018.
233. Calvin J, Grieser B, Bachman T. Enhancement of Well Production in the SCOOP Woodford Shale through the Application of Microproppant. *SPE Hydraul Fract Technol Conf Exhib Woodlands, Texas, 24-26 January SPE-184863-MS*. 2017.
234. Calvin J, Grieser B, Bachman T. Application of Microproppant in the SCOOP Woodford to Improve Well Production. *SPE Oklahoma City Oil Gas Symp Oklahoma City, Oklahoma, 27-31 March SPE-185121-MS*. 2017.
235. Nguyen PD, Vo LK, Mock BD, Loghry RA. Evaluating Treatment Methods for Enhancing Microfracture Conductivity in Tight Formations. *SPE Eur Annu Conf Exhib Barcelona, Spain, 14-17 June SPE-130043-MS*. 2013.
236. Dahl J, Calvin J, Siddiqui S, et al. Application of Micro-Proppant in Liquids-Rich, Unconventional Reservoirs to Improve Well Production: Laboratory Results, Field Results, and Numerical Simulations. *Abu Dhabi Int Pet Exhib Conf Abu Dhabi, UAE, 9-12 November SPE-177663-MS*. 2015.
237. Inyang U, Cortez-Montalvo J, Dusterhoft R, Apostolopoulou M, Striolo A, Stamatakis M. A Kinetic Monte Carlo Study to Investigate the Effective Permeability and Conductivity of Microfractures within Unconventional Reservoirs. *SPE Oklahoma City Oil Gas Symp held Oklahoma City, Oklahoma, 9-10 April SPE-195220-MS*. 2019.
238. Cole DR, Striolo A. The Influence of Nanoporosity on Carbon-Bearing Fluids. In: *Deep Carbon: Past to Present*. New York, USA: Cambridge University Press; 2019.
239. Sui H, Yao J, Zhang L. Molecular Simulation of Shale Gas Adsorption and Diffusion in Clay Nanopores. *Computation*. 2015;3(4):687-700.
240. Vasileiadis M, Peristeras LD, Papavasileiou KD, Economou IG. Transport Properties of Shale Gas in Relation to Kerogen Porosity. *J Phys Chem C*. 2018;122(11):6166-6177.
241. Wang S, Feng Q, Zha M, Javadpour F, Hu Q. Supercritical Methane Diffusion in Shale Nanopores: Effects of Pressure, Mineral Types, and Moisture Content. *Energy and Fuels*. 2018;32(1):169-180.
242. Apostolopoulou M, Dusterhoft R, Day R, Stamatakis M, Coppens MO, Striolo A. Estimating permeability in shales and other heterogeneous porous media: Deterministic vs. stochastic investigations. *Int J Coal Geol*. 2019;205:140-154.
243. Phan A, Cole DR, Striolo A. Preferential Adsorption from Liquid Water-Ethanol Mixtures in Alumina Pores. *Langmuir*. 2014;30:8066-8077.
244. Phan A, Cole DR, Striolo A. Aqueous Methane in Slit-Shaped Silica Nanopores: High Solubility and Traces of Hydrates. *J Phys Chem C*. 2014;118:4860-4868.
245. Argyris D, Ho T, Cole DR, Striolo A. Molecular Dynamics Studies of

- Interfacial Water at the Alumina Surface. *J Phys Chem C*. 2011;115:2038-2046.
246. Argyris D, Tummala NR, Striolo A. Molecular Structure and Dynamics in Thin Water Films at the Silica and Graphite Surfaces. *J Phys Chem C*. 2008;112:13587-13599.
247. Ho TA, Striolo A. Water and Methane in Shale Rocks: Flow Pattern Effects on Fluid Transport and Pore Structure. *AIChE J*. 2015;61(9):2993-2999.
248. Ho TA, Argyris D, Papavassiliou D V., Striolo A, Lee LL, Cole DR. Interfacial water on crystalline silica: a comparative molecular dynamics simulation study. *Mol Simul*. 2011;37(3):172-195.
249. Causa M, Dovesi R, Pisani C, Roetti C. Ab initio Hartree-Fock study of the MgO(001) surface. *Surf Sci*. 1986;175:551-560.
250. A. Scamehorn C, C. Hess A, I. McCarthy M. Correlation corrected periodic Hartree-Fock study of the interactions between water and the (001) magnesium oxide surface. *J Chem Phys*. 1993;99:2786-2795.
251. Cygan RT, Liang J-J, Kalinichev AG. Molecular Models of Hydroxide, Oxyhydroxide, and Clay Phases and the Development of a General Force Field. *J Phys Chem B*. 2004;108(4):1255-1266.
252. Xiao S, Edwards SA, Gräter F. A new transferable forcefield for simulating the mechanics of CaCO₃ crystals. *J Phys Chem C*. 2011;115(41):20067-20075.
253. Martin MG, Siepmann JI. Transferable Potentials for Phase Equilibria. 1. United-Atom Description of n-Alkanes. *J Phys Chem B*. 1998;102(97):2569-2577.
254. Jorgensen WL, Maxwell DS, Tirado-Rives J. Development and testing of the OPLS all-atom force field on conformational energetics and properties of organic liquids. *J Am Chem Soc*. 1996;118(45):11225-11236.
255. Essmann U, Perera L, Berkowitz ML, Darden T, Lee H, Pedersen LG. A smooth particle mesh Ewald method. *J Chem Phys*. 1995;103(19):8577-8593.
256. Lorentz HA. Ueber die Anwendung des Satzes vom Virial in der kinetischen Theorie der Gase. *Ann Phys*. 1881;248(1):127-136.
257. Berthelot D. Sur Le Mélange Des Gaz. *Compt Rendus*. 1898;126:1703-1706.
258. Siperstein F, Myers AL, Talu O. Long range corrections for computer simulations of adsorption. *Mol Phys*. 2002;100(13):2025-2030.
259. Van Der Spoel D, Lindahl E, Hess B, Groenhof G, Mark AE, Berendsen HJC. GROMACS: Fast, flexible, and free. *J Comput Chem*. 2005;26(16):1701-1718.
260. Hess B, Kutzner C, Van Der Spoel D, Lindahl E. GROMACS 4: Algorithms for highly efficient, load-balanced, and scalable molecular

- simulation. *J Chem Theory Comput.* 2008;4(3):435-447.
261. Nosé S. A molecular dynamics method for simulations in the canonical ensemble. *Mol Phys.* 1984;52(2):255-268.
262. Hoover WG. Canonical dynamics: Equilibrium phase-space distributions. *Phys Rev A.* 1985;31(3):1695-1697.
263. Hockney RW, Goel SP, Eastwood JW. Quiet High-Resolution Computer Models of a Plasma. *J Comput Phys.* 1974;14(2):148-158.
264. Crank J. Methods of solution when the diffusion coefficient is constant. In: *The Mathematics of Diffusion.* 2nd ed. Oxford, UK: Oxford University Press; 1975:11-27.
265. Franco LFM, Castier M, Economou IG. Anisotropic parallel self-diffusion coefficients near the calcite surface: A molecular dynamics study. *J Chem Phys.* 2016;145(8).
266. Kou R, Alafnan SFK, Akkutlu IY, Texas A, Station C. Coupling of Darcy ' s Equation with Molecular Transport and its Application to Upscaling Kerogen Permeability. *SPE Eur Featur 78th EAGE Conf Exhib 30 May-2 June, Vienna, Austria SPE-180112-MS.* 2016:1-16.
267. Energy Information Administration (EIA). Shale Gas Production. *Nat Gas.* 2014:123-152.
268. BP. *Energy Outlook.*; 2019.
269. Jarvie DM. Shale Resource Systems for Oil and Gas: Part 1—Shale-gas Resource Systems. Breyer JA, ed. *AAPG Mem.* 2012;97:69-87.
270. Bear J. Fluid and Porous Matrix Properties. In: *Dynamics of Fluids in Porous Media.* New York, USA: Dover Publications, INC; 1972:27-57.
271. Kwon O, Kronenberg AK, Gangi AF, Johnson B, Herbert BE. Permeability of illite-bearing shale: 1. Anisotropy and effects of clay content and loading. *J Geophys Res B Solid Earth.* 2004;109(10):1-19.
272. Sahimi M. Characterization of the Morphology of Porous Media. In: *Flow and Transport in Porous Media and Fractured Rock: From Classical Methods to Modern Approaches.* 2nd ed. Leipzig, Germany: Wiley-VCH Verlag GmbH & Co. KGa; 2011:39-108.
273. Chen S, Lee EKC, Chang Y. Effect of the coordination number of the pore-network on the transport and deposition of particles in porous media. *Sep Purif Technol.* 2003;30:11-26.
274. Vasilyev L, Raouf A, Nordbotten JM. Effect of Mean Network Coordination Number on Dispersivity Characteristics. *Transp Porous Media.* 2012;95:447-463.
275. Rabbani A, Ayatollahi S, Kharrat R, Dashti N. Advances in Water Resources Estimation of 3-D pore network coordination number of rocks from watershed segmentation of a single 2-D image. *Adv Water Resour.* 2016;94:264-277.

276. Dong H, Blunt MJ. Pore-network extraction from micro-computerized-tomography images. *Phys Rev E*. 2009;(036307):1-11.
277. Peng S, Hu Q, Dultz S, Zhang M. Using X-ray computed tomography in pore structure characterization for a Berea sandstone : Resolution effect. *J Hydrol*. 2012;472-473:254-261.
278. Mata VG, Lopes JCB, Dias MM. Porous Media Characterization Using Mercury Porosimetry Simulation . 2 . An Iterative Method for the Determination of the Real Pore Size Distribution and the Mean Coordination Number. *Ind Eng Chem Res*. 2001;40:4836-4843.
279. Tsakiroglou CD, Payatakes AC. Characterization of the pore structure of reservoir rocks with the aid of serial sectioning analysis , mercury porosimetry and network simulation. *Adv Water Resour*. 2000;23:773-789.
280. Davudov D, Moghanloo RG, Yuan B. Impact of Pore Connectivity and Topology on Gas Productivity in Barnett and Haynesville Shale Plays. *Unconv Resour Technol Conf held San Antonio, Texas, USA, 1-3 August 2016 URTEC -2461331*. 2016.
281. King HE, Eberle APR, Walters C, Kliewer CE, Ertas D, Huynh C. Pore Architecture and Connectivity in Gas Shale. *Energy and Fuels*. 2015;29:1375-1390.
282. Chalmers GR, Bustin RM, Power IM. Characterization of gas shale pore systems by porosimetry, pycnometry, surface area, and field emission scanning electron microscopy/ transmission electron microscopy image analyses: Examples from the Barnett, Woodford, Haynesville, Marcellus, and Doig units. *Am Assoc Pet Geol Bull*. 2012;96(6):1099-1119.
283. Hu Q, Ewing RP, Rowe HD. Low nanopore connectivity limits gas production in Barnett Formation. *J Geophys Res Solid Earth*. 2015;120.
284. King GE, Rainbolt MF, Swanson C, Corporation A. Frac Hit Induced Production Losses : Evaluating Root Causes , Damage Location , Possible Prevention Methods and Success of Remedial Treatments. *SPE Annu Tech Conf Exhib held San Antonio, Texas, USA, 9-11 October SPE-187192-MS*. 2017.
285. Yu W, Xu Y, Weijermars R, Wu K, Sepehrnoori K. Impact of Well Interference on Shale Oil Production Performance : A Numerical Model for Analyzing Pressure Response of Fracture Hits with Complex Geometries. *SPE Annu Tech Conf Exhib held Woodlands, Texas, USA, 24-26 January SPE-184825-MS*. 2017.
286. Davudov D, Moghanloo RG. International Journal of Coal Geology Impact of pore compressibility and connectivity loss on shale permeability. *Int J Coal Geol*. 2018;187:98-113.
287. Civan F. Scale Effect on Porosity and Permeability : Kinetics , Model , and Correlation. *AIChE J*. 2001;47(2).
288. Pape H, Clauser IC, Iffland J. Variation of Permeability with Porosity in Sandstone Diagenesis Interpreted with a Fractal Pore Space Model. *Pure*

- Appl Geophys.* 2000;157:603-619.
289. Thakur P. Porosity and Permeability of Coal. In: *Advanced Reservoir and Production Engineering for Coal Bed Methane*. Cambridge, MA, USA: Elsevier Inc.; 2017:33-49.
 290. Akintunde OM, Knapp CC, Knapp JH. Tectonophysics Tectonic significance of porosity and permeability regimes in the red beds formations of the South Georgia Rift Basin. *Tectonophysics*. 2014;632:1-7.
 291. Akinlotan O. Proceedings of the Geologists ' Association Porosity and permeability of the English (Lower Cretaceous) sandstones. *Proc Geol Assoc*. 2016;127(6):681-690.
 292. Archie GE. Introduction to Petrophysics of Reservoir Rocks. 1950;34(5):943-961.
 293. Shen X, Li L, Cui W, Feng Y. International Journal of Heat and Mass Transfer Improvement of fractal model for porosity and permeability in porous materials. *Int J Heat Mass Transf*. 2018;121:1307-1315.
 294. Magara K. Porosity-Permeability relationship in Shales. In: *Compaction and Fluid Migration*. Elsevier Inc.; 1978:201-216.
 295. Mandelbrot B. *The Fractal Geometry of Nature*. San Francisco, USA: W. H. Freeman and Company; 1985.
 296. Katz AJ, Thompson AH. Fractal Sandstone Pores: Implications for Conductivity and Pore Formation. *Phys Rev Lett*. 1985;54(12):1325-1328.
 297. Yu B, Li J. Some Fractal Characters of Porous Media. *Fractals*. 2001;9(3):365-372.
 298. Rieu M, Sposito G. Fractal Fragmentation, Soil Porosity, and Soil Water Properties: I. Theory. *Soil Sci Soc Am J*. 1991;55:1231-1238.
 299. Zhang H, Liu J, Elsworth D. How sorption-induced matrix deformation affects gas flow in coal seams : A new FE model. 2008;45:1226-1236.
 300. Sheng G, Javadpour F, Su Y. Dynamic porosity and apparent permeability in porous organic matter of shale gas reservoirs. *Fuel*. 2019;251(February):341-351.
 301. Jamialahmadi M, Javadpour FG. Relationship of permeability , porosity and depth using an artificial neural network. *J Pet Sci Eng*. 2000;26:235-239.
 302. Nelson PH. Pore-throat sizes in sandstones , tight sandstones , and shales. *Am Assoc Pet Geol Bull*. 2009;93(3):329-340.
 303. Zhang Y, Bao Z, Yang F, Mao S, Song J, Jiang L. The Controls of Pore-Throat Structure on Fluid Performance in Tight Clastic Rock Reservoir : A Case from the Upper Triassic of Chang 7 Member, Ordos Basin, China. *Geofluids*. 2018;(3403026):15-24.
 304. Katsube T., Issler D., Cox W. *Shale Permeability and Its Relation to Pore-Size Distribution*. Canadian Government Publishing; 1998.

305. Phan A, Cole DR, Striolo A. Factors governing the behaviour of aqueous methane in narrow pores. *Philos Trans R Soc A*. 2016;374:1-13.
306. Yang Y, Aplin AC. Permeability and petrophysical properties of 30 natural mudstones. *J Geophys Res Solid Earth*. 2007;112(3).
307. Merriman RJ, Highley DE, Cameron DG. *Definition and Characteristics of Very-Fine Grained Sedimentary Rocks: Clay, Mudstone, Shale and Slate.*; 2003.
308. Zou C. Shale gas. In: *Unconventional Petroleum Geology*. San Diego, CA, USA: Elsevier Inc.; 2013:149-190.
309. Prasianakis NI, Gatschet M, Abbasi A, Churakov S V. Upscaling Strategies of Porosity-Permeability Correlations in Reacting Environments from Pore-Scale Simulations. *Geofluids*. 2018;2018:1-9.
310. Al Ismail MI, Zoback MD. Effects of Rock Mineralogy and Pore Structure on Extremely Low Stress-Dependent Matrix Permeability of Unconventional Shale Gas and Shale Oil Samples. *R Soc Philos Trans A*. 2016;374(20150428):1-17.
311. Jaripatke OA, Barman I, Ndungu JG, Schein GW, Flumerfelt RW, Burnett N. Review of Permian Completion Designs and Results. *SPE Annu Tech Conf Exhib held Dallas, Texas, 24-26 Sept SPE-191560-MS*. 2018.
312. Sen V, Min KS, Ji L, Sullivan R, Corporation AP. Completions and Well Spacing Optimization by Dynamic SRV Modeling for Multi-Stage Hydraulic Fracturing Basics of Dynamic SRV (DSRV) Modeling Implementation of the DSRV Workflow. *SPE Annu Tech Conf Exhib held Dallas, Texas, USA, 24–26 Sept SPE 191571- MS*. 2018.
313. Sudakov O, Burnaev E, Koroteev D. Driving Digital Rock towards Machine Learning : predicting permeability with Gradient Boosting and Deep Neural Networks Driving Digital Rock towards Machine Learning : predicting permeability with Gradient Boosting and Deep Neural Networks. *Comput Geosci*. 2018;(127):91-98.